Modeling, Optimization, and Detailed Design of a Hydraulic Flywheel-Accumulator

A THESIS
SUBMITTED TO THE FACULTY OF THE
UNIVERISTY OF MINNESOTA
BY

Kyle Glenn Strohmaier

IN PARTIAL FULFILLMENT OF THE REQUIREMENTS
FOR THE DEGREE OF
MASTER OF SCIENCE

Adviser: James Van de Ven, Ph.D.

July 2014

I would like to thank my adviser, Dr. James Van de Ven, for providing me the opportunity to partake in this fascinating research and for his guidance and patience throughout the process.

This work was sponsored by the National Science Foundation through the Center for Compact and Efficient Fluid Power, grant EEC-0540834.

Abstract

Improving mobile energy storage technology is an important means of addressing concerns over fossil fuel scarcity and energy independence. Traditional hydraulic accumulator energy storage, though favorable in power density, durability, cost, and environmental impact, suffers from relatively low energy density and a pressure-dependent state of charge. The hydraulic flywheel-accumulator concept utilizes both the hydro-pneumatic and rotating kinetic energy domains by employing a rotating pressure vessel. This thesis provides an in-depth analysis of the hydraulic flywheel-accumulator concept and an assessment of the advantages it offers over traditional static accumulator energy storage.

After specifying a practical architecture for the hydraulic flywheel-accumulator, this thesis addresses the complex fluid phenomena and control implications associated with multi-domain energy storage. To facilitate rapid selection of the hydraulic flywheel-accumulator dimensions, computationally inexpensive material stress models are developed for each component. A drive cycle simulation strategy is also developed to assess the dynamic performance of the device. The stress models and performance simulation are combined to form a toolset that facilitates computationally-efficient model-based design.

The aforementioned toolset has been embedded into a multi-objective optimization algorithm that aims to minimize the mass of the hydraulic flywheel-accumulator system and to minimize the losses it incurs over the course of a drive cycle. Two optimizations have been performed – one with constraints that reflect a vehicle-scale application, and one with constraints that reflect a laboratory application. At both scales, the optimization results suggest that the hydraulic flywheel-accumulator offers at least an order of magnitude improvement over traditional static accumulator energy storage, while operating at efficiencies between 75% and 93%. A particular hydraulic flywheel-accumulator design has been selected from the set of laboratory-scale optimization results and subjected to a detailed design process. It is recommended that this selection be constructed and tested as a laboratory prototype.

Table of Contents

List of Tables

List of Figures

1 Introduction

1.1 Greenhouse Gas Emissions and Traditional Vehicles

The Industrial Revolution of the early 19th century led to enormous growth in carbon dioxide (CO_2) emissions, marking the beginning of the phenomenon known as climate change [1]. Since then, atmospheric CO_2 concentrations have continued to rise drastically, and climatologists have cited species extinction, forced mass migration, and more frequent natural disasters as some of the negative consequences [2, 3, 4]. The Intergovernmental Panel on Climate Change confirms that humans are at fault for climate change, stating in its Fourth Assessment Report that, with more than 90 percent certainty, "most of the observed increase in globally averaged temperatures since the mid-20th century" has been caused by humans via greenhouse gas (GHG) emissions [1]. Accompanying the human culpability of excessive GHG emissions is the ability to curtail them, thereby mitigating or reversing the potentially devastating impacts of climate change.

While many atmospheric gasses act as heat-trapping GHGs, CO_2 contributes to climate change far more than any other gas [1]. CO_2 is emitted primarily through the combustion of fossil fuels (coal, gasoline, etc.) during energy production, industrial processes, automobile propulsion, and other activities. Figure 1 [1] compares the relative contribution of various sectors to global GHG emissions. Clearly, the transportation sector is a significant contributor to global GHG emissions. In the U.S., the transportation sector is responsible for a full 28% of GHG emissions [5], second only to electricity generation. Because over 90% of the energy used for transportation comes from the burning of petroleum-based fuel [6], a changeover to cleaner, more efficient vehicle propulsion is a promising way to reduce GHG emissions [7], thereby helping to mitigate climate change.

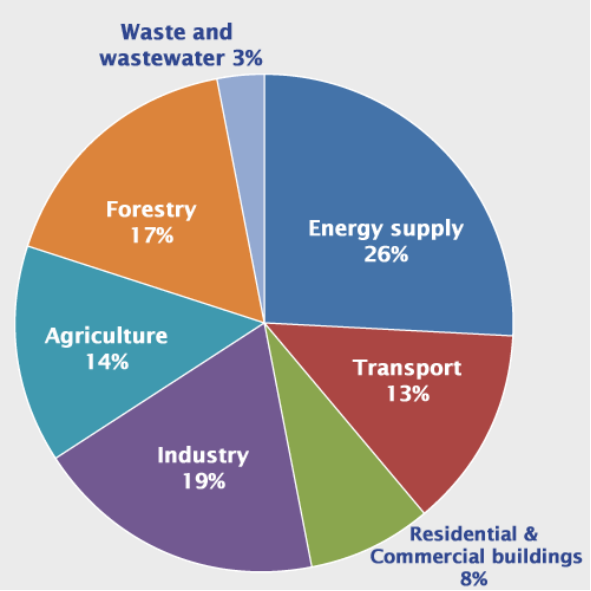

Figure 1: Global Greenhouse Gas Emissions by Sector [1]

The energy storage medium in a traditional passenger vehicle is a liquid fuel. An internal combustion engine (ICE) acts as an energy conversion mechanism, converting the energy stored in the chemical bonds of the fuel into rotational kinetic energy. For a diesel engine with a 16:1 compression ratio, the thermodynamic upper limit on efficiency is 57% [8]. However, due to imperfect combustion, mechanical losses, and non-ideal operating conditions, actual engine efficiency is far lower for a typically automobile duty cycle. In addition to being quite inefficient, the process by which an ICE produces mechanical power is irreversible; when the vehicle decelerates, the available kinetic energy cannot be converted back to stored chemical energy, but instead must be dissipated as heat by mechanical brakes. In other words, energy regeneration is not possible in vehicles with traditional powertrains.

1.2 Alternative Powertrains

In an effort to address the cited drawbacks of traditional ICE vehicles, hybrid powertrains have been the subject of much research and development for the last several decades. A

hybrid powertrain consists of two fundamentally different energy storage-conversion pairs. One of these pairs is generally a liquid fuel and ICE, as in a traditional vehicle. The secondary pair, which utilizes an energy domain that is capable of regeneration, interacts with the first pair in such a way to mitigate the drawbacks of fossil fuel energy conversion. Figure 2 depicts the two most basic hybrid powertrain architectures, series and parallel. The ICE energy storage-conversion pair is labeled "A," and the secondary pair is labeled "B."

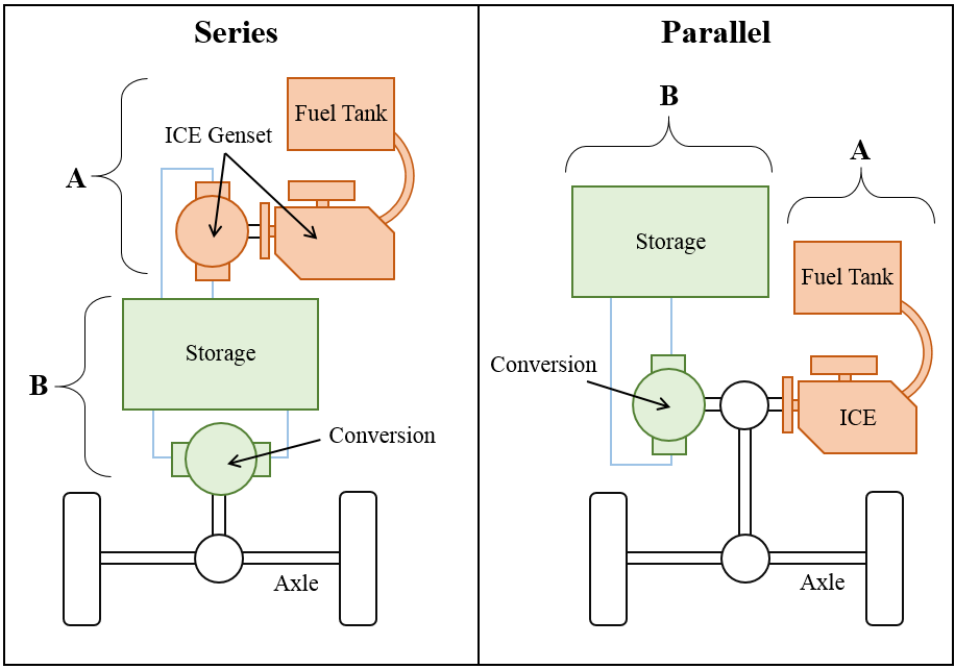

Figure 2: The Two Most Basic Hybrid Vehicle Powertrain Architectures, Series and Parallel. The ICE and secondary energy storage-conversion pairs are labelled "A" and "B," respectively.

In a series hybrid powertrain, all of the axle torque is provided by the secondary energy conversion machine, with the ICE generator set ("genset") replenishing the secondary energy storage device as necessary. A parallel hybrid powertrain, in contrast, provides axle torque using both the ICE and the secondary energy conversion machine, and the secondary energy storage device is recharged only via regenerative braking. It is common to construct "power-split" hybrid powertrains, which are capable of operating in both series and parallel modes. There are at least four means by which the benefits of a hybrid powertrain are realized:

1. In a parallel architecture, the ICE can be downsized and more heavily loaded during normal operation, with the secondary power source assisting during peak power demand. An ICE runs more efficiently when heavily loaded [8].
2. In a series architecture, the engine can be run at its most efficient operating point and can be turned off when the secondary energy storage system is sufficiently charged.
3. When the vehicle brakes, the secondary energy conversion mechanism can operate in generation mode, recharging its associated storage system with energy that would otherwise be converted to waste heat.
4. With "plug-in" capability, the secondary energy storage system can be charged using clean or renewable energy sources. Even when renewable sources are not available, using energy from traditional grid power generation methods generally results in fewer emissions per mile [9].

Among passenger hybrid vehicles, electrified powertrain components are the most common means of hybridization. The storage mechanism in this case is usually an electrochemical battery, although ultracapacitors or hydrogen fuel cells can also be used [10]. The energy conversion device is an electric machine, such as a DC, synchronous, or asynchronous motor. Electric powertrain components are capable of storing and converting energy very efficiently – often above 90% for the battery, motor and power electronics combined [11]. They offer clean, simple vehicle integration, and the very low number of moving parts makes these components more reliable than the engine and transmission used in a traditional powertrain. Electric components also offer versatile and highly-accurate controllability.

Generally, the weakest link in an electric powertrain is the energy storage medium. Electrochemical batteries are the most energy-dense electrical energy storage media at present (though they are still about two orders of magnitude less energy dense than liquid fossil fuels [8, 12]). However, they have poor power density and suffer from a limited shelf and cycle life [13]. Furthermore, rare earth metals, which are expensive and environmentally-unfriendly to mine, are required to manufacture high performance batteries. Ultracapacitors have been proposed as a replacement for electrochemical

batteries in electric powertrains. These devices are cheaper, more durable, and offer an order of magnitude higher power density than electrochemical batteries. Their energy density, however, is generally at least an order of magnitude lower [13].

As an alternative to electrified hybrid powertrains, there has been some research on using flywheels as a secondary energy storage system. Frank et al [14] reported a 33% improvement in fuel economy by coupling a flywheel a hydrostatic transmission in series with an ICE. A major drawback of this architecture is that all of the tractive power must be transmitted through the relatively inefficient hydrostatic transmission. More recently, Ricardo [15] has received accolades for its commercialization of an integrated carbon fiber composite flywheel and magnetic transmission. The energy density of this unit, however, is reportedly only 2 kJ/kg.

1.3 Hydraulic Powertrain Components

Given the cited drawbacks of powertrains that use electric components or pure flywheel systems, there is strong justification to consider hydraulics as an alternative means of automotive propulsion. Hydraulic systems utilize the pressure and flow of a fluid to produce power and/or achieve motion control. Compared to electric machines, hydraulic pumps and motors offer significantly higher power density and durability [16]. They are also far less expensive to manufacture. The traditional means of storing hydraulic energy is with a hydro-pneumatic accumulator, a pressure vessel in which a bladder, diaphragm, or piston separates a hydraulic fluid from a pre-charged gas. While the mass of the gas remains fixed (neglecting any leakage), its volume can be changed by pumping hydraulic fluid into or out of the accumulator. In changing its volume (and therefore pressure), the amount of pneumatic energy stored in the gas is changed. Figure 3 shows a diagram of a traditional piston-type hydraulic accumulator.

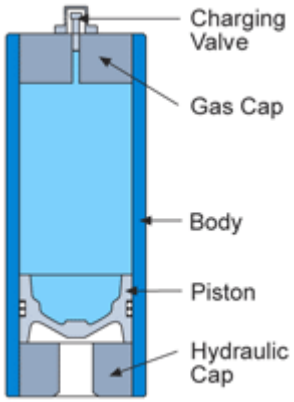

Figure 3: Illustration of a Traditional Piston-type Hydraulic Accumulator [17]

The energy density of a hydraulic accumulator is optimized when the volumetric expansion ratio is 2.71 if the gas compression is isothermal or 2.31 if the gas compression is adiabatic [18]. State-of-the-art hydraulic accumulators use composite materials to minimize the mass of the fluid containment while withstanding the high stresses imposed by the internal pressure. Even with these high performance materials, the energy density of accumulators today is about 6 kJ/kg at best [19], which is two orders of magnitude lower than current Li-Ion battery technology. Although hydraulic accumulators offer far higher power density and durability at a much lower cost than electrical energy storage media, the two order of magnitude discrepancy in energy density presents a difficult barrier to the viability of hydraulics as a means for alternative propulsion.

An additional drawback of traditional hydraulic energy storage is the coupling between pressure and state-of-charge (SOC). When an accumulator is charged, the volume and pressure of the gas are P_c and V_c, respectively. The gas pressure, P_p, is higher when the accumulator is storing usable energy, but thermodynamics dictate that P_p drops precipitously as energy is extracted from an accumulator. This relationship is shown in Fig. 4, with dimensionless energy on the x-axis and dimensionless pressure on the y-axis.

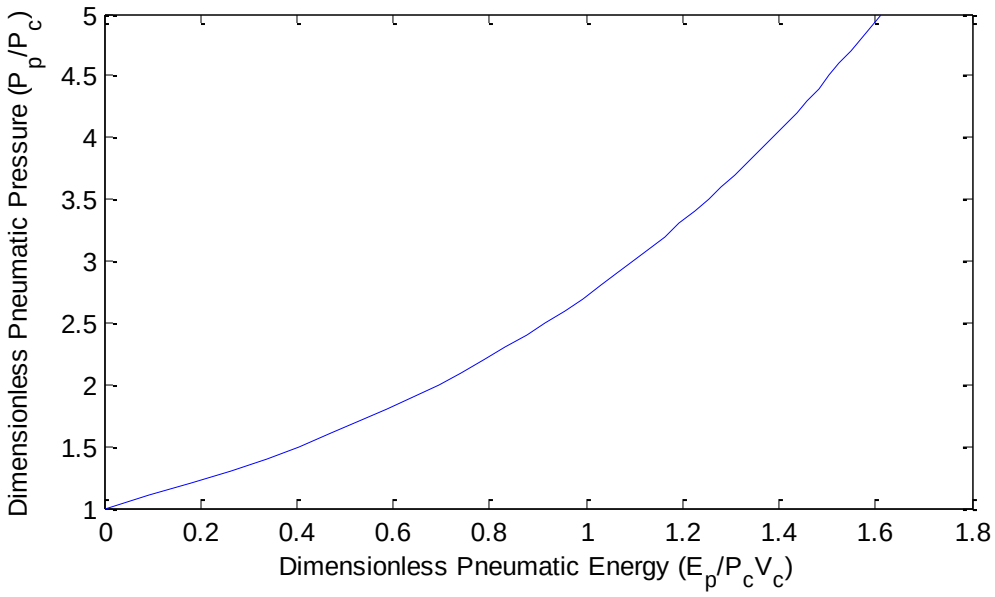

Figure 4: Dimensionless Pressure as a Function of Dimensionless Energy for a Traditional Accumulator

It is clear from Fig. 4 that, when operating at, say, 50% SOC, system pressure is well below 50% of the pressure at full SOC. Hydraulic pumps and motors are sized based on peak flow rate, and since hydraulic power is equal to the product of pressure and flow rate, a lower system pressure requires a higher flow rate to meet a given power demand. The major implication of the pressure-SOC coupling in a traditional accumulator, then, is that pumps and motors must be oversized to accommodate the low pressures associated with low states-of-charge. This adds both mass and cost to the hydraulic system.

Much of the past research on traditional hydraulic accumulators has focused on optimizing the efficiency of the gas compression process. By improving the convection coefficient between the gas and the outside environment, the compression and decompression of the gas within the accumulator can be made to approach isothermal processes. Researchers have placed elastomeric foams [19] or metallic strands [20] in the gas volume in an effort to increase convection without affecting the functionality of the accumulator. While these methods have shown some success, they offer only incremental improvements to hydraulic energy storage.

Li et al [18] have addressed the two cited drawbacks of hydraulic energy storage (low energy storage density and pressure-SOC coupling) with their open accumulator concept. In an open accumulator, the mass of the gas is not fixed, but rather can be added or extracted using a pneumatic compressor/motor. By using a non-fixed gas molarity, an open air accumulator can operate at very high expansion ratios, theoretically increasing energy density by an order of magnitude, compared to a traditional accumulator. The ability to change both the oil and gas masses in the open accumulator decouples pressure from the amount of stored energy. The main challenges with the open accumulator concept arise from the large amount of convective heat transfer required for near-isothermal (i.e. efficient) operation.

The strain energy accumulator is another concept aimed at overcoming the main drawbacks of traditional hydraulic energy storage. Instead of using gas compression as the fundamental energy storage mechanism, the strain energy accumulator stores energy in the strain of a polyurethane bladder. As a result, the strain energy accumulator increases energy density by an estimated 2-3 times over a traditional accumulator while mitigating compression losses and gas diffusion across the bladder [21]. The primary challenges with the strain energy accumulator are the complex hysteresis effects associated with elastic materials, as well as the difficulty of gripping a strong, highly-strained material [22].

1.4 The Hydraulic Flywheel-Accumulator Concept

The hydraulic flywheel-accumulator (HFA), proposed by Van de Ven [23], has the potential to overcome both of the major drawbacks of a traditional hydraulic accumulator, significantly increasing energy storage density while decoupling system pressure from state-of-charge. In the most basic sense, the HFA is a piston-type accumulator which is spun about its longitudinal axis. As in a traditional accumulator, pneumatic energy can be added or extracted via the addition or extraction of oil through a port. A special fluid coupling known as a “high-speed rotary union” (HSRU) facilitates this exchange of oil between the rotating HFA and the static environment. A hydraulic

pump-motor (PM) coupled to the gas-side of the HFA controls the rotational speed by applying a motoring or braking torque. This machine will be referred to as the "storage PM" to differentiate from the "traction PM" that is coupled to the vehicle's axle. A schematic of the hydraulic flywheel-accumulator implemented in a pure hydraulic powertrain is shown in Fig. 5.

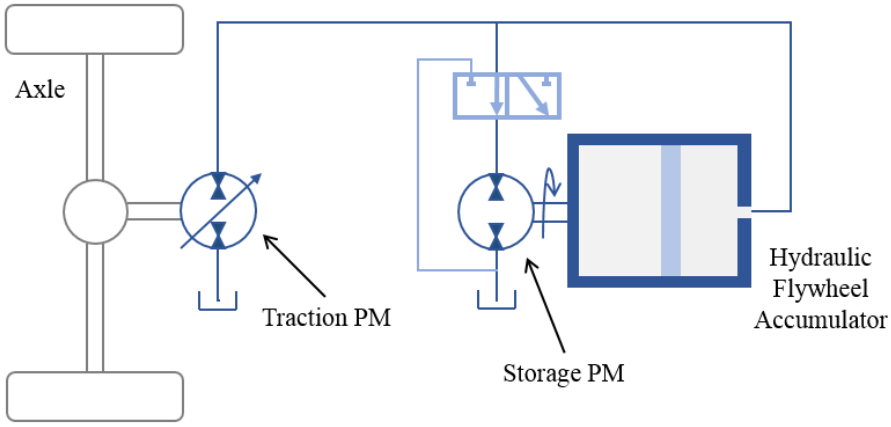

Figure 5: Pure Hydraulic Powertrain with a Hydraulic Flywheel Accumulator as the Sole Energy Storage Medium. Shown with a Fixed-Displacement Storage Pump-Motor

Kinetic energy is stored in the HFA by virtue of its rotation and the combined moment of inertia (henceforth referred to simply as "inertia") of the solid container and the internal fluid volume. Previous work on the HFA concept suggests that the employment of the kinetic energy domain can potentially increase energy storage density by an order of magnitude over traditional accumulator storage [23].

In addition to increasing energy density, imposing a rotation on a hydraulic accumulator leads to the centrifugation of the internal fluid. Van de Ven [23] showed that, as a result, the pressure distribution in the hydraulic oil is a parabolic function of radial position. As the position of the port coincides with the vertex of this parabola, the rest of the hydraulic system experiences a pressure that is lower than the average HFA pressure – that which defines the amount of stored pneumatic energy. This concept is illustrated in Fig. 6.

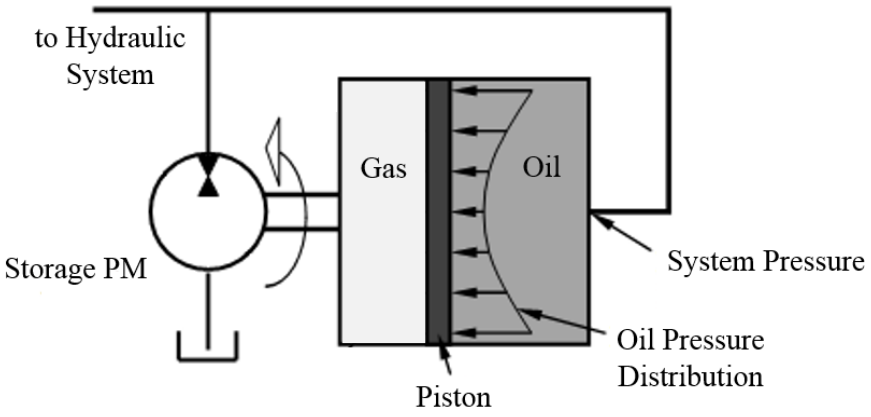

Figure 6: Illustration of the Parabolic Oil Pressure Distribution with System Pressure at the Vertex (Gas Pressure Distribution Not Shown)

The intensity of the parabola, which determines the difference between the system pressure and average HFA pressure, is a function of rotational speed, hydraulic fluid density, and container geometry. The ability to actively control rotational speed via the storage PM adds an additional control variable when compared to a traditional accumulator, effectively decoupling system pressure from SOC. This decoupling is explained in detail in Section 2.4.

1.5 Research Goals and Approach

The hydraulic flywheel-accumulator concept offers the opportunity to overcome the major issues associated with traditional hydraulic energy storage. This opportunity is accompanied by significant design challenges. The present research addresses these design challenges in an effort to prove the hydraulic flywheel-accumulator concept. In summary, the goals of this research are:

- To specify a physically feasible design that facilitates the HFA concept
- To facilitate model-driven design by modeling all of the relevant physics associated with the HFA
- To build computational tools that facilitate performance simulation of the HFA

- To use the developed tools to choose an optimal set of design parameters for a laboratory prototype

The scope of the present research includes the conceptual design, model development, optimization and detailed design of the HFA itself. This does not include the detailed design of the containment chamber, control strategy optimization, or hybrid powertrain integration. To remove the effect of variables that are outside the scope of the research, it is appropriate to consider the HFA in isolation from any other energy storage media. As such, this paper focuses on the context of the HFA operating in a purely hydraulic powertrain (or alternatively, in a hydraulic-hybrid powertrain operating in charge-depleting mode). All proceeding discussion presumes that the HFA is being designed for a system pressure of 21 MPa (3000 psi).

The remainder of this thesis documents how the goals of this research have been addressed. Chapter 2 provides a detailed description of the HFA concept, including the variables which define a particular HFA design, the basic equations that describe its stored energy, the means by which it is controlled, and the primary objectives in its design. In Chapter 3, analytical stress models are developed and materials are selected for each of the major components that constitute the HFA. Models for the various energy loss mechanisms are developed in Chapters 4 and 5, with the latter focusing on the complex behavior of the rotating fluid within the HFA. Chapter 6 describes the HFA performance simulation methods, including the selection of a simple control strategy.

The modeling and simulation tools developed in Chapters 3 through 6 have been interfaced and embedded into an optimization algorithm. Chapter 7 presents the results of design optimizations for a vehicle-scale and a laboratory-scale HFA and justifies the selection of a particular HFA solution for a laboratory prototype. A detailed design is conducted in Chapter 8 for this prototype. Chapter 9 closes the thesis by summarizing the methods and results of the present research and recommending future work for the HFA concept.

2 General Architecture and Operation

The most distinguishing feature of the HFA is its use of more than one energy domain. Combining kinetic and pneumatic energy storage into one device offers interesting benefits and requires thorough analysis of the coupling between the energy domains. This chapter begins with a general description of the HFA architecture. Next, the pneumatic and kinetic energy domains are addressed, first individually and then as a coupled system. An overview of a simple HFA control strategy is presented next, and the chapter closes by justifying the general optimization objectives and constraints.

2.1 Architecture and Design Variables of the Hydraulic Flywheel-Accumulator

Before any analysis or modeling can occur, a physically-feasible architecture for the HFA must be specified. This section justifies the selected architecture and describes the role of each component.

The main component of the HFA is the housing, a hollow circular cylinder which acts both as a flywheel rotor, storing the majority of the kinetic energy in the HFA, and as a mechanism to contain fluid pressure in the radial direction. The housing consists of a composite cylinder with a metallic liner, as shown in Fig. 7. Most of the strength of the housing is provided by the composite, while the liner facilitates sealing to prevent fluid leakage. The inner and outer radii if the housing are, respectively, r_i and r_o, and the housing has an overall length l_h. The liner has a thickness of th_l.

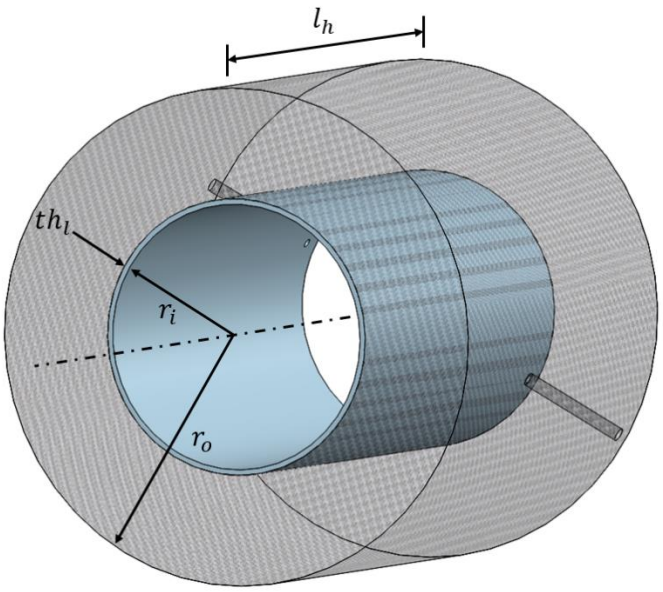

Figure 7: Hybrid Housing, Made of Metallic Liner and Composite Wrap

Two end caps fit inside of the housing, such that their outer radius is equal to the housing inner radius r_i. The end caps fit concentrically on an axle. The end cap and axle system, shown in Fig. 8, acts to contain fluid pressure in the axial direction. Retaining rings prevent outward axial movement of the end caps and, on the gas side, transmit torque between the end cap and the axle. The gas side of the axle is coupled to the storage PM. The axle has internal ports of diameter d_i on the oil side of the HFA to allow for addition and extraction of oil. The gas-side end cap, nearest to the storage PM, is constrained to the housing with radial pins, which prevent motion in the axial and tangential directions. The tangential constraint prevents relative angular movement between the gas-side end cap and the housing, allowing for transmission of torque between these two components. The axial constraint imposed by the pins prevents the housing from slipping axially on the end cap-axle assembly. The oil-side end cap is constrained to the housing only concentrically, such that the internal pressure of the HFA does not impose any axial stress on the housing via the end caps. Besides the compressive interaction that might arise during HFA operation, there is no radial constraint between the end caps and the housing.

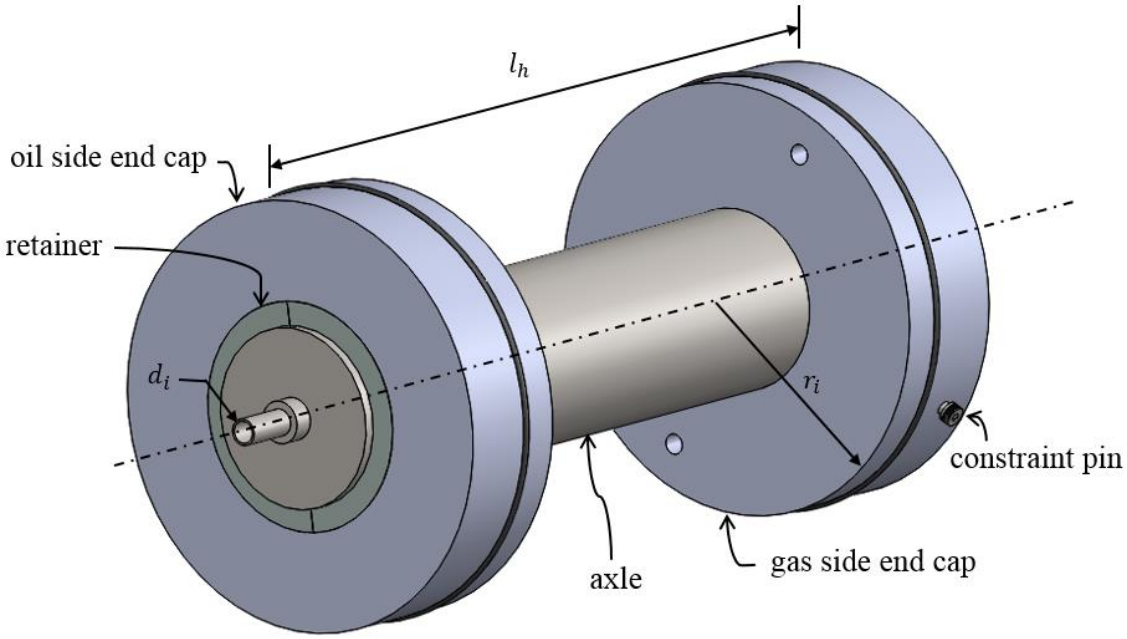

Figure 8: End Cap and Axle System

The piston, which separates the oil from the gas, has axially-sliding seals at both the axle and the housing. Figure 9 shows a radial cutaway view illustrating the spatial relations between the piston, axle and end caps. The piston seals and the location at which the storage PM applies a torque, T, to the axle are labeled.

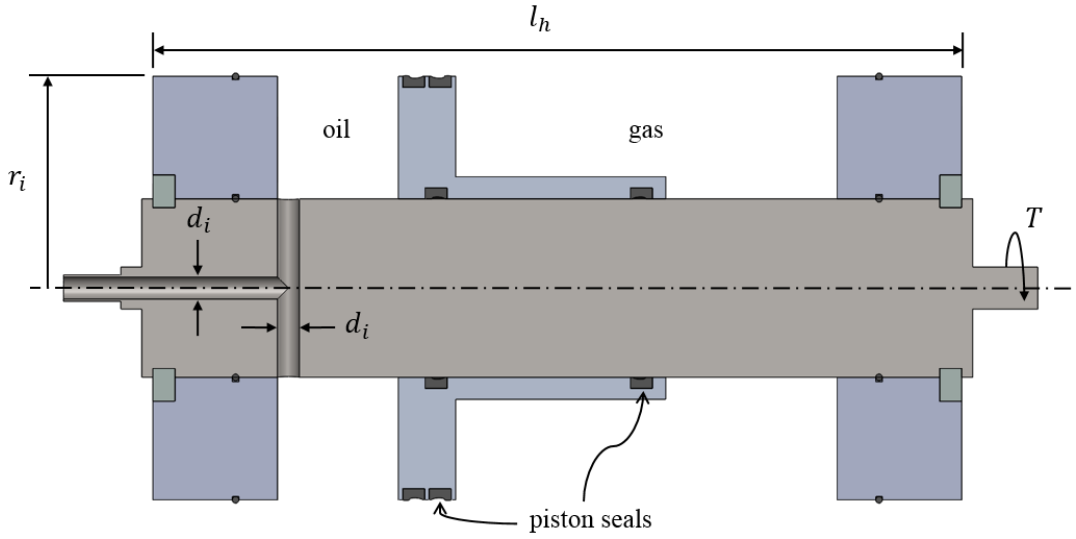

Figure 9: Illustration of the Spatial Relations between the Piston, Axle and End Caps

It is worth noting that the presence of the axle improves the bearing ratio of the sliding interface between the piston and housing. In other words, the parallelism between the central axes of the piston and the housing is more reliable than if the axle were absent [24].

The end of the oil side of the axle constitutes part of the high-speed rotary union (HSRU). The section of the axle with the smallest diameter protrudes into the HSRU case. The two form a non-contacting circumferential seal of clearance c_s and length l_s, the purpose of which is to control leakage without any solid-to-solid contact at the rotating interface. A schematic of the HSRU is shown in Fig. 10.

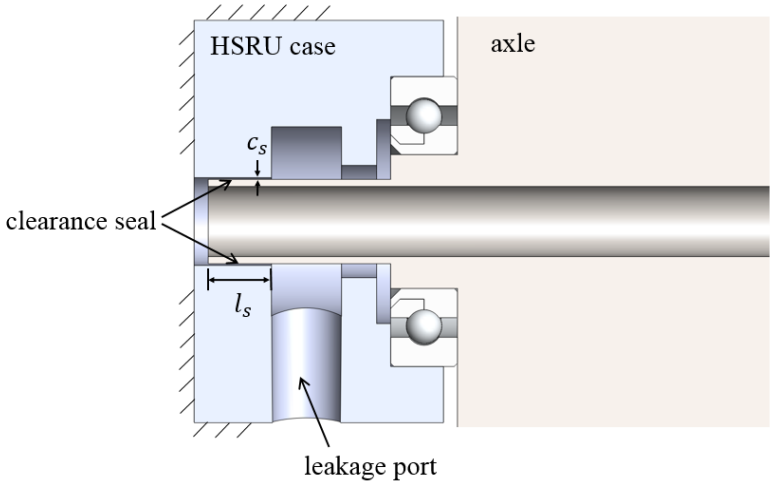

Figure 10: Schematic of the High-Speed Rotary Union (HSRU) Concept

The seven geometric dimensions that have been named in this section are design variables. In addition to the seven geometric design variables, there are two operational design variables: maximum allowable angular velocity, ω_{max}, and HFA charge pressure, P_c. The HFA design variables and the units with which their values are conveniently expressed are listed in Table 1. In the remainder of this paper, a particular set of values for the nine design variables will be referred to as a "design solution."

Table 1: The Nine Design Variables which Constitute a Design Solution for the HFA

Geometric	
Housing inner radius	r_i $[cm]$
Housing outer radius	r_o $[cm]$
Housing length	l_h $[cm]$
Housing liner thickness	th_l $[mm]$
Axle port diameter	d_i $[mm]$
HSRU seal clearance	c_s $[\mu m]$
HSRU seal length	l_s $[mm]$
Operational	
Maximum angular velocity	ω_{max} $[rad/s]$
Charge pressure	P_c $[MPa]$

In general, making a change in the value of a design variable affects at least one positive and one negative impact on the set of HFA performance metrics (mass, efficiency, etc.). Because of the performance tradeoffs associated with each design variable, there is no justifiable "direction" in which a particular design variable value should be driven. Instead, a design solution is specified using educated guesses or, more ideally, a heuristic optimization algorithm.

In this thesis, the remaining variables that describe the geometric and operational choices associated with the HFA will be called "non-design variables." In contrast to a design variable, a non-design variable does not exhibit a performance tradeoff, but rather facilitates a single logical goal (for example, minimizing the mass of a component by driving a dimension to its smallest value that will prevent mechanical failure). The logical processes by which non-design variable values are selected will be discussed in subsequent chapters.

As is the case for a traditional high-energy flywheel, there are two purposes of enclosing the HFA in a containment chamber. First, the chamber provides burst containment, protecting nearby people and equipment in the event of a catastrophic failure of the HFA.

Second, the air inside of the chamber can be partially voided to provide a vacuum environment, significantly reducing the aerodynamic drag on the rotating components. The details of the containment chamber are, for the most part, outside the scope of this research. As necessary, subsequent chapters will justify various assumptions about the containment chamber.

In designing the HFA, a decision must be made as to whether the HSRU and/or the storage PM, both of which leak oil, are located inside or outside of the containment chamber. The disadvantage of packaging these components on the inside is that chamber pressure is limited to values above the saturation pressure of the hydraulic oil (generally around 13 Pa). This restriction is lifted if the HSRU and storage PM on the outside; vacuum pressures an order of magnitude lower can be sustained, resulting in less aerodynamic drag. In this arrangement, however, special seals are required to allow both ends of the axle to pass through the chamber. These so-called feedthrough devices maintain a vacuum seal at a rotary interface, but incur frictional losses. They also add cost and complexity to the chamber design. Simulation experience has indicated a relatively equal tradeoff between the lower aerodynamic drag and added frictional seal drag of packaging the HSRU and storage PM outside the containment chamber. The internal arrangement is cheaper and simpler, and is therefore selected as the more favorable design for the HFA.

2.2 Basic Kinetic and Pneumatic Energy Storage

To understand how the HFA stores energy, it is helpful to first briefly discuss the energy storage fundamentals of a pure flywheel and a pure hydro-pneumatic accumulator. The kinetic energy stored in a traditional flywheel is [25]

$$E_k = \frac{1}{2} I_s \omega^2 \tag{1}$$

where

$$I_s = \frac{1}{2} m_s (b^2 + a^2) \tag{2}$$

is the mass moment of inertia of a hollow cylinder with inner and outer radii a and b, respectively, m_s is the mass of the cylinder, and ω is the angular velocity. The subscript s emphasizes that all of the rotating components in a traditional flywheel are solid. In attempting to increase the kinetic energy storage capacity of a flywheel, there are two reasons why increasing angular velocity is favorable to increasing inertia. First, kinetic energy is proportional to the square of angular velocity but only directly proportional to inertia. Second, increasing angular velocity does not affect flywheel mass or volume, whereas for a given material, adding inertia requires increasing at least one of these.

For the HFA, Eqn. 1 is modified to include a fluid inertial term, such that the stored kinetic energy is

$$E_k = \frac{1}{2} \left(I_s + I_f \right) \omega^2 \tag{3}$$

This equation is valid for steady-state operation, where the internal fluid is rotating as a rigid body at the same angular velocity, ω, as the solid components. As will be proven in Section 5.2, the effective moment of inertia, I_f, of a fluid volume in rigid body rotation can be calculated as if it were a solid. Characterizing the stored kinetic energy during angular velocity transients is somewhat more complex and will be addressed in depth in Chapter 5. Presently, Eqn. 3 is sufficient to assess the kinetic energy storage capacity of a particular HFA design solution.

The pneumatic domain of the HFA can be analyzed in a similar manner to a traditional accumulator. For a volume of gas, the isothermal compression model can be used if the ratio of compression to heat transfer time scales is large, or by implementing a heat transfer medium in the gas volume [19]. The relationship between pneumatic pressure, P_p, and gas volume, V_g, is then

$$P_p = P_c \frac{V_c}{V_g} \tag{4}$$

where P_c and V_c are the gas pressure and volume, respectively, at the time the accumulator is charged (i.e. at minimum oil volume).

The change in pneumatic energy stored in a gas whose pressure and/or volume has changed is described as

$$\Delta E_{1,2} = \int_{V_1}^{V_2} P_p \, dV_g \tag{5}$$

The usable stored energy in a hydraulic accumulator at any time must be stated in reference to the charge condition, since no additional pneumatic energy can be extracted when the accumulator has been completely drained of oil. Combining Eqns. 4 and 5 and integrating from the charge volume, V_c, to some arbitrary instantaneous gas volume, V_g, an expression for usable pneumatic energy, E_p, is

$$E_p = P_c V_c \ln\left(\frac{V_c}{V_g}\right) \tag{6}$$

2.3 Fluid Centrifugation

In a static hydraulic accumulator, the pressure is spatially constant in both the gas and oil volumes. The fluid in the HFA, in contrast, exhibits interesting spatial pressure distributions that result from centrifugal effects. Figure 11 shows the forces due to pressure, P, acting on an infinitesimal element of a fluid volume rotating as a rigid body at angular velocity ω.

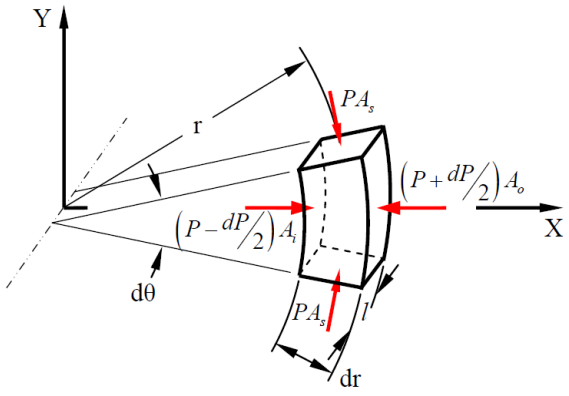

Figure 11: Force Balance on an Infinitesimal Fluid Element in a Rotating Fluid Volume [23]

To satisfy static equilibrium, these pressure forces must exactly balance the force on the fluid element due to angular acceleration. An expression for this force balance is

$$\left(P + \frac{dP}{2}\right) A_o - \left(P - \frac{dP}{2}\right) A_i - 2PA_s \frac{d\theta}{2} = dm\omega^2 r \tag{7}$$

where the differential mass of the fluid element is

$$dm = \rho d\forall = \rho l dr r d\theta \tag{8}$$

and the inner, outer, and side areas on which pressure is acting are

$$A_i = l\left(r - \frac{dr}{2}\right) d\theta \tag{9}$$

$$A_o = l\left(r + \frac{dr}{2}\right) d\theta \tag{10}$$

$$A_s = l dr \tag{11}$$

Combining and simplifying Eqns. 7 through 11 yields

$$dP = \rho\omega^2 r \, dr \tag{12}$$

Assuming a constant fluid density, Van de Ven [23] integrated Eqn. 12 to show that the oil side pressure distribution is

$$P_o(r) = P_s + \frac{1}{2}\rho_o \omega^2 r^2 \tag{13}$$

where P_s is system pressure, ρ_o is oil density, and r is radial position. It will be shown in Section 5.2 that Eqn. 13 is approximately true even during transient operation, when the fluid departs from rigid-body rotation.

On the gas side of the HFA, the fluid density is not constant, but rather is directly proportional to the ratio by which it has been compressed above atmospheric pressure.

$$\rho_g(r) = \rho_{atm} \frac{P_g(r)}{P_{atm}} \tag{14}$$

Combining Eqns. 12 and 14 yields

$$\int_{P_{g0}}^{P} \frac{dP_g}{P_g} = \int_{0}^{r} \frac{\rho_{atm}}{P_{atm}} P_g \, \omega^2 r dr \tag{15}$$

where P_{g0} is the presently unknown pressure at the center of the gas volume (note that this is a fictitious pressure, as the presence of the axle means that there is not actually gas at the location $r = 0$). Equation 15 can be integrated to describe the gas side pressure distribution as

$$P_g(r) = \exp\left[\frac{\rho_{atm}}{P_{atm}} \omega^2 \frac{r^2}{2} + ln\left(P_{g0}\right)\right] \tag{16}$$

The remaining unknown quantity, P_{g0}, is determined by using the fact that the average pressure as calculated by integrating Eqn. 16 must be equal to the average pneumatic pressure as defined by Eqn. 4. This equality is expressed as

$$\frac{1}{A_p} \int_{r_a}^{r_i} \int_{0}^{2\pi} \exp\left[\frac{\rho_{atm}}{P_{atm}} \omega^2 \frac{r^2}{2} + ln\left(P_{g0}\right)\right] r d\theta dr = P_c \frac{\cancel{V_c}}{\cancel{V_g}} \tag{17}$$

where the area of the piston exposed to pressure is

$$A_p = \pi(r_i^2 - r_a^2) \tag{18}$$

Defining the constants c_1 and c_2 as

$$c_1 = \frac{\rho_{atm}}{P_{atm}} \frac{\omega^2}{2} \tag{19}$$

$$c_2 = \frac{P_c \cancel{V_c} A_p}{2\pi \cancel{V_g}} \tag{20}$$

and integrating Eqn. 17, the pressure at the center of the gas volume is

$$P_{g0} = \frac{2c_1 c_2}{\exp(c_1 r_i^2) - \exp(c_1 r_a^2)} \tag{21}$$

Figure 12 qualitatively illustrates the difference between the centrifugal effects in a fluid of constant density (i.e. the oil volume) and a fluid that obeys ideal gas behavior (i.e. the gas volume). Pressure distributions are plotted for three different angular velocities, with

system pressure kept constant. The horizontal dotted line represents the axle and the vertical dotted line represents the piston. The gas and oil pressure distributions are shown on the left and right side, respectively, of the piston. The arrows indicate increasing angular velocity.

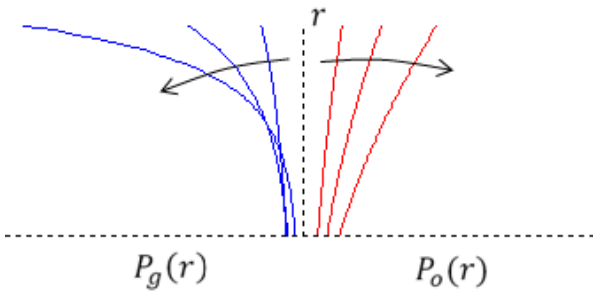

Figure 12: Qualitative Illustration of the Gas (Left) and Oil (Right) Pressure Distributions for Different Angular Velocities, with the Arrows Indicating Increasing Angular Velocity

Notice from Fig. 12 that when angular velocity is relatively low, the gas side pressure distribution closely resembles a parabola. At higher angular velocities, however, the pressure-density coupling begins to dominate and the gas side pressure distribution significantly departs from a parabola-like profile. Subsequent sections and chapters will reveal how the pressure distributions illustrated in Fig. 12 have implications on the effective stored energy, component stresses, and controlling the HFA.

2.4 Interaction of the Energy Storage Domains

From a stored energy perspective, analyzing the coupling between the pneumatic and kinetic domains of the HFA is trivial. The energy terms simply add together to yield a total stored energy, E, of

$$E = E_k + E_p = \frac{1}{2}\left(I_s + I_f\right)\omega^2 + P_c \cancel{V_c} \ln\left(\frac{\cancel{V_c}}{\cancel{V_g}}\right) \tag{22}$$

The design energy capacity, E_d, is defined as the total amount of energy stored when the HFA is at full SOC. It is useful to define the capacity ratio, R_c, as the ratio of stored kinetic to pneumatic energy at full SOC.

$$R_c = \left.\frac{E_k}{E_p}\right|_{SOC=100\%} \tag{23}$$

When compared to Eqn. 6, which describes the stored energy in a traditional accumulator, Eqn. 22 illustrates the reason that a comparably-sized HFA can store significantly more energy; with sufficient angular velocity and/or inertia, the kinetic term can be quite large. Because the addition of the kinetic term is the mechanism by which energy density is increased over traditional hydraulic energy storage, more energy-dense HFA designs will tend to have higher capacity ratios.

To understand the mechanism by which the interaction of the energy domains decouples pressure from SOC, a more in-depth analysis is required. Given the high expected operating pressures and the relatively low mass of the piston, the axial inertia of the piston can be neglected. Therefore, no matter the operating condition, a static force balance on the piston must yield zero net axial force. The area of the piston exposed to oil pressure spans the distance between the axle radius, r_a, and the housing inner radius, r_i. Like the gas side pressure distribution, the oil side pressure distribution must result in an average pressure equal to the pneumatic pressure.

$$P_c \frac{\cancel{V_c}}{\cancel{V_g}} = \frac{2\pi}{A_p} \int_{r_a}^{r_i} P_o(r)\, r dr = P_s + \frac{1}{4}\rho_o \omega^2 (r_i^2 + r_a^2) \tag{24}$$

An equation for system pressure can be obtained by combining Eqns. 4 and 24 to yield

$$P_s = P_p - \frac{1}{4}\rho_o \omega^2 (r_i^2 + r_a^2) \tag{25}$$

Whereas system pressure is a function only of gas volume in a traditional accumulator, system pressure for the HFA includes the additional independent variable of angular velocity. Therefore, with intelligent control over gas volume and angular velocity during some duty cycle, system pressure can be modulated independently of the amount of energy stored.

2.5 Controlling the Hydraulic Flywheel-Accumulator

The preceding sections have introduced the basic means by which the energy is stored in the HFA and the mechanism by which SOC is decoupled from system pressure. It is now of interest to discuss how these phenomena are most effectively managed. This section discusses how and why a control strategy might allocate the energy available to or demanded from the HFA between the kinetic and pneumatic domains.

For the present purpose of discussing potential control strategies, energy loss mechanisms are neglected, until otherwise noted. The overarching energy equation for the HFA equates tractive power (alternatively referred to as "total" or "road" power), $\dot{W}_t$, to the sum of power in the kinetic domain (mechanical power), $\dot{W}_k$, and power in the hydro-pneumatic domain (hydraulic power), $\dot{W}_p$.

$$\dot{W}_t = \dot{W}_k + \dot{W}_p \tag{26}$$

This equality is illustrated by Fig. 13, which also establishes the convention that power into the HFA (due, for example, to regenerative braking) is positive.

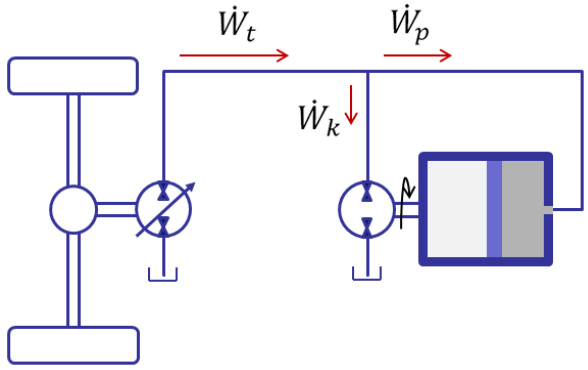

Figure 13: Sign Convention for Tractive (Total) Power, Power in the Kinetic Domain, and Power in the Pneumatic Domain

The task of the control strategy is to dictate the time-varying ratio of mechanical power to hydraulic power, $\dot{W}_k/\dot{W}_p$. The selection of this ratio is based on the instantaneous tractive power and the HFA operating state – the current angular velocity, ω, and the current pneumatic pressure, P_p.

It is extremely important to note that using the pneumatic domain will generally be significantly more energy efficient than using the kinetic domain. In a broad sense, this is due to the fact that converting between hydraulic and mechanical power using a hydraulic pump-motor tends to incur more losses than simply converting power within the pneumatic domain (i.e. using hydraulic power to compress a gas with a piston). The inferior efficiency of the kinetic domain implies that, system pressure implications aside, the control strategy should favor the pneumatic domain. Indeed, this is ultimately why the HFA is superior to a traditional flywheel coupled to a hydraulic PM; the energy density of each system is comparable, but the latter would require that all power conversion between the energy storage system and the traction PM be facilitated by a hydraulic machine.

It is also important to understand the effect that each energy domain's usage has on system pressure. Equation 25 provides a foundation for this understanding. Consider a vehicle braking event, where power from the tractive PM is available to charge the HFA. If all of the available flow is directed to the kinetic domain, a positive torque is applied to the HFA while the gas and oil volumes remain constant. The HFA accelerates, and Eqn. 25 dictates that system pressure decreases due to larger centrifugal effect imposed by the higher angular velocity.

Now consider the case where all of the available flow is directed to the pneumatic domain, such that no torque is applied to the HFA via the storage PM. The oil volume increases, adding inertia to the HFA, thereby slowing it down. The slower rotational speed, as indicated by Eqn. 25, corresponds to an increase in system pressure. Additionally, the gas volume decreases, causing a further increase in system pressure due to isothermal compression.

Given the preceding discussion on the efficiency and pressure implications of using each energy domain, the goal of the control strategy should be to choose ratios of mechanical power to hydraulic power that maximize drive cycle efficiency and minimize system pressure fluctuation. The former goal is obvious and requires no further discussion. The latter has been alluded to but will presently be justified more explicitly. Any drop in system pressure below some design pressure, P_d, represents a necessary increase in the

size (and therefore the mass, volume and cost) of the traction PM – an increase that would not be required if the system pressure never dropped below P_d. Conversely, any increase in system pressure above P_d tends to drive structural HFA components to larger dimensions, unnecessarily increasing the system mass. The challenge of devising an optimal control strategy lies in the fact that the goal of maximizing efficiency tends to be in conflict with the goal of minimizing pressure fluctuation.

The physical means by which the control strategy selects the ratio $\dot{W}_k/\dot{W}_p$ depends on the type of storage PM used. If the storage PM is a variable-displacement machine, the ratio can be infinitely varied by controlling the PM displacement, D. As a result, a perfect control strategy could theoretically hold system pressure exactly constant throughout a drive cycle. If a fixed displacement machine is used for the storage PM, the ratio $\dot{W}_k/\dot{W}_p$ cannot be varied continuously; rather, the kinetic domain is toggled on and off by declutching the storage PM and using a valve to isolate it from the high pressure rail. The magnitude of mechanical power when the kinetic domain is active is fixed by the HFA operating state. In accordance with Eqn. 26, energy regeneration occurs between the kinetic and pneumatic domains if mechanical power happens to exceed the tractive power demand or supply. Otherwise, the pneumatic domain makes up for the difference between tractive and mechanical power.

A fixed-displacement machine is recommended for use as the storage PM for two reasons. First, as will be shown in Section 6.2, it is generally not desirable to maintain a perfectly constant system pressure. This significantly reduces the appeal of a variable-displacement machine. Second, the efficiency a variable-displacement machine drops quickly with displacement [26]. This means that any pressure stability offered by using partial displacement positions would come with a severe penalty in efficiency. The first-generation laboratory prototype HFA will employ a fixed-displacement storage PM, and unless otherwise noted, the remainder of this paper will reflect this choice.

2.6 Optimization Objectives and Constraints

The design variables and the general operation of the HFA were presented in the preceding sections of this chapter. To contextualize the next several chapters of this paper, this section briefly discusses the two principal design optimization objectives and the means by which they are assessed for a specified design solution.

Consider an arbitrary vehicle energy storage system. The drive cycle energy, W_{dc}, which is defined as the amount of energy that must be removed from the energy storage system to complete some arbitrary duty cycle, is the sum of the tractive energy (the time-integral of the tractive power) and the powertrain losses, W_{loss}. To reflect the focus of this research, W_{loss} need only include the losses incurred in the energy storage system itself (A more comprehensive definition of W_{loss} might include the losses incurred in charging the energy storage system in addition to those incurred during the drive cycle itself, although this is not done for the present purposes).

As will be shown in Section 6.1, the tractive energy is proportional to vehicle mass, which in turn is proportional to the mass of the energy storage system, m_{sys}. The drive cycle energy can therefore be expressed as

$$W_{dc} = C_1 + C_2 m_{sys} + W_{loss} \tag{27}$$

where C_1 and C_2 are positive constants that represent the relationship between the mass of the energy storage system and the tractive energy. Whether the motivation is environmental or economic, it is indisputably advantageous to minimize W_{dc}. Eqn. 27 shows that, to do so, minimization of mass and energy losses should be the two primary objectives in designing a vehicle energy storage system.

In addition to the fuel economy benefits, lower-mass road vehicles tend to exhibit superior handling [27]. Minimizing system volume, which leads to more favorable packaging, could be used as an alternative (or complementary) objective. However, since lower mass solutions in general correlate to lower volume solutions, an objective on HFA volume is considered redundant for the present research. It can also be argued that solutions with lower mass tend to have less material and are therefore less expensive to

manufacture. While the mass calculation is fairly straightforward, calculating energy losses requires detailed modeling of the various loss mechanisms associated with the HFA and evaluating these losses over some duty cycle. In the present research, the HFA duty cycle is defined by the combination of selected vehicle parameters, a control strategy, and a drive cycle. This is thoroughly covered in Section 6.1.

The mass and energy loss objectives are subject to the following two constraints. First, all of the stresses in the HFA must remain sufficiently below the strength of the respective materials in which they act. Here, "sufficiently below" can be defined by a safety factor, SF, for material failure. Chapter 3 addresses the stress modeling and worst-case loading of each of the components in the HFA. As a second optimization constraint, the HFA must meet a minimum energy capacity requirement. As will be discussed in Section 6.1, the present research enforces this constraint by requiring that an HFA solution provide sufficient energy to complete a specified drive cycle.

Because system pressure fluctuation is not explicitly used as an optimization objective or constraint, it must be reflected by estimating the mass of the traction PM required to handle drops in system pressure. This is the only non-trivial task in calculating the HFA system mass, and it will be detailed in Section 6.2. Given some set of dimensions and materials, calculating the masses of the other HFA components is straightforward. It should be noted that the amount of oil needed to perform some duty cycle is nearly independent of the HFA design solution itself. Oil is therefore omitted from HFA mass calculation, as including it would unduly penalize HFA design solutions with lower capacity ratios. The containment chamber is also omitted from the HFA mass calculation. This is justified by the fact that the containment chamber design details are outside the scope of the present research and therefore have not been optimized.

3 Model-Based Structural Design

As mentioned in Section 2.1, values for all non-design variables can be logically selected based on a specified HFA design solution. A design sequence has been developed and implemented in code to automate the selection of these non-design variables. Given an arbitrary design solution, this code allows for structural feasibility, energy density, and various other metrics to be quickly calculated, facilitating rapid iterative model-based design.

Some of the proceeding discussion will illustrate the recursive nature of the design process; a drive cycle simulation relies on a particular dimension having been specified, but properly specifying this dimension relies on factors that depend on the results of a drive cycle simulation. Justifications for several assumptions made in this chapter are based on simulation experience, a reflection of the iterative design process which has characterized the present research.

This chapter begins with a discussion of system-level considerations. Next, each component is individually addressed, where the worst-case loading and stress models drive the selection of each component dimension. A safety factor, SF, for material failure is incorporated into each stress analysis. The end of this chapter includes a justification for material selections, as well as a discussion of assembly and maintenance considerations. In general, this chapter is structured to reflect the logical order in which the various HFA component dimensions must be selected.

3.1 System-Level Considerations

In designing an HFA application, one of the most basic system-level choices is the mounting orientation. The HFA axle is mounted in two bearings, which must support radial and axial loads. These loads, which will be discussed in greater detail in Section 3.2, arise from a combination of eccentric and gravitational acceleration, and pressure

acting on the axle. Figure 14 shows the forces which produce radial and axial bearing loads for a horizontal mounting orientation and two possible vertical mounting orientations (no intermediate orientations are considered).

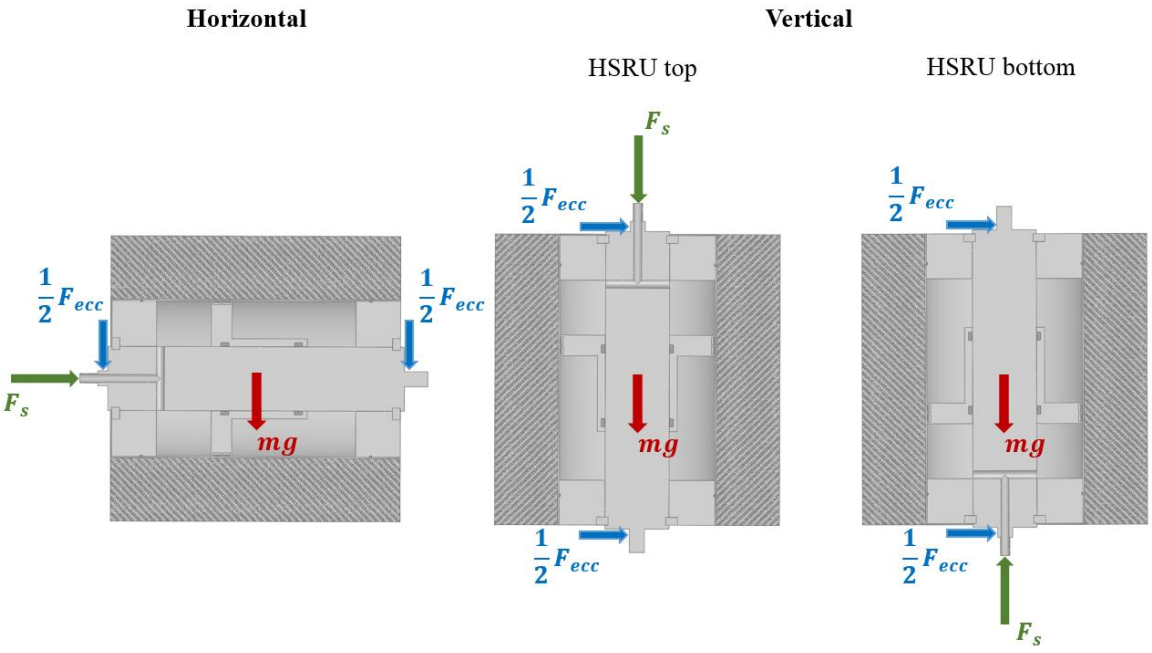

Figure 14: Three Possible Mounting Orientations for the HFA, Showing Forces that Contribute to Bearing Loads

In a horizontal orientation, the maximum radial bearing load occurs once per revolution and is the sum of an eccentric force and the HFA weight. All else equal, the radial load in a vertical orientation will always be lower, since the HFA weight acts axially and eccentric forces are the only contribution to radial load. Between the two possible vertical orientations, the one in which the HSRU is located at the bottom is favorable and is chosen for the design of a laboratory prototype. This orientation minimizes the net axial bearing load by setting the HFA weight and system pressure forces, which tend to be on the same order, in opposition to one another.

By the nature of its interaction with the end caps, the axle must withstand the large normal force, F_a, that arises from internal HFA pressure acting on the end caps. To accommodate the axial elongation that results from this normal force, the top bearing is allowed to translate axially within its static bearing block. A wave spring provides

downward force to continually load the axle against the bottom bearing. By seating the bearings directly against the main section of the axle, this architecture essentially eliminates bending in the shafts (the sections of the axle on which the bearings are seated). Figure 15 shows a cross section to demonstrate the HFA mounting, including a zoomed view of the upper bearing and bearing block.

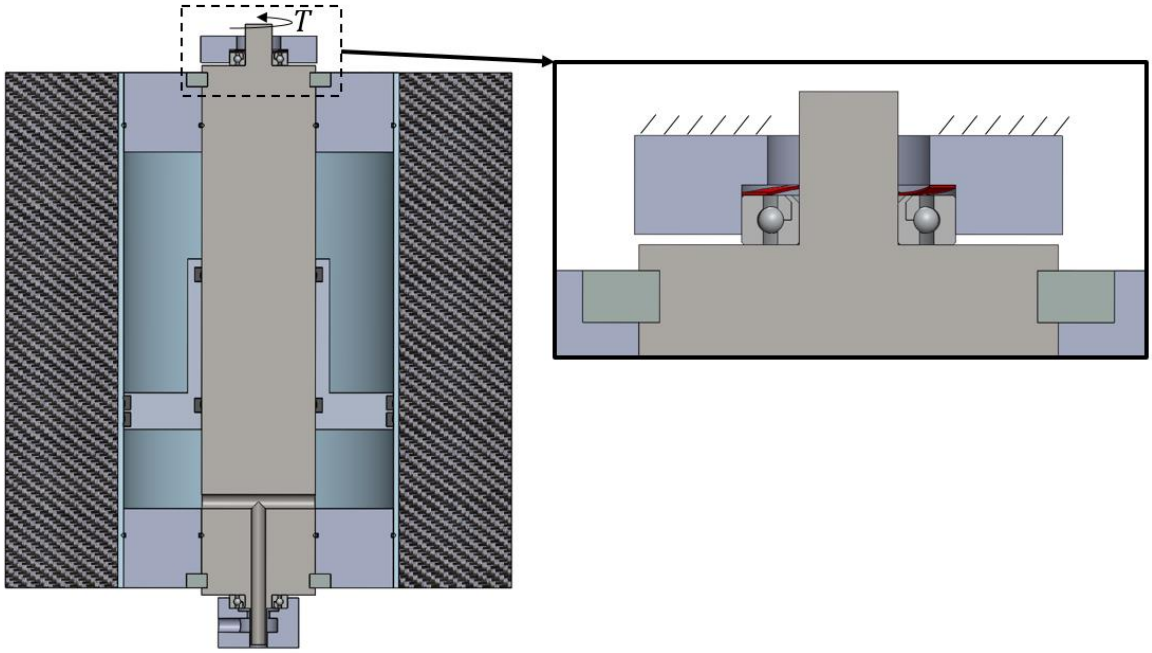

Figure 15: Illustration of the HFA Mounting Architecture

To change the stored kinetic energy of the HFA, the torque, T, applied by the storage PM to the gas side of the axle must be transmitted to the other inertia-contributing components – the end caps, piston and housing. In transmitting torque, any allowance of relative tangential movement between these components would induce frictional energy losses and material wear. The axle, gas side end cap, and housing must also remain axially constrained to one another. Relative axial movement between these components would threaten the structural integrity of the HFA assembly, potentially allowing for a catastrophic loss of pressure or invalidating the stress models presented in the following sections. Constraints on relative radial movement between components are somewhat more nuanced and are discussed separately in Section 8.7.

The axial and tangential constraints between the axle and the end caps are accomplished by using split retaining rings ("retainers") that are seated in grooves in the axle. When the HFA is fully-assembled, the retainers are nested within counterbores in the end caps, preventing the retainers from leaving the grooves in the axle. The retainers are lightweight, simple to fabricate, and allow for easy HFA assembly. An exploded view of the retainer system is shown in Fig. 16.

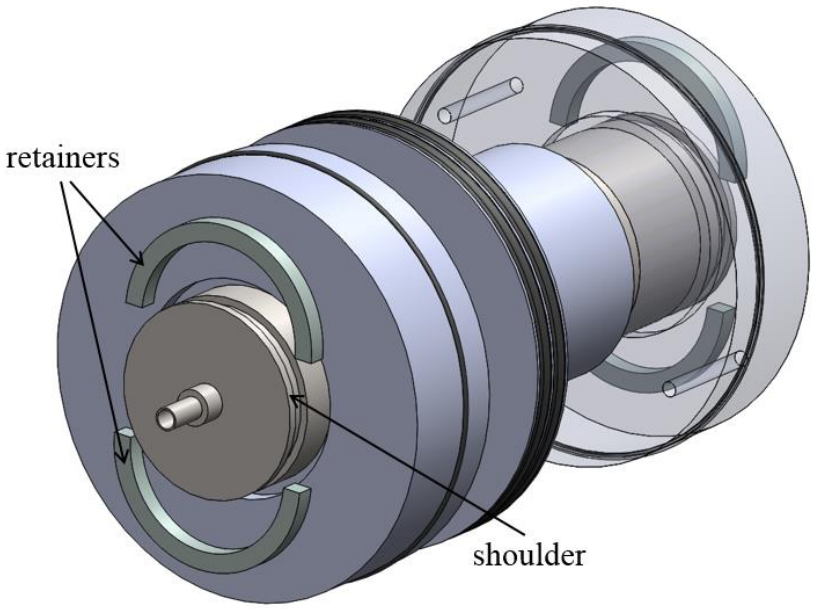

Figure 16: Exploded View of the Retaining Ring System for Torque Transmission between the Axle and End Caps

The internal pressurization of the HFA results in an axial force which imposes compression between the end caps and the retainers, and between the retainers and the axle shoulders. Because this axial force is so large for the entire range of expected operating conditions, torque transmission between the axle, retainers and end caps can be accomplished via friction.

As described in Section 2.1, the oil side end cap is axially and tangentially free-floating within the housing. Therefore, all of the torque transmitted to the housing is carried through the gas side end cap. As an analog to the retainer system that constrains the axle to the end caps, a set of pins is used to constrain the gas side end cap to the housing. This system of pins, some number N_{ss} of shoulder screws, carries torque between the gas side

end cap and axle and provides an axial constraint to react the downward gravitational force acting on the housing mass. Importantly, the pins do not impose a radial constraint. This ensures that the radial strain interaction between the housing and the gas side end cap is the same as the interaction at the oil side end cap. To facilitate assembly, radial holes are drilled through the housing. The pin system is shown in Fig. 17.

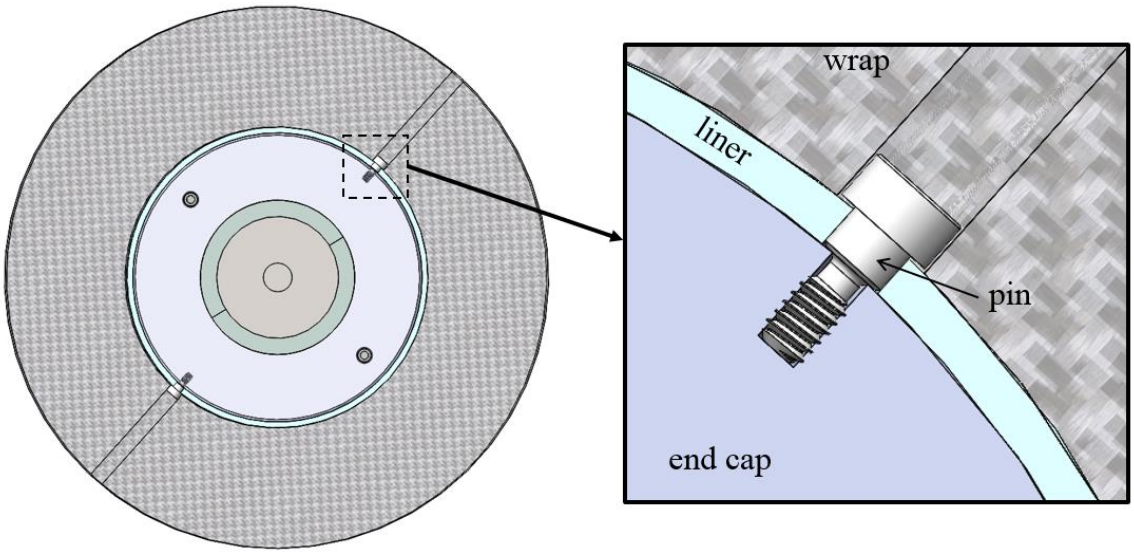

Figure 17: Illustration of the Pins (As Shown, $N_{ss} = 2$) which Produce an Axial and Tangential Constraint between the Housing and the Gas Side End Cap

Because the first manifestation of the HFA concept will be a laboratory prototype, the components have been designed for easy manufacture and to facilitate simple and non-destructive assembly and disassembly. The most frequent reasons for disassembly are expected to be general maintenance and monitoring of internal component health.

The assembly process of the HFA can be generally described with the following steps:

1. Insert the piston and O-ring seals into the appropriate glands in the piston and end caps.
2. Slide the piston onto the axle, and position it near the axial center.
3. Slide the end caps onto the axle so that both sit between the retainer grooves.
4. Insert the retainers into the grooves on the axle.

5. Slide each end cap back towards its respective end of the axle, such that the cutaways on the inner diameter of the end cap cover the retainers.
6. Slide the housing over the gas side end cap towards the oil side end cap. To prevent seal friction from carrying the gas side end cap with the housing, an effective handle (a bolt, for example) can be temporarily threaded into one of the gas charging ports.
7. Spin the housing with respect to the gas side end cap until the radial holes for the pin system are aligned. Thread the pins into the end cap.

Having completed the steps above, the HFA is mounted within its bearings, a process which depends on the application-specific design choices for the containment chamber.

3.2 Axle

The main purpose of the axle is to react the axial force due to internal pressure acting on the end caps. Figure 18 shows all of the axle dimensions.

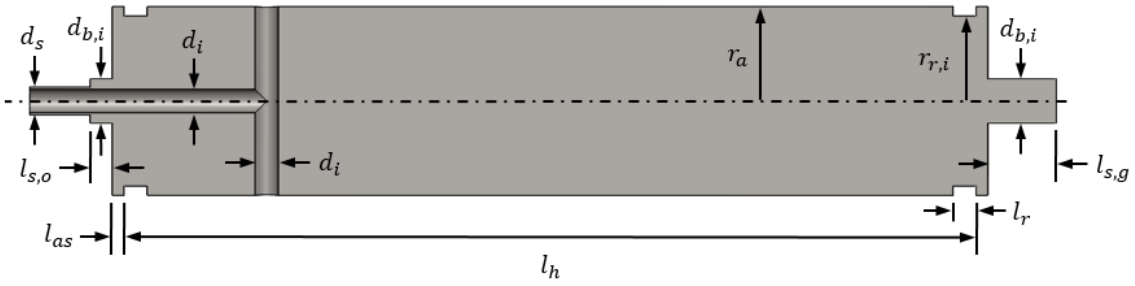

Figure 18: Axle Dimensions

Note that d_s is the circumferential seal diameter and is greater than d_i due to a finite wall thickness in the far-left portion of the axle that protrudes into the HSRU. The oil side shaft length, $l_{s,o}$, is equal to the width of the bearing (to be selected in Section 3.6) and the gas side shaft length, $l_{s,g}$, must be chosen in consideration the coupling between the axle and the storage PM. The details of the containment chamber dictate the nature of

this coupling, and therefore the selection of $l_{s,g}$ is not discussed further in the present work.

A system of ports interfaces with the HSRU to facilitate the transport of oil between the rotating HFA and the static environment. The radial ports are formed by a single cross-drilled hole, and the length of the axial port is selected such that radial ports enter the HFA just inside the inner face of the oil side end cap. There is some opportunity to minimize losses as oil is throttled through the axle by optimizing the number and diameter of the radial ports. However, the added complexity is deemed unnecessary for a first-generation prototype, and the diameter d_i is therefore applied to the entire port system. As will be shown in Section 4.3, the choice of the dimension d_i has conflicting impacts on different energy loss mechanisms, hence its designation as a design variable.

All of the remaining axle dimensions are stress-driven, and should be chosen to minimize the mass of the axle. Their proper selection begins with a free body diagram of the major loads on the axle-end cap system.

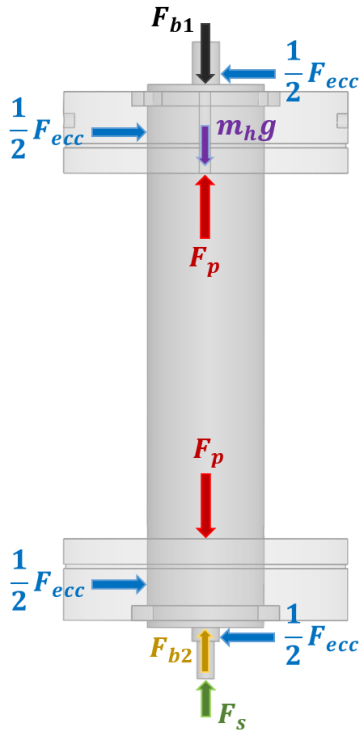

Figure 19: Free Body Diagram of the Major Loads on the Axle-End Cap System

The eccentric force, F_{ecc}, acts radially on the bearings and axle. Section 3.6 will discuss how this force is calculated and used to size the bearings, including the selection of the shaft diameter $d_{b,i}$. Note that the only component weight included in Fig. 19 is that of the housing, as the weights of the end caps and the axle itself tend to be much smaller. The pneumatic force, F_p, is the result of the pneumatic pressure, P_p, acting on the end caps. It is given by

$$F_p = \left[P_s + \frac{1}{4}\rho_o \omega^2 (r_i^2 + r_a^2)\right] \pi (r_i^2 - r_a^2) \tag{28}$$

and acts equally on both end caps.

The system pressure force, F_s, is the result of the system pressure acting upward on the oil side of the axle, where the diameter is d_s, the circumferential seal diameter. The value of F_s is the sum of system pressure and the area upon which it acts.

$$F_s = P_s \frac{\pi d_s^2}{4} \tag{29}$$

Note that d_s is presumed to be small enough that the pressure acting upon the axle is uniform and accurately represented by P_s.

The upper bearing force, F_{b1}, is equal to the force of the wave spring,

$$F_{b1} = k_s (x_o + \delta_a) \tag{30}$$

where k_s is the spring constant, x_o is the pre-compression (units of length) of the wave spring at assembly, and δ_a is the axial elongation of the axle with respect to its unstressed length. The lower bearing reaction force, F_{b2}, depends on the values of the other forces in Fig. 19. A static force balance on the vertical forces yields

$$F_s + F_{b2} = F_{b1} + m_h g \tag{31}$$

The next step in analyzing the axle entails assessing the maximum stress in the main portion. The axle outer radius, r_a, should be selected as the minimum possible value that prevents material failure, as any larger dimension adds mass to the axle that would be more efficiently placed in the housing. Smaller values of r_a also tend to maximize internal HFA volume (and therefore pneumatic energy capacity) and reduce the necessary

piston length. Because the distance between the eccentric forces and the bearing reactions (as shown in Fig. 19) is small, and because the housing provides considerable stiffness, bending and transverse shear in the main section of the axle are neglected. Stresses in the main section of the axle due to torque transmission, centrifugation and internal pressure acting directly on the axle are also quite small, and are therefore not considered in the selection of r_a.

In fact, the only stress that significantly impacts the necessary axle radius, r_a, is the axial tension that arises from the forces shown in Fig. 19. To asses this tension, a free body diagram (excluding radial forces) of the lower section of the axle is shown in Fig. 20.

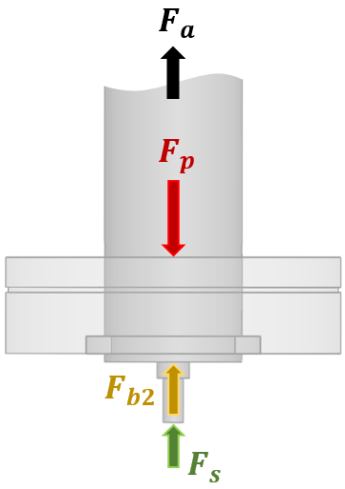

Figure 20: Free Body Diagram (Excluding Radial Forces) of the Lower Portion of the Axle

A static force balance on Fig. 20 yields the following expression for the axial force in the axle.

$$F_a = F_p - F_s - F_{b2} \tag{32}$$

Combining Eqn. 28 with Eqns. 30 through 32 yields

$$F_a = \left[P_s + \frac{1}{4}\rho_o \omega^2 (r_i^2 + r_a^2)\right] \pi (r_i^2 - r_a^2) - k_s (x_o + \delta_a) - m_h g \tag{33}$$

In calculating the axial elongation of the axle, δ_a, the normal stress is approximated as constant and acting over a length equal to the housing length, l_h. In other words, the smaller cross sections and larger stresses in the ported regions of the axle are neglected,

and it is deemed unnecessary to use the exact axle length (it is not yet known, in fact, because the end cap thickness, which itself depends on the dimension r_a, is yet to be determined). The axial elongation of the axle is, then

$$\delta_a = l_h \frac{\sigma_a}{E_a} \tag{34}$$

where the axial stress in the non-ported section of the axle is

$$\sigma_a = \frac{F_a}{\pi r_a^2} \tag{35}$$

and E_a is the Young's modulus of the axle material. The critical stress in the axle occurs at the location of the radial ports, where the cross-sectional area is smallest and the ports induce a stress concentration. This stress should be set to the maximum allowable value, such that

$$\frac{S_{y,a}}{SF} = k_n \frac{F_a}{A_{x,p}} \tag{36}$$

where the stress concentration factor, k_n, is an empirical function of d_p/r_a given by [28] and $A_{x,p}$ is the axle cross-sectional area at the radial ports, approximated as

$$A_{x,p} = \pi \left(r_a - \frac{d_i^2}{4} \right) - d_p(2r_a - d_i) \tag{37}$$

The spring constant and pre-compression must be selected before the system represented by Eqns. 28 through 37 can be solved. Larger pre-compression mitigates the critical stress in the axle at the expense of loading the bearings more heavily, and the opportunity exists to select the combination of spring constant and pre-compression that optimizes this tradeoff. This tradeoff study is omitted from the present model-based design tools, but should be conducted when actual parts are being sourced.

To prevent the HFA from ever lifting off of the bottom bearing, the spring constant should be selected such that the lower bearing force, F_{b2}, goes to zero only at the highest possible system pressure. Using Eqn. 31, letting F_{b2} go to zero, and inserting the appropriate expressions for the other forces, the following expression for the spring constant is obtained.

$$k_s = \frac{P_s \frac{\pi d_s^2}{4} - m_h g}{\delta_a} \tag{38}$$

Now, Eqns. 28 through 38 can be solved simultaneously to determine r_a and k_s. From the perspective of both stress and maintaining axial force on the bottom bearing, the worst case operating point is the maximum angular velocity, ω_{max}, and the maximum expected system pressure, $P_{s,max}$. While the former is a design variable chosen by an optimization strategy, the latter value must be specified by the designer in consideration of how well the chosen control strategy can limit pressure. Alternatively, if an absolute limit system pressure is implemented, for example with a relief valve, the cracking pressure can be used as the value for $P_{s,max}$.

The seal diameter d_s must be chosen to yield a wall thickness which prevents material failure of the axle portion that protrudes into the HSRU. For the purposes of calculating stresses, this section of the axle is modeled in isolation from the rest of the axle; it is treated as a thick-walled cylinder with free ends, where the pressure P_s acts on the internal wall and the front face. This load case is shown in Fig. 21.

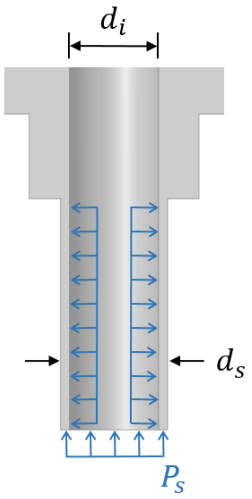

Figure 21: Loading on the Portion of Axle that Forms the Circumferential Seal

In reality, there will be an external pressure that varies linearly from P_s to zero along the length of the circumferential seal. From a stress perspective, however, the simplifying assumption of zero external pressure is conservative. Because the dimensions d_i and d_s

will tend to be small, torsion due to viscosity in the circumferential seal and centrifugal loading are both neglected. Lamé's equations [29] are used to solve for the stresses at the outer diameter, which is the critical stress location. The radial stress here is zero, while the circumferential and axial stresses are

$$\sigma_\theta = \frac{2P_s d_i^2}{d_s^2 - d_i^2} \tag{39}$$

$$\sigma_z = -P_s \tag{40}$$

The von Mises criterion is used to calculate the maximum equivalent stress, which is set to the maximum allowable stress.

$$\sigma_{vm,a}^2 = \sigma_\theta^2 - \sigma_\theta \sigma_z + \sigma_z^2 = \left(\frac{S_{y,a}}{SF}\right)^2 \tag{41}$$

Equations 39 through 41 can be solved implicitly to minimize the seal diameter, d_s. Again, the maximum expected system pressure, $P_{s,max}$, should be used to select the seal diameter, as this condition leads to the highest axial and hoop stresses.

Having specified the axle radius, r_a, and the seal diameter, d_s, the dimensions associated with the retainer system can now be selected. The radial dimensions of the retainers must provide contact areas with the axle and end caps that are sufficiently large to prevent compressive failure of these components when they are carrying the maximum pneumatic force,

$$F_{p,max} = \left[P_{s,max} + \frac{1}{4}\rho_o \omega_{max}^2 (r_i^2 + r_a^2)\right] \pi (r_i^2 - r_a^2) \tag{42}$$

The worst-case compressive stress, which is calculated as $F_{p,max}$ divided by the contact area, should be allowed to go to the maximum allowable stress for the component of interest. Therefore, the inner and outer radii of the retainers are, respectively

$$r_{r,i} = \sqrt{r_a^2 - \frac{(SF)F_{p,max}}{\pi S_{y,a}}} \tag{43}$$

$$r_{r,o} = \sqrt{r_a^2 + \frac{(SF)F_{p,max}}{\pi S_{y,e}}} \tag{44}$$

where r_a is the axle radius, and $S_{y,a}$ and $S_{y,e}$ are the compressive yield strengths (conservatively approximated as equal to the tensile yield strengths) of the axle and end caps, respectively. Assuming the strength of the retainers is comparable to the strength of the axle, Eqns. 43 and 44 ensure that the retainers themselves can withstand the compressive forces to which they are exposed.

The axle shoulder length, l_{as}, and retainer length, l_r, are chosen to be sufficiently long to prevent shear failure of these components. Maximum shear stress in the axle shoulder and retainer also occur when the axle is carrying $F_{p,max}$, such that the required length of each is, respectively

$$l_{as} = \frac{(SF)F_{p,max}}{2\pi r_{r,i}(0.58)S_{y,a}} \tag{45}$$

$$l_r = \frac{(SF)F_{p,max}}{2\pi r_a(0.58)S_{y,r}} \tag{46}$$

where the factor 0.58 is applied to approximate shear strength from normal tensile strength. Note that the dimension $r_{r,i}$ tends to be large enough that the critical stress location for the axle is still at the position of the radial ports. FEA analysis during detailed design will be used to confirm these assumptions.

3.3 End Caps

Compared to the housing, the end caps do not contribute mass-efficient inertia to the HFA; the same amount of mass would provide more inertia if it were concentrated at a larger radius. However, by virtue of their purpose in the HFA architecture (to contain the pressurized fluid), the end cap material must span the distance between the axle radius, r_a, and the housing inner radius, r_i. Because their inertia contribution is sub-optimal, the thickness, th_e, of the end caps should be minimized. The thickness must be large

enough, however, for the end cap to withstand the bending stresses that result from fluid pressure, as well as the stresses imposed by centrifugal force. Stresses due to gravity acting on the masses of the end caps are negligible. The bending and centrifugal forces are evaluated independently and then superimposed to assess the total stress in an end cap.

For a thick-walled cylinder made of an isotropic material (density ρ and Poisson ratio ν) exposed to loading only from centrifugal force, the radial and circumferential stress distributions are, respectively [25],

$$\sigma_{r,cent}(r) = \rho\omega^2 r_o^2 \frac{3+\nu}{8}\left[1 + \left(\frac{r_i}{r_o}\right)^2 - \left(\frac{r_i}{r_o}\right)^2 - \left(\frac{r}{r_o}\right)^2\right] \tag{47}$$

$$\sigma_{c,cent}(r) = \rho\omega^2 r_o^2 \frac{3+\nu}{8}\left[1 + \left(\frac{r_i}{r_o}\right)^2 + \left(\frac{r_i}{r_o}\right)^2 - \frac{1+3\nu}{3+\nu}\left(\frac{r}{r_o}\right)^2\right] \tag{48}$$

It is notable that the centrifugal stress distributions are independent of end cap thickness. This imposes some upper limit on angular velocity for a given material. When the HFA is exposed to centrifugal force, the small clearance between the end caps and housing that existed at assembly will likely close completely, due to the lower specific modulus of the end caps. For the purposes of estimating stresses in the end caps, however, it is conservative to neglect the resultant compressive interaction between the end caps and housing.

Modeling the bending stresses in an end cap is somewhat less straightforward than modeling centrifugal stresses. The retaining ring is presumed to apply a uniform reaction pressure, P_r, over its contact area, and the outer edge of the end cap is assumed to be free of any reaction force or moment. The latter assumption is conservative, especially for the gas side end cap, where the housing weight provides a small downward force that tends to reduce the bending moments. Additionally, the contact between the end caps and housing will in practice provide some moment reaction, which will also tend to reduce maximum bending stress.

The loading scenario that results from internal pressure on the oil side end cap is illustrated in Fig. 22, with an arbitrary oil pressure profile acting downward and the retainer reaction pressure acting upward. The loading scenario for the gas side end cap is qualitatively identical.

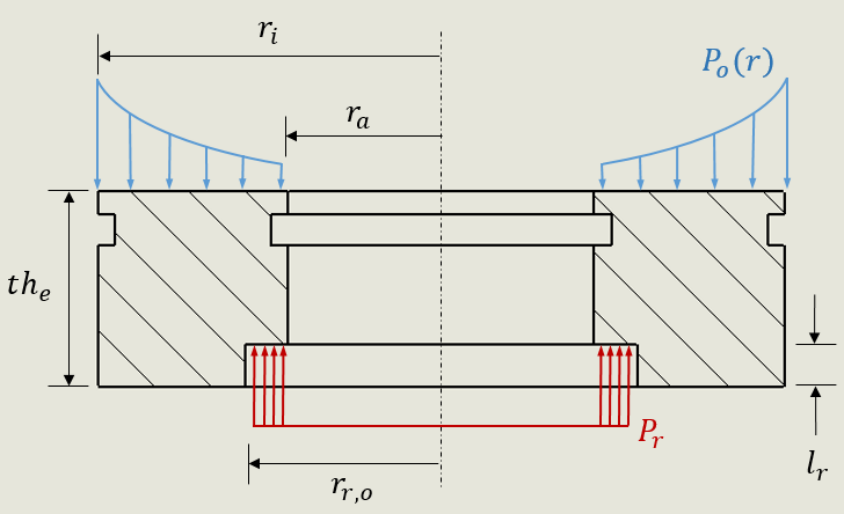

Figure 22: Pressure Loading on the Oil Side End Cap (Retainer Pressure P_r Acts on the Counterbore Surface)

The end caps are modeled as circular plates of uniform thickness th_e, and plate theory is used to estimate the bending stresses. Shear and normal axial stresses are assumed to be zero, and bending stresses on either side of the plate are modeled as equal and opposite [30]. Note that the pocket of radius $r_{r,o}$ and depth l_r, which serves to cover the retainers, makes the uniform thickness assumption somewhat of a simplification. Additionally, as the ratio th_e/r_i grows, shear stresses become important, and the validity of plate theory wanes. However, FEA performed on various end cap geometries suggests that the plate model presented here is appropriate for a design optimization, as it tends to be only slightly conservative for thick plates.

Heap [31] derived analytical equations to calculate bending moment profiles (in Newton-meters per meter thickness) that result from a circular line load at an arbitrary radius on a plate. These equations are omitted here for brevity but can be found on pg. 257 in Appendix B. A code has been written which discretizes the pressure distribution on the end cap into 50 line loads and superimposes the resultant bending moments to yield the

total radial and circumferential bending moment profiles, $M_r(r)$ and $M_c(r)$, respectively (again, in Nm/m). From these bending moments, the radial and circumferential bending stress profiles are calculated as

$$\sigma_{r,bend}(r) = \frac{6M_r(r)}{th_e^2} \tag{49}$$

$$\sigma_{c,bend}(r) = \frac{6M_c(r)}{th_e^2} \tag{50}$$

Superimposing the centrifugal and bending stresses, and using the von Mises criterion, the maximum equivalent stress in an end cap is

$$\begin{aligned}\sigma_{vm,e} = \max\Big[&\Big(\sigma_{r,cent}(r) + \sigma_{r,bend}(r)\Big)^2 + \Big(\sigma_{c,cent}(r) + \sigma_{c,bend}(r)\Big)^2 \\ &- \Big(\sigma_{r,cent}(r) + \sigma_{r,bend}(r)\Big)\Big(\sigma_{c,cent}(r) + \sigma_{c,bend}(r)\Big)\Big]\end{aligned} \tag{51}$$

Evaluation of Eqn. 51 suggests that the maximum stress in the end caps occurs at the inner radius. Therefore, it is assumed that the stress concentrations induced by minor design features (i.e. the pin system and gas charging holes) near the outer radius do not affect the structural integrity of the end cap. The O-ring seal glands are also assumed to have a negligible impact on the peak end cap stresses, and their axial location will be selected in Section 8.2. These assumptions are confirmed using FEA in detailed design.

Equations 13 and 16, which describe the oil and gas side pressure distributions, indicate that worst-case bending for both end caps occurs at maximum HFA pressure and maximum angular velocity. At this operating condition, the net force is greatest and is most concentrated at the outer radius of the end caps, away from the retainer reaction force. Maximum angular velocity also imposes the worst case loading from the perspective of centrifugal stresses.

Though the loading on the two end caps is slightly different, both are designed to have the same thickness, th_e, to simplify manufacturing. This thickness is dictated by the more extreme loading. Given the maximum angular velocities and pressures expected in the present optimization, the oil-side distribution will tend to cause more severe bending. Nonetheless, a bending analysis is carried out for both end caps in the model-based

design process. Programmatically, the end cap thickness is chosen by incrementally increasing th_e from some very small initial guess and until the maximum von Mises stress, as calculated by Eqn. 51, for both end caps at ω_{max} and $P_{s,max}$ is less than $S_{y,e}/SF$.

3.4 Piston

The purpose of the piston, which translates upon the axle and within the housing, is to separate the compressed gas from the hydraulic oil. Like the end caps, the piston does not contribute mass-efficient inertia to the HFA, and its dimensions should therefore be selected to minimize mass. For the present purposes, the piston is analyzed in two portions – the bearing section, which is axially long and ensures smooth translation, and the disc section, which is axially short and provides the actual barrier between the oil and the gas.

In a system of two concentric cylinders that contact each other at a diameter d over a length l, smooth axial translation is ensured when the bearing ratio, l/d, satisfies the inequality [24]

$$\frac{l}{d} \geq 1.5 \tag{52}$$

Therefore, the length of the bearing section of the piston is selected to be

$$l_p = (1.5)(2r_a) \tag{53}$$

Notice that the axle diameter, $2r_a$, has been used in Eqn. 53 rather than the housing inner diameter, $2r_i$. Effectively, the presence of the axle decreases the length, l_p, that is required to prevent the piston from cocking. It is unnecessary for the piston to have the axial dimension l_p across its entire radius, and therefore, the piston is designed with an L-shaped circumferential cross-section, as shown in Fig. 23.

The bearing section of the piston is subject to relatively small loadings, and therefore the dimension th_b can be made quite small. For simplicity, the value of th_b is

conservatively chosen to be twice the height of the piston seal groove, H_g. The seal groove height is approximately constant for any HFA design solution, and chosen based on commercial literature to be 5 mm [32].

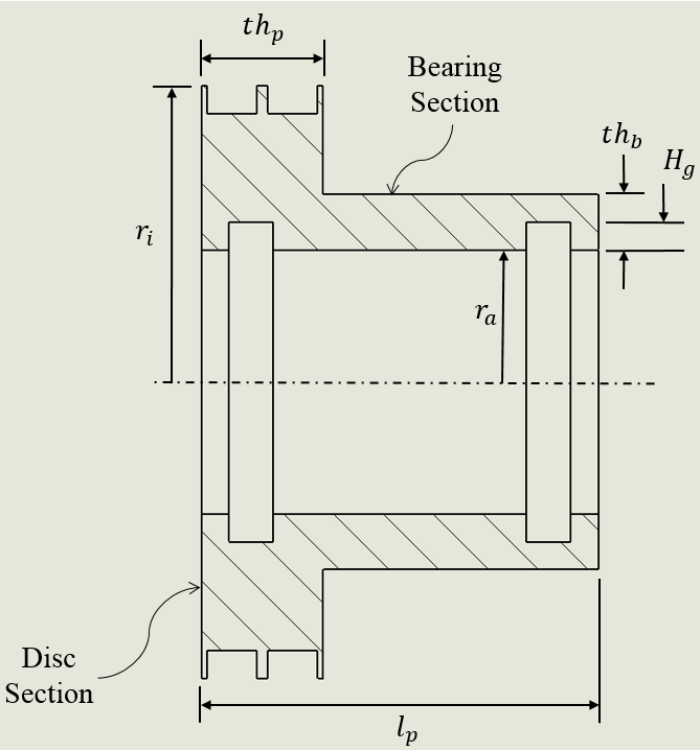

Figure 23: Piston Design

In selecting the thickness, th_p, of the disc section of the piston, the first consideration involves packaging the seals at the interface between the piston and housing. Two oppositely-facing, single-acting seals are seated in two grooves at the outer radius of the piston, as shown in Fig. 24.

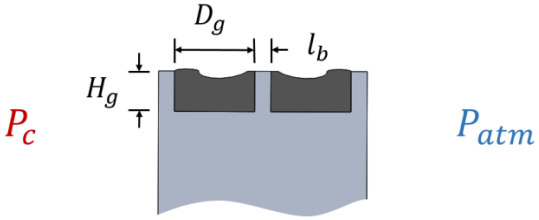

Figure 24: Packaging Region of the Piston Seals

The boss that separates the two seals is exposed to a pressure differential that is highest at the time that the accumulator is charged, when the pneumatic pressure is equal to P_c and the system pressure is equal to P_{atm}. The length l_b is selected to be sufficiently large to prevent transverse shear failure of the boss due to the pressure differential $P_c - P_{atm}$ (which is approximately equal to P_c). This minimum required length is

$$l_b = H_g \frac{(SF)P_c}{(0.58)S_{y,p}} \tag{54}$$

where H_g is the groove height, and the factor of 0.58 multiplied by the tensile yield strength of the piston, $S_{y,p}$, is conventional to estimate the material shear strength. The two outer bosses are not exposed to pressure differentials, so they can be quite thin. Their thicknesses are neglected until final detailed design. Given the packaging considerations of the two piston seals at the piston-housing interface, the thickness th_p is constrained by

$$th_p \geq 2D_g + l_b \tag{55}$$

where D_g is the width of a single seal groove. Like the seal groove height, the value of D_g can be treated as a constant for the purposes of optimization. It is estimated from commercial literature to be 1 cm [32]. The axial positions of the inner piston seals (those which seal against the axle) are selected and justified in Section 8.3.

While seal packaging constraints generally impose a stricter lower bound on piston thickness, bending stresses in the disc section must also be evaluated. At zero angular velocity, pressure in the HFA is uniform, and the piston experiences only axial compressive stress. For any non-zero angular velocity, a radially-dependent pressure distribution arises across the piston as the result of the difference between the oil and gas densities. The equation that describes the net pressure distribution, P_{net}, across the piston can be found by taking the difference between the oil side and gas side pressure distributions, given by Eqns. 13 and 16, respectively.

$$\begin{aligned} P_{net}(r) &= P_o(r) - P_g(r) \\ &= P_s + \frac{1}{2}\rho_o\omega^2 r^2 - \exp\left[\frac{\rho_{atm}}{P_{atm}}\omega^2\frac{r^2}{2} + \ln\left(P_{g0}\right)\right] \end{aligned} \tag{56}$$

This pressure distribution causes bending stresses in the disc section of the piston. The same theory and methods used to analyze the end cap bending and centrifugation can be used for the piston. The disc section of the piston is isolated from the bearing section for this bending analysis, although the bearing section is assumed to provide a reaction moment.

Because it is a combined parabolic and exponential function, Eqn. 56 does not clearly indicate the worst-case loading condition for the piston. In fact, for a given piston geometry, there may be a set of several different conditions that could be considered "equally worst-case." To illustrate this point, Fig. 25 qualitatively shows how different angular velocities cause significant differences in the nature of the net pressure distribution. The maximum von Mises stress (scaled by pneumatic pressure) is plotted against angular velocity for two piston geometries. System pressure is held constant at 21 MPa throughout.

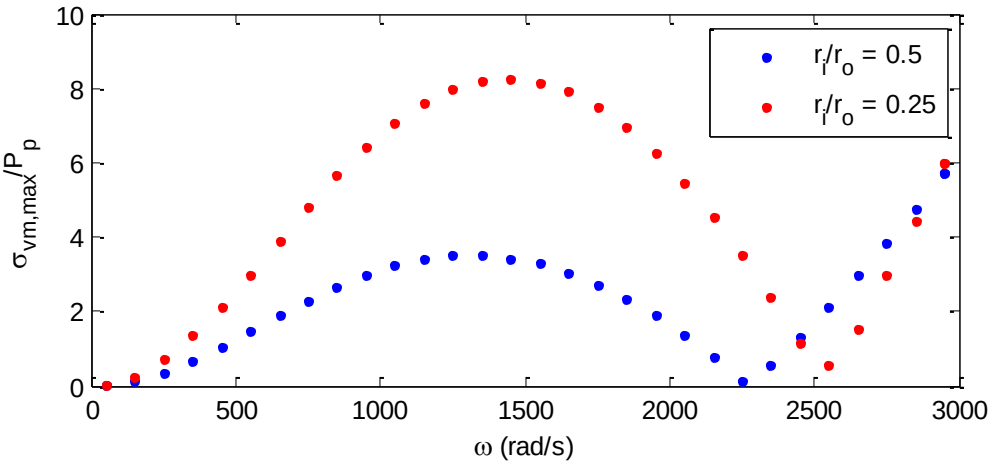

Figure 25: Maximum von Mises Stress (Non-dimensionalized) for the Same System Pressure at Different Angular Velocities; Two Piston Geometries Shown

Notice that, for the range of data plotted, there are up to three different operating speeds that produce the same ratio of $\max(\sigma_{vm,p})/P_p$ (in all cases, this maximum stress occurs at the inner radius of the piston, r_a). To illustrate why this is the case, Fig. 26 shows the net pressure distributions for a particular HFA design solution operating at three different angular velocities, each of which results in the same maximum von Mises stress.

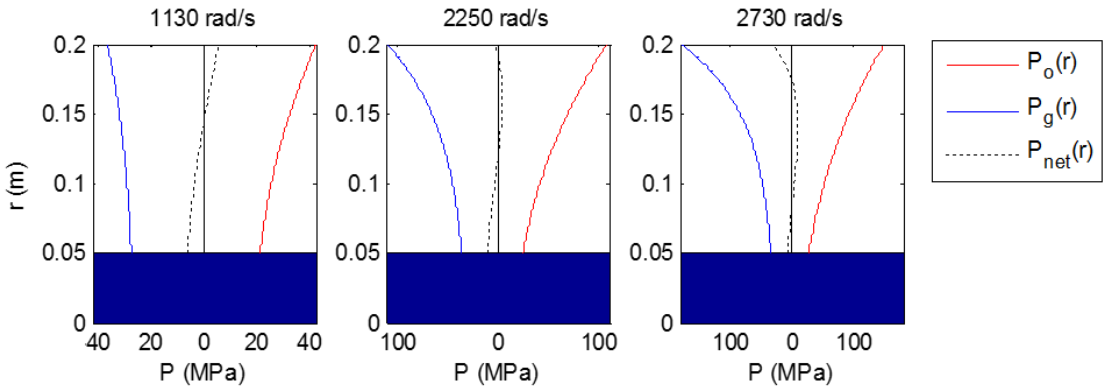

Figure 26: Oil, Gas, and Net Pressure Distributions for Three Different Angular Velocities which Produce the Same Maximum von Mises Stress for a Given HFA Geometry and System Pressure

At low speeds, the gas density stratification is subdued. The higher oil density causes more pronounced centrifugal effects, and bending stresses are exacerbated by increasing speed. At some speed above 1130 rad/s, the intensifying gas density stratification actually begins to mitigate bending by producing a pressure distribution that more closely matches the oil side. Interestingly, the net pressure distribution in this region does not increase monotonically. By 2250 rad/s, this effect has reduced the maximum bending stress to the value seen at 1130 rad/s, and stresses continue to fall as angular velocity increases. Eventually, however, the gas density stratification becomes so extreme that a high concentration of net force arises at the outer radius. Maximum bending stress begins to increase again with speed (at 2730 rad/s reaching the value observed at the 1130 and 2250 rad/s cases), a trend that continues indefinitely. Note that the speeds at which these transitions occur is a function of the specific HFA geometry.

For the laboratory prototype, speeds and pressures will probably not be high enough to encounter these interesting bending phenomena. There will likely be a single operating point which presents the worst case loading on the piston, and this will almost certainly be at maximum pressure and angular velocity. Therefore, $P_{s,max}$ and ω_{max} are used to calculate a minimum allowable piston thickness, th_p, to prevent material failure. This value is then compared to the packaging constraint given by Eqn. 55, and the larger of the two is used for the final selection of th_p. FEA is used in the detailed design process to

confirm that the selection of th_p provides sufficient protection against failure of the piston.

3.5 Housing

In facilitating the fundamental HFA concept of coupling pneumatic and kinetic energy storage, the HFA housing is truly a multi-purpose component; its presence is required in order to contain the pressurized fluid, but it can also be considered a flywheel rotor. The theoretical maximum kinetic energy density for a thin-walled rotor is [33]

$$\left.\frac{E}{m}\right|_{max} = \frac{1}{2}\frac{S_y}{\rho} \tag{57}$$

In practice, flywheel rotors tend to be thick-walled, resulting in a relation similar to Eqn. 57, but with the factor of $\frac{1}{2}$ replaced by some other factor that depends on the rotor geometry, material(s), and the flywheel architecture.

To understand why energy density scales with the strength-to-density ratio of the rotor, consider the two means by which rotational kinetic energy can be increased without adding mass to the housing. First, the moment of inertia can be increased by concentrating material at a larger radius (see Eqn. 2 for the definition of inertia). Second, the rotational speed can be increased. Equations 47 and 48 suggest that both techniques increase centrifugal stress, which is proportional to the square of radial position and the square of angular velocity. Because centrifugal stress is also inversely proportional to material density, a high strength-to-density ratio tends to promote high energy density. Composite materials, therefore, are excellent candidates for rotor construction and will be assumed as the housing material of choice for all HFA applications.

Cylinder-type composite flywheel rotors are typically manufactured by winding a filament wetted with epoxy around a rotating mandrel [34], which may or may not be removed after the winding process. The mandrel rotates at a constant speed to ensure axisymmetry, while the axial trajectory of the filament feeding tool dictates the wind

angle. The simplest tool trajectory is a constant forward speed, which results in a nearly-circumferential fiber direction. This fiber orientation results in the maximum achievable circumferential strength in tension. The radial and axial directions of the rotor exhibit the material's transverse strength, which is the minimum strength exhibited by a composite material.

The radial and circumferential centrifugal stress distributions due to centrifugation of an isotropic rotor (Eqns. 47 and 48), which are qualitatively similar for an anisotropic (i.e. composite) rotor, are shown in Fig. 27. They have been non-dimensionalized and are shown for several values of r_i/r_o (arrows indicate increasing wall thickness), with a Poisson ratio of $\nu = 0.3$.

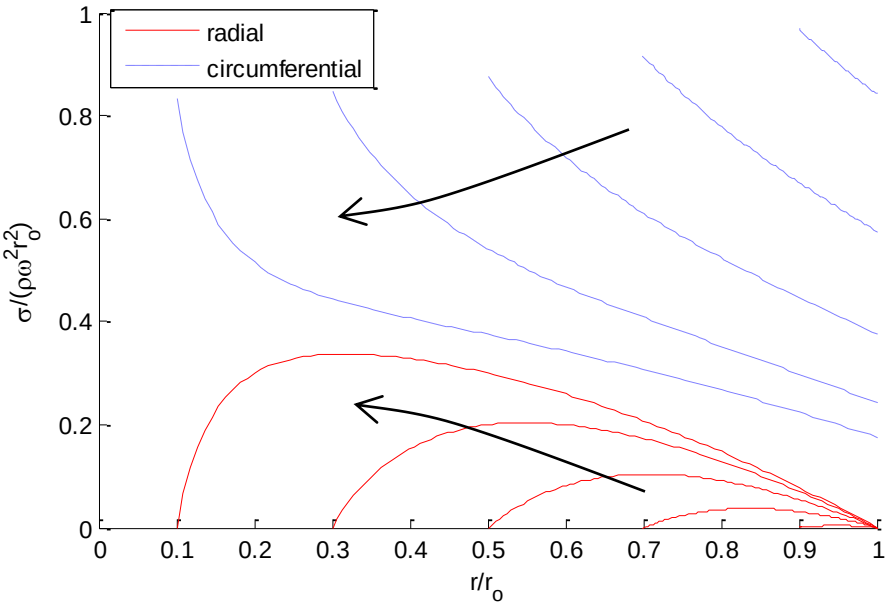

Figure 27: Non-dimensional Radial and Circumferential Stress Distributions due to Centrifugation of an Isotropic Hollow Cylinder

Note that the peak circumferential stress due to centrifugation is generally several times greater than peak radial stress. For an isotropic material, this means that the rotor failure mode is by hoop stress. However, for a composite cylinder exposed to centrifugal force, where the radial tensile strength may be several times lower than the circumferential strength, the failure mode may very well be delamination due to interlaminar tension.

Many methods have been proposed to address the issue of radial tension in a composite rotor. Nearly all are hinged on the fact that, in general, a composite material has a higher transverse compressive strength than transverse tensile strength [35]. The proposed methods can be roughly split into two categories. The first category includes those methods which induce a residual compressive radial stress during manufacturing or assembly. Upon rotation, the initial compressive stress causes the radial stress distribution to either remain compressive or be low enough in tension to avoid delamination. This concept can be accomplished by one or a combination of the following means:

a) Design for a press-fit between the rotor and hub [36]
b) Separately manufacture several circumferentially-wound cylinders of different dimensions and subsequently press-fit them to form a single rotor [37]
c) Utilize high tension in the filament-winding process [38]

Of these proposed methods, option a) is physically inconsistent with the HFA architecture, and options b) and c) increase manufacturing cost and complexity.

The second category of methods for addressing concerns about radial tension includes those in which the rotor is designed to have mechanical properties that vary in the radial direction. By designing for higher density and/or lower stiffness at lower radial locations, centrifugal force will cause lower radial locations to tend to strain more, thereby "pushing" on higher radial locations, mitigating or eliminating radial tensile stresses that would otherwise arise. Some of the proposed means by which to accomplish these variable rotor properties are:

d) Use a variable filament winding angle, with some axial component at lower radii, increasing to purely circumferential winding at the outer radius [39]
e) Use multiple cylinders of dissimilar materials, with denser and/or more compliant materials on the inside [35]
f) Use a variable fiber content, with lower fiber volume fraction at lower radii [25]
g) Ballast inner layers by embedding dense particles [25]

All of these methods require a complex optimization and design process and significantly increase manufacturing cost.

Fortunately, the construction of the HFA housing and the loadings to which it is exposed during operation provide a natural solution to the issue of radial tension. The HFA housing will be manufactured via the filament-winding process described at the beginning of this section, with a circumferential fiber angle. To ensure proper sealing between the piston and housing, the steel mandrel used in this process will not be removed, but will instead become the liner of the housing. A graphical representation of the liner-composite housing was shown in Fig. 7. The higher density and compliance of the liner help to mitigate radial tension via the same mechanism as methods *d* through *g* above. Furthermore, Eqns. 13 and 16 show that the internal wall of the liner is exposed to a pressure of

$$P_o(r_i) = P_s + \frac{1}{2}\rho_o \omega^2 r_i^2 \tag{58}$$

on the oil side of the HFA and

$$P_g(r_i) = \exp\left[\frac{\rho_{atm}}{P_{atm}}\omega^2 \frac{r_i^2}{2} + ln\left(P_{g0}\right)\right] \tag{59}$$

on the gas side.

The fluid pressure acting on the liner imposes compression between the liner and housing, mitigating the issue of radial tensile stress in a similar fashion as methods *a* and *b* above. Whether the internal fluid pressure and the use of a hybrid rotor prevent delamination of the wrap depends on the loads imposed by the operating conditions, as well as the thicknesses and mechanical properties of the liner and the wrap. Because of their complex implications on mass, stress, energy capacity, and efficiency, the liner and wrap thicknesses are used by the optimization algorithm as design variables.

Examination of Eqns. 58 and 59 suggests that, at non-zero angular velocity, the internal wall pressures on the gas and oil sides of the HFA are generally unequal; for the operating conditions, HFA geometry, and fluid properties expected in a first-generation prototype, the internal wall pressure on the oil side tends to be somewhat larger.

However, the discrepancy is relatively small, and therefore a single internal pressure, $P_{int} = P_o(r_i)$, can be used as the conservative worst-case maximum wall pressure. This pressure is also assumed to act in the gap between the piston and the housing. As will be illustrated in Section 8.4, FEA confirms that this uniform pressure assumption yields very accurate housing stress predictions, even though the real loading is axially non-uniform.

A code has been created, based on methods presented by Arnold [37], to model the radial and circumferential stresses in the liner-composite system. The analysis is based on the radial stress and displacement compatibility conditions at the interface between the liner and the wrap. The loading on the housing can include centrifugal force and internal pressure. It is assumed that residual stresses due to the manufacturing process are negligible compared to the centrifugal and pressure loadings imposed during HFA operation. Furthermore, the weight due to gravity acting on the housing is neglected, such that axial stresses are assumed to be zero. Finally, torsion due to motoring or braking of the HFA is neglected. It is easily verifiable during a drive cycle simulation that loading due to torsion and the weight of the housing are negligible compared to pressure and centrifugal loading.

To illustrate the interactive effects of internal pressure, angular velocity, and liner thickness on stresses in the housing, a brief study is presented here. The liner and composite properties for the study have been selected to represent a typical steel and carbon fiber composite, respectively. Three cases are tested, each with a different operating state, as summarized in Table 2. For all cases, the housing inner and outer radii are 10 cm and 30 cm, respectively, while liner thickness is varied between 5% and 65% of total wall thickness.

Table 2: Load Cases for a Study on Stresses in a Hybrid Housing

	Case 1	**Case 2**	**Case 3**
$\boldsymbol{P_s}$	0	$21\ MPa$	$21\ MPa$
$\boldsymbol{\omega}$	$1200\ rad/s$	$1200\ rad/s$	$0\ rad/s$

In each figure below, the plot on the left shows $\sigma_r(r)$, the radial stress distribution as a function of radius. The plot on the right shows $\sigma_\theta(r)$, the circumferential stress distribution as a function of radius. The liner is shown with the lighter curve, and the wrap is shown with the darker curve. Arrows indicate the direction of increasing liner thickness. Note that there is a radial stress continuity enforced at the liner-wrap interface. As no such continuity is necessary for circumferential stress, dotted lines have been included to connect the liner curve to its corresponding wrap curve for the plots on the right.

Case 1, which illustrates the effect of liner thickness on stress distributions at high angular velocity and zero internal pressure, is shown in Fig. 28. This represents the load case that would occur if the gas-side end cap seal were to fail, relieving pressure in both the gas and oil volumes, when the kinetic SOC was high.

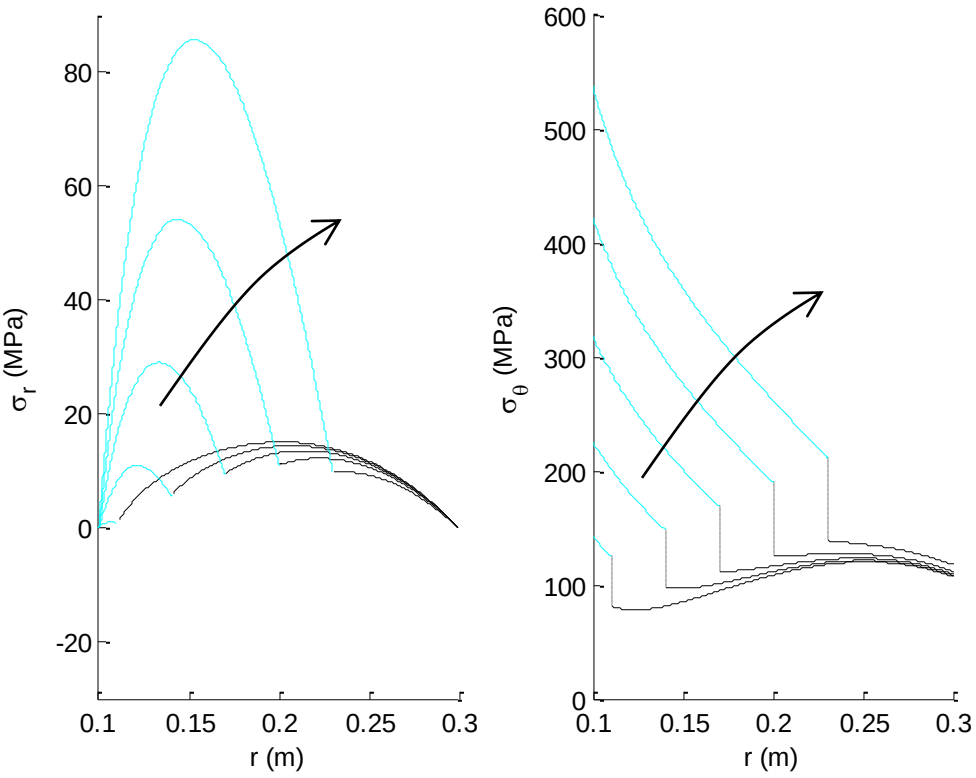

Figure 28: Hybrid Rotor Load Case 1 - Unpressurized at High Speed

When loading is due to centrifugation only, hoop and radial stresses are tensile everywhere, both in the liner and wrap. The radial stress plot (left) confirms that tension in the wrap is mitigated by the presence of a higher-density material inside it; the larger the liner, the lower the maximum stress in the wrap. When the liner is 10 cm thick (i.e. the liner-wrap interface is at r = 20 cm), the peak radial stress in the liner is more than four times the peak radial stress in the wrap. Even so, given the very low transverse tensile strength of a typical composite material, the wrap may be much nearer to failure than the liner is. Therefore, case 1 represents the worst-case loading from the perspective of potential delamination.

Figure 29 shows load case 2, where the high pressure and angular velocity represent the HFA operating near full SOC.

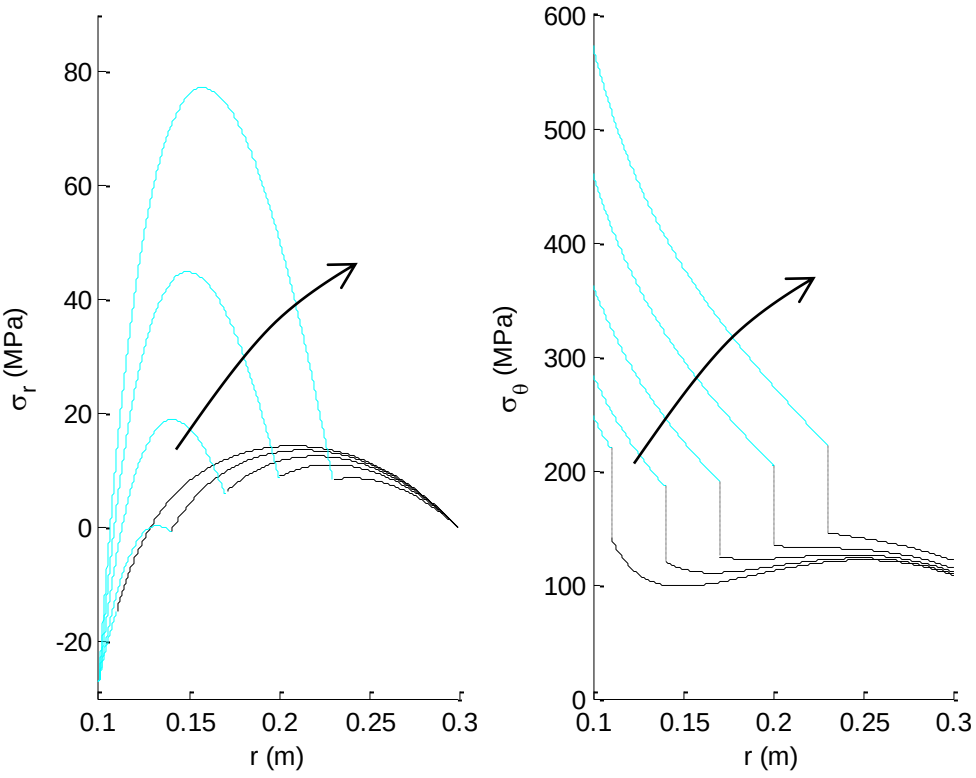

Figure 29: Hybrid Rotor Load Case 2 - Pressurized at High Speed

From the plot on the left, it is clear that internal pressure results in at least some relief of radial tension by imposing compression between the liner and wrap. While it is difficult to discern by visually comparing Figures 28 and 29, the pressurization in this study reduces peak radial tension in the wrap by about 5% to 15%, depending on the liner thickness. This benefit comes at the expense of a marginal increase in peak hoop stress in both the liner and wrap. Generally, this is a worthwhile tradeoff, since the radial tension tends to be the stress nearest to causing failure of the housing. Given these trends, case 2 represents the worst-case loading from the perspective of a tensile hoop failure of the liner.

Finally, Fig. 30 shows case 3, where the HFA is not rotating, but the system is fully pressurized. Note that the pressure at the liner wall is lower in this case than in the previous, since there is no centrifugal force acting on the oil in the present case. Because the stresses are quite different than those in the previous two cases, the scales in Fig. 30 are different than those in Figures 28 and 29.

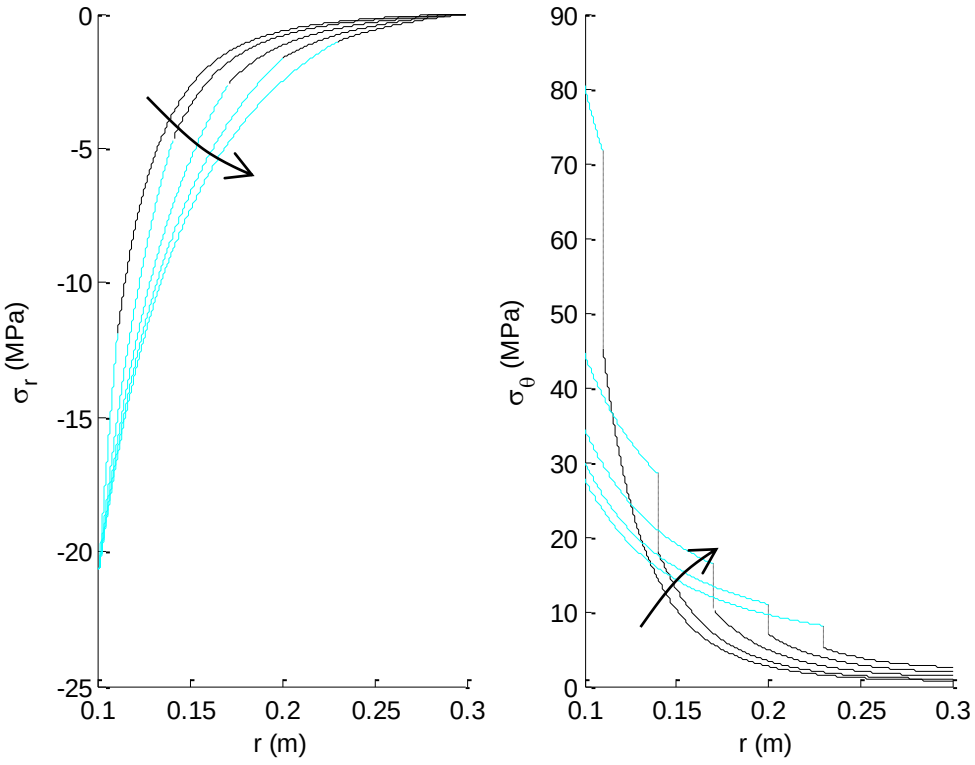

Figure 30: Hybrid Rotor Load Case 3 - Pressurized at Zero Speed

Without centrifugal force, radial stresses are compressive everywhere. Hoop stresses are positive, although they are far lower than in the previous two cases. The key aspect of the stress distributions in this load case is the relatively high compression in the wrap when liner thickness is small. Though generally higher than transverse tensile strength, the transverse compressive strength of a typical composite is significantly lower than that of a metal. Therefore, load case 3 represents the worst-case loading from the perspective of radial compressive failure of the wrap.

The study presented above indicates that the housing stresses must be evaluated at three possible worst-case loadings in order to determine the safety factor against material failure. The liner safety factor is calculated using the von Mises criterion as

$$SF_l = \frac{S_{y,l}}{\max\left[\sqrt{\sigma_r(r)^2 + \sigma_c(r) - \sigma_r(r)\sigma_c(r)}\right]} \tag{60}$$

and the wrap safety factor is calculated using the Tsai-Hill criterion [40] as

$$SF_w = \frac{1}{\max\left[\left(\frac{\sigma_c(r)}{X_w}\right)^2 + \left(\frac{\sigma_r(r)}{Y_w}\right)^2 - \frac{\sigma_c(r)\sigma_r(r)}{X_w^2}\right]} \tag{61}$$

where X_w and Y_w are the longitudinal and transverse tensile strengths of the composite material, respectively. Equations 60 and 61 are evaluated at each of the three potential worst-case loadings, and the lowest of the six resultant safety factors is chosen as the overall housing safety factor.

3.6 Bearing Selection

The purpose of the bearings is to spatially constrain the HFA while allowing it to rotate about its longitudinal axis with relatively little frictional drag. As shown in Fig. 19, the bearings and the shafts on which they reside are subject to the radial force F_{ecc}. This force is the result of a non-zero radius of eccentricity, r_{ecc}, of the HFA center of mass about the axis of rotation, and is given by

$$F_{ecc} = (m + m_o)\omega^2 r_{ecc} \tag{62}$$

Where m_o is the mass of the oil volume and m is the mass of the primary HFA components (the housing, axle, end caps and piston),

$$m = m_h + m_a + 2m_e + m_p \tag{63}$$

The centers of mass of thee piston, oil volume and gas volume translate axially only a small amount during HFA operation, such that the radial load on each bearing should be roughly equal. To be conservative, however, the bearings are sized such that each can withstand the full eccentric force, F_{ecc}.

Note that oil mass, m_o, is not a constant. To be conservative in sizing the bearings, the maximum expected oil volume should be used. Maximum oil volume is a function of the control strategy, making it somewhat challenging to predict. However, as the oil generally contributes a relatively small amount of mass to the HFA, an accurate estimate of maximum oil volume is relatively unimportant. For the present purposes, the mass of oil in the HFA at full SOC is used as m_o. The mass of the gas volume is even smaller than m_o and is therefore neglected.

It is clear from Eqn. 62 that the eccentric force is greatest when $\omega = \omega_{max}$ and the HFA contains the maximum oil volume. Any eccentricity is the result of manufacturing error and balancing imperfection. It is up to the designer to specify a conservative estimate for the radius of eccentricity. Rotor balancing standards dictate that, for flywheels, the product of the radius of eccentricity and the maximum operating angular velocity should not exceed 6.3 mm/s [41]. Assuming that this standard can be met in the manufacture of the HFA, the radius of eccentricity (in meters) is

$$r_{ecc} = \frac{6.3(10^{-3})}{\omega_{max}} \tag{64}$$

Because there is a considerable amount of uncertainty in the quality of the balancing procedure for the HFA, and because the integrity of the bearings is of utmost importance, a safety factor of 10 is applied to the radius of eccentricity for the purposes of estimating maximum radial load. The eccentric force on the bearings is then

$$F_{ecc} = (m + m_o)\omega_{max}(10)6.3(10^{-3}) \tag{65}$$

In addition to the radial eccentric force, the top and bottom bearings are also subject to the axial loads F_{b1} and F_{b2}, respectively, as discussed in Section 3.2. Because the wave spring pre-compression has been set to zero, the greatest axial force on the bottom bearing occurs when the HFA is unpressurized and the weight of the HFA is acting upon it.

$$F_{b2}|_{max} = mg \tag{66}$$

The maximum axial force on the top bearing tends to be much larger, occurring when a surge in system pressure causes the HFA to lift off of the bottom bearing. The value of $F_{b1}|_{max}$ is calculating in the process of solving the system of Eqns. 28 through 38, as described in Section 3.2.

Note that small bearing diameters are generally desirable, as they exhibit lower power dissipation [42]. Stresses in the gas and oil side shafts, however, impose a lower limit on the bearing inner diameter, $d_{b,i}$. As mentioned in Section 3.2, the small distance between the eccentric radial force and the bearing reaction justifies the omission of bending stresses from the analysis of the axle shafts. Shear stresses in the axle that result from the radial eccentric force should, however, be assessed to determine the minimum allowable value of $d_{b,i}$. This maximum transverse shear stress in the oil side shaft is [28]

$$\tau_{V,os} = \frac{16}{3}\frac{F_{ecc}}{\pi(d_{b,i}^2 - d_i^2)} \tag{67}$$

The torque is minimal on the oil side, due only to viscous shearing in the circumferential seal. The critical stress is at the outer radius, $d_{b,i}/2$, where the system pressure imposes tensile hoop stress and compressive normal axial stress, in addition to the transverse shear stress due to F_{ecc}. The former can be calculated using Eqn. 39 (hoop stress in a thick-walled cylinder), and the compressive normal stress is

$$\sigma_{z,os} = k_{n,os}\frac{4F_{s,max}}{\pi\left(d_{b,i}^2 - d_i^2\right)} \tag{68}$$

where $F_{s,max}$ is the force imposed by the maximum expected system pressure acting on the oil side face of the axle (given by Eqn. 29) and $k_{n,os}$ is a normal stress concentration factor.

The gas side shaft does not experience internal pressure but must withstand the transverse shear loading due to F_{ecc} and the torsional shear loading from the storage PM torque. Any normal stress that might be imposed by the shaft coupling between the axle and storage PM is assumed to be negligible. The total stress in the gas side shaft is simply equal to the sum of the maximum transverse and torsional shear, which are, respectively [28]

$$\tau_{V,gs} = \frac{16}{3}\frac{F_{ecc}}{\pi d_{b,i}^2} \tag{69}$$

$$\tau_{T,gs} = k_{t,gs}\frac{16T_{max}}{\pi d_{b,i}^3} \tag{70}$$

where T_{max} is the maximum expected torque and $k_{t,gs}$ is a torsional stress concentration factor. Figure 31 shows correlations for the stress concentration factors, based on data from Juvinall et al [28], used in the gas and oil side shaft stress calculations. These factors are functions of the fillet radius, r_f, where the shaft meets the main section of the axle.

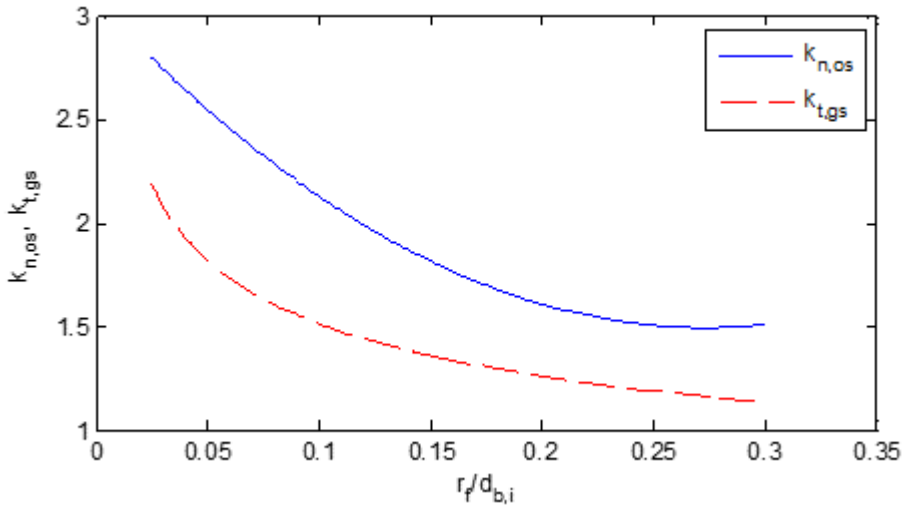

Figure 31: Normal and Torsional Stress Concentration Factors Used in the Axle Shaft Stress Calculations

The von Mises stress criterion is used to calculate the maximum equivalent stresses in the gas and oil side shafts. Clearly, these maximum stresses will not be equal, due the fact that the geometries and load cases of the gas and oil shafts are different. For simplicity in sourcing bearings, both the gas and oil side shafts will have the same outer diameter, $d_{b,i}$, with the greater maximum equivalent stress dictating the lower bound on $d_{b,i}$. Programmatically, this lower bound is found by guessing $d_{b,i} = d_s$ and then incrementally increasing $d_{b,i}$ until neither of the shafts fail at their worst case loading condition.

Although shaft stresses impose a lower bound on the bearing inner diameter, the static load ratings of the bearings generally drive $d_{b,i}$ to larger values. Because of their relatively low friction and ability to handle significant radial and axial loads, angular contact ball bearings are chosen for application in the HFA. In detailed design, the bearings will be carefully selected by the designer. However, to facilitate efficient model-driven design and simulation, a code has been written to query a database of commercially available angular contact bearings and select the one with the minimum possible inner and outer diameters that can withstand the maximum expected loads.

First, the algorithm cycles through the bearings, beginning with the smallest, until it reaches a bearing with an inner diameter that satisfies the lower bound imposed by shaft stresses. Next, the equivalent dynamic load is calculated as

$$P_{eq} = XF_{ecc} + YF_{b1}|_{max} \tag{71}$$

where X and Y are determined as follows [43]. The database contains a combination of bearings with 25 degree and 15 degree contact angles. For units with a 25 degree contact angle,

$$X = 1, \qquad Y = 0 \tag{72}$$

unless $F_{b1}|_{max}/F_{ecc} > 0.68$, in which case

$$X = 0.41, \qquad Y = 0.87 \tag{73}$$

Calculating equivalent load for bearings with a 15 degree contact angle is somewhat more involved. First, a value of the variable e is determined using Fig. 32. If the inequality $F_{b1}|_{max}/F_{ecc} > e$ is true, then

$$X = 0.44 \tag{74}$$

and Y is determined using Fig. 32.

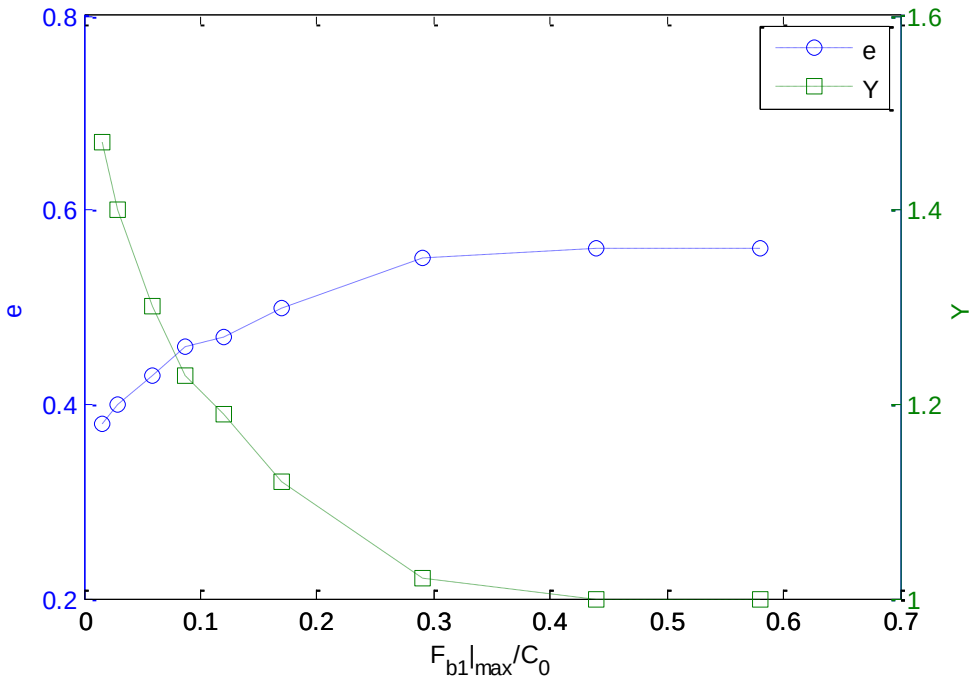

Figure 32: Plots Used to Determine *e* and *Y* Values for Calculating Equivalent Bearing Load

Otherwise, Eqn. 72 holds true. Next, the equivalent static load, $P_{eq,0}$ is calculated as

$$P_{eq,0} = (0.5)F_{ecc} + Y_0 F_{b1}|_{max} \tag{75}$$

where Y_0 is equal to 0.46 and 0.38 for bearings with contact angles of 15 degrees and 25 degrees, respectively. The bearing is deemed sufficient if the calculated equivalent static and dynamic loads do not exceed the load ratings of the bearing, and if the speed rating of the bearing is less than ω_{max}. These ratings are stored in the bearing database. If the bearing has not been correctly-sized, the algorithm moves on to try the next bearing in the database, and the process summarized in Eqns. 71 through 75 continues until a bearing is found that meets the load and speed requirements.

3.7 Material Selection and Static Calculations

Section 3.5 discussed the merits of a high strength-to-density ratio for flywheel rotors. In general, this principle extends to all of the major rotating components in the HFA. While bounds may be imposed on system pressure, operating speed, and packaging volume, it is often material strength that ultimately limits the energy density of a candidate HFA design solution. Therefore, strength is generally the primary criterion in selecting a component material, with factors like wear resistance, cost and availability as secondary criteria. This section summarizes and justifies the selected materials for the major HFA components, and presents the basic mass and inertia calculations for each.

For a given system pressure, maximum operating speed, and housing dimensions, minimization of the axle dimensions is best accomplished by using a high-strength material. Because of its excellent strength, toughness, and fatigue properties, AISI 4340 steel is well-suited for axle-type applications [44]. For the range of expected axle diameters, oil quenching AISI 4340 at 800 C and tempering at 540 C can achieve a yield strength of 1000 MPa [45]. Stresses in the end caps and piston tend to be smaller, and therefore a material with a somewhat lower strength can be used. Aluminum 7075-T6 is chosen for its relatively high strength-to-density ratio.

The housing liner is made of steel for several reasons. To avoid excessive wear in the event of sliding contact, it should be constructed of a dissimilar material to the end caps and piston [46]. High strength is also extremely important liner, although high density is not necessarily objectionable, as a higher specific modulus of the liner tends to mitigate radial tension in the composite wrap (see Section 3.5). Because the liner tends to be quite thin in the radial direction, heat treatment can be very effective in increasing its strength. Quenched and tempered at 205 C, AISI 4140 steel achieves a yield strength of 1515 MPa [45].

For the housing wrap, T300 carbon fibers with a series #2500 resin are selected to constitute the composite-epoxy matrix. These materials are widely available and provide the high strength-to-density ratio demanded by the HFA housing. The T300/#2500

composite matrix has a longitudinal strength of 1800 MPa and a density of 1600 kg/m^3 [35].

The retainers are made of the same AISI 4340 steel as the liner, as the high strength allows for the retainer thickness, and therefore axle length, to be minimized. To protect the axle from damage in the event that the HSRU circumferential seal fails and allows contact between the axle and HSRU case, class 40 gray iron is selected as the case material. This is a cheap and easily-machinable material with good wear and galling resistance [44].

Tables 3 and 4 summarize the material selections for the various rotating HFA components, along with relevant material properties. Because of its anisotropic mechanical properties, the carbon fiber composite is summarized separately in Table 4. Properties for the composite are categorized as longitudinal (those in the direction of the fibers) and transverse (perpendicular to the fiber direction).

Table 3: Selected Materials and their Mechanical Properties [45]

	Material	**Grade**	**Density** kg/m^3	**Elastic Modulus** GPa	**Poisson Ratio**	**Yield Strength** MPa
Liner	Steel	AISI 4140	7850	200	0.30	1515
Axle	Steel	AISI 4340	7850	200	0.30	1000
End caps	Aluminum	7075-T6	2810	72	0.33	503
Piston	Aluminum	6061-T6	2700	69	0.33	276
Retainers	Steel	AISI 4140	7850	200	0.30	415
HSRU case	Gray Iron	Class 40	7150	110	0.29	290

Table 4: Properties of the Composite Material for the Housing Wrap [35]

	Elastic Modulus GPa	**Poisson Ratio**	**Tensile Yield Strength** MPa	**Compressive Yield Strength** MPa
Longitudinal	130	0.30	1800	1400
Transverse	9	0.021	27	200

For the purposes of calculating mass and inertia, all of the major rotating solid HFA components can be modeled as simple cylinders (or, in the case of the piston, a combination of two cylinders). Minor design features (e.g. pin system, axle ports) are neglected, as they have little influence on the accuracy of these calculations. The small mass of the HSRU case is omitted from the calculation of the HFA mass and can be considered a component of the containment chamber. The mass of cylindrical component i, which has a length l, inner radius a, and outer radius b, is

$$m_i = \rho_i l_i \pi (b_i^2 - a_i^2) \tag{76}$$

The calculation of the moment of inertia of a cylinder was given in Eqn. 2.

4 Energy Loss Mechanisms

There are various aspects of the HFA concept and architecture that will incur energy losses during operation. These losses can be generally categorized into those which effectively decrease the stored pneumatic energy and those which effectively decrease the stored kinetic energy. The loss mechanisms that are considered significant enough to include in the performance assessment of the HFA are listed in Table 5.

Table 5: List of Energy Loss Mechanisms and their Symbols (Given as Rates of Energy Dissipation), Categorized as Kinetic or Pneumatic

Kinetic
Bearing friction, $\dot{W}_b$
Aerodynamic drag, $\dot{W}_w$
HSRU viscous drag, $\dot{W}_{vh}$
Internal viscous dissipation, $\dot{W}_v$
Storage PM losses, $\dot{W}_{PM}$
Pneumatic
HSRU leakage, $\dot{W}_l$
Axle port losses, $\dot{W}_a$

Energy losses due to fluid compressibility and sliding friction at the piston seals are not modeled in the present research, since they tend to be insignificant compared to other losses and should not significantly affect the dynamics of the HFA. As has already been discussed, the isothermal compression assumption is used in modeling pneumatic energy domain, such that gas compression and decompression are considered lossless. The HFA efficiency is not penalized by losses in the traction PM, which is not actually an HFA component and must be included in a vehicle regardless of the hydraulic energy storage system. The energy required to establish and maintain a vacuum in the containment chamber does not fit into either category in Table 5, but rather can be considered a parasitic energy consumption.

This chapter details the various energy loss models developed for the mechanisms listed in Table 5. First, bearing and aerodynamic losses are addressed, followed by a discussion of the hydraulic pump-motor efficiency model. Next, the HSRU viscous, leakage and axle port losses are discussed together, in order to illustrate their shared dependence on the design variable d_i. The chapter concludes with a presentation of the methods used to model the vacuum pumping system. The internal viscous dissipation, which occurs as a result of velocity gradients in the rotating oil volume, is by far the most complex energy loss mechanism. It is therefore not discussed here, but is rather the sole focus of the next chapter.

4.1 Bearing and Aerodynamic Drag

As previously mentioned, angular contact ball bearings have been chosen for use in the HFA. Ball bearings generally incur two types of frictional torque. The first is due to the sliding of the rolling elements within the bearing and the second is due to hydrodynamic forces imposed by the lubricant. The HFA will employ bearings with ceramic rolling elements, which require no lubrication and therefore eliminate the latter torque component. While sophisticated analytical models of frictional bearing torque exist [47], such detail is unnecessary for the purposes of simulating the HFA. Following procedures in commercial literature [48], the frictional torque in a single bearing can be estimated as

$$T_b = \frac{\mu_b F_r d_{b,i}}{2} \tag{77}$$

where μ_b is an empirical frictional torque coefficient, F_r is the radial load on the bearing, and $d_{b,i}$ is the bearing inner diameter (shaft diameter). Given the discussion on HFA mounting, the radial force on each bearing, F_r, is half of the eccentric force.

$$F_r = \frac{(m + m_o)}{2}\, \omega^2 r_{ecc} \tag{78}$$

The total power dissipation due to bearing friction is then

$$\dot{W}_b = 2\omega T_b = \frac{\mu_b (m + m_o)\omega^3 r_{ecc} d_{b,i}}{2} \tag{79}$$

The friction coefficient is estimated to be $\mu_b = 0.001$, which, according to commercial data, is conservatively high for ceramic angular contact ball bearings [49, 50]. After obtaining the bearings for a particular HFA application, the actual value of μ_b can be characterized to provide more accurate simulation results. Whereas safety was the main concern in sizing the bearings and axle shafts, accuracy of predicted energy losses is most important in modeling bearing drag. The radius of eccentricity, r_{ecc}, can be simply calculated using Eqn. 64, and no safety factor need be applied.

Methods presented by Genta [25] are used to model the HFA aerodynamic losses. The torque due to aerodynamic drag on a rotating disk can be characterized by a moment coefficient,

$$C_m = \frac{T_w}{\rho_{ch}\omega^2 r_o^5} \tag{80}$$

where T_w is the aerodynamic ("windage") torque, ρ_{ch} is the density of the gas in the containment chamber, ω is the angular velocity, and r_o is the HFA outer radius. The value of the moment coefficient is a function of the Reynolds number and the Knudsen number. The former is calculated as

$$Re = \frac{\rho_{ch}\omega r_o^2}{\mu_{ch}} \tag{81}$$

where μ_{ch} is the dynamic viscosity of the gas in the chamber. The Knudsen number characterizes the degree to which the gas in the chamber can be modeled as a continuous medium. It is calculated by comparing the mean free path between gas molecules, λ, and a length scale of the HFA rotor, as shown below

$$Kn = \frac{\lambda}{l_h} \tag{82}$$

$$\lambda = \frac{M_{ch}}{\sqrt{2} a_{ch}^2 \rho_{ch} \pi} \tag{83}$$

where M_{ch} and a_{ch} are, respectively, the molecular mass and the effective molecular diameter of the gas within the chamber. Both of these values are available from property tables, but the latter should be adjusted for temperature by the equation

$$a_{ch} = a_{ch}^{*}\left(1 + \frac{113[K]}{T_{ch}}\right) \tag{84}$$

where T_{ch} is the expected absolute temperature of the gas in the containment chamber and a_{ch}^{*} is a reference effective molecular diameter. The viscosity of the chamber gas is calculated as

$$\mu_{ch} \cong \frac{\sqrt{KM_{ch}T_{ch}}}{a_{ch}^{2}\pi^{\frac{3}{2}}} \tag{85}$$

where $K = 1.38(10^{-23})$ is the Boltzmann constant. Equation 85 reflects the behavior of real gasses and corrects for the non-Maxwellian nature of the velocity distribution. In using Eqns. 84 and 85, it is the task of the designer to select an appropriate prediction of the gas temperature. For the purposes of design optimization, this is done by guessing $T_{ch} = T_{atm}$; in a detailed design, a full heat transfer analysis can be carried out.

The unrestricted boundary layer thickness, δ, can be calculated as

$$\delta = \begin{cases} \sqrt{\dfrac{\mu_{ch}}{\rho_{ch}\omega}}, & Re \le 3(10^{5}) \\ r_o^{\frac{3}{5}}\left(\dfrac{\mu_{ch}}{\rho_{ch}\omega}\right)^{\frac{1}{5}}, & Re > 3(10^{5}) \end{cases} \tag{86}$$

If the unrestricted boundary layer is thicker than the clearance, c_{ch}, between the HFA housing and the containment chamber, the moment coefficient is a function of only Reynolds number and can be calculated using the following empirical relations.

$$C_m = \begin{cases} 2.67Re^{-\frac{1}{2}}, & Re \le 3(10^{5}) \\ 0.0622Re^{-\frac{1}{5}}, & Re > 3(10^{5}) \end{cases} \tag{87}$$

If the clearance is large enough to accommodate the entire boundary layer, however, the Knudsen number becomes important in calculating the moment coefficient and the

critical Reynolds number changes. For $Kn < 0.1$, the gas in the containment chamber can be modeled as a continuous medium, and the moment coefficient is

$$C_m = \begin{cases} 3.87Re^{-\frac{1}{2}}, & Re \leq 5(10^4) \\ 0.146Re^{-\frac{1}{5}}, & Re > 5(10^4) \end{cases} \quad (88)$$

For $Kn > 10$, the gas is modeled as a free molecular flow, and the moment coefficient is

$$C_m = \frac{1}{\omega r_o}\sqrt{\frac{M_{ch}}{2KT}} \quad (89)$$

If $0.1 < Kn < 10$, the gas is said to behave as a transitional medium (somewhere between a continuous medium and free molecular flow). In this case the moment coefficient should be determined by linearly interpolating, based on Kn, between the values provided by Eqns. 88 and 89.

The correlations for moment coefficient presented above take into account each wall on a disk-type flywheel. To account for the cylindrical wall, the value of C_m obtained from the equations above should be multiplied by the factor $(r_o + \frac{5}{2}l_h)/r_o$, where l_h is the length of the HFA housing [25]. After calculating the moment coefficient, the rate at which energy is dissipated due to aerodynamic torque is

$$\dot{W}_w = T_w\omega \quad (90)$$

It should be mentioned that, as shown in the equations above, aerodynamic losses are a strong function of the chamber gas density. Lower density leads to lower energy dissipation, which is the motivation for operating the HFA in a vacuum environment. The tradeoff between expending energy to create a vacuum and dissipating energy via aerodynamic drag is further discussed in 4.4. Interestingly, the presence of a chamber actually reduces aerodynamic drag, even if a vacuum environment is not established [25]. In empirical correlations for the aerodynamic moment coefficient, some authors [51] use a very weak dependence on the ratio c_{ch}/r_o, while others [52] have found that C_m is independent of the chamber clearance.

In the absence of experimental data, the methods presented above serve as a reasonable approximation for aerodynamic losses. As in the case of the bearings, however, aerodynamic losses can be most reliably projected by characterizing the actual rotating system once it is constructed. In the case of a laboratory prototype, for example, this can be done with relative ease using a spin-down test. In such a test, the HFA, empty of oil, is allowed to decelerate from its maximum allowable speed, without an externally-applied torque. During deceleration, angular velocity is measured as a function of time. This can be time-differentiated to yield deceleration as a function of time, which, along with the known inertia of the HFA, allows for calculation of braking torque as a function of angular velocity. In a spin-down test, this torque is due only to bearing and aerodynamic drag. If the bearing torque has already been characterized, aerodynamic torque can be isolated, and the gathered data for $T_w = f(\omega)$ can be fit to the form of Eqn. 80 to calculate a value for C_m. Note that, if chamber gas density is expected to vary significantly, several spin-down tests should be performed using different gas densities in order to characterize the function $C_m = f(\rho_{ch})$.

4.2 Storage Pump-Motor Losses

Losses incurred by the storage PM are strongly dependent on the machine architecture. The axial piston machine is selected for use as the HFA storage PM, as it is one of the most common hydraulic pump-motor architectures and can achieve relatively high efficiency. Commercially-available aerospace axial piston pump-motors are capable of very high operating speeds [53], which allows the storage PM to be directly coupled to and spin at the same angular velocity, ω, as the HFA.

Two types of losses arise in hydraulic pump-motors. Volumetric losses result from the imperfect utilization of the hydraulic fluid flow through the PM, and mechanical losses are caused by the friction between various moving parts. A modified McCandlish and Dorey model [26] is used to predict volumetric and mechanical losses, both of which are functions of operating state (system pressure and angular velocity), hydraulic fluid properties, and empirical constants that characterize the particular PM. In the proceeding

discussion, D is the maximum displacement of the PM (units of volume per radian of rotation), x is the fractional displacement position (values of 0 to 1), and β_o is the bulk modulus of the oil (roughly 1660 MPa for most hydraulic oils). It is convenient to define the two following dimensionless numbers.

$$S = \frac{\mu_o \omega}{P_s} \tag{91}$$

$$\sigma = \frac{\omega D^{\frac{1}{3}}}{\sqrt{2\frac{P_s}{\rho_o}}} \tag{92}$$

As before, the subscript o indicates hydraulic oil properties.

The definitions of volumetric efficiency, η_v, and mechanical efficiency, η_m, depend on whether the PM is operating as a pump (extracting kinetic energy from the HFA) or a motor (adding kinetic energy to the HFA). Table 6 summarizes these definitions, where $\dot{V}$ is the volumetric flow rate of oil, T is the shaft torque of the PM, and the subscripts a and i indicate actual and ideal values, respectively.

Table 6: Volumetric and Mechanical Efficiency Definitions for Pumping and Motoring

	Pumping	**Motoring**
Volumetric efficiency, η_v	$\eta_v = \dot{V}_a/\dot{V}_i$	$\eta_v = \dot{V}_i/\dot{V}_a$
Mechanical efficiency, η_m	$\eta_m = T_i/T_a$	$\eta_m = T_a/T_i$

To qualitatively understand the preceding efficiency definitions, consider the case where the PM is operating in pumping mode. The real machine will produce less actual flow rate than the ideal machine, and it will require more actual torque to produce this flow rate than an ideal machine would require. These notions are consistent with values of efficiency that are less than unity.

In pumping mode, the volumetric and mechanical efficiencies of an axial piston PM are [26]

$$\eta_v = 1 - \frac{C_s}{xS} - \frac{P_s}{\beta_o} - \frac{C_{st}}{x\sigma} \tag{93}$$

$$\eta_m = \frac{1}{1 + \frac{C_v S}{x} + \frac{C_f}{x} + C_h x^2 \sigma^2} \tag{94}$$

where the values of C_s, C_{st}, C_v, C_f, and C_h are empirical loss coefficients that are unique to the particular PM being used. For a fixed-displacement machine, the displacement position is simply set to $x = 1$. Efficiencies in pumping and motoring mode are related by

$$\eta_{v,motor} = \frac{1}{2 - \eta_{v,pump}} \tag{95}$$

$$\eta_{m,motor} = 2 - \frac{1}{\eta_{m,pump}} \tag{96}$$

The fact that the empirical loss coefficients are specific to a particular PM makes it difficult to develop a general model for PM efficiency that can be embedded into a design optimization. In other words, one set of values for these loss coefficients may not accurately characterize the entire range of PM sizes observed in a design optimization. In the absence of a method to intelligently select these values based on PM size, however, a single set must be used for the present research. The selected values, along with the definition of each loss coefficient, are shown in Table 7.

Table 7: Selected Loss Coefficients for the Storage Pump-Motor [54]

C_s	**laminar coefficient of slip**	$4.26(10^{-9})$
C_{st}	**turbulent coefficient of slip**	0
C_v	**coefficient of viscous drag**	$2.35(10^4)$
C_f	**coefficient of friction**	0.0537
C_h	**hydrodynamic loss coefficient**	53.6

The values in Table 7 are taken from the manufacturer data for a Rexroth A2V pump-motor with a displacement $D = 107\ cm^3/rev$ [54]. It is assumed that these PM characteristics sufficiently reflect the efficiency discrepancy between the kinetic and

pneumatic domains of the HFA, thereby driving the design optimization in the appropriate direction. After a detailed design, when a particular PM has been selected, manufacturer data may be available to replace the values in Table 7 and facilitate more accurate projections of HFA efficiency.

4.3 Losses Related to the High-Speed Rotary Union

There are three distinct loss mechanisms related to the HSRU. Viscous dissipation and leakage occur at the circumferential seal, and axle port losses occur due to pressure drop as oil is transported between the HFA and the static environment. The two former mechanisms occur whenever the HFA is operating, while the latter occurs only during charging and discharging of the pneumatic domain. These three losses are presented together in this section to emphasize their interrelatedness and their shared dependence on various geometric dimensions.

Flow losses arise from the no slip condition at the walls of the conductor though which a fluid is passing. The zero wall velocity and non-zero mean flow velocity necessarily result in velocity gradients, and therefore viscous energy dissipation. In the HFA, these effects are most pronounced in the flow region constituted by the radial and axial ports in the axle, which are shown in Fig. 33 (HFA charging, as indicated by the arrows).

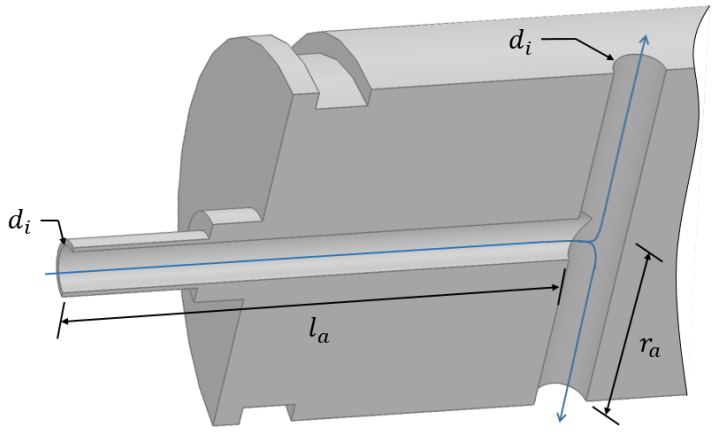

Figure 33: Axle Flow Passages, Shown with Oil Flowing Into the HFA

Flow losses in the rest of the hydraulic system are neglected, as the hose diameters, unlike d_i, can be increased with relatively little negative impact.

To calculate the total pressure drop across the axle ports, the axial and radial sections of the flow region shown in Fig. 33 are treated separately. With the assumption that the fluid behaves as a fully-developed flow, classical duct flow theory is used to calculate pressure drop, ΔP, in a circular duct as

$$\Delta P = \frac{1}{2}\rho_o \bar{u}^2 \left(\frac{\bar{f} l}{d} + k\right) \tag{97}$$

where $\bar{u}$ is the mean velocity of the fluid, $\bar{f}$ is the average friction factor, l and d are the length and diameter of the duct, respectively, and k is the sum of the minor loss coefficients. The average friction factor is calculated as [55]

$$\bar{f} = \begin{cases} \dfrac{4}{Re}\left[\dfrac{3.44}{\sqrt{L^+}} + \dfrac{\frac{1.25}{4L^+} + \frac{64}{4} - \frac{3.44}{\sqrt{L^+}}}{1 + \frac{0.00021}{(L^+)^2}}\right], & Re < 2800 \\ \left\{-2.0\log_{10}\left[\dfrac{2e}{7.54D} - \dfrac{5.02}{Re}\log_{10}\left(\dfrac{2e}{7.54D} + \dfrac{13}{Re}\right)\right]\right\}^{-2}, & Re \geq 2800 \end{cases} \tag{98}$$

where

$$Re = \frac{\rho_o u D}{\mu_o} \tag{99}$$

$$L^+ = \frac{l}{DRe} \tag{100}$$

and e is the surface roughness of the pipe (about 1.6 micron for a machining operation [56]). The laminar correlation in Eqn. 98 takes into account the hydrodynamic development length. It is not necessary to take this length into account for turbulent flow, as it is negligibly short [55].

Selected values for the minor loss coefficients are listed in Table 8 [57].

Table 8: Selected Values for the Minor Loss Coefficients in the Axial Ports

$k_{entrance}$	0.4
k_{exit}	1.0
k_{tee}	0.3

The pressure drop in each section of the axle is then calculated as

$$\Delta P_{axial} = 8\rho_o \left(\frac{\dot{V}_o}{\pi d_i^2}\right)^2 \left(\frac{\bar{f}_{axial} l_a}{d_i} + k_{axial}\right) \tag{101}$$

$$\Delta P_{radial} = 2\rho_o \left(\frac{\dot{V}_o}{\pi d_i^2}\right)^2 \left(\frac{\bar{f}_{radial} r_a}{d_i} + k_{radial}\right) \tag{102}$$

where $\dot{V}_o$, is the volume flow rate of oil into (+) or out of (-) the HFA. The axial port length, l_a, is approximated as

$$l_a = th_e + l_r + l_{as} + w_{br} + d_l + l_s \tag{103}$$

where th_e is the thickness of an end cap, l_r is the length of a retainer, l_{as} is the axle shoulder length, w_{br} is the width of a bearing, d_l is the diameter of the HSRU case leakage port and l_s is the circumferential seal length. The difference between the leading coefficients in Eqns. 101 and 102 is due to the fact that the volume flow rate in each radial section is half of the total volume flow rate. The minor loss coefficient sums, k_{axial} and k_{radial}, depend on whether the HFA is being charged or discharged. Table 9 summarizes how these sums are treated.

Table 9: Minor Loss Coefficients in Pneumatic Charging and Discharging

	Charging	Discharging
Axial minor losses	$k_{axial} = k_{entrance} + k_{tee}$	$k_{axial} = k_{tee} + k_{exit}$
Radial minor losses	$k_{radial} = k_{exit}$	$k_{radial} = k_{entrance}$

Notice that the tee loss coefficient is always applied to the axial section. This is conservative, as the flow rate here is twice that in the radial section, and the length of the

axial section is also generally larger. As such, the tee loss coefficient always multiplies the larger component of pressure drop.

Having calculated the pressure drop in each section, the total power dissipation due to pressure drop in the axle ports is

$$\dot{W}_a = \dot{V}_o(\Delta P_{axial} + \Delta P_{radial}) \tag{104}$$

The HSRU also incurs leakage and viscous losses in the annular flow area that constitutes the non-contacting circumferential seal. This flow area is shown in Fig. 34, where the HSRU case is represented by the outer cylinder, and the axle is represented by the inner cylinder. The seal clearance dimension, c_s, has been greatly exaggerated.

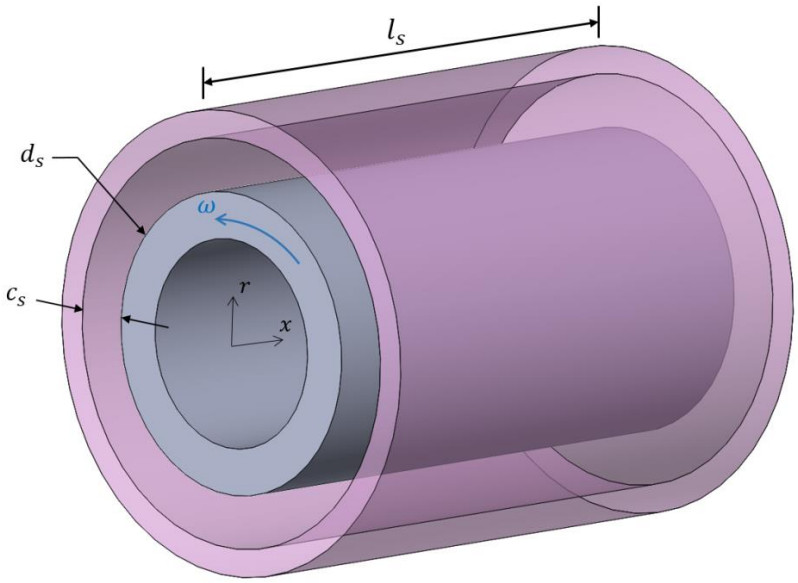

Figure 34: Actual Flow Geometry for Non-contacting Circumferential Seal, Shown with Exaggerated Clearance

Because the flow is axisymmetric and $c_s \ll d_s$, the circumferential seal can be approximated as planar flow between semi-infinite plates, where the cylindrical coordinates x-r-θ transform to x-y-z. Here, "semi-infinite" means that there are no end effects along the width (tangential direction). This approximate geometry is shown in Fig. 35.

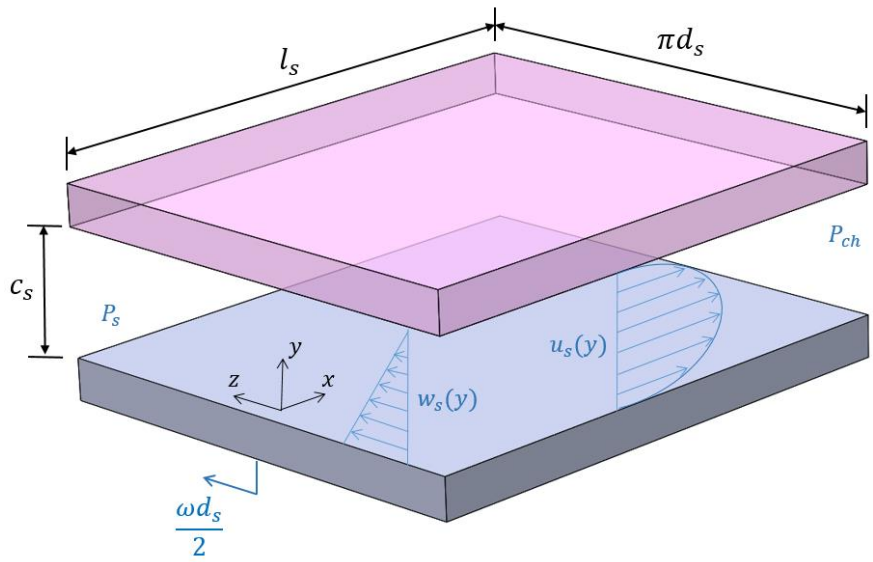

Figure 35: Semi-Infinite Planar Approximation of Non-contacting Circumferential Seal Flow Geometry

To characterize leakage and viscous losses, it is necessary to derive the velocity profiles $\boldsymbol{u_s} = (u_s, v_s, w_s)$ that correspond to the three principle directions $\boldsymbol{x} = (x, y, z)$. The continuity and Navier-Stokes equations are used, with the assumptions listed in Table 10.

Table 10: Assumptions for the Reduction of the Navier-Stokes Equations for Flow in the Circumferential Seal

Assumption	Result
Steady-state	$\partial/\partial t = 0$
Semi-infinite (axisymmetric)	$\partial/\partial z = 0$
Fully-developed in the axial direction	$\partial \boldsymbol{u_s}/\partial x = 0$
Incompressible	$\rho = constant$

The assumption of fully-developed flow in the axial direction is justified by the fact that, for practical seal designs, $c_s \ll l_s$. For brevity, the subscript o on oil properties has been dropped for the following analysis.

The continuity equation,

$$\frac{\partial \rho}{\partial t} + \left(\frac{\partial \rho u_s}{\partial x} + \frac{\partial \rho v_s}{\partial y} + \frac{\partial \rho w_s}{\partial z} \right) \tag{105}$$

using the assumptions in Table 10, reduces to

$$\rho \frac{\partial v_s}{\partial y} = 0 \tag{106}$$

This indicates that v is a constant, and since the walls are impermeable,

$$v_s = 0 \tag{107}$$

must be true everywhere. The x-, y- and z-momentum equations reduce to

$$\frac{\partial P}{\partial x} = \mu \frac{\partial^2 u_s}{\partial y^2} \tag{108}$$

$$\frac{\partial P}{\partial y} = 0 \tag{109}$$

$$\frac{\partial^2 w_s}{\partial y^2} = 0 \tag{110}$$

The equations above suggest that the u_s and w_s velocity profiles are each a function of y only, such that the volumetric viscous dissipation expression reduces to

$$\dot{q} = \mu \left[\left(\frac{du_s}{dy} \right)^2 + \left(\frac{dw_s}{dy} \right)^2 \right] \tag{111}$$

The left side of Eqn. 108 can be replaced by $-\mathrm{P_s}/l_s$, the total pressure drop across the seal divided by the seal length. The result can then be integrated, with the no-slip condition at the walls providing the boundary conditions $u_s(y = 0) = 0$ and $u_s(y = c_s) = 0$. This yields the following axial velocity profile.

$$u_s(y) = -\frac{P_s}{\mu l_s} y^2 + \frac{P_s c_s}{\mu l_s} y \tag{112}$$

Equation 112 is simply an expression for fully-developed Poiselle flow between parallel plates. The leakage flow rate, $\dot{V}_l$, associated with this velocity profile is

$$\dot{V}_l = \frac{P_s \pi d_s c_s^3}{12 \mu_o l_s} \tag{113}$$

and the power loss, $\dot{W}_l$, resulting from this leakage is

$$\dot{W}_l = P_s \dot{V}_l = \frac{P_s^2 \pi d_s c_s^3}{12 \mu_o l_s} \tag{114}$$

The no-slip condition also dictates $w_s(y = 0) = \omega d_s/2$ and $w_s(y = c_s) = 0$, where the quantity $\omega d_s/2$ is the peripheral velocity of the axle at the seal. Using these as boundary conditions, Eqn. 110 can be integrated to yield the following tangential velocity profile.

$$w(y) = -\frac{\omega d_s}{2c_s} y + \frac{\omega d_s}{2} \tag{115}$$

Equation 115 is an expression for Couette flow between parallel plates. The viscous dissipation rate, $\dot{W}_{vh}$, associated with this flow is

$$\dot{W}_{vh} = \mu_o \left(\frac{\partial w_s}{\partial y}\right)^2 = \frac{\mu_o \pi d_s^3 l_s \omega^2}{4c_s} \tag{116}$$

Comparison of Eqns. 114 and 116 illustrates the energy loss tradeoffs associated with the design variables c_s and l_s. Larger seal clearances reduce viscous dissipation due to the shear flow by decreasing the velocity gradient, but allow for more leakage power loss by decreasing restriction to leakage flow. Conversely, longer seal lengths mitigate leakage but result in higher viscous dissipation rate, as the shear flow losses are integrated over a larger area.

It is also interesting to note the coupling between the two loss mechanisms in the seal and the axle port losses discussed earlier in this section. While d_i does not appear explicitly in the expressions for the seal losses, it is clear that, since the wall thickness $\frac{1}{2}(d_s - d_i)$ was minimized in Section 3.2, d_i scales with d_s. By examination of Eqns. 101, 102, and 104, using larger axle diameters mitigates axle port losses. Equations 114 and 116 show that the opposite is true for both of the seal loss mechanisms. This energy loss tradeoff justifies using d_i as a design variable.

4.4 Vacuum Pumping Energy Consumption

Operating the HFA in a vacuum leads to two forms of energy consumption. First, some amount of energy is required to establish the desired vacuum each time the HFA is

assembled. This process is referred to as "pumpdown." Second, the imperfect sealing of the containment chamber requires some amount of sustained energy input to maintain vacuum at or near the desired level. Sealing imperfections are a combination of various phenomena including gas permeation, material outgassing, and real leaks, which are collectively referred to as "gas loads" [58]. Gas loads, denoted as Q_{gas}, are specified in units of pressure-volume per time, and therefore represent a power dissipation.

The vacuum in the containment chamber is established and maintained by a vacuum pump, whose capacity is generally referred to as its "pumping speed," S_p, and is given in units of volume per time. For a particular vacuum pump, S_p is not constant, but rather is a function of the instantaneous gas conductance of the surrounding plumbing [59]. For relatively high vacuum systems, a "backing pump" is often used in series with the primary vacuum pump [60]. Because the detailed modeling of the vacuum system is outside the scope of this research, the HFA is modeled as using a single vacuum pump with perfect mechanical efficiency and a constant pumping speed, S_p.

Assuming adiabatic compression, the power consumed by the vacuum pump is [61],

$$\dot{W}_{vac} = \frac{\gamma}{\gamma - 1} S_p P_{ch} \left[\left(\frac{P_{amb}}{P_{ch}} \right)^{\frac{\gamma - 1}{\gamma}} - 1 \right] \tag{117}$$

where the ratio of specific heats of air is $\gamma = 1.4$. The rate of change of the containment chamber pressure, P_{ch}, is [62]

$$\frac{dP_{ch}}{dt} = \frac{Q_{gas} - P_{ch} S_p}{V_{ch}} \tag{118}$$

The parameter V_{ch} refers to the volume of gas in the containment chamber. Figure 36 shows a rough schematic of the containment chamber packaging.

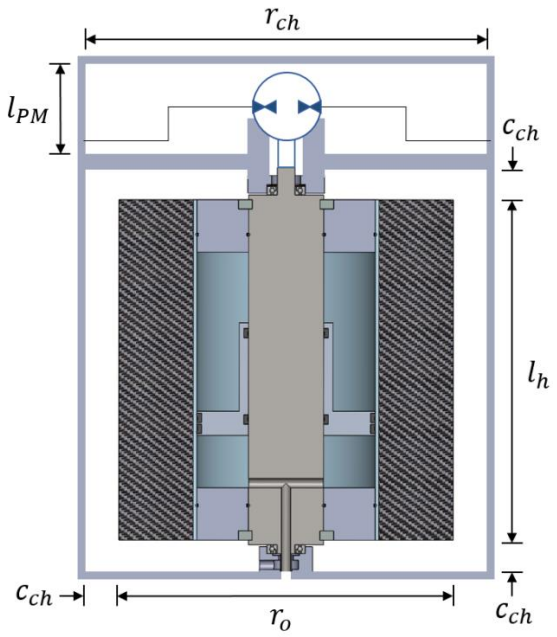

Figure 36: Schematic of the Containment Chamber Packaging

The overall internal length of the containment chamber is the sum of the HFA housing length, l_h, the approximate length required for packaging the storage PM, l_{PM}, and twice the chamber clearance, c_{ch}. The internal radius of the containment chamber, r_{ch}, is equal to the HFA housing outer radius, r_o, plus the chamber clearance. Though the size of the storage PM varies between different HFA design solutions, the parameter l_{PM} is estimated to be a constant 25 cm for the purposes of optimization.

While the details of burst protection are outside the scope of the present research, choosing a small value for c_{ch} tends to reduce the chamber wall thickness required to adequately absorb all of the energy released in the event of a catastrophic failure. A small chamber clearance also reduces the amount of time and energy required for pumpdown after assembly of the HFA. In an effort to take advantage of these benefits while also providing a safe distance between the rotating and stationary components, a clearance of 1 cm is selected for the laboratory prototype.

Given the dimensions in Fig. 36, the gas volume in the containment chamber is approximated as

$$\forall_{ch} = \pi r_{ch}^2 (l_h + l_{PM} + 2c_{ch}) - \pi r_o^2 l_h \tag{119}$$

Note that the quantity given by Eqn. 119 is the "dry" volume of the containment chamber; $\forall_{ch}$ shrinks throughout the course of HFA operation, as oil leaks from the HSRU into the containment chamber.

For the purposes of modeling the vacuum system energy consumption, material outgassing is neglected, since it is a complex and time-dependent phenomenon [63], and its effects are minimal if vacuum can be maintained between periods of HFA operation [25]. It is assumed that the containment chamber is manufactured without any real leaks, such that the only gas load is the result of permeation through the materials that constitute the chamber. A gas species permeates through a material at a rate of [64]

$$Q_{perm} = \frac{k_p A_q}{l_q} \Delta P \tag{120}$$

where k_p is the permeation constant (a characteristic of the particular combination of gas species and material), A_q is the area exposed to permeation, ΔP is the partial pressure differential, and l_q is the distance across the material. Barring any specific details, the containment chamber will likely be constructed mainly of steel, with polymeric O-rings sealing a removable cover. Because the permeability of steel is quite low [64], the majority of the gas permeation will occur through the O-rings.

For the present purposes, it is assumed that two removable covers are sealed with O-rings, each with a radius that is roughly equal to the radius of the containment chamber, r_{ch}. The permeation distance, l_q, for an O-ring is roughly half of the O-ring thickness, t_o, but since the area exposed to permeation is

$$A_q = 2\pi r_{ch} t_o \tag{121}$$

the O-ring thickness cancels out of Eqn. 120 and therefore need not be specified here.

For simplicity, the ambient air is modeled as being composed of 80% Nitrogen and 20% Oxygen, such that the total gas load is

$$Q_{gas} = 4\pi r_{ch} P_{atm} \left[(0.8) k_{d,N} + (0.2) k_{d,O} \right] \tag{122}$$

Sondregger [64] gives the Nitrogen and Oxygen permeation constants associated with the common O-ring material VITON® as $k_{d,N} = 6(10^{-13})$ and $k_{d,O} = 1(10^{-12})\ m^2/s$.

Equation 118 shows that, if the vacuum pump runs continuously, the chamber pressure will approach some steady value as the quantity $Q_{gas} - P_{ch}S_p$ goes to zero. The vacuum pump must be sized such that this steady state value is equal to or below the desired chamber pressure. Given the simplicity of the present model, the selection of S_p does not affect the net vacuum system energy consumption for pumpdown and HFA simulation. Therefore, the vacuum pump capacity can be sized arbitrarily, as long as it satisfies

$$S_p \geq \frac{Q_{gas}}{P_{ch}} \tag{123}$$

During a performance simulation of the HFA, the vacuum pump is toggled on and off using simple deadband control. Given a sufficiently-long simulation, the choice of deadband size does not have an effect on the net vacuum system energy consumption. However, to minimize the effect of chamber pressure fluctuation on aerodynamic losses, the deadband is chosen to be 0.5% of the desired chamber pressure.

In general, a flywheel system presents the opportunity to select the optimal chamber pressure which minimizes the sum of vacuum pumping and aerodynamic losses. Because the modeling presented above predicts very low values of vacuum power consumption, such an optimization would drive chamber pressure to values below the saturation vapor pressure of hydraulic oil. To prevent vaporization of the oil that leaks into the containment chamber, therefore, the desired chamber pressure, $P_{ch,d}$, is set equal to the saturation vapor pressure of hydraulic oil (roughly 13 Pa), and no such optimization need be performed.

5 Internal Fluid Modeling

This chapter addresses the viscous energy dissipation that results from oil shearing within the HFA in response to some arbitrary transient power profile. Because of its complexity, this energy loss mechanism is treated separately from those discussed in Chapter 4. Also addressed in the present chapter are time-varying fluid velocity and pressure distributions that result from an arbitrary power profile. These have implications on performance metrics (e.g. energy conversion efficiency, system pressure fluctuation) and necessary design features (e.g. wall thickness, rated bearing speed). For the purposes of design optimization, it is necessary to accurately predict the dynamic response of the HFA to any possible transient power profile.

The remainder of this chapter describes the method by which the rotating fluid behavior is modeled. First, a more thorough motivation for fluid modeling is provided. The second section reviews some theory on rotating flows, then puts forth and defends a key assumption for the fluid model. In the next section, the general approach to fluid modeling is presented and a dimensional analysis is carried out. The following section describes the experimental methods and results used to develop the fluid model. Next, the theory and the experimental results are mated, and an evaluation of the model is carried out. The chapter concludes with remarks on the strengths and shortcomings of the model and recommendations for future work.

5.1 Motivation for Fluid Modeling

Though the HFA contains two fluid volumes – a gas and an oil – the present investigation treats only a single homogenous fluid volume. In this way, the results are applicable to the general study of rotating axisymmetric flows. In a drive cycle simulation, the results of this chapter will be applied to the oil volume only. Therefore, the term “fluid” will henceforth be interchangeable with “oil,” and the term “container” will refer to the solid components that enclose the oil (i.e. the piston, oil side end cap, and housing).

Use of the pneumatic domain entails changing the volume of oil in the HFA. While this certainly results in interesting transient phenomena by altering the inertia of the HFA, it is not the topic of this chapter, and therefore constant oil volume is implied in all of the discussion in this chapter. The focus here is instead on the transient fluid behavior that results from using the kinetic domain, where the HFA experiences angular acceleration or deceleration by the application of positive or negative torque.

The simplest way to simulate HFA performance would be to assume the fluid volume responds to a torque as if it were a solid. In this case, the fluid would always be rotating as a rigid body at the speed of the container. In modeling inertial behavior, Newton's second law could be applied simply using the sum of the fluid and solid inertias, and no viscous dissipation would occur. Pressure at the fluid inlet could be inferred at any time by simply measuring the velocity of the container (which, by virtue of the present assumption, would also indicate the velocity of the fluid volume). For a detailed design optimization, this simplistic approach is insufficient. The nuances of the rotating fluid must be considered in the performance modeling, and therefore a more thorough understanding of transient fluid behavior is sought.

Leaving exact details for later discussion, it is intuitive that, as a torque is applied to the container, the fluid volume will not necessarily behave as a solid. Should the container maintain a constant angular velocity for a sufficiently long period of time, however, the fluid volume should eventually reach rigid body rotation. This condition – where the fluid is rotating as a rigid body at the same angular velocity as the container – is referred to as "steady state." Understanding the nature by which the fluid volume departs from steady state during angular velocity transients is important for two reasons:

- Fluid behavior impacts the applicability of Eqns. 22 (total stored energy in the HFA) and 25 (system pressure as a function of pneumatic pressure and angular velocity) to regions of transient operation
- Viscous dissipation of energy occurs as a result of induced velocity gradients whenever the fluid is not rotating as a rigid body

To model transient HFA behavior for any power profile of reasonable duration and temporal resolution, full CFD would result in far too much computational cost. This is especially true in the context of a heuristic design optimization, where the thousands of potential HFA designs must be evaluated via simulation. The ideal model for fluid behavior, therefore, must be accurate enough to realistically predict HFA behavior and computationally cheap enough that simulation and optimization can be carried out in a reasonable amount of time.

5.2 Theory and Assumptions

A rich body of research, which could be collectively called "Ekman spin-up theory," provides valuable insight into the expected transient behavior of the fluid volume. Most of the research is a variation on the following theme: An axisymmetric fluid volume is initially rotating at steady state when its container is impulsively accelerated to a new angular velocity that is $\Delta\Omega$ greater than the initial angular velocity. Generally, the process of fluid spin-down is the reverse of spin-up, so the following brief review of Ekman spin-up theory can be applied to a container which is impulsively accelerated or decelerated. Figure 37 shows a container of finite wall thickness with important dimensions and name conventions labeled.

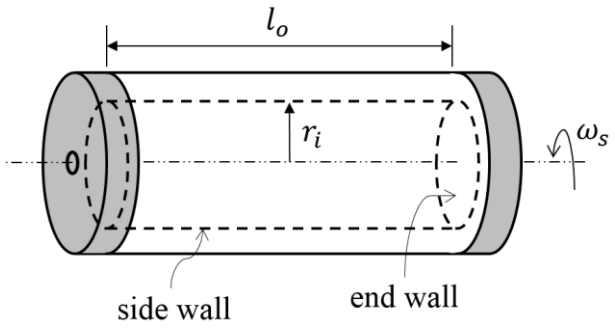

Figure 37: Container and fluid volume with dimensions

Note that the axle is omitted from the present study on fluid behavior. Review of the Ekman spin-up literature suggests that the fluid behavior is fundamentally the same, regardless of whether the axle is present. The parameter ω_s refers to the container angular velocity, where the subscript "s" emphasizes that the container is composed of solid components.

In the limiting case of an infinitely long ($l_o = \infty$) cylindrical fluid volume, any departure from fluid rigid body rotation manifests itself as a one-dimensional flow relative to the container. In this special case, all fluid velocity remains azimuthal (although its magnitude varies with radial location), and transport of momentum within the fluid is accomplished purely through viscous diffusion. However, for any reasonable set of geometric dimensions, the HFA aspect ratio (l_o/r_i) is far too low for infinite length to be a suitable approximation [65].

Instead, it turns out that the relative flow during transience is quite three-dimensional (though still axisymmetric), with the end walls playing an extremely important role [66]. Due to the no-slip condition, an impulsive increase in the container angular velocity results in a thin layer of fluid at each wall that rotates faster than the core flow. These thin layers of fluid are subject, then, to a centrifugal field that overcomes the prevailing pressure gradient (the pressure gradient imposed by the rotation of the core flow). Consequently, fluid at the end walls is accelerated radially outward in what has become known as an Ekman boundary layer. To satisfy continuity, the radial outflow is accompanied by an axial inflow to the Ekman layer along the longitudinal axis of the cylinder. Fluid leaving the Ekman layer at the outer radius is turned and travels axially within the sidewall boundary layer. Near the meridian, the flow is turned again, such that it travels radially inward to replace the axial inflow to the Ekman layer.

The radial inflow at the meridian can be envisioned as fluid rings which approximately conserve angular momentum; as they travel inward, their angular velocity increases, effectively spinning up the fluid. It is clear, then, that the dominant mechanism for fluid spin-up is advective, not viscous. As a result, spin-up is accomplished much faster than it would be is viscosity were the dominant mechanism. Specifically, spin-up is complete in a time on the order of [66]

$$t_E = \frac{l_o}{\sqrt{\nu_o \Omega}} \tag{124}$$

where ν_o is the kinematic viscosity of the fluid and Ω is a characteristic angular velocity. Generally, Ω is chosen as larger of the initial and final angular velocities that define the impulsive spin-up event. Note that the use of upper-case omegas in this chapter is reserved for constants which describe a spin-up event, while lower-case omegas refer to an instantaneous and time-varying angular velocities.

To contextualize the Ekman time constant, t_E, consider a cylindrical container of roughly 1 m length and aspect ratio $l_o/r_i = O(1)$. The container is filled with hydraulic oil (kinematic viscosity of 46 cSt) initially at steady state and is impulsively accelerated from its original speed to 523.6 rad/s (5000 RPM). Equation 124 predicts (and experiments have confirmed [66]) that spin-up is 95% complete in a time $O(10\ s)$. If the end wall Ekman effects were not present and momentum exchange was accomplished purely via viscous diffusion, spin-up would be accomplished in a time scale l_o^2/ν_o. This turns out to be $O(1000\ s)$ – two orders of magnitude higher than the advective spin-up time.

Though conceptually useful, the theory developed in Ekman spin-up literature is insufficient to actually model transient HFA behavior. Scenarios studied in the literature analyze discrete spin-up events with well-defined initial and final conditions of steady state rotation at specified angular velocities. The present situation is quite different, in that an arbitrary power profile (as opposed to an angular velocity step change) is the simulation input, and steady state rotation is not necessarily ever reached. To the author's knowledge, none of the literature treats the energy, which must include viscous dissipation, required to accomplish a spin-up event, and none attempts to the model fluid behavior that results from an arbitrary power profile.

Despite the infeasibility of direct application to a simulation, the Ekman spin-up theory will be used to justify a key modeling assumption – and several extensions thereof – for the development of the HFA fluid model. At all times, the fluid volume will be presumed to act approximately as a rigid body spinning at angular velocity ω_f. The difference between the fluid angular velocity and its container is

$$\Delta\omega = \omega_s - \omega_f \tag{125}$$

At steady state, $\Delta\omega = 0$, but during transience, $\Delta\omega \neq 0$. The proceeding arguments provide justification for the fluid rigid body assumption, which may at first seem contradictory to the preceding description of the three-dimensional flow phenomena and to the arguments in Section 5.1.

Benton [67] provides the following rough approximations for the absolute radial, azimuthal, and axial components of velocity in the core of the fluid. The equations are valid for the case of an impulsive change in angular velocity of the container, from an initial state of rigid-body rotation.

$$u_r \cong \frac{1}{2} r\Delta\Omega \sqrt{\frac{\nu_o}{l_o^2\Omega}} \tag{126}$$

$$u_\theta \cong r(\Omega - \Delta\Omega) + r\Delta\Omega\left[1 - \exp\left(-\frac{\sqrt{\nu_o\Omega}t}{l_o}\right)\right] \tag{127}$$

$$u_z \cong \frac{\Delta\Omega}{\Omega}\sqrt{\nu_o\Omega} \tag{128}$$

In these equations, r and t are radial location and time, respectively. It is clear from Eqns. 126 through 128 that, for any appreciable angular velocity and fluid viscosity, the azimuthal component of fluid velocity is much greater than the radial and axial components, which arise only due to Ekman circulation. The absolute kinetic energy in the fluid consequently manifests itself primarily in the azimuthal flow component. Therefore, although they are essential to the advective nature of fluid spin-up, the radial and axial components of fluid velocity will be henceforth neglected in quantifying the instantaneous amount of kinetic energy stored in the fluid.

Equation 127 offers two important points. First, azimuthal velocity is linearly dependent on radial location and is independent of axial and tangential location, which is the definition of rigid body rotation. Therefore, Benton's azimuthal velocity equation serves as the primary justification for the "fluid rigid body assumption," the approximation that the fluid volume spins roughly as a rigid body at an angular velocity ω_f, even during transient events.

The same equation also leads to the first extension of the fluid rigid body assumption: The fluid angular velocity exhibits a first-order time response to a change, impulsive or otherwise, in container angular velocity. In the case of Benton's equation, the change in container angular velocity is impulsive. To make it applicable to a simulation, several modifications to Eqn. 127 must be introduced. Specifically, the linear velocity distribution is converted to a fluid angular velocity, the constant $\Delta\Omega$ is replaced by the variable $\Delta\omega$ (defined by Eqn. 125), and the Ekman time constant (defined by Eqn. 124) is replaced by a dynamic time constant, τ_d.

$$\omega_f^{n+1} = \omega_f^n + \Delta\omega^n[1 - \exp(-\Delta t/\tau_d^n)] \tag{129}$$

The qualifier "dynamic" for τ_d is used to reflect the fact that, if Eqn. 129 is applied to each time step in a simulation, it is not expected that the Ekman time constant should provide an appropriate estimate of fluid response (indeed, the constant Ω does not exist for an arbitrary angular velocity profile). Instead, the degree to which the fluid "catches up" to its container during a time step is expected to depend on various parameters that describe the state of the HFA.

Wiedman [68] discusses the scenario where the container spins up at a constant finite (non-impulsive) rate of acceleration. While he does not provide a time constant, he suggests that the response of the fluid depends on the parameters in Eqn. 124, as well as the rate of acceleration of the container, α_s. Because the duty cycle to be used in the present research is arbitrary, the theory presented by neither Benton nor Weidman is directly applicable.

The second important extension of the fluid rigid body assumption is that the pressure at the center is indicative of the kinetic energy contained in the fluid volume. For any flow, the kinetic energy contained in the fluid is equal to the volume integral of the specific kinetic energy. For a constant-density fluid in rigid body rotation, with negligible radial and axial velocity components, this becomes

$$E_{k,f} = \int_V \frac{1}{2}\rho_o u_\theta^2 \, dV = \rho\pi l_o \int_{r=0}^{r_i} r^2\omega_f^2 \, r dr \tag{130}$$

Evaluation of the integral in Eqn. 130, unsurprisingly, yields an expression for kinetic energy that is identical to that for a solid body.

$$E_{k,f} = \frac{1}{4}\rho_o \pi l_o r_i^4 \omega_f^2 = \frac{1}{2} I_f \omega_f^2 \tag{131}$$

Since constant rigid body fluid rotation is assumed, Eqn. 25 (system pressure as a function of pneumatic pressure and angular velocity) with $\omega = \omega_f$ should hold, even during transients. Rearranging, this equation yields Eqn. 132, which can be inserted into Eqn. 131 to produce Eqn. 133, an expression for kinetic energy as a function of inlet pressure.

$$\omega_f = \left[\frac{4}{\rho_o r_i^2}\left(P_p - P_s\right)\right]^{1/2} \tag{132}$$

$$E_{k,f} = \pi l_o r_i^2 \left(P_p - P_s\right) \tag{133}$$

Thus, fluid angular velocity and the amount of kinetic energy stored in the fluid volume can be inferred from the pressure, P_s, at the inlet of the HFA.

The final extension of the fluid rigid body assumption relates to regions of viscous dissipation. It can be assumed that viscous effects are essentially confined to the boundary layers [67, 69]. Besides lending credibility to the rigid fluid body model by implying that velocity gradients in the core are quite small, this notion helps in identifying parameters that are important to viscous dissipation rate. The picture of spin-up developed so far illustrates a viscous flow scenario similar to cylindrical Couette flow where the fluid and solid volumes are, respectively, the inner and outer cylinders, and the boundary layers mate the azimuthal velocities of each. Whereas in canonical Couette flow there is only a cylindrical viscous flow, in the present situation there is also a boundary layer at each end wall (the Ekman layers). Both the Ekman and side wall boundary layers scale as

$$\delta \sim \sqrt{\frac{\nu_o}{\Omega}} \tag{134}$$

and are roughly constant throughout the spin-up process [67].

5.3 Modeling Approach

To take into account viscous losses and fluid inertial behavior, simulation of HFA response to a power profile is more complicated than simply applying Newton's second law. Instead, the kinetic energy equation below is used, where $\dot{W}_t$ is tractive power (allocated completely to the kinetic domain for the purposes of the present chapter), the known input to the simulation.

$$\dot{W}_t = \frac{d}{dt}E_{k,s} + \frac{d}{dt}E_{k,f} + \dot{W}_v \tag{135}$$

Notice that tractive power (positive when charging the HFA) is distributed between three terms: One which changes the kinetic energy of the solid components, $E_{k,s}$; one which changes the kinetic energy of the fluid components, $E_{k,f}$; and one which represents viscous dissipation rate, $\dot{W}_v$. The latter, which is always positive, acts to decrease the amount of kinetic energy gain during charging and increase the kinetic energy loss during discharging.

Evaluating the derivatives in Eqn. 135 and using the fluid rigid body assumption leads to a new form of the kinetic energy equation:

$$\dot{W}_t = I_s\alpha_s\omega_s + I_f\alpha_f\omega_f + \dot{W}_v \tag{136}$$

To highlight the expected nature of the fluid response, it is convenient to express α_f as the average acceleration over a time step for a first order response.

$$\alpha_f = \frac{\Delta\omega}{\Delta t}\left(1 - \exp\left(\frac{\Delta t}{\tau_d}\right)\right) \tag{137}$$

Equations 136 and 137 represent a system of two equations and four unknowns (α_s, α_f, $\dot{W}_v$, and τ_d). To render the simulation solvable, two empirical correlations must be developed, one for the dynamic time constant and one for the viscous dissipation rate. Algorithmically, the simulation is carried out by sequentially solving the following equations, which are written in finite difference form.

$$\alpha_f^{n+1} = \frac{\Delta\omega^n}{\Delta t}\left(1 - \exp\left(\frac{\Delta t}{\tau_d^n}\right)\right) \tag{138}$$

$$\omega_f^{n+1} = \omega_f^n + \alpha_f^{n+1}\Delta t \tag{139}$$

$$\alpha_s^{n+1} = \frac{1}{I_s\omega_s^n}\left(\dot{W}_t^{n+1} - I_f\omega_f^{n+1}\alpha_f^{n+1} - \dot{W}_v^n\right) \tag{140}$$

$$\omega_s^{n+1} = \omega_s^n + \alpha_s^{n+1}\Delta t \tag{141}$$

$$\dot{W}_v^{n+1} = f_1(\dots) \tag{142}$$

$$\tau_d^{n+1} = f_2(\dots) \tag{143}$$

Note that Eqn. 140 is simply the kinetic energy equation (Eqn. 136) rearranged to solve for the container angular velocity. Equations 142 and 143 are generic representations of the two desired empirical correlations, where the ellipses represent some combination of known parameters from time step n.

The first step in developing the actual predictive equations represented by Eqns. 142 and 143 is to perform dimensional analysis. It is reasonable to assume that viscous dissipation rate during a fluid transient will be affected by fluid properties, container geometry, the boundary layer thickness, and the difference between the fluid and container angular velocities. Given these assumptions, the dimensional analysis problem is posed as

$$\dot{W}_v^n = f_1(\rho_o, \mu_o, l_o, r_i, \Delta\omega, \omega_s) \tag{144}$$

This yields four dimensionless groups, each of which has been oriented (i.e. selection of the numerator versus the denominator) to reflect its expected impact on viscous dissipation rate.

$$\frac{\dot{W}_v}{\mu_o r_i^3 \Delta\omega^2} = \phi_1\left(\sqrt{\frac{\rho_o\omega_s l_o^2}{\mu_o}}, \frac{l_o}{r_i}, \frac{\Delta\omega}{\omega_s}\right) = \phi_1(l_o/\delta, AR, \epsilon_d) \tag{145}$$

Scaling parameters in the dependent dimensionless group are chosen such that viscous dissipation rate goes to zero as $\Delta\omega$ goes to zero, a condition that is physically expected.

Returning to the expression for boundary layer thickness (Eqn. 134), the first independent group in Eqn. 145 can be considered the inverse of a dimensionless boundary layer thickness (It could also be considered the square root of a Reynold's number). The

second independent term is a container aspect ratio, defined to be consistent with the notion that spin-up in longer cylinders tends to be dominated by viscous, not advective, effects. The final independent dimensionless group is deemed the dynamic Rossby number (a transient counterpart to the Rossy number, $\Delta\Omega/\Omega$, used in spin-up literature to describe an impulsive acceleration event [66]) Again, this group is oriented such that its value goes to zero when there is no relative velocity between the fluid and its container.

In consideration of the discussion of spin-up literature, it is expected that angular velocity and acceleration of the container, as well as fluid viscosity and container length, are important parameters in predicting the dynamic time constant. The dimensional analysis problem is therefore posed as

$$\tau_d = f_2(\nu_o, l_o, \omega_s, \alpha_s) \tag{146}$$

This yields the following dimensionless relationship.

$$\frac{1}{\tau_d \omega_s} = \phi_2\left(\frac{l_o^4 \alpha_s}{\nu_o^2}, \frac{\alpha_s}{\omega_s^2}\right) \tag{147}$$

To avoid a divide-by-zero error for $\alpha_s \to 0$, container acceleration must be placed in the numerator of the independent groups. Then, the dynamic time constant is placed in the denominator of the dependent group to reflect the experimental observation that τ_d decreases as α_s increases.

Equations 145 and 147 indicate the dimensionless groups that are expected to be important in predicting the viscous dissipation rate and dynamic time constant, respectively. Now, experiments can be used to obtain actual mathematical expressions that describe the relationships between these groups.

5.4 Experimental Approach

The experimental apparatus must apply a transient power trace to a rotating fluid volume. During an experiment, it is necessary to measure several physical quantities is order to calculate the various parameters in Eqns. 145 and 147. Then, a curve-fitting algorithm

can be used to derive an actual mathematical relationship between the dimensionless groups. Figure 38 illustrates the experimental setup.

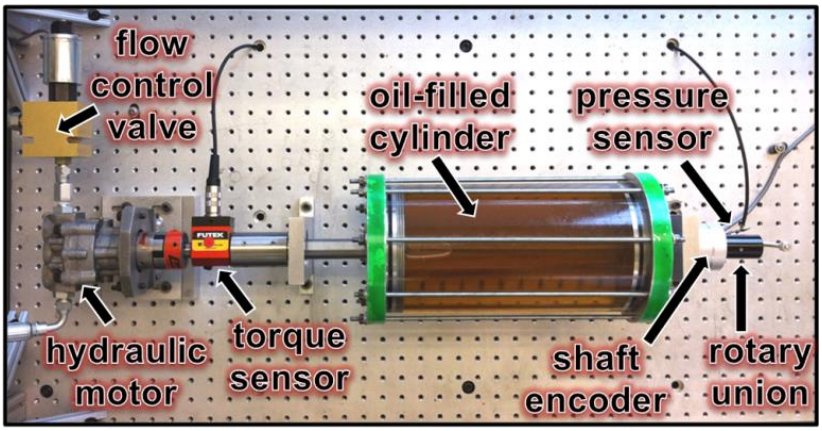

Figure 38: Experimental Setup with Instrumentation

A rotating cylinder filled with oil is driven by a hydraulic motor. Flow rate through the motor is metered using a proportioning flow control valve in a feedback control loop. In this way, the angular velocity of the rotating cylinder can be accurately-controlled. A rotary torque sensor and shaft encoder facilitate torque and speed measurements, and a rotary union allows for an internal pressure tap at the center of an end cap. Because the cylinder is not charged, the pneumatic pressure is effectively zero at all times. The system pressure equation (Eqn. 25) indicates that gage pressure at the center should then be negative for any nonzero rotational speed. Tables 11 and 12 provide relevant specifications for the experimental setup.

Table 11: General Specifications for the Experimental Setup

Oil length, l_o $[cm]$	30
Oil radius, r_i $[cm]$	5.7
Oil density, ρ_o $[kg/m^3]$	879
Oil kinematic viscosity, ν_o $[cSt]$	46
Maximum speed $[RPM]$	1100
Sampling frequency $[Hz]$	1000

Table 12: Specifications of the Equipment Used for the Experimental Setup

Hydraulic pump-motor	
Manufacturer	Parker
Model number	MGG20020
Displacement [cc/rev]	7.4
Rated pressure (continuous) [bar]	138.0
Rated pressure (intermittent) [bar]	172.5
Rated flow per 1000 RPM [lpm]	7.4
Proportional flow control valve	
Manufacturer	Eaton
Model number	EPFB-10
Rated pressure (continuous) [bar]	350
Rated flow [lpm]	30.3
Power supply	24 VDC, 1.1 amps
Valve cavity	#C1030
Torque sensor	
Manufacturer	Futek
Model number	TRS300
Item number	FSH01988
Torque capacity [Nm]	20
Maximum speed [RPM]	3000
Shaft encoder	
Manufacturer	US Digital
Model	ETACH2
Max. input frequency [Hz]	12.7 MHz (adjustable)
Vacuum gauge	
Manufacturer	Honeywell
Part number	40PC015V2A
Pressure range [psi]	0 to -15

Note that angular velocity is the prescribed physical quantity for any given experiment, and therefore the applied power is, in a sense, incidental. For the purposes of characterizing viscous dissipation rate and dynamic time constant, this is perfectly acceptable, as the actual shape of the power profile is non-critical; the important point is that the applied power can be extracted from the measured data.

To confirm repeatability of measurements, the prescribed angular velocity traces are non-arbitrary. Instead, they resemble near-impulsive acceleration events, and to maximize the signal to noise ratio of the torque sensor, the angular velocity traces are rather aggressive. As shown in the complete results in Appendix C, such events tend to utilize between 10% and 25% of the range of the torque sensor. Figure 39 shows an example angular velocity trace used for model development, along with its equivalent ideal (step change) trace. Though not fully shown in the plot, container angular velocity is held constant before and after the transient for a time deemed sufficient to guarantee steady state (at least six Ekman time constants, as defined by Eqn. 124).

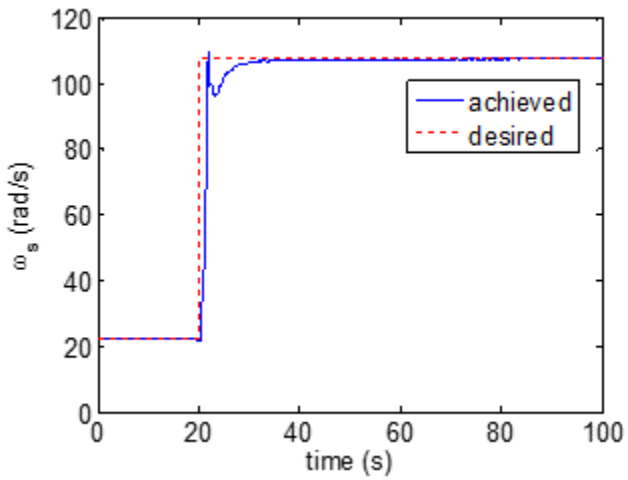

Figure 39: Example of an Attempted Step Change from 200 RPM to 1000 RPM, Desired and Achieved

The extraction of the applied power profile for an experiment and the subsequent calculations of other important parameters are carried out as follows. The torque on the experimental setup due to bearing friction and aerodynamic drag has been characterized as a function of angular velocity. For any experiment, this is subtracted from the

measured torque, T_m, the result of which is multiplied by angular velocity to calculate the applied power profile,

$$\dot{W}_t = (T_m - T_b - T_w)\omega_s = T\omega_s \tag{148}$$

The measured system pressure is used to calculate fluid angular velocity using Eqn. 132. Doing so relies on the reasonable assumption that the pressure gradient across the Ekman boundary layer is negligible [70].

Due to the high sampling frequency, even a small amount of noise in the fluid and solid angular velocity profiles makes it difficult to obtain coherent traces of their time derivatives. To cope with this issue, the angular velocity traces are filtered and then smoothed with cubic splines. The corresponding angular acceleration traces can then be obtained by using the analytical derivatives of the splines. Figure 40 illustrates the utility of this strategy with an example profile of fluid angular acceleration. The lighter curve has been produced by using a low-pass filter on angular velocity data and then numerically differentiating the result. The darker line has been produced by spline-fitting the filtered angular velocity data and analytically differentiating the result. The cutoff frequency of the filter is 30 Hz and the spline has been constructed using a rate of 5.8 knots per second of data. To illustrate the accuracy of the fluid angular acceleration curve produced by the spline strategy, the plot also includes a dotted curve showing the solid angular acceleration, which should be qualitatively similar.

The importance of the spline strategy is made clear upon examination of Fig. 40, where the curve produced from the filtered but un-splined data is noisy to the point of uselessness. In the course of post-processing, the number of knots used in the spline is manually-adjusted for each dataset, such that a smooth fit to the filtered angular velocity data is produced without the spline actually following the noise of the signal. For all of the present datasets, this can be accomplished using a rate of 20 knots per second or less.

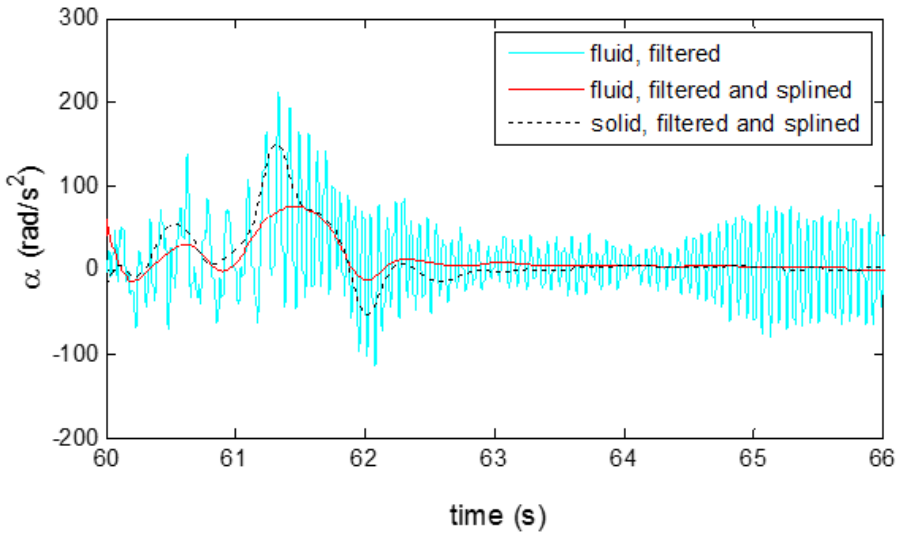

Figure 40: Example of Spline-fitting Strategy to Produce Smooth Acceleration

Having calculated the angular acceleration traces, distribution of the applied power can be inferred. The power to the solid components (the container) can be calculated as the rate of change of its kinetic energy,

$$\dot{W}_s = I_s \alpha_s \omega_s \tag{149}$$

and the power to the fluid components is calculated as the difference between the applied power (Eqn. 148) and the power going to the solid components (Eqn. 149):

$$\dot{W}_f = \dot{W}_t - \dot{W}_s \tag{150}$$

The power to the fluid components can be further split into that which contributes to changing the kinetic energy of the fluid volume and that which is dissipated by viscosity. Thus, viscous dissipation rate is

$$\dot{W}_v = \dot{W}_f - I_f \alpha_f \omega_f \tag{151}$$

Finally, the dynamic time constant is calculated as

$$\tau_d = -\frac{\Delta t}{\ln\left(1 - \frac{\alpha_f \Delta t}{\Delta \omega}\right)} \tag{152}$$

Hence all quantities in Eqns. 145 and 147 have been either measured directly or calculated based on measurements, such that values for the actual dimensionless groups

can be calculated. It is now possible to begin tying together the theoretical and experimental approaches.

5.5 Model Development

For all experimental datasets, the signal-to-noise ratio of the torque sensor is most favorable during the transient section, when a significant portion of the sensor capacity is utilized. For this reason, only the data in the transient section is used in generating correlations for the fluid model.

Because the experimental setup has a fixed geometry, the second dimensionless group in the viscous dissipation correlation is constant for all experiments. Therefore, the correlation space is three-dimensional for both the viscous dissipation rate and the dynamic time constant. In choosing the form of an equation for the correlations, however, three-dimensional scatter plots offer fairly little insight. Lacking any justification based on fluid mechanics, polynomial fits are chosen in anticipation of them being the most versatile. Equation 153 illustrates the form of a correlation, where π_1 is the dependent dimensionless group, the Π_j's are the independent dimensionless groups, k_o is a constant, and k_{jn} is the coefficient for term which raises the j^{th} independent group to the n^{th} power.

$$\Pi_1 = k_o + \sum_{2}^{j} \sum_{1}^{n} k_{jn} \Pi_j^n \tag{153}$$

For both correlations, $j = 2$. The viscous dissipation data is found to fit quite well to a third-order polynomial and the dynamic time constant data to a second-order polynomial. The optimal coefficients for each correlation (7 coefficients for the viscous dissipation rate and 5 for the time constant) are found by using a genetic algorithm that minimizes the sum of squared errors.

Eleven experiments have been run with the desired angular velocity trace shown in Fig. 39 (200 RPM to 1000 RPM, near-impulsive), and the complete data for each are provided

in Appendix C. Each experiment yields a dataset from which both a viscous dissipation and a dynamic time constant correlation can be developed. The two correlations from each dataset can and should be assessed completely independently from one another. That is, the time constant correlation from experiment #1 is no more "related" to the viscous dissipation correlation from experiment #1 than it is to the viscous dissipation correlation from experiment #2. Therefore, the experiments yield twenty-two independent correlations, eleven candidates for the best viscous dissipation correlation and eleven candidates for the best dynamic time constant correlation.

The validity of each of the correlations is assessed by applying it to each of the power profiles from the other ten experimental datasets. In other words, a correlation developed by curve-fitting data from experiment #1 can be tested by running a simulation where the power profile from experiment #2 is the input, and then comparing the resultant simulated data (viscous dissipation rate, fluid and solid angular velocity, etc.) to the measured data from experiment #2. In this way, twenty-two different correlations (eleven each for the two desired parameters) are evaluated via 220 simulations.

Over the course of a simulation, the accuracy of the dynamic time constant correlation affects the indicated accuracy of the viscous dissipation correlation, and vice versa. For example, should the dynamic time constant correlation tend to under-predict the correct (measured) value, the viscous dissipation rate will consequently be under-predicted. This is intuitive, as a lower-than-realistic $\Delta\omega$ should result in lower-than-realistic viscous dissipation. For this reason, while the viscous dissipation correlations are being evaluated and compared, the dynamic time constant is intentionally forced to its measured value. Then, once the best viscous dissipation correlation has been identified, it is permanently embedded in the simulation code, such that its effects are included during the evaluation and comparison of the candidate dynamic time constant correlations.

Quantitatively, the performance of a correlation is judged by how well it predicts container and fluid angular velocities. To constitute such a judgment, the coefficient of determination, defined as

$$R^2 = \frac{R_s^2 + R_f^2}{2} \tag{154}$$

is used, where

$$R_i^2 = 1 - \frac{\sum\left(\omega_{i,measured} - \omega_{i,predicted}\right)^2}{\sum \omega_{i,measured}^2} \tag{155}$$

To provide more qualitative insight into how a given correlation performs, two different coefficients of determination can be calculated:

- R_{95}^2, which includes the highly transient region between the initial acceleration and the time at which the measured fluid angular velocity has reached 95% of its steady state value, and
- R_{99}^2, which includes the region between the initial acceleration and the time at which the measured fluid angular velocity has reached 99% of its steady state value. This generally includes a much larger amount of near-steady state behavior

Any given correlation might perform quite differently in the highly transient section compared to the near-steady state section; examination of the two different coefficients of determination defined above provides insight into this difference.

Table 13 shows the values of R_{95}^2, R_{99}^2, and $R_{overall}^2 = (R_{95}^2 + R_{99}^2)/2$, for each of the eleven candidate viscous dissipation correlations. All of these R^2 values encompass data from all ten simulations for a given correlation, such that they represent its average performance. The correlations are ranked by $R_{overall}^2$.

Table 13: Ranked Performance of the Viscous Dissipation Rate Correlations, Based on Coefficient of Determination

Corr. #	Rank	$R^2_{overall}$	R^2_{95}	R^2_{99}
7	1	**0.99845**	0.998825	0.998067
9	2	**0.99843**	0.999039	0.997830
3	3	**0.99816**	0.998836	0.997490
4	4	**0.99805**	0.998773	0.997335
1	5	**0.99795**	0.999171	0.996733
6	6	**0.99794**	0.998850	0.997036
8	7	**0.99781**	0.998125	0.997489
2	8	**0.99685**	0.998603	0.995093
11	9	**0.99675**	0.998599	0.994908
5	10	**0.99646**	0.998460	0.994452
10	11	**0.99624**	0.998629	0.993850
Average		**0.99755**	0.998719	0.996389
Standard Dev.		**0.00081**	0.000284	0.001511

On average, a viscous dissipation correlation predicts the container and fluid angular velocities with at $R^2_{overall} = 0.998$. Quantitatively, there is relatively little difference in how well the correlations behave through 95% of steady state. Including data through 99% causes in increase in total squared error for all correlations and reveals more variation amongst them, increasing standard deviation by an order of magnitude. In other words, there is a wider range of performance amongst the correlations for steady state, but each performs worse at steady state than it does during transience.

Because it produces the highest value of $R^2_{overall}$, viscous dissipation correlation #7 is selected for use in the fluid model. As indicated in Table 13, this correlation performs better than all but two in transience, and better than any other when data through 99% of steady state is included. The full expression for the selected viscous dissipation correlation is:

$$\frac{\dot{W}_v}{\mu_o r^3 \Delta\omega^2} = 4.16(10^3) + 6.69\sqrt{\frac{\rho_o \omega_s l_o^2}{\mu_o}} \ldots$$

$$-1.77(10^{-2})\left[\sqrt{\frac{\rho_o \omega_s l_o^2}{\mu_o}}\right]^2 + 1.95(10^{-5})\left[\sqrt{\frac{\rho_o \omega_s l_o^2}{\mu_o}}\right]^3 \ldots \quad (156)$$

$$-2.18(10^4)\frac{\Delta\omega}{\omega_s} + 1.38(10^5)\left[\frac{\Delta\omega}{\omega_s}\right]^3$$

Notice that the first independent group contributes a full cubic polynomial to the correlation, while only a linear and a cubic term are contributed by the second independent group (the quadratic coefficient was forced to zero by the curve-fitting algorithm). Figure 41 illustrates the relative contribution of each independent group for the transient portion of an example simulation. For ease of plotting, the constant k_o has been grouped with the terms contributed by the second independent group.

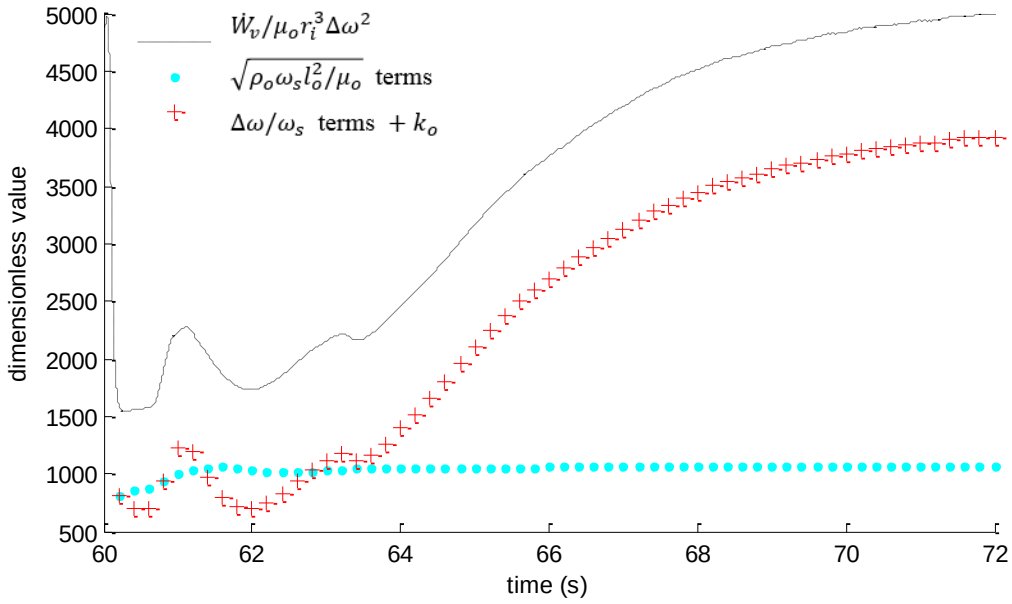

Figure 41: Example Dataset Showing the Relative Contributions of Independent Groups in the Viscous Dissipation Correlation

Figure 41 expresses what is difficult to discern from simply examining Eqn. 156. Most of the transient behavior of the dependent group, $\dot{W}_v/\mu_o r_i^3 \Delta\omega^2$, is contributed by the

second independent group, $\Delta\omega/\omega_s$, while the first independent group, $\sqrt{\rho_o \omega_s l_o^2/\mu_o}$, acts somewhat like a constant offset. This observation suggests that the fluid angular velocity relative to its container is more important than the estimated boundary layer thickness in predicting viscous dissipation rate.

Having identified the best viscous dissipation rate correlation, it can now be embedded into the simulation in order to assess the performance of the eleven candidate dynamic time constant correlations. During evaluation, three are deemed invalid due to observed instability during one or more simulations. The remaining time constant correlations are ranked in Table 14 by their overall combined performance with the selected viscous dissipation correlation.

Table 14: Ranked Performance of the Dynamic Time Constant Correlations, Based on Coefficient of Determination

Corr. #	Rank	$R^2_{overall}$	R^2_{95}	R^2_{99}
8	1	**0.99549**	0.99726	0.99371
6	2	**0.99513**	0.99749	0.99276
7	3	**0.99444**	0.99614	0.99274
11	4	**0.99371**	0.99697	0.99045
5	5	**0.99286**	0.99692	0.98879
9	6	**0.99247**	0.99670	0.98823
1	7	**0.99151**	0.99585	0.98718
10	8	**0.64704**	0.64414	0.64995
Average		**0.95033**	0.95268	0.94798
Standard Dev.		**0.12257**	0.12467	0.12044

As expected, the average $R^2_{overall}$ for the simulations presented in Table 14 is lower than those in Table 13, where, instead of using a correlation, dynamic time constant was forced to the correct value. Still, the quality of simulations is quite high, especially in the transient 95% region.

Again using the criterion of highest $R^2_{overall}$, the dynamic time constant correlation #8 is chosen for use in the fluid model. Its full expression is:

$$\frac{1}{\tau_d \omega_s} = 3.90(10^{-3}) - 3.76(10^{-19})\left[\frac{l_o^4 \alpha_s}{\nu_o^2}\right]^2 + 2.54\frac{\alpha_s}{\omega_s^2} + 4.07\left[\frac{\alpha_s}{\omega_s^2}\right]^2 \qquad (157)$$

While the dependent quantity $1/\tau_d \omega_s$ exhibits both linear and quadratic dependence on the second independent group, the linear term from the first independent group was eliminated by the curve-fitting algorithm. The exact value of the small constant offset turns out not to matter, as it contributes a negligible amount to the value of $1/\tau_d \omega_s$. The offset exists only as a numerical barrier to calculating an infinite dynamic time constant when acceleration rate goes to zero. Figure 42 shows an excerpt from a simulation that illustrates the relative importance of the two independent groups in the dynamic time constant correlation.

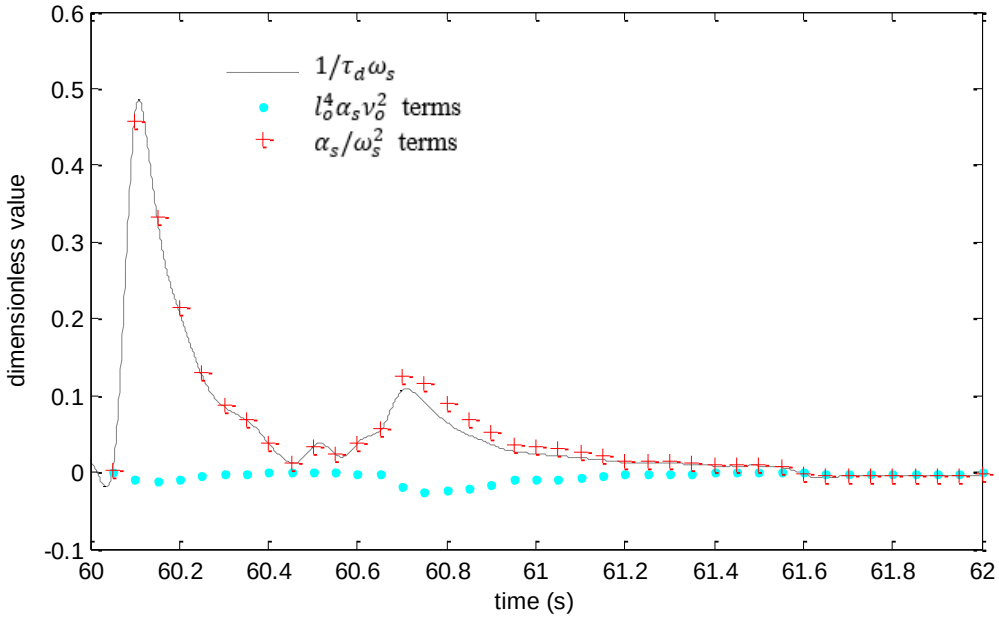

Figure 42: Example Dataset Showing the Relative Contributions of Terms in the Dynamic Time Constant Correlation

As was the case for the viscous dissipation correlation, the relative contribution from the two independent variables is rather lopsided. The dependent variable response is dictated

mostly by the behavior of the term α_s/ω_s^2 and corrected only slightly by the $l_o^4\alpha_s/\nu_o$ term.

It is worth noting that, as steady state is approached, error in the predicted dynamic time constant becomes simultaneously greater in value and less important in effect. The former is true because the time constant is inversely proportional to the container acceleration and therefore more sensitive to error as acceleration goes to zero. The latter is true because, as steady state is approached, $\Delta\omega$ shrinks, and therefore any error in the predicted time constant is multiplied by a smaller value in the calculation of the fluid velocity for the subsequent time step.

5.6 Model Validation

The predictive model, whose development has been detailed in the preceding sections, can be executed with only a few lines of code. To prove this, various simulations were run using MATLAB® on a modest processor. Even without any attempt to maximize computational efficiency, three minutes of physical time with one millisecond temporal resolution can be simulated in approximately one second of computational time. In this regard, the requirement that the model be computationally inexpensive has been overwhelmingly achieved.

In addition the requirement of computational simplicity, the fluid model must realistically predict HFA behavior. Before assessing the model performance in this regard, a certain unanticipated nuance in the measured fluid behavior must be described. In experiments with significant overshoot and rapid recovery of container angular velocity to the command step signal, a negative measured time constant can be observed for a small period of time. An example is illustrated in Fig. 43, where the fluid angular velocity can be seen to follow a qualitatively similar profile as the container angular velocity, peaking and beginning to decrease, even though $\Delta\omega$ never ceases to be positive.

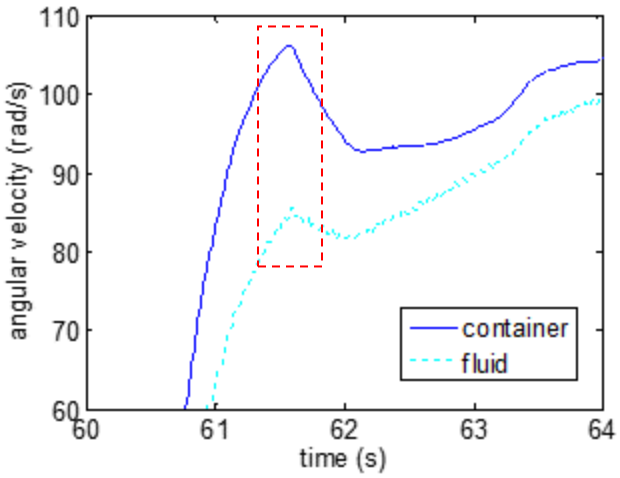

Figure 43: Example of a Region with an Observed Negative Dynamic Time Constant

To the author's knowledge, there is no physical explanation for the region of observed negative time constant shown in Fig. 43; the fluid angular velocity should increase as long as it remains below the container angular velocity. It is therefore postulated that, during strong acceleration, flow phenomena in the Ekman boundary layer generate a pressure gradient that causes the pressure sensor to read somewhat lower (more vacuum) than the true value in the fluid core. This is translated via Eqn. 132 to a somewhat over-predicted fluid angular velocity. A sudden deceleration of the container is accompanied by a reversal in the aforementioned flow phenomena, the net result of which is to generate a fluid angular velocity trace which exhibits some non-physical behavior.

It must be noted that characterizing a dynamic time constant is extremely useful, regardless of how well the measured pressure actually indicates fluid angular velocity. Regardless of whether it is valid to assume that no pressure gradient exists across the Ekman layer, the pressure measured in the present experiments is, in fact, the pressure that the hydraulic system would experience in an actual HFA application. The ability to predict the transient system pressure behavior is essential in developing an effective control strategy. The detrimental effect of the non-physical behavior shown in Fig. 43, then, is to overestimate (in positive acceleration) the rate of change of fluid kinetic energy, thereby introducing some error into the energy equation (Eqn. 136). For the

purposes of assessing model performance, the remainder of the discussion relies on the assumption that the calculated fluid angular velocity is reasonably accurate.

As a general illustration of the performance of the model, Figures 44, 45 and 46 show angular velocities, dynamic time constant, and viscous dissipation rate, respectively, for the transient portion of an example simulation. The plots show simulated quantities and their corresponding measured quantities. This example comes from a dataset that, importantly, is not the same one that generated either of the correlations chosen for the fluid model. For this example, $R_{95}^2 = 0.9998$.

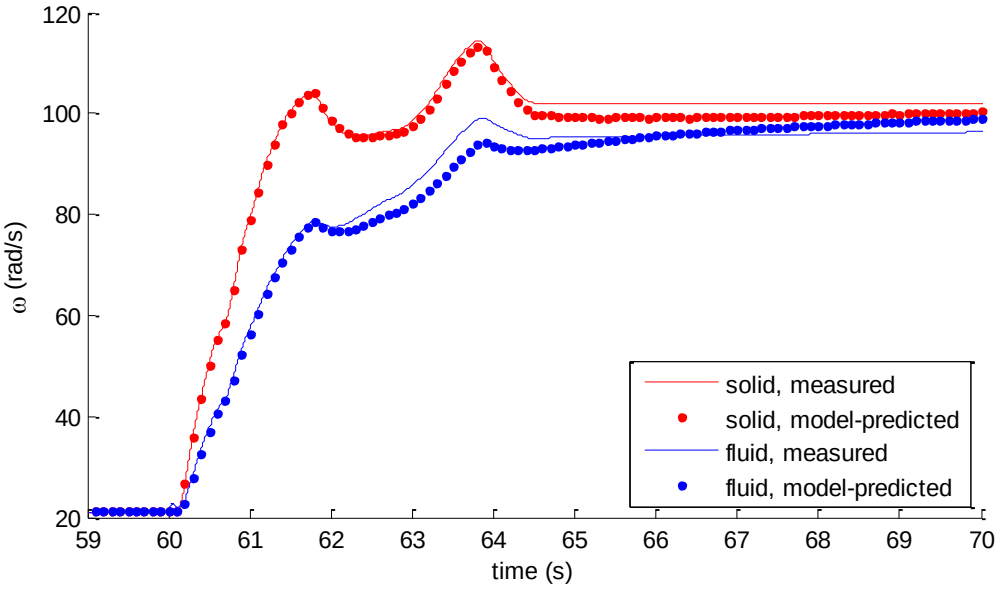

Figure 44: Fluid and Container Angular Velocities, Measured Versus Simulated, Near-Impulsive Acceleration from 200-1000 RPM

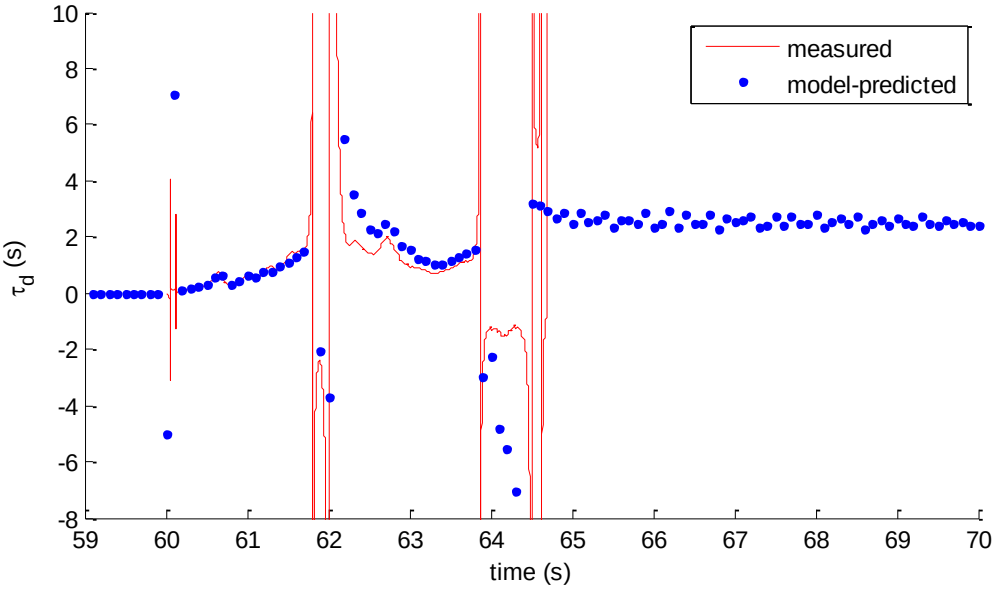

Figure 45: Dynamic Time Constant, Measured Versus Simulated, Near-Impulsive Acceleration from 200-1000 RPM

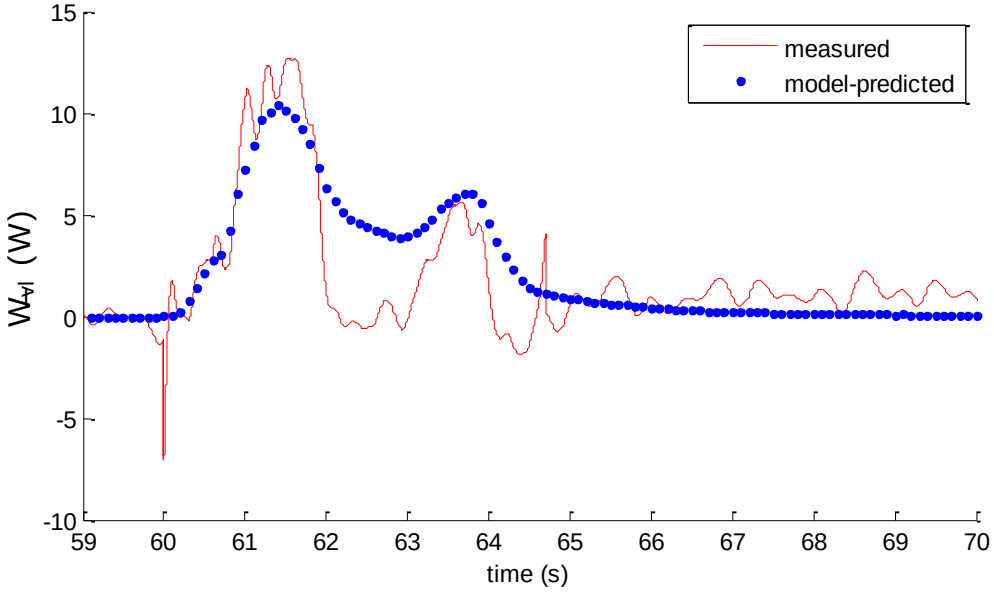

Figure 46: Viscous Dissipation Rate, Measured Versus Simulated, Near-Impulsive Acceleration from 200-1000 RPM

Figure 44 shows that, qualitatively, the fluid model predicts container and fluid angular velocities quite well for the transient section of an aggressive acceleration event. For the first two seconds after the onset of acceleration, time constant and viscous dissipation rate

are very well-predicted, leading to near perfect agreement between measured and simulated angular velocities. The first spike in container angular velocity is initially handled well, but near 62 seconds, Fig. 45 shows that the time constant begins to be over-predicted. This has the effect of predicting a $\Delta\omega$ that is slightly too large, which in turns leads to an over-prediction of viscous dissipation, which can be seen in Fig. 46. When steady state is nearly reached, the time constant begins to be under-predicted, such that simulated fluid and solid angular velocities converge somewhat too early.

Though there is noticeable error in the predicted viscous dissipation rate, its integral is very near that of the measured viscous dissipation rate. Therefore, the net dissipated energy is predicted quite accurately, and the simulated angular velocities converge to the correct value. Negative values of measured dissipation rate are non-physical and are attributed to noise in the data. Figure 46 shows that the formulation of Eqn. 157 properly avoids the prediction of any negative dissipation rate.

Recall that, to maximize the utilized range of the torque sensor, only experimental runs with the relatively aggressive case of near-impulsive 200-1000 RPM have been used in the development of the fluid model. The model performance is diminished to varying extents when applied to other transient cases. Figure 47 shows measured and predicted angular velocity traces for the smaller near-impulsive acceleration event of 200-600 RPM. For this transient section, $R_{95}^2 = 0.9979$, slightly lower than the 200-1000 RPM case. The same qualitative trends are observed for both cases. Time constant and viscous dissipation rate are initially predicted quite well. The spike in container angular velocity has a small detrimental effect on the latter, causing the simulated angular velocities to reach steady state too soon. A slight over-prediction in net dissipated energy causes the final simulated angular velocity to be a few radians per second lower than the measured value. In full, the model proves to be fairly robust for the 200-600 RPM near-impulsive case.

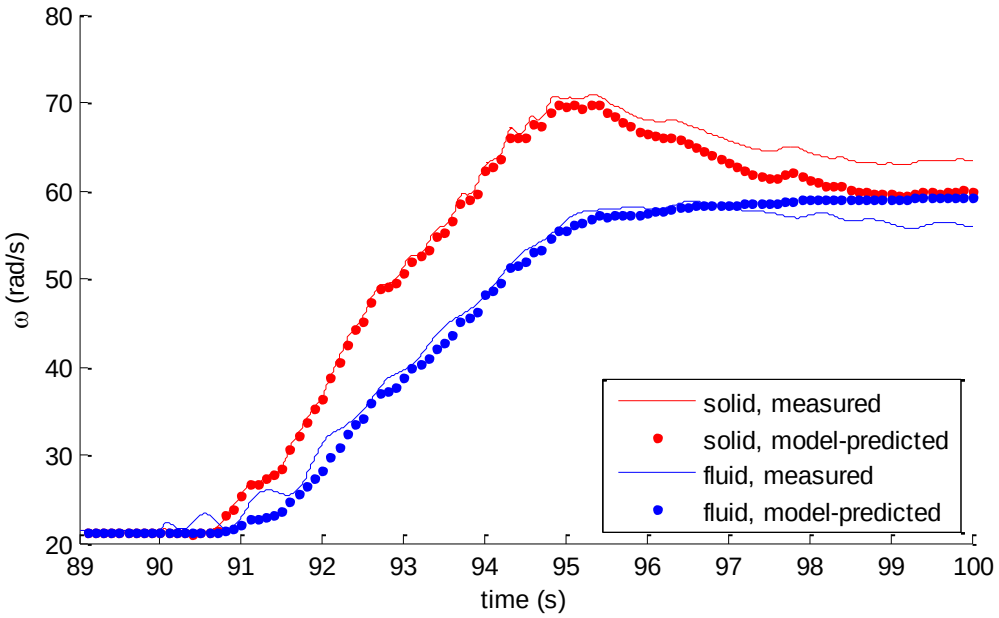

Figure 47: Fluid and Container Angular Velocities, Measured Versus Simulated, Near-Impulsive Acceleration from 200-600 RPM

The model performance suffers much more when the initial angular velocity is different than that which was used to produce the correlations. Figure 48 shows the case of near-impulsive acceleration from 600-1000 RPM. In this case, $R^2_{95} = 0.9874$, which is significantly lower than either of the previously presented cases. The model substantially over-predicts the dynamic time constant from the beginning of the transient. While predicted container angular velocity is initially quite accurate, the artificially large $\Delta\omega$ generates an erroneously high simulated rate of viscous diffusion. This drags the predicted steady state angular velocity down to a value significantly below the correct value.

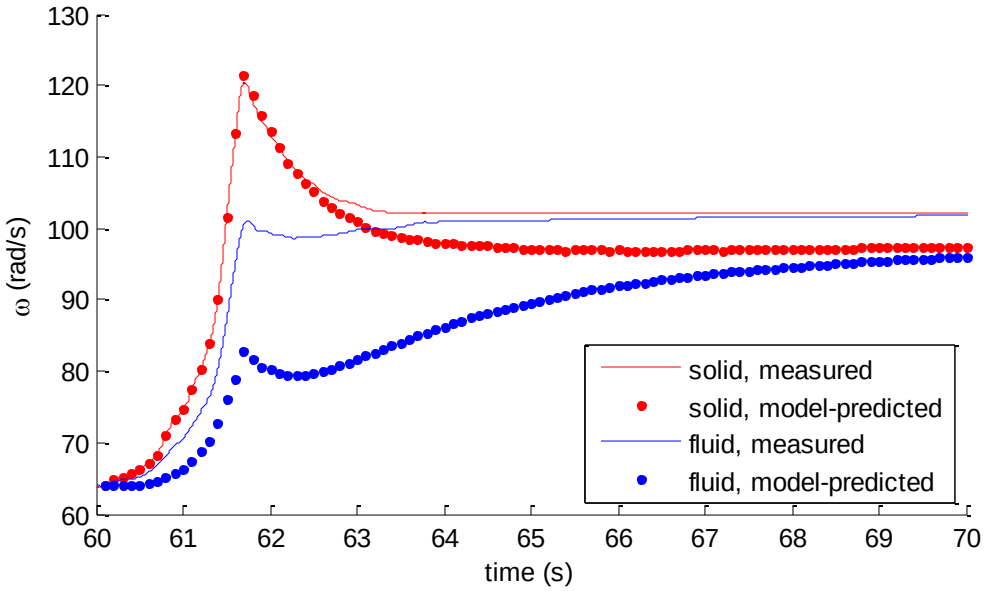

Figure 48: Fluid and Container Angular Velocities, Measured Versus Simulated, Near-Impulsive Acceleration from 600-1000 RPM

As a final example of the versatility of the fluid model, it is useful to examine the case of a non-impulsive acceleration. Figure 49 shows the predicted and measured angular velocities for the case of a mild acceleration from 100-800 RPM over the course of about 12.5 seconds. Compared to the near-impulsive 200-1000 RPM example illustrated in Figures 44 through 46, the average acceleration for this milder case is lower by a factor of three, and the maximum observed rate of acceleration is lower by a factor of ten.

Qualitatively, the model performance for this transient section falls somewhere between the two shorter, near-impulsive cases shown in Figures 47 and 48. Here, however, the viscous dissipation rate is the more error-prone correlation. The measured viscous dissipation rate is so close to zero that the model tends to over-predict it. The result of this it under-predict both angular velocities, even though the time constant is reasonably accurate.

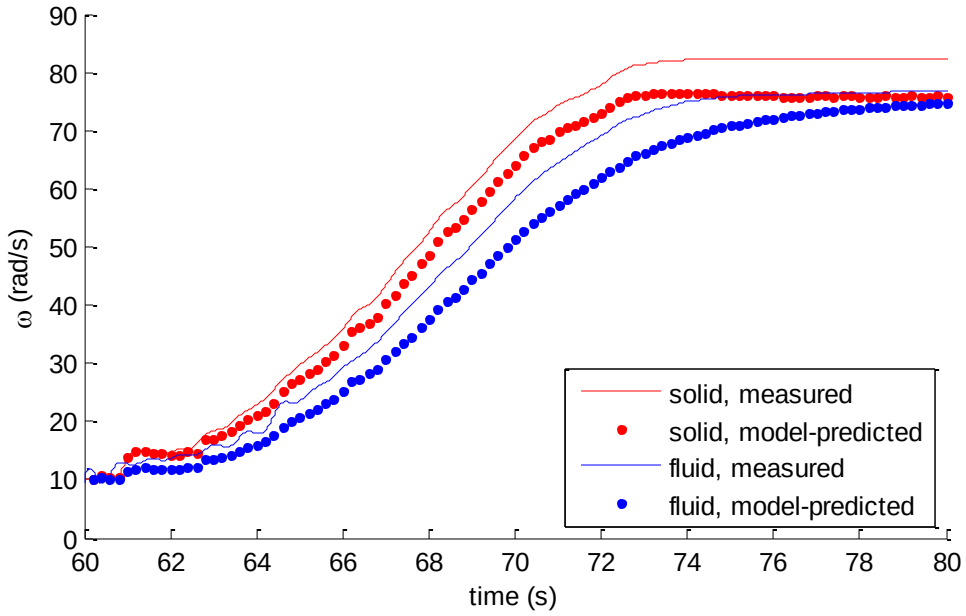

Figure 49: Fluid and Container Angular Velocities, Measured Versus Simulated, Gradual Acceleration from 100-800 RPM

5.7 Closing Remarks about the Internal Fluid Modeling

The model developed in this chapter relies on the assumption that, under applied power, the fluid volume accelerates roughly as a rigid body and lags behind its container in a manner that can be modeled as a first-order time response. The simplicity of the model allows it to simulate the transient HFA performance orders of magnitude more quickly than would be possible if CFD were used. This makes it quite applicable to a highly-resolved drive cycle simulation nested within a comprehensive design optimization.

By comparing simulations to measured data, the fluid model was shown to perform well for transient sections of intense acceleration and large $\Delta\Omega$. To varying degrees, the performance of the model was observed to decrease when applied to other types of transients. For intense accelerations in general, the model predicts viscous dissipation rate quite well. However, when the initial angular velocity is very far from that used to

develop the correlation (200 RPM), prediction of the dynamic time constant is notably hindered. Conversely, for cases where acceleration is milder, time constant is accurately predicted, while viscous dissipation rate tends to be over-predicted. To improve the robustness of the model, experimental data representing a wider variety of transients will be used in future work.

During experimental data collection, pressure was measured at $r = 0$ at the face of one of the container end caps. There is some uncertainty as to how well this pressure measurement indicates the true pressure in the fluid core. Future work will deal with this uncertainty by either modifying the experimental apparatus to measure pressure away from the end cap, or by attempting to characterize the pressure gradient across the boundary layer that might arise from Ekman flow phenomena.

Finally, it is important to note that the model developed and assessed in this chapter is specific to the experimental setup used to create it. Container aspect ratio, which was included as an independent group in the dimensional analysis, was not varied in the experiments, and was therefore not correlated. To make the model more reliable for use in a design optimization, all relevant dimensionless groups must be correlated. Future work will include the ability to vary the geometry of the container and/or the fluid properties used in the experiments. Lacking a variable-geometry experimental apparatus at the time writing, the fluid behavior model defined by Eqns. 156 and 157 is assumed to be sufficient for the design optimization presented in Chapter 7. The fact that internal viscous energy dissipation turns out to be very small compared to several other loss mechanisms helps to justify this assumption.

6 Drive Cycle Simulation

The ability to accurately simulate the performance of the HFA by using computer models is extremely valuable. To select an HFA design solution by optimizing a duty cycle-dependent performance metric (e.g. efficiency, peak power), it is essential to embed a performance simulation into the optimization algorithm. Duty cycle simulation can also facilitate tradeoff studies on alternative control strategies and powertrain architectures. This chapter details the development of tools that facilitate simulation of the HFA operation and assessment of its performance. First, the selections of a particular duty cycle and control strategy are justified. This is followed by a step-by-step description of the calculation sequence that constitutes a simulation. The chapter concludes by describing the calculations behind several important HFA performance metrics.

6.1 Road Loads and Vehicle Parameters

Section 2.1 defined the concept of specifying a particular HFA as a design solution (a set of design variables), and Chapter 3 detailed the static calculations that can be performed on such a design solution (e.g. selecting the remaining component dimensions, calculating HFA mass). In addition to these specifications and calculations, a duty cycle and a control strategy must be specified before carrying out a performance simulation. The simulation tools developed in the present research facilitate easy exchange of alternative duty cycles and control strategies. However, for various reasons, some choices that pertain to performance simulation have become conventional over the course of the research. These choices are detailed in this and the following sections.

A time-varying power profile, $\dot{W}_t(t)$, constitutes a duty cycle, which serves as the input to a performance simulation of an energy storage system. In the case of simulating the HFA performance, $\dot{W}_t(t)$ is the tractive power that was introduced in Section 2.5. While this power profile can be specified directly, it is more conventional in road vehicle performance modeling to calculate transient power from the combination of a time-

varying velocity profile and a set of specified vehicle parameters. There are many standard vehicle velocity profiles, referred to as "drive cycles," created and used by vehicle manufacturers and regulatory agencies. Because of it is well-known, is widely-used, and includes at least some high and low speed driving, the Urban Dynamometer Driving Schedule (UDDS) [71] is selected for the general simulation of the HFA. This drive cycle, which was developed by the Environmental Protection Agency, is shown in Fig. 50, and several characteristics of it are summarized in Table 15.

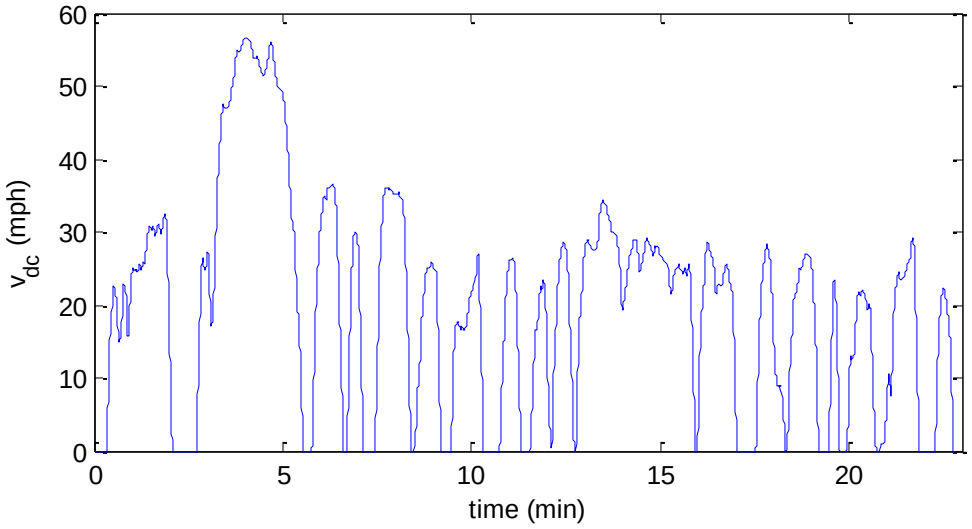

Figure 50: Urban Dynamometer Driving Schedule (UDDS)

Table 15: Characteristics of the Urban Dynamometer Driving Schedule (UDDS)

Total time	22.8 min.
Total distance	7.45 mi.
Maximum speed	56.7 mph
Average speed	19.6 mph
Temporal resolution	1 sec.

The time-varying velocity profile, $v_{dc}(t)$, of the UDDS must be converted to the power profile $\dot{W}_t(t)$ to which the HFA is subjected. In doing so, it is assumed that the vehicle has a purely hydraulic powertrain or a hydraulic-hybrid powertrain operating in charge-

depleting mode. In either case, the point of this assumption is to establish the HFA as the sole energy storage mechanism that is active during the drive cycle. Then, tractive power can be used as the input to the HFA simulation, such that power into the HFA is

$$\dot{W}_t(t) = -F_t v(t) \tag{158}$$

where the tractive force, F_t, is a time-varying function of the drive cycle velocity profile, $v(t)$, and several vehicle parameters. Here, the subscript "dc" is dropped to indicate that velocity has been converted from mph, as provided by the UDDS, to m/s. Tractive force is the sum of the force required to change the velocity of the vehicle and the force required to overcome road load, F_{rl}.

$$F_t = (m_v + m)\frac{dv}{dt} + F_{rl} \tag{159}$$

In Eqn. 159, m_v is the vehicle mass (excluding the HFA), m is the mass of the primary rotating HFA components. The traction and storage PM masses, $m_{PM,t}$ and $m_{PM,s}$ are excluded from tractive force calculations, as they have yet to be determined. These exclusions tend to have only a small effect on drive cycle power.

Notice from Eqns. 158 and 159 that the chosen sign convention dictates that producing acceleration and overcoming road load correspond to negative values of $\dot{W}_t(t)$, indicating that the HFA is being discharged. Methods presented by Gillespie [27] are used to model the components of road load. For simplicity, road grades and wind velocity are presumed to be zero, such that road load is the sum of aerodynamic drag, F_{aero}, and rolling resistance, F_{roll}. These are calculated as

$$F_{aero} = \frac{1}{2}\rho_{atm} v^2 C_D A_f \tag{160}$$

$$F_{roll} = f_r(m_v + m)g \tag{161}$$

where ρ_{atm} is the air density (at STP), C_D is the vehicle drag coefficient, A_f is the vehicle frontal area, and g is the acceleration of gravity. The rolling coefficient, f_r, is a function of a basic coefficient, f_o, and a speed coefficient, f_s, both of which depend on tire inflation pressure [72].

$$f_r = f_o + 2.43(10^{-4}) f_s v^{2.5} \tag{162}$$

The vehicle parameters used for general simulation purposes in the present research have been selected to reflect a typical mid-size passenger sedan. They are listed in Table 16.

Table 16: Vehicle Characteristics for Drive Cycle Simulation, Selected to Represent a Typical Mid-Size Passenger Sedan

Mass, m_v	1800 kg
Drag coefficient, C_D	0.3
Frontal area, A_f	2.3 m^2
Tire inflation pressure	35 psi
Basic rolling coefficient, f_o	0.0090
Speed rolling coefficient, f_s	0.0035

Combining Eqns. 158 through 161, the input to the HFA performance simulation is

$$\dot{W}_t(t) = -(m_v + m)\left(\frac{dv}{dt} + f_r g\right)v - \frac{1}{2}\rho_{atm} v^3 C_D A_f \tag{163}$$

Given the signs of the various terms in Eqn. 163, the HFA can recapture energy via regenerative braking only when the vehicle acceleration force, $(m_v + m)dv/dt$, is negative and sufficiently large to overcome the sum of aerodynamic and rolling forces, which is always positive.

6.2 Control Strategy and Pump-Motor Selection

As was discussed in Section 2.5, a control strategy should dynamically allocate $\dot{W}_t(t)$ between the kinetic and pneumatic domains in such a way that efficiency is maximized and pressure fluctuation is minimized. To characterize the degree to which a particular control strategy favors one energy domain over the other, it is convenient to define the usage ratio, R_u, as the ratio of kinetic energy conversion to the ratio of energy demand/supply met purely by the pneumatic domain during a drive cycle. Mathematically, this can be written as

$$R_u = \frac{\int_t \left|\dot{W}_k\right| dt}{W_{pp}} \tag{164}$$

where W_{pp} is the "purely pneumatic" energy conversion, calculated as

$$W_{pp} = \int_t \left|\dot{W}_t\right|_{\dot{W}_k=0} dt \tag{165}$$

The large inherent losses of hydraulic pump-motors render the kinetic domain less efficient than the pneumatic domain, and therefore lower values of R_u will tend to correspond to higher drive cycle efficiencies. Absolute values are used in the definition of R_u since energy losses are incurred in either direction of energy conversion – vehicle braking and acceleration.

In theory, by using a variable-displacement machine for the storage PM, it is possible maintain a perfectly constant system pressure throughout a drive cycle by intelligently selecting PM displacement, D. A control equation has been derived [65] to properly select the displacement command as a function of the current HFA state and tractive power at each time step. Employment of this control strategy, however, generally results in a very high usage ratio, and therefore low drive cycle efficiency. Variable-displacement machines, in particular, suffer from very high losses when operating at low displacements. Since constant-pressure control relies on operating the storage pump-motor across its entire range of displacements, the inefficiency of the kinetic domain is exacerbated by this strategy.

A simple, computationally inexpensive, and realistic alternative to constant pressure control, henceforth referred to as "band control," is used for general simulation and optimization purposes in the present research. The idea behind band control is that, because it can facilitate higher drive cycle efficiency, some system pressure fluctuation is tolerable. A control fraction, $f_{control}$, defines a "control band" of system pressure values, within which the kinetic domain is inactive. In other words, the control strategy defaults to using only the pneumatic domain when

$$\left(1 - \frac{f_{control}}{2}\right) P_d \leq P_s \leq \left(1 + \frac{f_{control}}{2}\right) P_d \tag{166}$$

is true, where P_d is the design system pressure (21 MPa for the present research) and P_s is the actual system pressure, which varies throughout the drive cycle. When system pressure strays outside of the control band, the kinetic domain is activated, provided that its use will tend to bring system pressure back to within the control band.

Limits on piston travel impose two special cases in which the default logic might need to be bypassed. First, if power is demanded from the HFA but the piston is all the way at the oil end (oil volume is at its minimum possible value), the pneumatic domain cannot be used because no more oil can be extracted. The second case is the inverse of the first – power is available for charging the HFA, but the piston is all the way at the gas end such that no more oil can be accepted into the HFA.

In a real vehicle application, rapid activation and deactivation of the storage PM could lead to excessive noise, vibration and harshness (NVH). To reflect this concern, an upper limit is imposed on the frequency, f_{switch}, at which the control strategy can switch the kinetic domain on and off. In other words, the storage PM can only be activated or deactivated if it has been in its current state for at least $1/f_{switch}$ seconds. Programmatically, the maximum switching frequency is enforced using the variable $t_{switch,last}$. Whenever the kinetic domain is switched on or off, the value of $t_{switch,last}$ is set to the current time. The psuedocode for the band control strategy is shown below.

```
//zero tractive power
if no power is supplied to or demanded from the HFA
      kinetic domain off


//special cases
else if power is demanded from the HFA but there is insufficient
pneumatic energy
      kinetic domain on
else if power is supplied to the HFA but no more oil can be
accepted
      kinetic domain on
else if the minimum switching period has not been met
      use previous state of kinetic domain
```

```
//standard logic
else if power is demanded from the HFA
      if system pressure is below the control band
            kinetic domain on
      else
            kinetic domain off
else if power is supplied to the HFA
      if system pressure is above the control band
            kinetic domain on
      else
            kinetic domain off
end if

if new kinetic state is different from last kinetic state
      record current time for enforcement of minimum switching
      period
end if
```

When the kinetic domain is active, the mechanical power, $\dot{W}_k$, is fixed by the HFA state as

$$\dot{W}_k = \frac{|\dot{W}_t|}{\dot{W}_t}\frac{P_s D \omega_s}{2\pi} \tag{167}$$

where the term $|\dot{W}_t|/\dot{W}_t$ ensures, from a mathematical standpoint, that mechanical power is positive in charging and negative in discharging. Physically, this change in sign is accomplished via a three-way valve that is capable of inverting the tank and pressure ports of the storage PM depending on whether positive or negative torque is appropriate. When the kinetic domain is inactive, the valve connects both PM ports to tank and the storage PM is declutched from the HFA, such that pump-motor frictional losses are eliminated. The details of the storage PM toggling system, along with the losses it incurs, are outside the scope of this research and therefore neglected in the HFA performance simulation.

In case the pneumatic domain is depleted at the instant of maximum power, the storage PM should sized to meet 100% of the peak power of the drive cycle, $\left|\dot{W}_t\right|_{max}$. However, to exactly satisfy this requirement, the HFA state at the moment of peak power would have to be known before the drive cycle simulation begins. As this is not possible, the storage PM is sized using the equation

$$D = \frac{2\pi\left|\dot{W}_t\right|_{max}}{P_d\,\omega_{max}} \tag{168}$$

Note that the use of ω_{max} here tends to undersize the PM, because PM speed will have always decreased by the time that peak power occurs (this is true, at least, the band control strategy is used and the duty cycle is the UDDS). In contrast, it is difficult to predict whether the use of P_d in Eqn. 168 will tend to oversize or undersize the PM. With the design and simulation tools developed as a part of the present research, it is possible to implement an iterative pump-sizing strategy, where a drive cycle simulation is carried out, and the observed HFA state at the time of peak power is used to resize the storage PM for the next simulation. For the purpose of a design optimization, which is sensitive to computation time, iterative pump-sizing is not employed.

Commercial data [53] has been correlated to approximate the mass of a variable-displacement axial piston pump-motor as a function of its displacement. The data suggests that PM mass, m_{PM}, follows a roughly linear relationship with displacement, D. The best fit line is described by

$$m_{PM} = 0.236\left[kg/\frac{cc}{rev}\right]D + 1.12[kg] \tag{169}$$

where the units of D are cc/rev. Equation 169 can be used to estimate the masses of both the traction PM and the storage PM.

6.3 Studies on the Band Control Strategy Parameters

Having justified the selection of the band control strategy, various parameters that define the control strategy must be chosen. In general, a wider control band increases the usage

ratio by favoring the pneumatic domain, and therefore results in higher drive cycle efficiency. Unsurprisingly, it also leads to higher fluctuations in system pressure. In assessing the degree to which the band control strategy effectively controls system pressure during a drive cycle, it is convenient to define the pressure fraction as

$$f_{pressure} = \frac{P_s|_{max} - P_s|_{min}}{P_d} \tag{170}$$

The range of observed system pressures (the numerator in Eqn. 170) is referred to as the "pressure band." It is important to understand that under certain operating conditions, activating the kinetic domain may only reduce the magnitude of dP_s/dt, rather than actually reversing the sign of dP_s/dt. Therefore, the pressure band will always (for the UDDS, at least) exceed the control band, due to the occasional inability of the control strategy and storage PM to rapidly correct system pressure when it strays outside of the control band. In light of this, if a particular HFA application is especially sensitive to the pressure band, $f_{pressure}$, the control band, $f_{control}$, should be carefully and conservatively selected.

It must be noted in the present discussion that most standard drive cycles are specified with a time resolution of 1 second. This affects the quality of the control strategy by naturally imposing a maximum switching frequency of $f_{switch} = 1\ Hz$. Additionally, a time resolution of 1 second causes significant numerical error in some of the physical calculations involved in the HFA simulation. Therefore, for the purposes of general simulation, the temporal resolution is artificially increased by linearly interpolating between the original drive cycle data. A code has been developed to perform this interpolation where the user specifies the desired time step. An example section of a drive cycle is shown in Fig. 51, where the time step has been decreased from 1 second to 0.2 seconds.

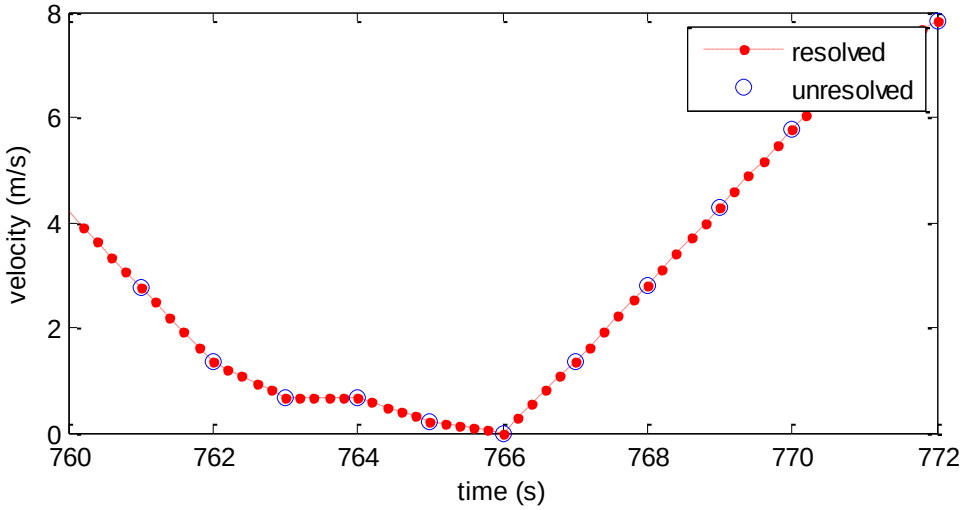

Figure 51: Example Section of a Drive Cycle Illustrating an Artificially-Increased Temporal Resolution

The selected values for the control band, maximum switching frequency, and simulation temporal resolution all affect the degree to which the band control strategy can maximize energy efficiency and regulate system pressure. A few studies are presented below to illustrate the impact of each of these parameters on the quality of the control strategy. In each study, several simulations are run using the same drive cycle and HFA design solution, but one control strategy parameter is varied. The HFA design solution and baseline control strategy parameters used for this study are listed in Tables 17 and 18. Note that this HFA design solution is not optimized, but rather has been arbitrarily specified.

In interpreting the results of the following studies, recall that a large pressure fraction is detrimental to the vehicle mass because it requires the traction PM to be significantly oversized and/or overly thick (heavy) HFA components.

Table 17: HFA Design Solution for the Control Strategy Study

Geometric	
Housing inner radius	10 cm
Housing outer radius	30 cm
Housing length	94 cm
Housing liner thickness	3 mm
Axle port diameter	2 cm
HSRU seal clearance	22 μm
HSRU seal length	3 cm
Operational	
Maximum angular velocity	1000 rad/s
Charge pressure	16 MPa

Table 18: Selected Control Strategy Parameter Values for the Control Strategy Study

Control fraction	0.06
Maximum switching frequency	2 Hz
Drive cycle temporal resolution	0.125 sec

Figure 52 illustrates the effect on the usage ratio, R_u, and pressure fraction, $f_{pressure}$, of varying the control fraction between 0.01 and 0.2. As expected, widening the control fraction causes the pressure fraction to increase. However, it also decreases the usage ratio (presumably improving efficiency) by limiting the range of HFA states where the pneumatic domain is used by default. Note that, unlike the usage ratio, pressure fraction does not increase monotonically with control fraction. Simply stated, this is because R_u is calculated as an integral quantity over the entire drive cycle, whereas pressure fraction is calculated using just two observed values during the drive cycle. The nuanced interaction between tractive power and the various control strategy parameters introduces some amount of randomness which causes the observed unsteady trend in the maximum and minimum observed pressures.

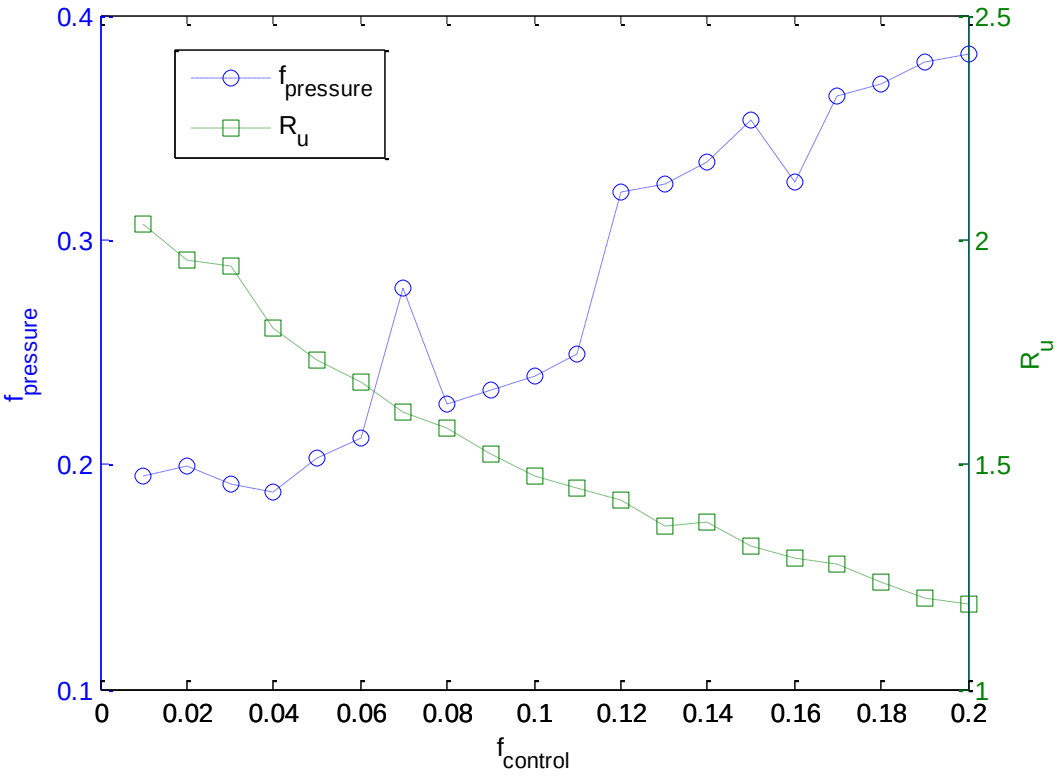

Figure 52: Study on Pressure Fraction and Usage Ratio as Functions of Control Fraction

It is also worth noting that, the lower the control fraction, the more the pressure fraction exceeds it. This is shown in Fig. 53, where the ratio $f_{pressure}/f_{control}$ is plotted as a function of $f_{control}$.

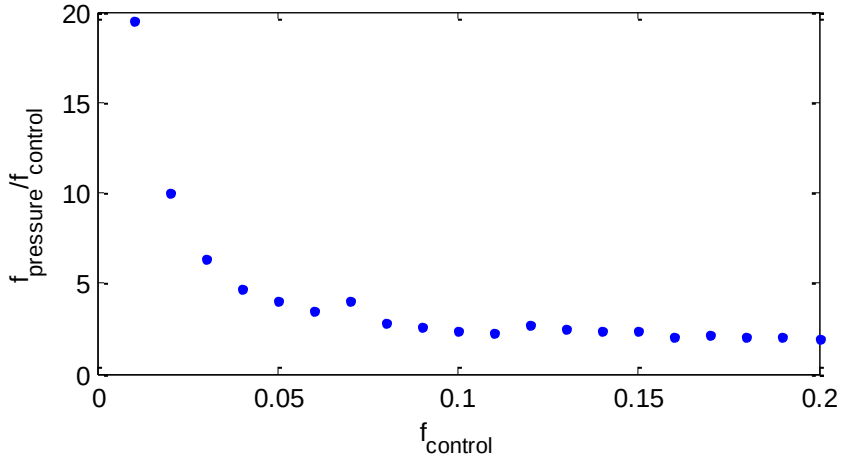

Figure 53: Study on the Degree to Which the Pressure Fraction Exceeds the Control Fraction

With the baseline control fraction of 0.06, the pressure fraction exceeds the control fraction by a factor of 3.5. However, when the control fraction is lowered to 0.01, the pressure fraction exceeds it by almost twenty-fold. This increasing discrepancy between the control band and the resultant pressure band gives way to diminishing returns on decreasing the control band.

Figure 54 shows that increasing the maximum switching frequency is beneficial to both the usage ratio and pressure fraction.

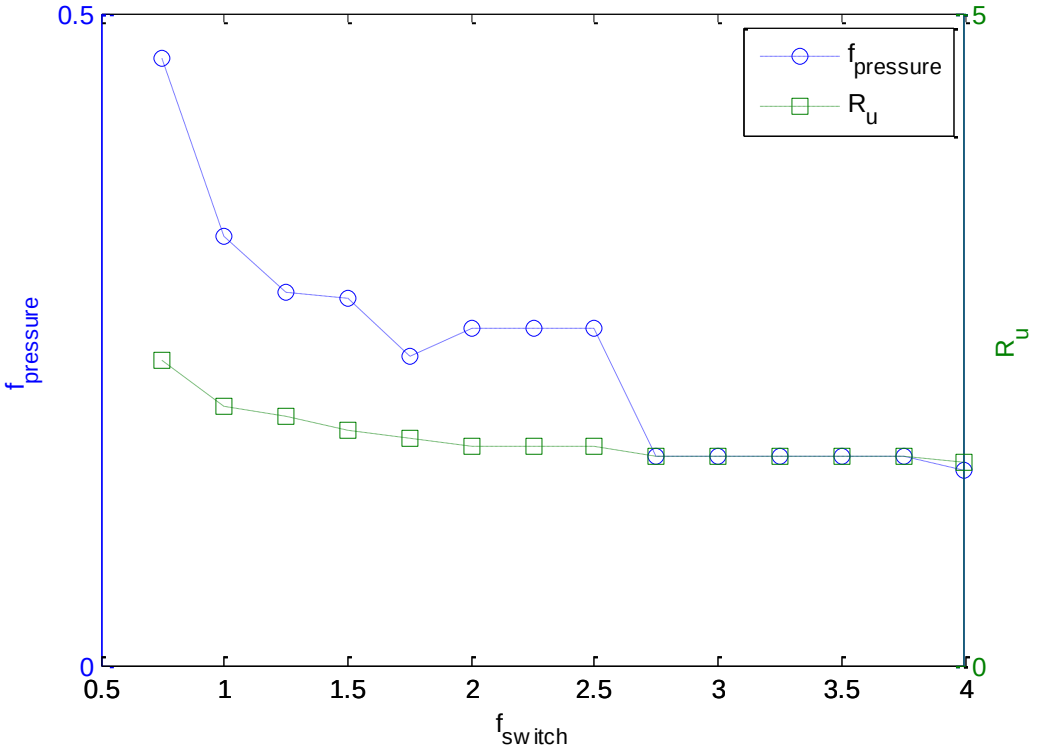

Figure 54: Study on Pressure Fraction and Usage Ratio as Functions of Maximum Switching Frequency

These trends are intuitive, since relaxing the constraints on the control strategy should allow it to more effectively accomplish its goals of maximizing the usage ratio and minimizing pressure fraction. In practice, the optimal f_{switch} should be selected by the

designer to make the best use of the control strategy while limiting NVH to acceptable levels.

Increasing the time resolution can affect the simulation results in both a numerical and a physical way. A finer time resolution leads to less numerical error, which is confirmed by observing the minimum feasible drive cycle energy (W_{dc} for a lossless powertrain) as a function of the simulation frequency. This relationship is plotted in Figure 55.

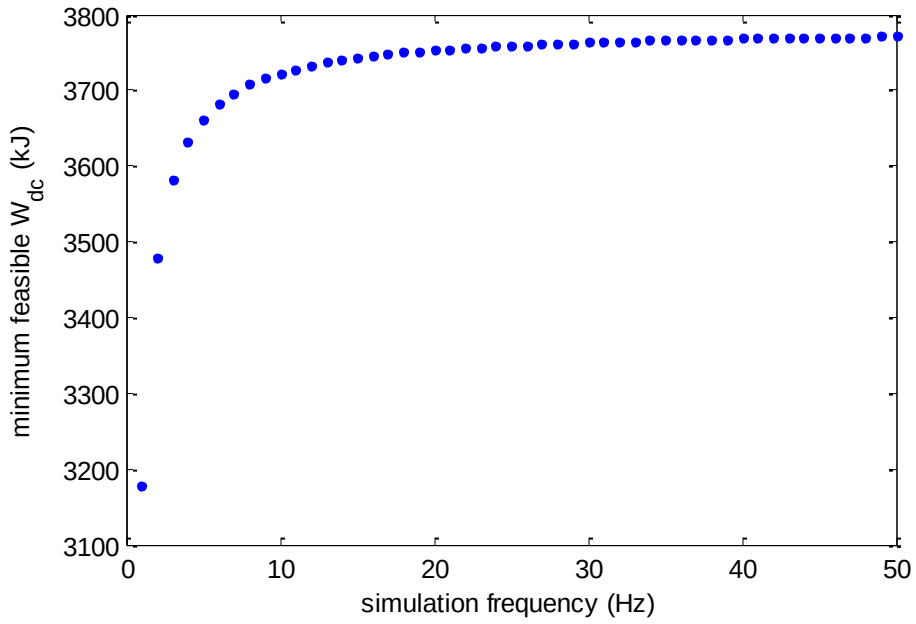

Figure 55: Study on Kinetic Energy Conservation as a Function of Temporal Resolution

Figure 55 shows that the temporal resolution has a significant effect on the accuracy of the finite difference calculations. Keeping in mind that computation time is proportional to the simulation frequency, however, there are clearly diminishing returns. At a frequency of 8 Hz, the value of W_{dc} is more than 98% of the value for a 50 Hz simulation frequency. This is deemed adequate for the present purposes, so the time step size for the simulations within the design optimization is set to 0.125 seconds.

It should be noted that, for some purposes, there may be a reason to increase time resolution to a value beyond that which produces sufficient numerical accuracy. This is because the time step size not only affects the frequency at which physical quantities are

computed, but also the frequency at which the control strategy is allowed to sample and react. This is true even when the minimum switching time, $1/f_{switch}$, is greater than the simulation time step size.

The baseline control strategy parameter values from this study (see Table 18) are selected for use in the design optimization that will be presented in Chapter 7. The studies presented above suggest that a control fraction $f_{control} = 0.06$ and maximum switching frequency $f_{switch} = 2\ Hz$ allow the control strategy to operate effectively with realistic protection against excessive NVH. A maximum expected system pressure, $P_{s,max}$, must be specified before a drive cycle simulation in order to appropriately select various dimensions using the processes detailed in Chapter 3. Based on simulation experience, $P_{s,max}$ is chosen for the present research to be 20% greater than the upper bound of the control band.

6.4 Calculation Sequence

As part of the present research, various scripts and functions have been written to execute a drive cycle simulation in MATLAB©. The pseudocode below is a general summary of the simulation process.

```
//initial operations
pre-calculate groups of constants
initialize matrices
set initial conditions

//loop through time steps in drive cycle
for t = 0 to t_last
      calculate HFA state
      calculate HFA stored energy and SOC
      calculate chamber pressure and implement vacuum pump control
      execute control strategy
      calculate storage PM volumetric and mechanical efficiencies
      execute pneumatic energy equations
```

```
      calculate pneumatic losses
      perform calculations based on fluid behavior model
      calculate kinetic losses
      execute kinetic energy equations
      check for energy conservation
      check for physical or computational failure
end loop

//post-process
execute calculations on performance metrics
```

For the purposes of optimization, maximizing computational efficiency is extremely important. Computation time can be decreased by making several calculations before the drive cycle loop is commenced. For example, the quantity $\rho_o(r_i^2 + r_a^2)/4$, which appears in various performance-related equations, consists only of constants and can therefore be calculated once per candidate design solution instead of being recalculated at each time step. Initializing matrices also improves computational efficiency in MATLAB©.

The initial conditions are chosen such that the HFA is at full SOC at the beginning of the drive cycle. This is done by simply setting the system pressure equal to the design pressure ($P_s = P_d$) and setting the HFA angular velocity to its full SOC value, with the fluid angular velocity at steady state ($\omega_s = \omega_f = \omega_{max}$). The gas pressure in the containment chamber is set to the desired value of 14 Pa (just above the saturation pressure of hydraulic oil), and $t_{switch,last}$ is set to $-\infty$.

The drive cycle loop begins with a calculation of the new HFA state at time step n. Angular velocities are calculated with simple finite-difference equations (FDE), using the angular velocity and angular acceleration from the previous time step.

$$\omega_s^n = \omega_s^{n-1} + \alpha_s^{n-1}\Delta t \tag{171}$$

$$\omega_f^n = \omega_f^{n-1} + \alpha_f^{n-1}\Delta t \tag{172}$$

Oil and gas volumes are also calculated using FDEs. Notice that both the oil and gas volumes can be calculated using the previous oil volume flow rate.

$$\forall_o^n = \forall_o^{n-1} + \dot{\forall}_o^{n-1}\Delta t \tag{173}$$

$$\forall_g^n = \forall_g^{n-1} - \dot{\forall}_o^{n-1}\Delta t \tag{174}$$

From the new oil volume, the inertia and length of the oil volume are, respectively

$$I_o^n = \frac{1}{2}\rho_o \forall_o^n (r_i^2 + r_a^2) \tag{175}$$

$$l_o^n = \frac{\forall_o^n}{\pi(r_i^2 - r_a^2)} \tag{176}$$

Knowledge of the gas volume allows gas pressure and the pressure at the center of the oil volume, P_o, to be calculated as

$$P_g^n = P_c \frac{\forall_c}{\forall_g^n} \tag{177}$$

$$P_o^n = P_g^n - \frac{1}{4}\rho_o \left(\omega_f^n\right)^2 (r_i^2 + r_a^2) \tag{178}$$

Note that P_o^n is not the current system pressure, but differs by a value of ΔP^n, which has yet to be calculated.

Having specified the new HFA state, the stored kinetic, pneumatic and total energy can be calculated as

$$E_k^n = \frac{1}{2} I_s (\omega_s^n)^2 + \frac{1}{2} I_o^n \left(\omega_f^n\right)^2 \tag{179}$$

$$E_p^n = P_c \forall_c \ln\left(\frac{P_g^n}{P_c}\right) \tag{180}$$

$$E^n = E_k^n + E_p^n \tag{181}$$

Next, the state of the gas in the containment chamber must be assessed. The new chamber pressure and gas density are calculated as

$$P_{ch}^n = P_{ch}^{n-1} + \dot{P}_{ch}^{n-1}\Delta t \tag{182}$$

$$\rho_{ch}^n = \rho_{atm} \frac{P_{ch}^n}{P_{atm}} \tag{183}$$

The chamber volume is then adjusted to account for oil that leaked from the HSRU during the previous time step.

$$\forall_{ch}^{n} = \forall_{ch}^{n-1} - \dot{\forall}_{l}^{n-1}\Delta t \tag{184}$$

Based on the new chamber pressure, deadband control is executed to determine whether the vacuum pump should be on ($vacOn^n = 1$) or off ($vacOn^n = 0$). Then, the vacuum pumping power consumption at the current time step is

$$\dot{W}_{vac}^{n} = (vacOn^n)P_{ch}^{n}S_p\frac{\gamma}{\gamma-1}\left[\left(\frac{P_{atm}}{P_{ch}^{n}}\right)^{\frac{\gamma-1}{\gamma}} - 1\right] \tag{185}$$

and the rate of change in chamber pressure is

$$\dot{P}_{ch}^{n} = \frac{Q - P_{ch}^{n}S_p + P_{ch}^{n}\dot{\forall}_{l}^{n-1}}{\forall_{ch}^{n}} \tag{186}$$

Now the control strategy references the current tractive power and various HFA parameters (as detailed in Section 6.2) to determine whether or not the kinetic domain should be used. If the control strategy has dictated that the kinetic domain be inactive for the current time step, the mechanical power, $\dot{W}_k^n$, and the storage PM shaft power, $\dot{W}_s^n$, are both set to zero. If the kinetic domain is active, the volumetric and mechanical efficiencies, η_v^n and η_m^n, respectively, are calculated using $\dot{W}_t^n$, ω_s^n and P_s^{n-1}. For brevity, the equations used to calculate these efficiencies, as well as kinetic and PM shaft power, are omitted here. Refer to Section 4.2 for the full set of equations.

Having calculated mechanical power, hydraulic power is calculated simply as the difference between tractive and mechanical power.

$$\dot{W}_p^n = \dot{W}_t^n - \dot{W}_k^n \tag{187}$$

Note that this equation is valid regardless of whether regeneration between the energy domains is occurring.

The pressure drop through the axle, ΔP^n, is calculated next. Because system pressure and HSRU leakage have yet to be calculated, the current volume flow rate in the pneumatic domain, $\dot{\forall}_o^n$, is still unknown. The volume flow rate at the previous time step is therefore used to calculate ΔP^n. The pressure drop through the axle is a function of volume flow rate only, and again, the detailed equations are omitted here for brevity. They can be found in Section 4.3.

Now, system pressure can be calculated using the pressure at the center of the oil volume and the pressure drop across the axle.

$$P_s^n = P_o^n + \frac{\left|\dot{W}_p^n\right|}{\dot{W}_p^n}\Delta P^n \tag{188}$$

The quantity $\left|\dot{W}_p^n\right|/\dot{W}_p^n$ properly reflects the fluid mechanics of the flow through the axle ports, ensuring, for example, that P_s^n is lower than P_o^n when the pneumatic domain is being discharged.

Knowing system pressure, the HSRU leakage rate, the associated leakage power loss, and the cumulative leakage volume can be calculated as

$$\dot{\forall}_l^n = \frac{P_s^n \pi d_s c_s^3}{12\mu_o l_s} \tag{189}$$

$$\dot{W}_l^n = \dot{\forall}_l^n P_s^n \tag{190}$$

$$\forall_l^n = \forall_l^{n-1} + \dot{\forall}_l^n \Delta t \tag{191}$$

Volume flow rate in the pneumatic domain is calculated as a function of the current hydraulic power, $\dot{W}_p^n$, and leakage flow rate.

$$\dot{\forall}_o^n = \frac{\dot{W}_p^n}{P_s^n} - \dot{\forall}_l^n \tag{192}$$

With the volume flow rate in the pneumatic domain known, the power dissipation due to pressure drop through the axle is

$$\dot{W}_a^n = \dot{\forall}_o^n \Delta P^n \tag{193}$$

and the rate of change in the inertia of the oil volume is

$$\dot{I}_o^n = \frac{1}{2}\rho_o \dot{\forall}_o^n (r_i^2 + r_a^2) \tag{194}$$

Having completed calculations in the pneumatic domain, the kinetic losses are now evaluated. The viscous losses in the HSRU, the bearing losses, and storage PM losses at the current time step are

$$\dot{W}_{vh}^n = \frac{\mu_o \pi d_s^3 l_s (\omega_s)^2}{4c_s} \tag{195}$$

$$\dot{W}_b^n = \frac{\mu_b (m + \rho_o V_o^n)(\omega_s^n)^3 r_{ecc} d_{b,i}}{2} \tag{196}$$

$$\dot{W}_{PM}^n = \dot{W}_k^n - \dot{W}_s^n \tag{197}$$

Notice that sign conventions are properly followed in calculating kinetic and shaft power, such that storage PM losses, $\dot{W}_{PM}^n$, are always non-negative. For brevity, the full set of equations used to calculate the two remaining kinetic loss mechanisms – aerodynamic drag and internal viscous dissipation – are omitted. The parameter dependencies of these two loss mechanisms are

$$\dot{W}_w^n = \dot{W}_w^n(\omega_s^n, \rho_{ch}^n) \tag{198}$$

$$\dot{W}_v^n = \dot{W}_v^n\left(l_o^n, \omega_s^n, \omega_f^n\right) \tag{199}$$

The actual means by which aerodynamic and internal viscous losses are calculated were thoroughly presented in Section 4.1 and Chapter 5, respectively.

Finally, the kinetic equations can be used to calculate the new fluid and solid acceleration rates,

$$\alpha_f^n = \frac{\left(\omega_s^n - \omega_f^n\right)}{\Delta t}\left[1 - \exp\left(\frac{\Delta t}{\tau_d^n}\right)\right] \tag{200}$$

$$\alpha_s^n = \frac{1}{I_s \omega_s^n}\left(\dot{W}_k^n - I_o^n \omega_f^n \alpha_f^n - \frac{1}{2}\dot{I}_o^n\left(\omega_f^n\right)^2 - \sum \dot{W}_{loss,kinetic}^n - \dot{W}_{vac}^n\right) \tag{201}$$

where

$$\tau_d^n = \tau_d^n(l_o^n, \omega_s^n, \alpha_s^{n-1}) \tag{202}$$

$$\sum \dot{W}_{loss,kinetic}^n = \dot{W}_v^n + \dot{W}_{vh}^n + \dot{W}_w^n + \dot{W}_b^n + \dot{W}_{PM}^n \tag{203}$$

There are two key differences between Eqn. 203 and the solid kinetic energy equation developed in Section 5.3. The former takes into account all kinetic loss mechanisms, instead of just internal viscous dissipation. It also includes the term $\dot{I}_o^n\left(\omega_f^n\right)^2/2$ which represents a perfect exchange of kinetic energy between the oil and the solid components as the volume of oil changes.

Inclusion of this kinetic energy exchange term dictates that all of the kinetic energy stored in the oil is transmitted to the solid components as the pneumatic domain is

discharged. In practice, of course, this exchange is imperfect, but since the oil volume tends to represent a very small proportion of the total stored kinetic energy in the HFA, this imperfection can be ignored for the present purposes. Future work might include investigating the nature of the kinetic energy exchange between the fluid and the solid components while the pneumatic domain is used. It is possible that this exchange could be promoted by using an end cap with radial ports that transport oil to the radius r_i, rather than the axle introducing oil to the HFA at the radius r_a.

The final operation at each time step is to check for failures. The simulation is aborted if there is insufficient stored energy to meet the energy demand at the next time step,

$$E^n < \dot{W}_t^{n+1} \Delta t \tag{204}$$

Even when the stored energy in the HFA is greater than that required at the next time step, the simulation must be aborted if the tractive power demand cannot be met. This can occur if the HFA is empty of oil and the storage PM is too small to produce all of the required flow given the current system pressure. Failure to meet the power demand can also occur if the flow extracted from the pneumatic domain is so large that the axle port losses cause system pressure to drop to zero.

A failure mode that is unrelated to power or energy, the oil that has leaked into the containment chamber must not be allowed to contact the lower bearing, as this would cause a sudden drastic increase in drag. The simulation is therefore aborted if

$$\forall_l^n > \forall_{l,max} \tag{205}$$

To avoid specifying the design details of the HSRU case here, for the purposes of design optimization, the oil is simply allowed to reach a height of 5 cm. The maximum allowable leakage volume, $\forall_{l,max}$, is therefore approximately

$$\forall_{l,max} = (0.05\ m)\pi(r_o + c_{ch})^2 \tag{206}$$

where $r_o + c_{ch}$ is the inner radius of the containment chamber, presumed to be much larger than the radius of the HSRU case. In a real HFA application, a leakage failure would be prevented by actively monitoring the amount of leakage oil in the chamber.

6.5 Calculation of Performance Metrics

Once the drive cycle is complete (or has been terminated due to one of the failure modes), several performance metrics can be assessed. Drive cycle losses are calculated as the time-integral of the sum of all power dissipation mechanisms, plus a vacuum pumping energy consumption term, W_{vac}.

$$W_{loss} = \int_{t=0}^{t_{dc}} \left[\dot{W}_v + \dot{W}_{vh} + \dot{W}_w + \dot{W}_b + \dot{W}_{PM} + \dot{W}_l + \dot{W}_a\right] dt + W_{vac} \tag{207}$$

The vacuum term is the time-integral of vacuum pump power, $\dot{W}_{vac}$, plus the amount of pumpdown energy, $W_{pumpdown}$, required to return the containment chamber to the desired pressure from the pressure at the end of the drive cycle.

$$W_{vac} = \int_{t=0}^{t_{dc}} \dot{W}_{vac}\, dt + W_{pumpdown} \tag{208}$$

The methods used to calculate the pumpdown energy were presented in Section 4.4. Note that W_{vac} does not include the energy required for pumpdown from atmospheric pressure after assembly. The decision to omit this energy consumption stems from the assumption that, in a real HFA application, disassembly and reassembly should seldom be required, and therefore vacuum can be maintained between HFA uses with little energy input.

Drive cycle efficiency is defined using the drive cycle losses, W_{loss}, incurred in the HFA as a proportion of the cumulative energy conversion at the HFA.

$$\eta = 1 - \frac{W_{loss}}{\int_t \left|\dot{W}_t\right| dt + W_{loss}} \tag{209}$$

With the knowledge of system pressure at every time step, the traction PM displacement required to complete the drive cycle is calculated as

$$D_t = \left|\frac{2\pi \dot{W}_t}{P_s \omega_t}\right|_{max} \tag{210}$$

where ω_t is the angular velocity of the traction PM. For simplicity, it is assumed that the vehicle differential has a 1:1 gear ratio, such that the traction PM angular velocity is a function of vehicle velocity, v, and tire diameter, d_t.

$$\omega_t = \frac{2v}{d_t} \tag{211}$$

The traction PM mass, $m_{PM,t}$, is calculated using the correlation of commercial data given in Eqn. 169. Recall that smaller fluctuation in system pressure tends to allow for a smaller traction PM. A candidate HFA solution should therefore be judged not only by the mass-efficiency of its stored energy but also by its ability to minimize system pressure fluctuation. The performance metric that incorporates both of these criteria is system mass, m_{sys}, defined as the sum of the mass of the primary HFA components, m, along with the masses of the storage and traction pump-motors.

$$m_{sys} = m + m_{PM,s} + m_{PM,t} \tag{212}$$

The energy density, u_d, of an HFA solution is calculated as the amount of energy stored (at full SOC) per unit mass of the energy storage system.

$$u_d = \frac{E_d}{m + m_{PM,s}} \tag{213}$$

Note that, because it is not actually a part of the energy storage system, the mass of the traction PM is excluded from the energy density calculation.

The unfinished distance, d_{unf}, is simply the difference between the total drive cycle distance and the cumulative distance traveled when the simulation ended. If no failure occurred during the drive cycle simulation, then $d_{unf} = 0$.

The housing safety factor is determined using the methods presented in Section 3.5. Note that the safety factor is assessed after the drive cycle is complete, such that the observed values of maximum angular velocity and maximum pressure at the internal wall of the liner can be used in calculating housing stress.

7 Design Optimization

Chapters 2 and 3 thoroughly discussed the HFA concept and the process by which various design choices are made. The development of performance modeling and simulation tools was presented in Chapters 4 through 6. These processes and tools are now embedded into an optimization algorithm to find the best HFA design solutions for two specified applications – a vehicle-scale energy storage system and laboratory-scale prototype. The two applications are differentiated only by differences in power and energy capacities and volumetric constraints.

This chapter begins by describing the optimization strategy and the technical posing of the optimization problem. Next, the results are presented for two optimizations – one for a vehicle-scale application and one for a laboratory-scale application. These two sets of optimization results are then compared to one another and discussed within the context of vehicle energy storage systems in general. The chapter concludes by justifying the selection of a particular HFA design solution from the laboratory-scale optimization results to be constructed as a prototype.

7.1 Optimization Strategy

As outlined in Section 2.6, the design optimization of the HFA is multi-objective, where the first objective is to minimize HFA system mass (which, by Eqn. 212, includes the masses of the storage and traction pump-motors) and the second objective is to minimize energy losses over a drive cycle. These optimization objectives can be expressed mathematically as

$$\text{minimize}\left[m_{sys}, W_{loss}\right] \tag{214}$$

Unlike a single-objective optimization, a multi-objective optimization does not yield one uniquely optimal solution. Instead, it finds a set of Pareto-optimal (PO) solutions, none of which is dominated by (i.e. inferior to, with regard to both objectives) any other solution.

It is then the task of the designer to make an intelligent selection from the Pareto-optimal set.

In pursuit of the objectives expressed by Eqn. 214, the optimization is subject to two constraints. The first dictates that an HFA design solution must exhibit a material safety factor of 3. For each candidate solution, the optimization algorithm need only check the safety factor of the housing, whose dimensions are design variables; the safety factors for all of the other components will have already been forced to be 3 by intelligently selecting their dimensions. The second constraint on the optimization is that an HFA design solution must allow the vehicle to complete one drive cycle. As discussed in Section 6.1, this is enforced by mandating that an acceptable solution leave no unfinished distance, d_{unf}, in performing the UDDS. Failure to complete the UDDS is generally the result of insufficient power or energy storage capacity, but can also result from excessive oil leakage through the HSRU (see Section 6.4).

When expressed in terms of the design variables, the equations involved in evaluating the objective and constraint values are highly nonlinear. In fact, since the UDDS is given as a dataset rather than an equation, there is no way to specify gradients of all the equations involved in calculating the HFA performance metrics. High nonlinearity and lack of smoothness reduce the effectiveness of gradient-based optimization methods, sometimes to the point of uselessness. These factors, along with the multi-objectivity of the problem and the convex solution space, motivate the use of metaheuristics. Because of its robustness and relatively straightforward implementation, a genetic algorithm is selected as the optimization strategy.

A genetic algorithm is commenced by creating an initial population of candidate design solutions, where the values of the design variables are randomly selected within some specified bounds. The design variable values are converted to binary representation and concatenated to form objects that are analogous to chromosomes. A series of operations is then performed on this population of chromosomes to simulate genetic recombination and mutation. The resultant offspring chromosomes are converted back to real value representation, such that the objective values can be calculated. This process is repeated for some specified number of generations.

The specific strategy used in this study is the NSGAII [73]. This is an "elitist" genetic algorithm, where the parents in each generation are evaluated alongside and compete with their offspring, and the "best" half of this double population is chosen to constitute the parents for the next generation. This technique ensures that optimal solutions are not lost. Constraints are enforced while comparing each solution for domination over every other solution. Any infeasible solution is prohibited from dominating any feasible solution, regardless of the objective values. When comparing two infeasible solutions, one dominates the other if it has violated constraints to a lesser extent (i.e. smaller unfinished distance and/or safety factor closer to 3). This constraint-handling method is superior to outright rejection of infeasible individuals [74], which can kill off genes that might eventually comprise an optimal solution.

Table 19 summarizes the genetic algorithm parameters used for the two optimizations presented in this chapter.

Table 19: Summary of the Genetic Algorithm Parameters

# Design parameters	9
# Objectives	2
# Constraints	2
# Generations	400
# Individuals	200
Binary precision (bits)	7

Notice that, for each optimization, eighty-thousand candidate solutions are evaluated, and by the nature of the genetic algorithm, each succeeding generation offers candidate solutions that are superior to the last. The number of candidate solutions was chosen to be small enough for the optimization to be performed in a reasonable amount of time, but large enough to promote thorough exploration of the solution space and convergence to the true PO set.

7.2 Posing the Optimization Problem

The concept of specifying a unique HFA design by using a set of nine design variables was introduced in Section 2.1. To prevent the genetic algorithm from attempting to evaluate geometrically infeasible candidate solutions, four of the design variables are redefined as follows. The thickness fraction, f_{th}, specifies the fraction of the outer radius that constitutes the wall. Inner radius is therefore calculated as

$$r_i = f_{th} r_o \tag{215}$$

Bounding f_{th} to values between 0 and 1 prohibits the production of a design solution with an inner radius that is greater than the outer radius.

The design variable liner thickness, th_l, is replaced by liner fraction, f_l, which is the fraction of the wall thickness that is constituted by the liner. The relationship between liner thickness and liner fraction is then

$$th_l = f_l(r_o - r_i) \tag{216}$$

The rationale for this new design variable is the same as that for the thickness fraction; bounding f_l between 0 and 1 prevents the liner thickness from exceeding the total wall thickness.

The original design variable housing length, l_h, is replaced with inner length, l_i, defined as the distance between the inner faces of the two end caps. Housing length can then be calculated as

$$l_h = l_i + 2th_e \tag{217}$$

where th_e is the thickness of each end cap. Because th_e is finite and both end caps must fit inside the housing, using l_i with a lower bound of zero ensures non-negative internal HFA volume. The upper bound on inner length is chosen based on packaging constraints.

The design variable port diameter fraction, $f_{d,i}$, replaces the axle port diameter, d_i, where the two are related by

$$d_i = f_{d,i} 2 r_i \tag{218}$$

When $f_{d,i}$ is bounded between 0 and 1, this formulation prevents the axle port diameter from exceeding the inner diameter of the HFA.

Although it has no bearing on the geometric feasibility of a design solution, the original design variable charge pressure, P_c, is converted to a charge fraction, f_c, where

$$P_c = f_c P_d \tag{219}$$

This change is enacted with the intent of making the optimization results somewhat simpler to interpret.

The remaining original design variables need not be redefined. The new design solution definition, along with its relationship to the old, is summarized in Table 20.

Table 20: Redefined Design Solution, Used for the Purposes of a Design Optimization

Variable	Symbol	Translation
Geometric		
Housing outer radius	r_o	–
Thickness fraction	f_{th}	$f_{th} = r_i / r_o$
Liner fraction	f_l	$f_l = th_l / (r_o - r_i)$
Inner length	l_i	$l_i = l_h - 2th_e$
Port diameter fraction	$f_{d,i}$	$f_{d,i} = d_i / (2r_i)$
HSRU seal clearance	c_s	–
HSRU seal length	l_s	–
Operational		
Maximum angular velocity	ω_{max}	–
Charge fraction	f_c	$f_c = P_c / P_d$

It is important to note that this new definition of a design solution is fundamentally the same as the original definition given in Section 2.1 and used throughout the preceding chapters. Both represent the same HFA design choices, but the new definition is more algorithmically practical, in that it allows for bound selections that avoid geometrically infeasible designs. The original set was selected for its clear and intuitive description of

the HFA geometry, and it will therefore be used for the purposes of discussing the optimization results in subsequent sections.

The selected bounds on the design variables are given in Table 21.

Table 21: Design Variable Bounds for the Design Optimization

Variable	Lower Bound	Upper Bound	Units
r_o	1	[app. specific]	cm
l_i	1	[app. specific]	cm
f_{th}	0	0.95	-
f_l	0	0.1	-
$f_{d,i}$	0	0.5	-
l_s	0.5	50	mm
c_s	10	30	μm
ω_{max}	2,865	1,885	rad/s
f_c	0.35	1	-

The thickness fraction, f_{th}, liner fraction, f_l, and port diameter fraction, $f_{d,i}$, were defined earlier in this section such that values of 0 to 1 prohibited geometrically infeasible solutions. In practice, however, intelligently selecting more realistic upper bounds for these design variables promotes faster convergence to the true PO set without excluding potentially optimal regions of the solution space. For example, engineering intuition would suggest that the port diameter should certainly never need to be more than 50% of the HFA inner diameter, as losses associated with the HSRU should actually drive d_i to be far lower. Similar arguments can be made for the other fractional design variables and their validity confirmed by observing that the selected upper bounds are not encroached upon during the optimization.

As is the case for the fractional design variables, logical arguments allow practical bounds to be selected for the circumferential seal dimensions, l_s and c_s, and the charge fraction, f_c. Again, the design variables values have been monitored during the design optimization to ensure that the selections shown in Table 21 are not overly restrictive.

In practice, maximum allowable angular velocity, ω_{max}, is limited by a number of factors. Radial bearing load due to eccentricity increases with the square of angular velocity. Heat generation in the bearings is directly proportional to the product of

angular velocity and radial load, and heating due to aerodynamic drag scales with the cube of angular velocity. At very high rotational speeds, the rotor material strength becomes an issue, as centrifugal force on the rotor induces high stress. Finally, dynamic stability can be an issue with high speed flywheels [25]. Given the axial piston pump-motors that appear to be suitable for the HFA [53], the upper bound on maximum angular velocity is set to 1,885 rad/s (18,000 RPM). To avoid solutions with impractically-low energy density, the lower bound on ω_{max} is chosen to be 2,865 rad/s (3,000 RPM).

The upper bounds on outer radius, r_o, and housing inner length, l_i, impose a limit on the packaging volume of the HFA. Note that this is a "soft" limit, as the total housing length also includes the length of the end caps, and neither r_o nor l_i fully reflect the containment chamber dimensions. Since the limit on packaging volume is application-specific, the selected upper bounds on outer radius and inner length are different for the vehicle- and the laboratory-scale optimizations detailed in the following two sections. The lower bounds on these variables are each set to 1 cm to avoid testing pure flywheels. In practice, inner lengths of the optimal design solutions do not encroach upon the lower bound of 1 cm, as the efficiency of the pneumatic domain promotes reasonably large internal HFA volumes. The outer radii of the optimal solutions do not encroach upon their lower bound either, because values significantly greater than 1 cm are required for reasonable kinetic and pneumatic energy capacities.

7.3 Vehicle-Scale Optimization Results

Section 6.1 described the methods by which vehicle road loads are calculated. The combination of the selected vehicle parameters (chosen to represent a typical mid-size sedan and summarized in Table 16) and the UDDS dictate the minimum power capacity and the energy storage capacity required for a candidate design solution to be considered acceptable for a vehicle-scale application. To reflect a reasonable packaging volume for a passenger vehicle energy storage system, upper bounds for the present optimization are selected to be 50 cm for the outer radius and 150 cm for the housing inner length.

The most general results of any two-objective optimization can be gleaned by examination of the PO front, a two dimensional plot of the solution set with each axis corresponding to an objective value. The PO front for the vehicle-scale optimization is shown in Fig. 56, with m_{sys} on the x-axis and W_{loss} on the y-axis.

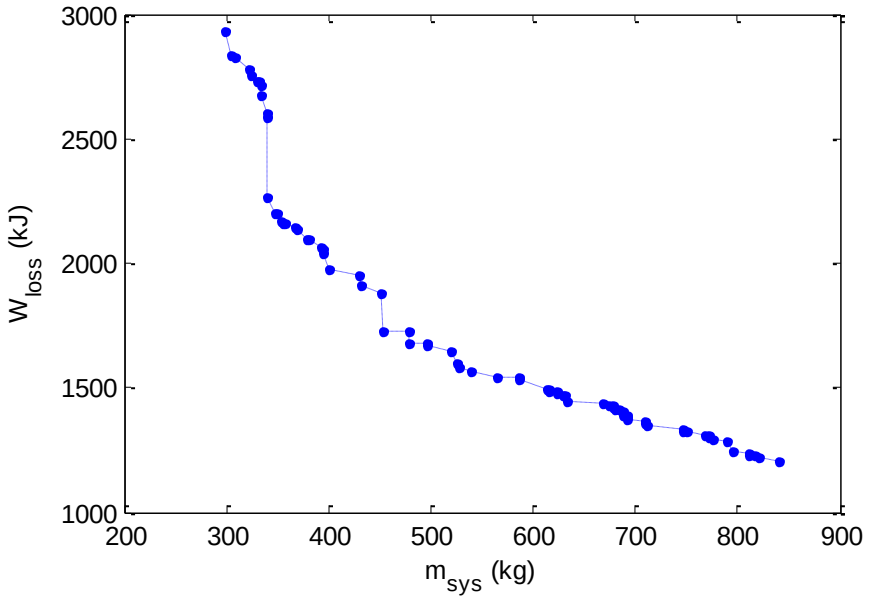

Figure 56: Pareto-optimal Front for the Vehicle-scale Design Optimization

The most fundamental observation available from the PO front is that there is, as expected, a tradeoff between HFA system mass and drive cycle energy losses. From the shape of the curve, it is clear that there are diminishing returns on pursuing either objective; the lower the mass is driven, the higher the marginal penalty in losses. While the PO front does not explicitly reveal anything about design parameter values, the following is generally true. Solutions near the upper-left end of the PO front approach disk-style pure kinetic flywheels, characterized by short housings, small inner radii, thick walls, and high maximum angular velocities. Conversely, solutions near the lower-right more closely resemble static hydraulic accumulators, with long housings, large radii, thin walls, and low maximum angular velocities.

To compare the HFA concept with other energy storage media, it is useful to assess the range of energy densities and efficiencies offered by the solutions in the PO set. These

performance metrics, whose calculations were given by Eqns. 213 and 209, respectively, are plotted against one another in Fig. 57.

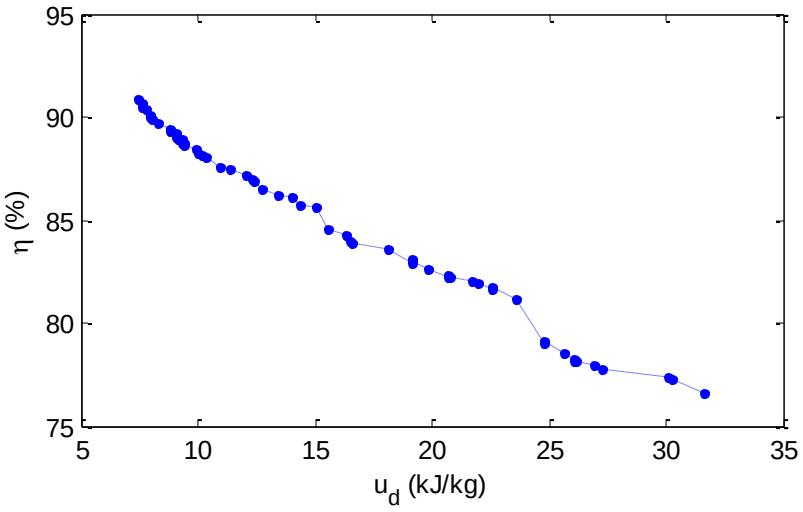

Figure 57: Drive Cycle Efficiency vs. Energy Density for the Vehicle-scale Pareto-optimal Set

Because energy density and drive cycle efficiency are inversely related to the objective values of system mass and drive cycle losses, respectively, Fig. 57 resembles somewhat of an inverted PO front. The energy-dense but inefficient flywheel-like solutions are near the lower-right, while the efficient but low-energy density accumulator-like solutions are near the upper-left. Table 22 summarizes the extreme ends of the PO set.

Table 22: Summary of the Extreme Pareto-optimal Solutions from the Vehicle-Scale Optimization

	system mass (kg)	losses (kJ)	energy density (kJ/kg)	efficiency (%)
most accumulator-like	1204	840	7.47	90.85
most flywheel-like	299	2929	31.6	76.6

Having described the range of performance offered by the vehicle-scale PO solutions, it is now of interest to examine their actual designs. It is convenient to analyze the PO set as a progression from flywheel-like to accumulator-like solutions. In doing so, the various trends in the design variable values will be described as a "strategy" to gradually

reduce energy losses (which, as mentioned, comes at the penalty of increased system mass). This is, of course, a fictitious strategy, as the design trends have arisen as the consequence of an evolutionary process.

Figure 58 illustrates how various geometric and operational parameters change as system mass increases. Subfigure a) shows the primary dimensions of the housing and subfigure b) shows the maximum angular velocity and charge pressure.

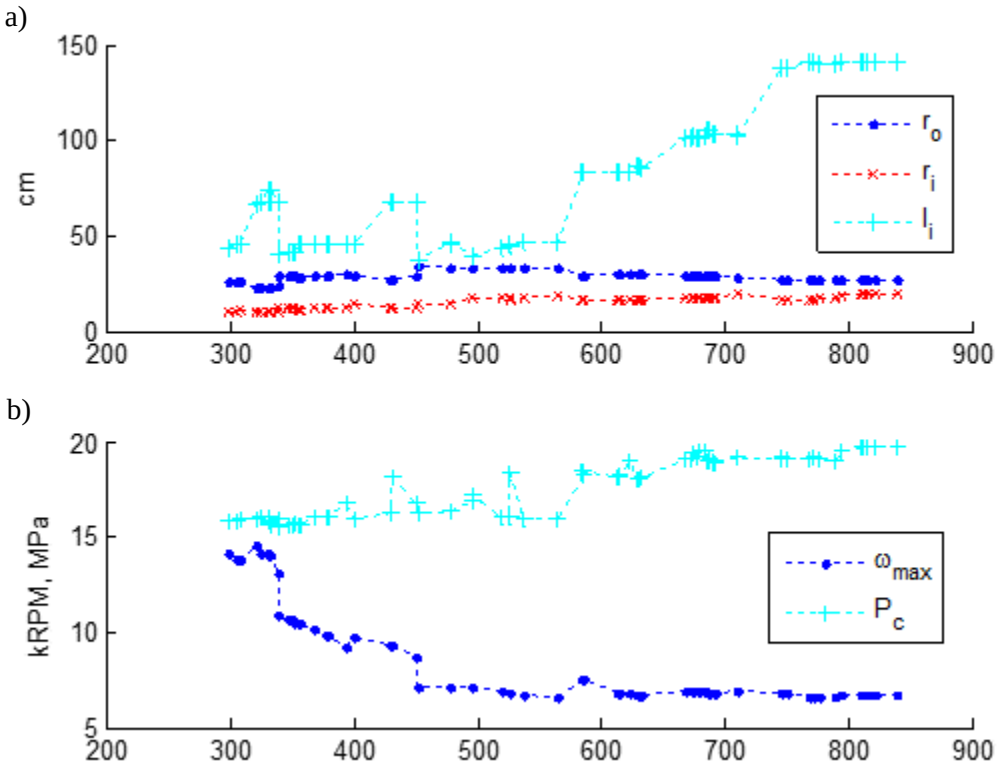

Figure 58: Design Trends as Functions of System Mass for the Vehicle-Scale Pareto-optimal Set

Simply stated, the flywheel-like solutions near the far left of the plots in Fig. 58 achieve low system masses because they have small geometric dimensions. Small dimensions generally correlate to low inertia, so these solutions must operate at high angular velocities in order to store sufficient energy.

The high energy density of the flywheel-like solutions comes with a penalty of high drive cycle losses, as illustrated in the PO front of Fig. 56. This is intuitive, as bearing drag,

HSRU viscous loss, aerodynamic drag, and storage PM losses are all proportional to angular velocity. The latter two loss mechanisms are particularly severe for the flywheel-like solutions, as their proportionality to angular velocity is fairly high-order. Note that any given HFA operates over a wide range of angular velocities during a drive cycle simulation. However, the design parameter ω_{max} is a good indicator of the "average" operating speed for a particular solution, since each solution begins the simulation at its respective value of ω_{max}, and each tends to finish near zero speed (fully-depleted). The basic "strategy" by which drive cycle losses are decreased, therefore, is to tend towards lower values of maximum angular velocity.

In order to maintain sufficient energy capacity, however, the strategy of decreasing ω_{max} must also include growth of the HFA dimensions. In effect, angular velocity is exchanged for inertia, which serves to maintain a reasonably high energy capacity in the kinetic domain. As shown by Eqn. 80, the aerodynamic drag torque has a fifth-order dependence on the outer radius of the housing (although this is slightly offset by the modest dependence of the moment coefficient on outer radius). It is therefore more favorable to add inertia by increasing housing length, rather than outer radius, because of the smaller aerodynamic penalty it incurs.

Figure 59 illustrates the impact on energy losses of lowering ω_{max}. Subfigure a) shows ω_{max} as a function of m_{sys}, and subfigure b) shows the corresponding aerodynamic, bearing, and storage PM losses. So that they can be plotted on the same axes, the values of each loss mechanism have been scaled with their maximum observed value during the drive cycle. In actuality, storage PM losses tend to be an order of magnitude higher than the other mechanisms, making up between 80 and 90% of total losses. Aerodynamic losses tend to account for 4% to 7%, and bearing losses 1% to 2%. The viscous internal losses make up less than 1% of W_{loss}.

As mass is increased and angular velocity is decreased, all three of the loss mechanisms in Fig. 59 are initially reduced. At about 450 kg, maximum angular velocity levels out. After this point, bearing losses actually begin to rise again, as the larger masses lead to larger radial bearing loads. Housing length increases and outer radius decreases slightly

for solutions greater than 450 kg (see Fig. 58), the combination of which leads to roughly constant aerodynamic losses.

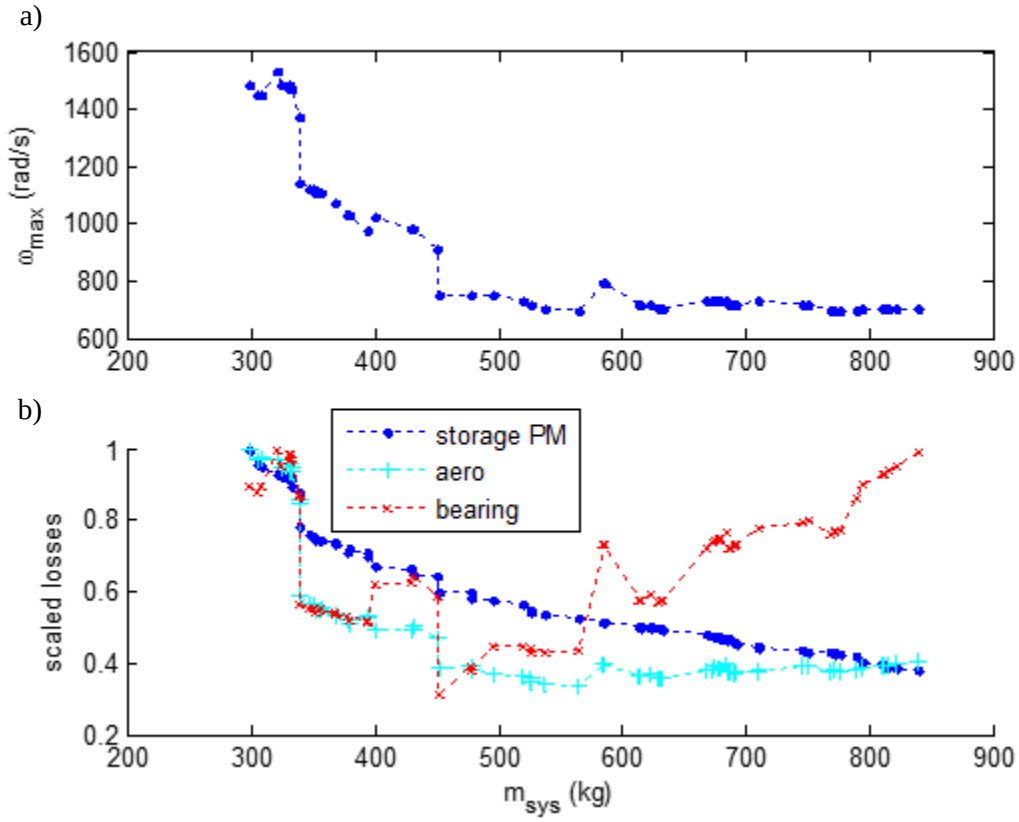

Figure 59: Trends in Storage PM, Aerodynamic, and Bearing Losses as Functions of System Mass

While lowering aerodynamic drag is beneficial, the most important consequence of using lower-speed designs is to decrease storage PM losses. The first mechanism by which these losses are reduced is that axial piston hydraulic machines tend to be more efficient at lower speeds. This relationship, which can be deduced from the equations in Section 4.2, is shown in Fig. 60 for the vehicle-scale PO solutions.

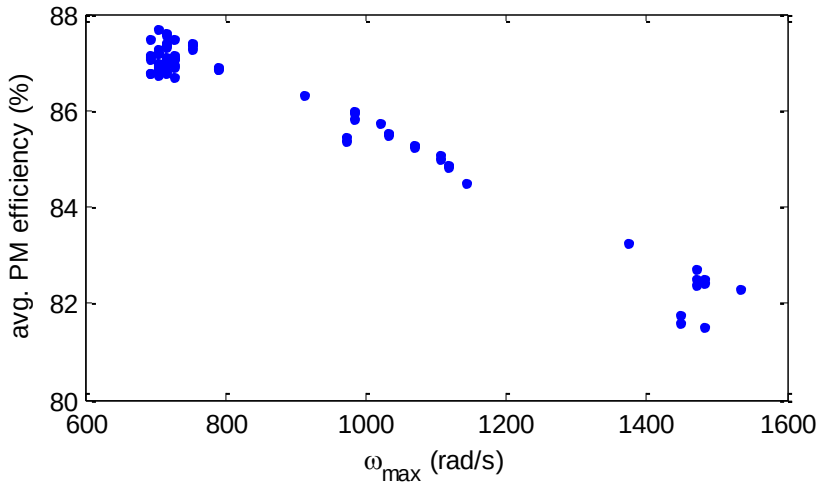

Figure 60: Storage PM Efficiency, Averaged over the UDDS, for the Vehicle-scale Pareto-optimal Set

Interestingly, the speed-dependence of the storage PM efficiency shown in Fig. 60 is only one of the mechanisms by which slower-spinning solutions exhibit fewer storage PM losses. The second mechanism is simply that these solutions are less dependent on the inefficient kinetic domain. The following paragraphs explain how this occurs.

As previously mentioned, a growth in HFA dimensions accompanies a decrease in ω_{max} in order to maintain a reasonable kinetic energy capacity. An additional result of this growth – namely longer housing lengths and inner radii – is to actually increase pneumatic energy storage by increasing the internal HFA volume (see Eqn. 22). This phenomenon is illustrated in Fig. 61, where pneumatic and kinetic energy storage capacities are plotted against system mass in subfigure a) and the corresponding capacity ratio, R_c (the ratio of kinetic to pneumatic energy stored at full SOC, Eqn. 23), in subfigure b).

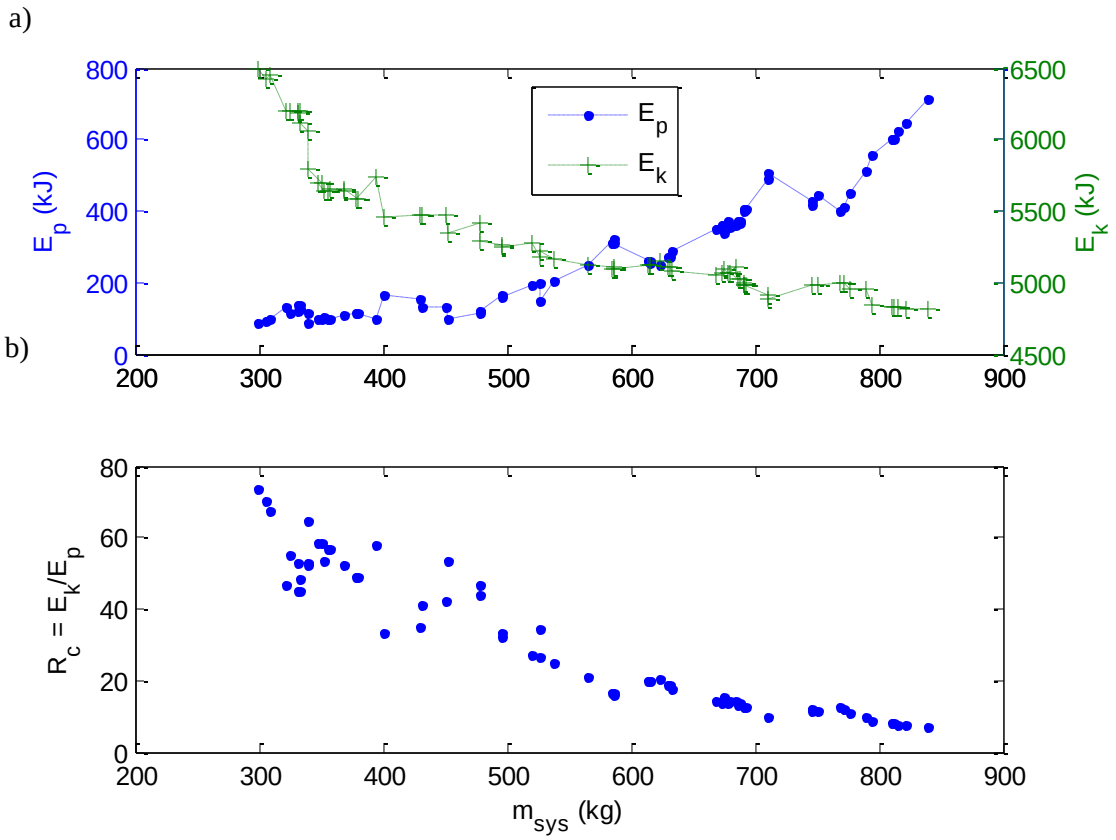

Figure 61: Energy Capacity by Domain, and Corresponding Capacity Ratio, for the Vehicle-scale Pareto-optimal Set

Over the course of the transition from flywheel-like to accumulator-like solutions, the kinetic energy storage capacity decreases by about a quarter, while pneumatic energy capacity increases more than seven-fold. This progression represents a 90% decrease in the capacity ratio. Unsurprisingly, the PO solutions with lower capacity ratios also exhibit lower usage ratios, R_u (the ratio of energy converted through the kinetic domain to the tractive energy demand/supply met purely by using the pneumatic domain, Eqn. 164). This trend is shown in Fig. 62.

It is notable that R_u is significantly lower than R_c for all of the design solutions. For example, one particular solution uses exactly the same amount of pure pneumatic energy as kinetic energy during the UDDS, even though it stores over 14 times more kinetic energy at full SOC. This is a direct result of the band control strategy described in Section 6.2 heavily favoring the pneumatic domain.

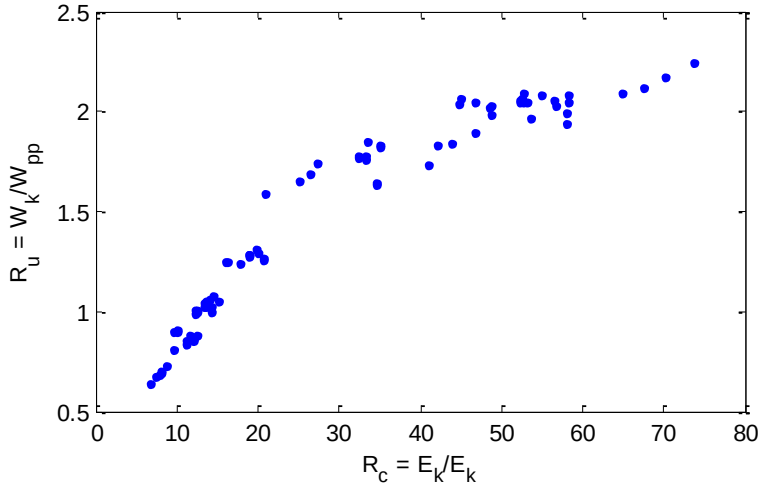

Figure 62: Usage Ratio vs. Capacity Ratio for the Vehicle-scale Pareto-optimal Set

It has now been shown that the strategy of slower-spinning and larger PO solutions leads to low capacity ratios, which, in turn, lead to lower usage ratios. By its very definition, low values of the usage ratio correspond to sparser usage of the storage PM. In Section 2.5, it was argued that heavier reliance on the pneumatic domain would lead to more efficient HFA operation. As indicated by Fig. 63, the optimization results prove that this is, in fact, true. Because it is the dominant loss mechanism, reducing storage PM losses is the most effective way to reduce overall drive cycle losses.

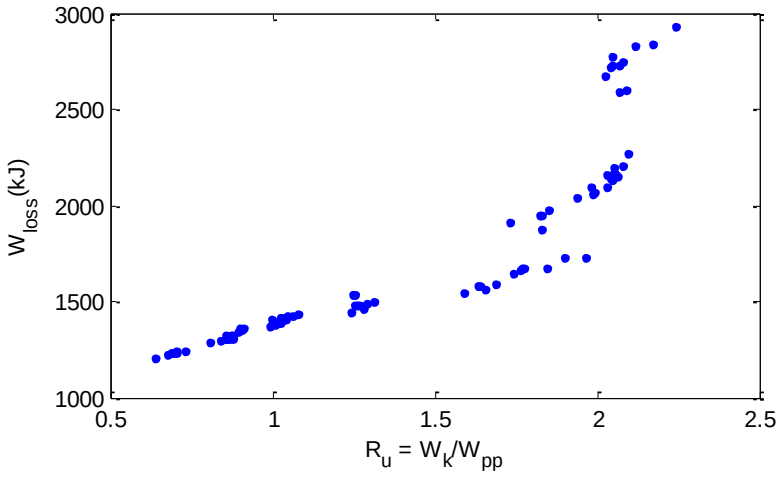

Figure 63: Drive Cycle Losses vs. Usage Ratio for the Vehicle-scale Pareto-optimal Set

Equation 168 described how the storage PM displacement, D, is selected before a drive cycle. As a point of interest, the storage PM displacements for the vehicle-scale PO solutions are plotted against m_{sys} in Fig. 64.

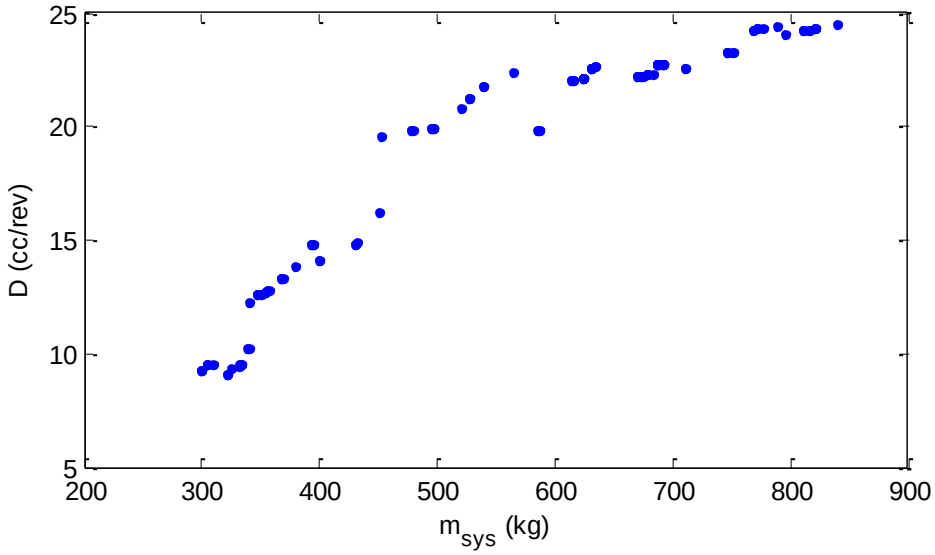

Figure 64: Storage PM Displacement vs. System Mass for the Vehicle-scale Pareto-optimal Set

As shown in Eqn. 167, the mechanical power produced by a fixed-displacement hydraulic motor is proportional to its rotational speed and its displacement. To meet the power demands of the UDDS, an accumulator-like solution must compensate for its slower speed by using a larger storage PM.

Recall from Section 4.3 that leakage, axle port and HSRU viscous losses are all strong functions of the axle port diameter, d_i. In the present discussion, they have not been plotted against system mass, as there are no clearly-defined trends. This is not surprising, as the HSRU dimensions have no direct influence on the kinetic or pneumatic capacity of an HFA design solution.

The trends in d_i can be thought of as a reaction to the progression from accumulator- to flywheel-like solutions, responding to it rather than influencing it. As the major HFA dimensions and operating parameters are varied, the axle port diameter reacts with somewhat of a sub-optimization on leakage, axle port and HSRU viscous losses. This is

shown in Fig. 65, where d_i is plotted against system mass for the vehicle-scale PO solutions.

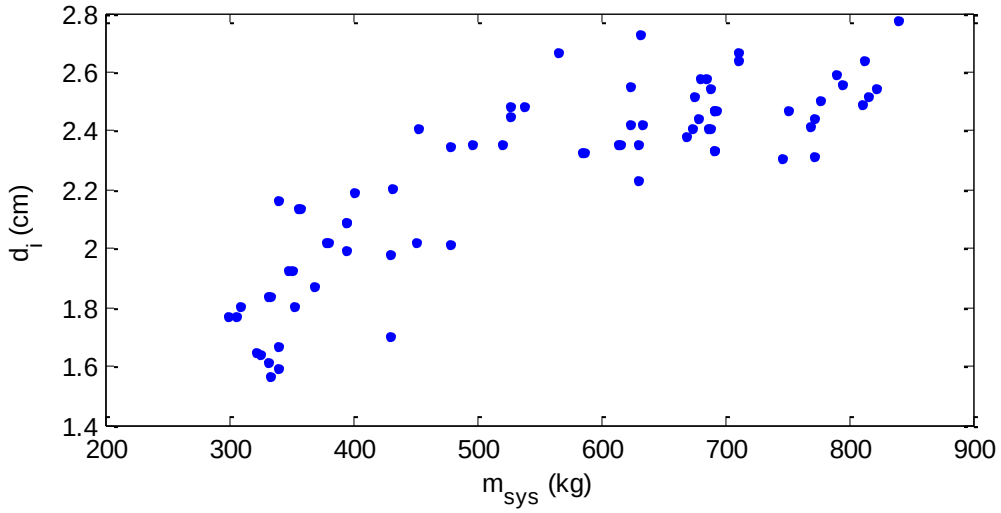

Figure 65: Axle Port Diameter vs. System Mass for the Vehicle-scale Pareto-optimal Set

Although system mass is plotted as the independent variable, changes in the axle port diameter are more directly a response to the decreasing angular velocity. As indicated by Eqn. 116, viscous HSRU power dissipation increases with ω^2 and d_i^3. The decreasing angular velocity associated with more accumulator-like solutions allows d_i to increase without any significant penalty in HSRU viscous losses. The motivation for increasing d_i is clear from Eqns. 101 through 104, which show that power dissipation in the axle ports is proportional to $\dot{V}_o$ (the volume flow rate in the pneumatic domain) and inversely proportional to d_i^4. Using larger axle port diameters, therefore, keeps axle port losses in check for the accumulator-like solutions, even as these solutions rely more on the pneumatic domain (i.e. experience more integrated $\left|\dot{V}_o\right|$).

One of only two design variables to encroach upon its imposed lower bound, the circumferential seal clearance, c_s, is about 10 μm for all solutions. Per Eqn. 114, leakage power dissipation, $\dot{W}_l$, is proportional to c_s^3. For clearance values greater than about 10 μm, leakage losses and net leakage volume become substantial. To offset the penalty in HSRU viscous losses of very small clearance values (by Eqn. 116, $\dot{W}_{vh}$ scales with c_s^{-1})

the seal length, l_s, remains between about 2 mm and 6 mm, near the lower values of its acceptable bounds. For the range of PO solutions, the leakage, axle port and HSRU loss mechanisms each make up between 1% and 5% of total drive cycle losses.

Like the seal clearance, the liner fraction, f_l, also encroaches upon its lower bound. To store sufficient kinetic energy, the HFA design solutions tend towards large wall thicknesses, which add inertia by increasing both mass and radius. Obviously, the latter is more mass-efficient and is more effectively accomplished using the carbon fiber wrap rather than the steel liner. Using a very thick wrap effectively reduces the stresses in the liner, allowing the liner to be quite thin. Although Section 3.5 cited a reduction in radial tensile stresses in the wrap as a benefit of using a moderately-thick liner, the high internal pressures observed in the PO solutions render this unnecessary.

It is worthwhile to examine the factors which limit the expanse of the PO front. At the accumulator-like end, the housing inner length, l_i, encroaches upon its upper bound of 1.5 m. In theory, then, if vehicle packaging constraints were lifted, drive cycle losses could continue to be reduced below the best values observed in the optimization results.

In contrast, none of the design parameters (other than the seal clearance and liner fraction, as mentioned previously) are encroached upon for the flywheel-like solutions. This indicates that physical phenomena are acting to limit the expanse of the PO front. To further decrease the mass of the solutions at the high energy density end (i.e. to push solutions to be even more like flywheels), the optimization trends would suggest that r_i, r_o, l_h and d_i should continue to be reduced as ω_{max} is increased. Doing so, however, decreases the pneumatic energy and power capacities to unacceptably small values.

Recall that the pump-sizing scheme used in the optimization (Eqn. 168) dictates that all possible solutions have roughly the same mechanical power capacity. During the most intense vehicle accelerations of the UDDS, it is critical that the pneumatic domain assist in meeting the power demand. A solution with a very small axle port diameter may fail in such a region of intense acceleration, as small values of d_i exacerbate pressure drop across the axle, thereby limiting the amount of power that can be supplied by the pneumatic domain. Alternatively, a solution with a miniscule pneumatic domain may fail

because the small amount of stored pneumatic energy has been fully depleted before the end of an intense acceleration event.

The preceding arguments explain that there is some lower limit on the power that can be supplied using the pneumatic domain. Rather than any design variable bounds artificially imposed on the optimization, this is the basic physical limitation that terminates the PO front at the flywheel-like end. To a certain extent, this lower limit can be reduced (allowing for even faster-spinning solutions with smaller pneumatic domains and smaller axle port diameters) by using a pump-sizing algorithm that tends to select larger storage PM displacements. In practice, however, this only serves to delay the onset of failure. As discussed previously, several major energy loss mechanisms increase rapidly with ω_{max}. The practical result of this is that the stored kinetic energy – and therefore the angular velocity – drops to very low values before the drive cycle is complete. The mechanical power capacity is severely reduced from its original value, requiring a large portion of tractive power demand to be met by the pneumatic domain. Using a larger storage PM, therefore, only increases the mechanical power capacity when the HFA is operating at high speeds; the strategy backfires at low SOC.

7.4 Laboratory-Scale Optimization Results

From a high-level view, the goal of the present research is to prove the HFA concept. In future work, this will be done by constructing a prototype that can be tested in a laboratory setting. To reduce the cost and complexity of manufacturing the HFA, and to accommodate limits imposed by the laboratory capabilities, the HFA energy and power capacities must be scaled down for the laboratory prototype.

It is convenient to define two scaling constants, the mass factor, f_m, and the frontal area factor, f_{af}, as

$$f_m = \frac{m_{v,scaled}}{m_v} \tag{220}$$

$$f_{af} = \frac{A_{f,scaled}}{A_f} \tag{221}$$

where the values in the denominators are the vehicle parameters selected to represent a real sedan (given in Table 16). Examination of the road load calculations presented in Section 6.1 suggests that the drive cycle power should scale roughly with vehicle mass, m_v, and the energy required to complete the drive cycle should scale roughly with the frontal area of the vehicle, A_f.

In simulating a drive cycle, the laboratory hydraulic power supply must motor the prototype when vehicle deceleration is sufficiently strong to make the tractive power, $\dot{W}$, positive (power into the HFA). The peak acceleration power during the UDDS is of little interest, as it is assumed that the hydraulic power supply can absorb far more power than it can produce. The mass factor and frontal area factor must be selected to limit the peak UDDS braking power, $\dot{W}_t|_{max}$, to values below 6.5 kW, which is the capacity of the hydraulic power supply that will be used to test the prototype. The plot on the left of Fig. 66 shows values of peak UDDS braking power for a range of f_m-f_{af} combinations that satisfy this constraint. For this range of acceptable scaling factor combinations, the plot on the right shows the minimum possible drive cycle energy, W_{dc}. In both plots, the uncolored regions represent f_m-f_{af} combinations that produce unacceptably large values of peak power.

A particular pair of mass factor and frontal area factor values must be selected from the acceptable (colored) area in the f_m-f_{af} plane. Establishing the goal of having a safety factor of 3 on the rated power of the hydraulic power supply, candidate pairs can be narrowed down to the teal region of the left plot, where $\dot{W}_t|_{max} \cong 3$. To further narrow down this region to a single pair of mass and frontal area factors, a desired energy capacity must be specified. Note that the drive cycle energies in the right plot of Fig. 66 are "ideal," calculated under the assumption that the HFA is lossless. Nonetheless, as the HFA designs tend to have fairly high efficiency, the scale above will be taken as approximately true. One ongoing research project at the University of Minnesota involves a small hydraulic hybrid vehicle [75]. The hydraulic energy storage capacity of this vehicle is on the order of 100 kJ. Increasing this capacity by an order of magnitude will serve as the approximate energy capacity goal for the laboratory-scale prototype.

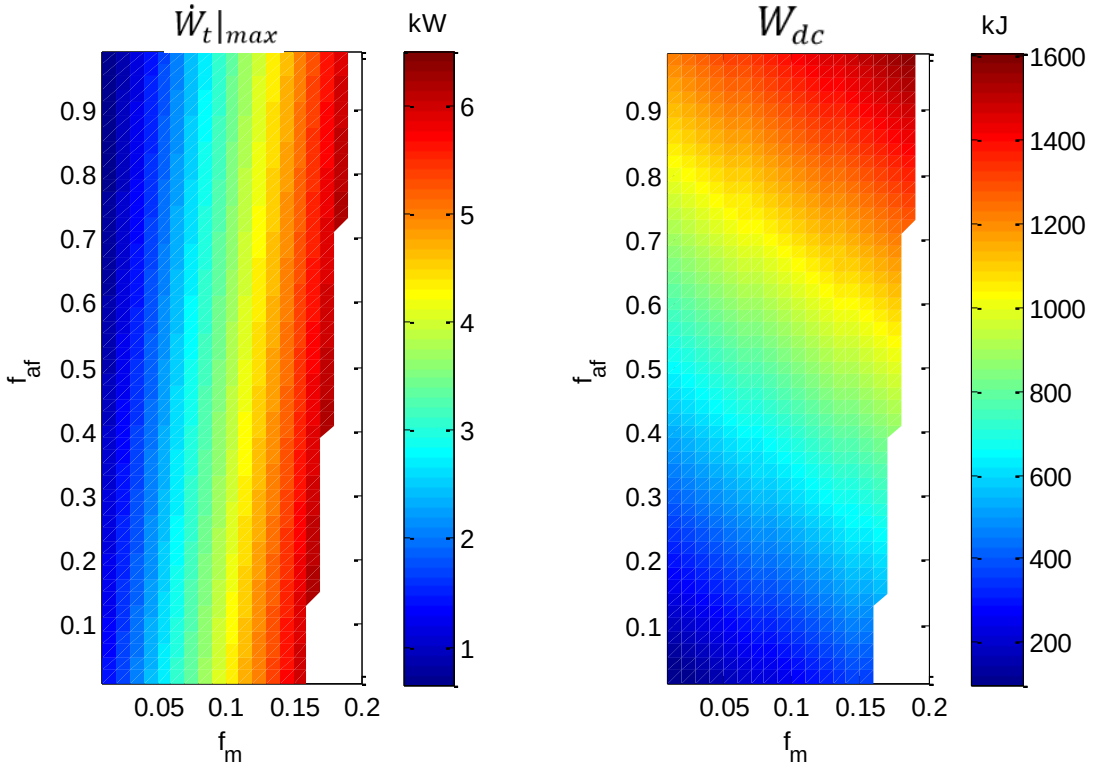

Figure 66: Peak Braking Power and Drive Cycle Energy for the UDDS as Functions of Mass Factor and Frontal Area Factor

Transposing the target peak power region from the left plot onto the right plot and finding the point that yields an energy capacity of 1000 kJ, the mass factor is chosen to be 0.04 and frontal area factor are chosen to be 0.08. It should be mentioned that drive cycle energy and power are functions of the overall vehicle mass, which includes the mass of the onboard energy storage system. To produce the plots in Fig. 66, the HFA system mass was set to 60 kg, and the processes by which the mass and frontal area factors have been selected is understood to be approximate.

To reflect spatial constraints in the laboratory, the upper bounds for the present optimization are selected to be 25 cm for the outer radius and 50 cm for the housing inner length. Given these upper bounds, the acceptable packaging volume for the laboratory prototype is about twelve times less than that for the vehicle-scale energy storage system. The remaining design variable bounds are unchanged, and can be found in Table 21.

Many of the qualitative trends discussed in the vehicle-scale optimization results are also observed at the laboratory-scale. The presentation of the laboratory-scale results, therefore, will follow a similar form. To avoid redundancy, the discussion will focus on the few differences.

As the most general results of the laboratory-scale optimization, Fig. 67 shows the PO front, and Fig. 68 plots the drive cycle efficiency as a function of energy density. It is important to remember that the solutions are inverted between these two plots, with the most flywheel-like at the upper-left end of Fig. 67 and the lower-right end of Fig. 68. The solutions at the extreme ends of these plots are summarized in Table 23.

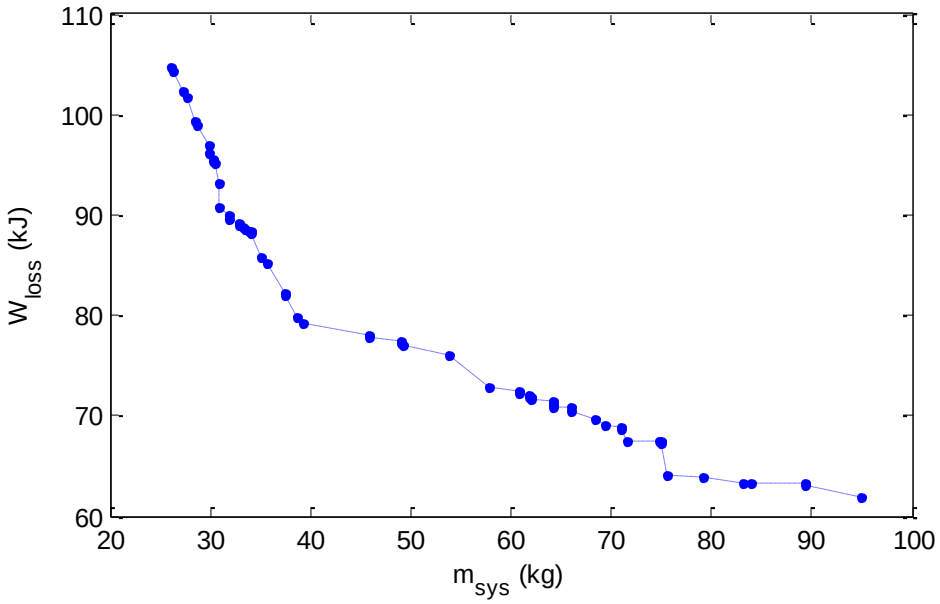

Figure 67: Pareto-optimal Front for the Laboratory-scale Design Optimization

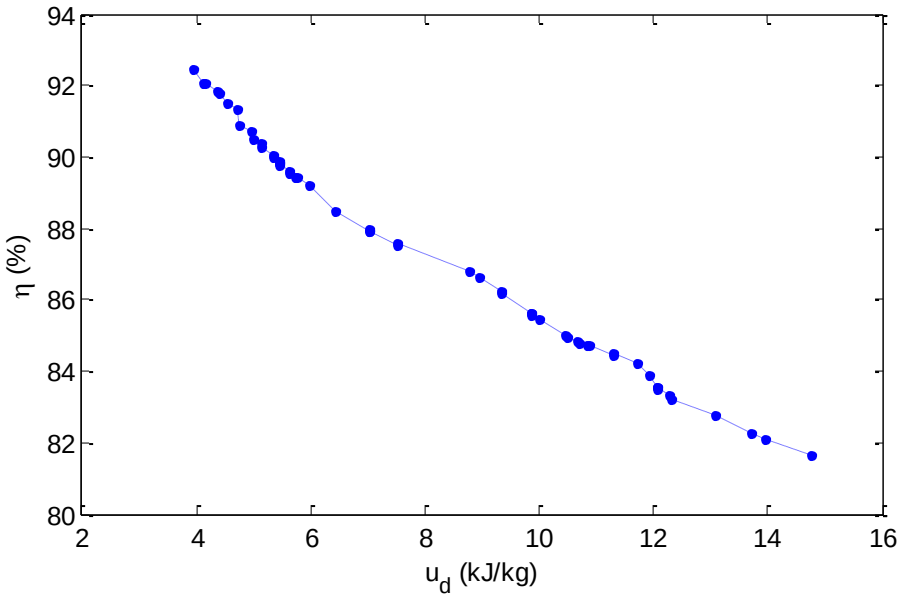

Figure 68: Drive Cycle Efficiency vs. Energy Density for the Laboratory-scale Pareto-optimal Set

Table 23: Summary of the Extreme Pareto-optimal Solutions from the Laboratory-Scale Optimization

	system mass (kg)	losses (kJ)	energy density (kJ/kg)	efficiency (%)
most accumulator-like	95.0	62.0	3.94	92.5
most flywheel-like	26.1	104.7	14.8	81.6

The trends in the design parameters for the laboratory-scale optimization are shown in Fig. 69. These trends are very similar to those observed at the vehicle scale. The progression from flywheel- to accumulator-like solutions occurs via the same "strategy" of lowering losses by decreasing ω_{max} while maintaining sufficient energy capacity (both kinetic and pneumatic) by increasing the geometric dimensions.

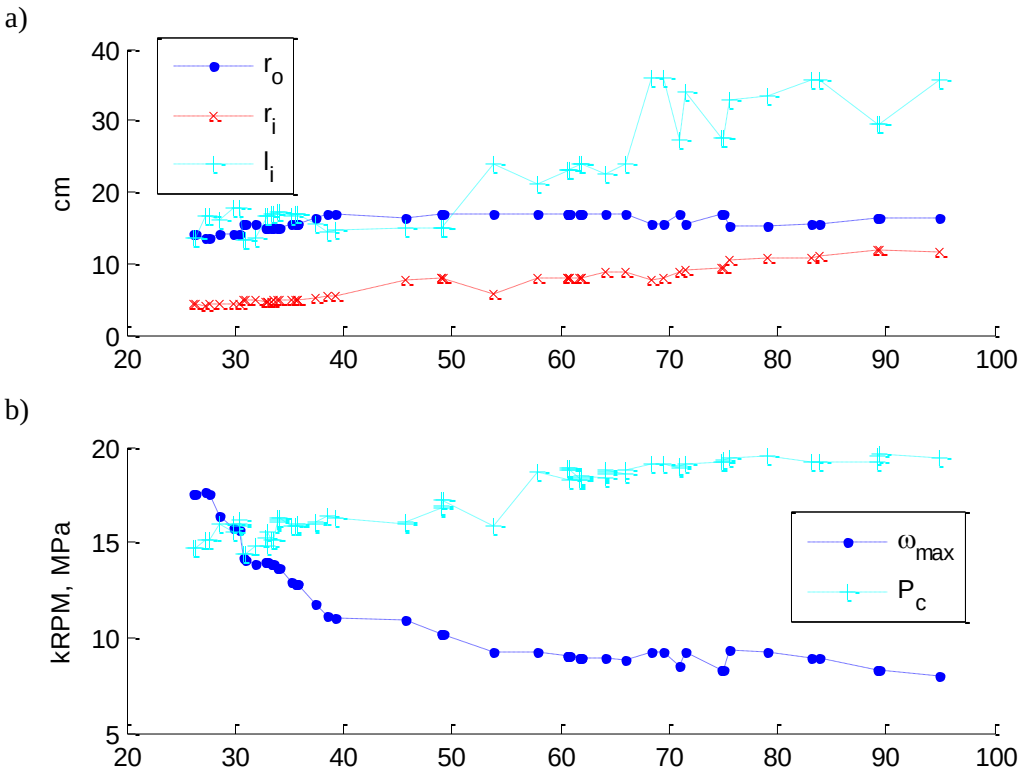

Figure 69: Design Trends as Functions of System Mass for the Laboratory-Scale Pareto-optimal Set

Energy capacity by domain, along with the corresponding capacity ratio, is plotted in Fig. 70. Notice that the capacity ratios exhibited by the laboratory-scale PO solutions are very close to those at the vehicle scale; the same is true for the usage ratios.

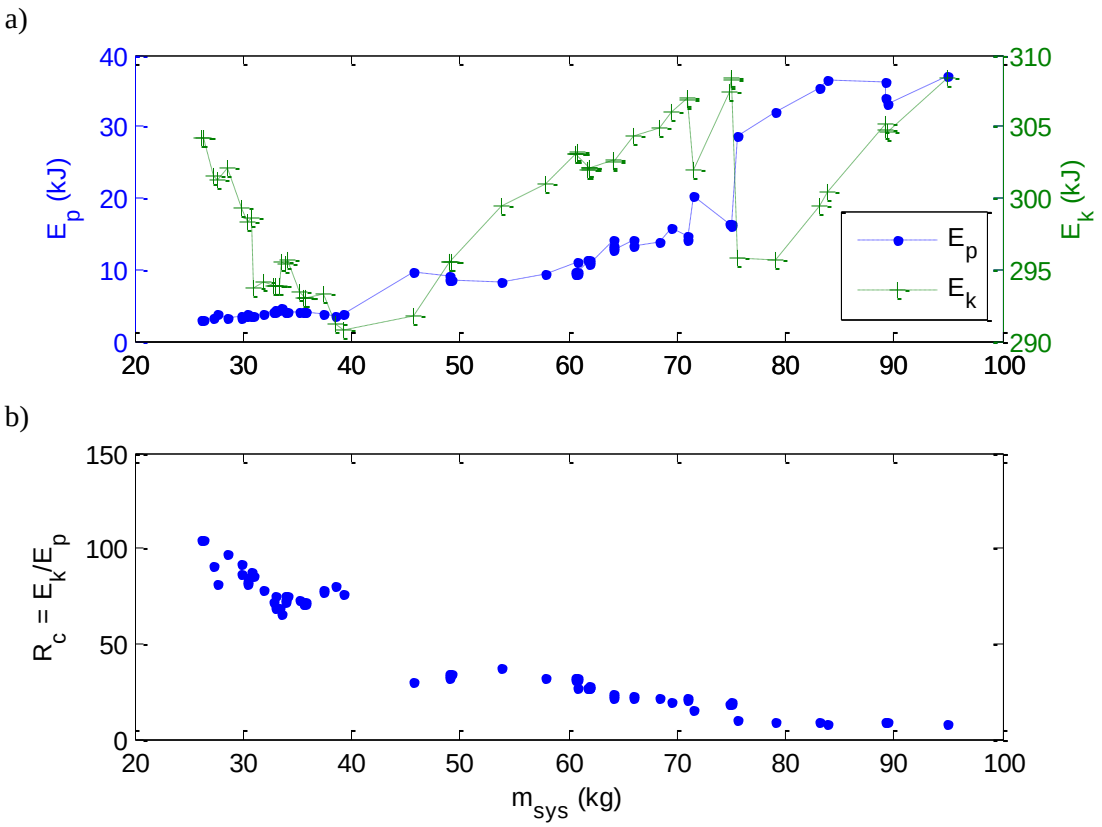

Figure 70: Energy Capacity by Domain, and Corresponding Capacity Ratio, for the Laboratory-scale Pareto-optimal Set

At the laboratory scale, most of the energy loss mechanisms scale down with the reduced tractive power. Lower tractive power leads to lower flow rates, so smaller axle port diameters can be implemented while axle port losses actually decrease. These smaller values of d_i reduce viscous and leakage losses at the HSRU. Lower values of tractive power at the laboratory scale also lead to lower mechanical power demand and therefore fewer storage PM losses. The reduced energy demand allows for smaller and lighter HFA designs, which reduces internal viscous dissipation and bearing losses. As a result of these scaling phenomena, most of the losses by proportion of W_{loss} are very similar at both scales. Leakage, axle port, and HSRU viscous losses make up between 1% and 5% each, and bearing and internal viscous losses between 1% and 2%.

In fact, the only mechanism that does not scale down in proportion to tractive power is aerodynamic loss. This is due primarily to the fact that the upper bound on ω_{max} is the

same for both scales (and fully-utilized at the laboratory scale). While the geometric dimensions are somewhat smaller at the laboratory scale, the difference is not large enough to reduce aerodynamic drag in proportion to tractive power (recall that the vehicle mass and frontal area have been scaled to 4% and 8%, respectively). As a result, when comparing the laboratory and vehicle scales, there is a tradeoff between storage PM and aerodynamic losses in their respective proportion of W_{loss}.

Aerodynamic losses make up 12% to 20% of W_{loss} at the laboratory scale, compared to 4% to 7% at the vehicle scale. Conversely, the storage PM losses make up between 60% and 75% of drive cycle losses at the laboratory scale, compared to 80% to 90% for the vehicle-scale PO solutions. Because storage PM losses are the dominant mechanism at either scale, however, there is somewhat less opportunity to decrease W_{loss} at the laboratory scale by improving reducing ω_{max} and R_u. This explains why the most accumulator-like solution at the laboratory scale has only 40% lower energy loss than the most flywheel-like solution, whereas the reduction was 71% at the vehicle scale.

When compared to the vehicle-scale results, one notable difference at the laboratory scale is that the upper bound on l_i is inactive, even for the accumulator-like solutions. This suggests that continuing to increase l_h and r_i will not lead to fewer drive cycle losses. Recall that the reason that this strategy might lower W_{loss} is by increasing the pneumatic energy storage capacity, thereby improving the usage ratio. The pneumatic energy capacity does, in fact, increase if l_h and r_i are increased slightly above their values for the most accumulator-like solution in the PO set. The longer housing does, of course, add some aerodynamic losses. However, the more important consequence is that, even if l_h and r_i are changed in a way that keeps the housing mass constant, the larger inner radius leads to larger forces acting on the end caps. The axle radius, r_a, must increase in order to withstand the greater forces. Because it is proportional to r_a^2 and l_h, axle mass increases rapidly. This phenomenon can be observed in Fig. 71, which shows the component masses of the laboratory-scale PO set as functions of m_{sys}.

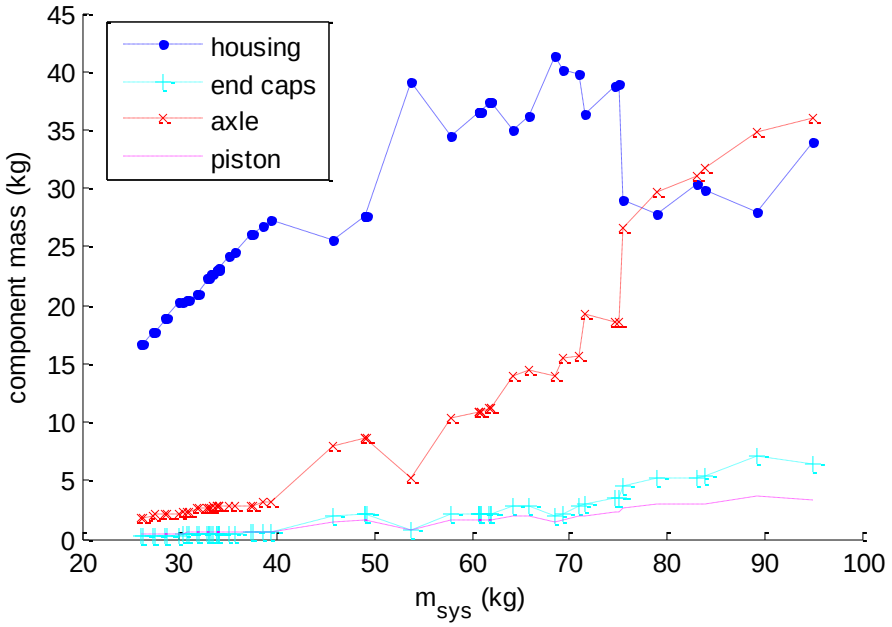

Figure 71: Mass Contribution of the Primary Components as Functions of System Mass for the Laboratory-scale Pareto-optimal Set

Notice that the penalty in axle mass increases as the solutions become more accumulator-like. This exacerbates bearing losses which, along with the larger aerodynamic losses that result from the longer housing, depletes the HFA before it completes the UDDS.

To address the aforementioned issues, the increases in l_h and r_i could be accompanied by a decrease in ω_{max}. However, with the decrease in ω_{max} required to sufficiently-offset the aerodynamic and pressure force penalties of larger l_h and r_i, the kinetic energy storage is reduced to such an extent that, again, the HFA is depleted before completion of the drive cycle.

The preceding discussion pointed out an interesting difference between the vehicle- and laboratory-scale PO solution sets – the former is limited at the accumulator-like extreme by the upper bound on housing length, while the latter is limited by physical phenomena. As it happens, the opposite is true at the flywheel-like extreme. While lower limits on pneumatic energy and power capacity prevented any lower-mass solutions in the vehicle-scale PO set, the laboratory-scale results are limited simply by the upper bound ω_{max}. When ω_{max} is allowed to exceed 1885 rad/s, it is easy to find solutions that satisfy the

optimization constraints and have a lower mass than the most flywheel-like solution from the PO set. This is also one of the reasons that the highest observed energy density in the laboratory-scale PO set is 14.8 kJ/kg, while the highest at the vehicle scale is 31.6 kJ/kg. Eventually, of course, the same limit as encountered at the vehicle scale becomes active as ω_{max} is increased above 1885 rad/s. It just so happens that this limit falls outside the design variable bounds chosen for the laboratory-scale optimization.

For completeness, the range of storage PM displacements associated with the laboratory-scale optimization results is plotted in Fig. 72.

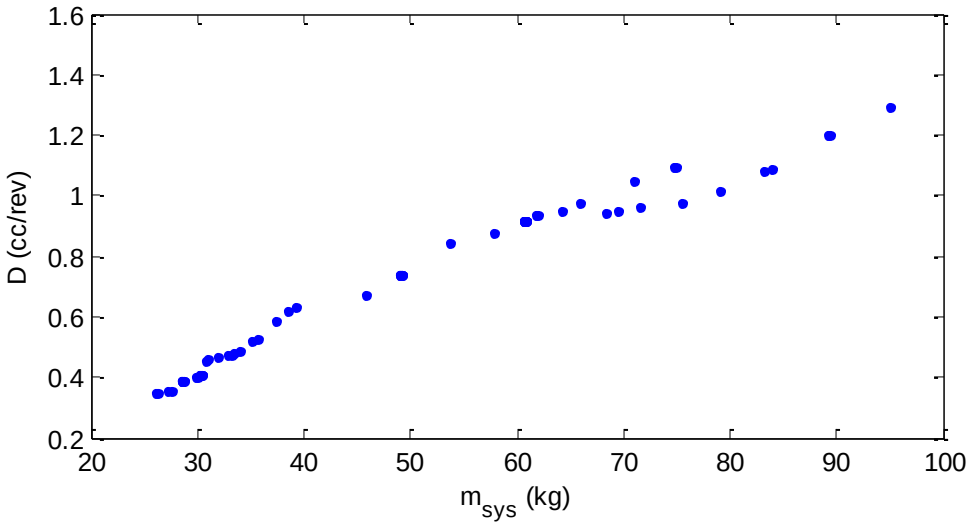

Figure 72: Storage PM Displacement vs. System Mass for the Laboratory-scale Pareto-optimal Set

7.5 Contextualizing the Optimization Results

Having discussed the performance capabilities of the optimized HFA designs, it is now important to provide context for these capabilities. In the general discussion of hydraulic energy storage in Chapter 1, state-of-the art static hydraulic accumulators were said to be capable of about 6 kJ/kg energy storage density. However, optimizing the energy storage density of a static accumulator using the exact tools developed in the present research can

provide a more direct assessment of how progressive the HFA concept actually is. Simply put, this can be done by using the energy capacity equations discussed in Chapter 2 and the stress models developed in Chapter 3, and letting ω go to zero. This effectively selects the proper dimensions of a static hydraulic accumulator with the same architecture as the HFA.

For a static accumulator, axle port losses can be alleviated by arbitrarily increasing d_i without a penalty in HSRU viscous or leakage losses. In fact, no rotational or leakage losses occur, so the efficiency of any possible static accumulator design solution should be roughly equal. Therefore, it is illogical to use drive cycle losses as an optimization objective, and the optimization can be performed without simulating a drive cycle.

As was done for the HFA, the static accumulator has been optimized at the laboratory- and vehicle-scale. Recall that the HFA optimizations used vehicle parameters and a drive cycle to effectively impose a lower bound on E_d. To simplify the present study, the lowest-observed design energy capacity of the corresponding HFA PO set is used as the lower bound on E_d for the static accumulator optimization. The spatial constraints are identical to those used in the HFA optimizations.

It is arguably "unfair" to force the static accumulator to comply with the architecture selected for the HFA, as this architecture may not actually be optimal for a static accumulator. To account for this, two sets of static accumulator optimization results are presented for each application scale. The first is a conservative result that uses a safety factor of 3 on all components – the same safety factor used in the HFA optimizations. The second uses a safety factor of 1 and excludes the mass of the axle from the calculation of energy density.

Note that the HFA optimizations used mass and energy loss as the optimization objectives. Posing the problem this way drives the masses and energy capacities of the PO solutions to their lowest possible values, and the resultant energy density is an incidental metric. For the static accumulator, on the other hand, energy density has been used as the actual optimization objective. Again, the intent in doing this is to compensate

for the fact that the selected HFA architecture may be suboptimal for a static accumulator.

As a final comment on imposing the HFA architecture on a static accumulator, it should be noted that this architecture is not necessarily optimal for the HFA itself. Many of the design decisions in the present research have been made to facilitate model-driven design in the absence of extensive experimental resources, as well as simple and inexpensive manufacture and assembly.

The results of the energy density comparison study are summarized in Table 24, where the "HFA improvement factor" is the ratio of the highest energy density achieved by an HFA solution in the PO set to the optimal static accumulator energy density.

Table 24: Results of the Energy Density Comparison Study

Vehicle Scale Max. length: 1.5 m Max. diameter: 1.0 m Min. energy capacity: 1700 W-h			
SF	**Axle mass**	**Max. energy density (kJ/kg)**	**HFA improvement factor**
3	included	1.2	**26**
1	excluded	5.1	**6**
Laboratory Scale Max. length: 0.5 m Max. diameter: 0.5 m Min. energy capacity: 80 W-h			
SF	**Axle mass**	**Max. energy density (kJ/kg)**	**HFA improvement factor**
3	included	0.57	**26**
1	excluded	1.3	**11**

From the perspective of energy density (energy losses were not considered in this study), the HFA clearly offers a significant benefit over traditional means of hydraulic energy storage. This benefit is slightly more pronounced at the laboratory scale, where the static accumulator achieves an energy density of only 1.3 kJ/kg, even with the liberal

assumptions. To understand why the optimized static accumulator energy density is so much lower at the laboratory scale, consider a very simple model of a static piston-type accumulator that is constructed from a homogenous, isotropic thin-walled material. For now, the volumes and masses of the end caps and pistons are neglected; only the housing is considered, such that the charge volume is

$$V_c = \pi r_i^2 l_h \tag{222}$$

where r_i and l_h are the radius and length of the housing, respectively. Given the definition of the charge fraction, the energy storage capacity is

$$E_d = P_c V_c \ln\left(\frac{P_d}{P_c}\right) = P_d \pi r^2 l_h f_c \ln\left(\frac{1}{f_c}\right) \tag{223}$$

The maximum hoop stress, $\sigma_{h,max}$, which is the largest stress in the thin-walled pressure vessel assumption, occurs when the accumulator is operating at the design pressure, P_d, and is inversely proportional to the wall thickness, th.

$$\sigma_{h,max} = \frac{P_d r_i}{th} \tag{224}$$

To safely prevent material failure, the wall thickness must be

$$th = r_i(SF)\frac{P_d}{S_{y,h}} \tag{225}$$

where $S_{y,h}$ is the housing yield strength. The mass of the accumulator is equal to the housing mass,

$$m_h = \rho_h 2\pi r_i (th) l_h = \rho_h 2\pi l_h r_i^2 (SF)\frac{P_d}{S_{y,h}} \tag{226}$$

Inserting Eqns. 223 and 226 into Eqn. 213 (the definition of energy density) yields

$$u_d = \frac{1}{2\rho_h}\frac{S_{y,h}}{SF}\, f_c \ln\left(\frac{1}{f_c}\right) \tag{227}$$

As expected, Eqn. 227 indicates that the energy density of the housing-only static accumulator model is proportional to the housing material strength and inversely proportional to the density and the selected safety factor (It is also proportional to the quantity $f_c \ln(1/f_c)$, which yields a peak energy density at a charge fraction of 0.3679). Note that, for this simple static accumulator model, energy density is not a function of any geometric parameters, and therefore is independent of the energy capacity.

Now the end caps are included in the model and are assumed to be integrated in this static accumulator in a similar fashion as they are in the HFA. The axle is still neglected, and we assume that the end caps are implemented such that the charge volume is unaffected. Though the end cap bending stress model is rather complex, the end cap length required to prevent failure can be stated as

$$l_e = k_e SF \frac{P_d}{S_{y,e}} \tag{228}$$

where $S_{y,e}$ is the end cap material strength and k_e is a dimensionless constant that captures the circular plate bending mechanics for the given loading and support case. Each end cap therefore has a mass of

$$m_e = \rho_e \pi r_i^2 l_e = \rho_e \pi r_i^2 k_e SF \frac{P_d}{S_{y,e}} \tag{229}$$

and the total accumulator mass is

$$m = m_h + 2m_e = 2\pi (SF) P_d r_i^2 \left(\frac{\rho_h l_h}{S_{y,h}} + \frac{\rho_e k_e r_i}{S_{y,e}} \right) \tag{230}$$

Because the presence of the end caps does not change the stored energy, the energy density is now

$$u_d = \frac{l_h f_c \ln\left(\frac{1}{f_c}\right)}{2SF\left(\frac{\rho_h l_h}{S_{y,h}} + \frac{\rho_e k_e r_i}{S_{y,e}} \right)} = \frac{f_c \ln\left(\frac{1}{f_c}\right)}{2SF} \frac{1}{\frac{\rho_h}{S_{y,h}} + \frac{\rho_e k_e}{S_{y,e}} \left(\frac{r_i}{l_h}\right)} \tag{231}$$

As before, high strength-to-density ratios are favorable, and the optimal charge fraction remains unchanged. However, Eqn. 231 shows that, with the end caps included in the static accumulator model, solutions with higher aspect ratios, l_h/r_i, exhibit higher energy densities. If the sophistication of the static accumulator model can be further increased, approaching the actual architecture used in the energy density comparison study, the positive correlation between the aspect ratio and the energy density holds. This explains why the energy density of the optimized vehicle-scale static accumulator is so much larger than the optimized laboratory-scale accumulator. Driving towards the largest possible aspect ratio, the optimization converged upon solutions that fully-utilized the upper bound on housing length. Since the packaging constraints at the laboratory scale were more stringent, the energy density of these solutions suffered.

Interestingly, flywheels follow nearly the opposite trend. Consider the simplest possible flywheel model, where the rotor is a simple, hollow cylinder of mass m and inner and outer radii of r_i and r_o, respectively. The energy density is

$$u_d = \frac{\frac{1}{2} I \omega^2}{m} = \frac{\frac{1}{2} m (r_o^2 - r_i^2) \omega^2}{m} = \frac{1}{2} (r_o^2 - r_i^2) \omega^2 \tag{232}$$

Using this model, energy density tends to increase with the radial dimensions and is completely insensitive to the length of the rotor. An equivalent statement that takes into consideration the full HFA architecture is cumbersome to derive and analyze. However, it is easy to defend the general statement that kinetic energy storage increases with the fourth power of radial dimensions while mass increases with only the square of radial dimensions.

The preceding arguments explain the economies of scale observed when comparing the results of the vehicle- and laboratory-scale optimization results. It has been shown that pneumatic energy storage is more mass-efficient at higher aspect ratios. However, the fact that the capacity ratios of the HFA tend to be $O(10)$ suppresses this phenomenon, and the flywheel-related energy density trends are more relevant to the HFA. Larger radial dimensions tend to produce higher energy densities, and because the vehicle-scale solutions were required to store more energy, they tended to be physically larger – including their radial dimensions.

7.6 Selection of a Design Solution for the Laboratory Prototype

The previous section presented a range of optimal HFA solutions that conform to the specified laboratory constraints. To guide the selection of a particular HFA design solution for a laboratory prototype, several goals have been established. First, to prove the advantage of the HFA, the prototype should at least quadruple the energy storage density of traditional accumulator storage. For the laboratory-scale spatial constraints, the analysis above liberally estimated the maximum energy of a traditional accumulator to be 1.3 kJ/kg. The HFA prototype should there for be at least 5.2 kJ/kg, which narrows the field of candidate solutions to those with system masses below about 66 kg.

To facilitate easy handling the prototype and reduce material costs, an upper bound on the mass of the primary components, m, of 39 kg is imposed. This turns out to be more restrictive than the energy density requirement, limiting the candidates to those with system masses below about 46 kg. From a safety and reliability standpoint, a maximum angular velocity of 1,257 rad/s (12,000 RPM) is also imposed. Given these limits, the field of candidate solutions for the prototype has been narrowed to those with system masses between 37 and 46 kg (corresponding to a range of energy densities from about 7.5 to 9.3 kJ/kg).

Although the prototype is not intended for vehicle implementation, the HFA research as a whole is based upon the goal of improving energy storage for mobile hydraulics. To make a final selection from the narrowed field of candidate solutions for the prototype, then, it is prudent to return to vehicle-oriented considerations. Recall from Section 2.6 that, as the mass of and energy losses incurred by a vehicle energy storage system increase, so does the energy required to complete a drive cycle, W_{dc}. In the present methods of simulation and optimization, each solution has been allowed to begin the drive cycle at full SOC (i.e. at its design energy capacity, E_d). The interaction between the mass-minimization objective and the constraint on unfinished distance results in each PO solution being fully-depleted by the end of the drive cycle, having stored just enough energy to complete it. Therefore, $W_{dc} \cong E_d$ for the purposes of the present discussion.

It is important to understand that, due to the range of HFA masses and losses, there is significant variation in the drive cycle energy, and therefore the design energy capacity, of the solutions in the PO set. In selecting a particular solution from the PO set for a final design, E_d is arguably the most important metric. This is the amount of energy that must be "paid for," in the cost of energy and in GHG emissions. Figure 73 shows the design energy capacities and system masses of the laboratory-scale PO set, plotted against energy density. Solutions between the dotted vertical lines are the candidates for the laboratory prototype.

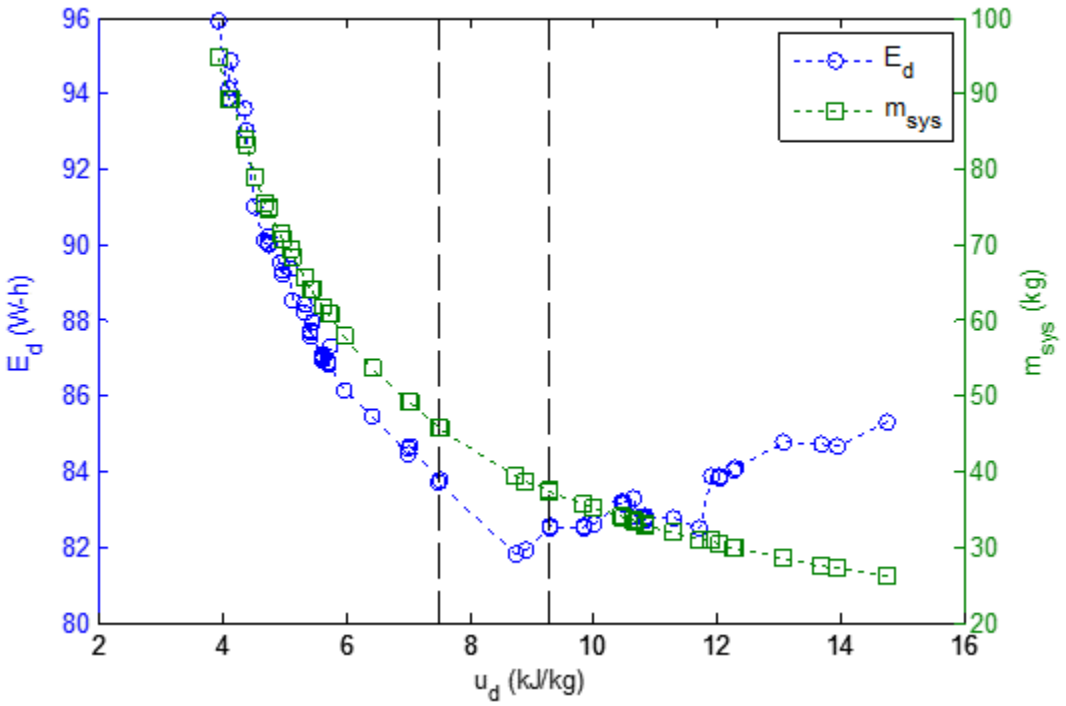

Figure 73: Energy Capacity and System Mass vs. Energy Density for the Laboratory-scale Pareto-optimal Set

Figure 73 illustrates an extremely important trend in the PO results. Beginning with the most accumulator-like solutions (the far-left of this plot), increasing energy density of the HFA allows the design energy capacity to decrease. This is primarily due to the fact that a vehicle with a lower-mass energy storage system incurs less rolling resistance (see Eqn. 161). However, at a certain point (near 9 kJ/kg for the laboratory-scale PO set), increases in energy density cease to pay off, at least from the perspective of E_d. The higher

operating speeds required by the most energy-dense solutions lead to large drive cycle losses. To compensate, these solutions must actually have a higher energy capacity, even though the road loads continue to decrease with mass. In light of this phenomenon, the logical choice for the laboratory prototype is the solution at the minimum of the E_d curve shown in Fig. 73.

There are, of course, metrics other than E_d that should be considered in selecting an HFA design solution from a PO set (Indeed, if the design energy capacity were the only important consideration, it would have been more appropriate to pose the optimization as single-objective, with the aim of minimizing E_d). For example, Section 2.6 pointed out that lower-mass solutions tend to provide better vehicle handling, have a smaller packaging volume, and be less expensive to manufacture. Nonetheless, the solution that requires the lowest energy capacity to complete the UDDS is selected as the laboratory prototype design. Tables 25 and 26 summarize various design characteristics of this solution, and Fig. 74 provides an illustration of it.

Table 25: Design Variable Values for the Selected Laboratory Prototype Design

Housing inner radius, r_i	5.36 cm
Housing outer radius, r_o	17.0 cm
Housing length, l_h	20.8 cm
Housing liner thickness, th_l	0.2 mm
Axle port diameter, d_i	5.40 mm
HSRU seal clearance, c_s	10.2 μm
HSRU seal length, l_s	8.17 mm
Maximum angular velocity, ω_{max}	1154 rad/s
Charge pressure, P_c	16.4 MPa

Table 26: Non-design Variables of Interest for the Selected Laboratory Prototype Design

End cap thickness, th_e	3.05 cm
Retainer length, l_r	6.61 mm
Axle radius, r_a	2.39 cm
Piston bearing length, l_p	7.18 cm
Piston disc thickness, th_p	2.08 cm

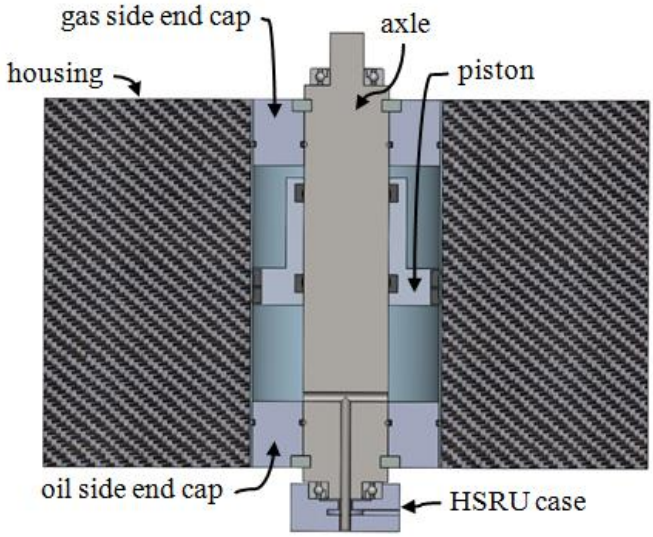

Figure 74: Cutaway View Illustrating the Design Characteristics of the Solution Selected for the Laboratory Prototype

Notice that the optimization has driven the liner thickness of the selected design to a value of 0.2 mm. For the sake of practicality, this dimension is changed to 1 mm. The algorithm detailed in Section 7.1 has selected bearings with an inner and outer diameter of 9 mm and 26 mm, respectively. Assuming an average operating speed of 577 rad/s (half of ω_{max}), these bearings should provide a cycle life of 24 hours with a reliability factor of 95%. Various plots of the projected dynamic drive cycle performance are provided in Appendix D.

The static performance metrics for the prototype are provided in Table 27, and the projected drive cycle performance is summarized in Table 28.

Table 27: Static Performance Metrics for the Selected Laboratory Prototype Design

System mass, m_{sys}	39.3 kg
Energy density, u_d	8.77 kJ/kg
Energy capacity, E_d	81.8 kW-h
Mass, excluding PMs	32.3 kg
Capacity ratio, R_c	76.3
Housing safety factor	7.35
Storage PM displacement, D	0.63 cc/rev
Packaging volume (approx.)	48.6 liters

Table 28: Drive Cycle (UDDS) Performance Metrics for the Selected Laboratory Prototype Design

Drive cycle losses, W_{loss}	79.2 kJ
Drive cycle efficiency, η	86.8 %
Usage ratio, R_u	1.97
Pressure fraction, $f_{pressure}$	48.0 % (+26.8 % / -21.2 %)

8 Detailed Design

The design optimization presented in Chapter 7 used simple stress models and neglected various detailed design considerations. Having selected a design solution for the HFA laboratory prototype from the optimization results, these considerations must now be addressed. This chapter begins with a detailed specification and validation of the torque transmission mechanisms. In the following sections, the minor design features of the end caps, piston, housing and axle are addressed. The analytical stress models for each of these components are confirmed using FEA. Next, the detailed design of the HSRU case is presented. The chapter ends with a study on the relative radial strains of the rotating components.

8.1 Torque Transmission Mechanisms

Chapter 3 introduced the retainer system and the pin system, depicted in Fig. 75, which facilitate the transmission of torque between the storage PM and the various rotating components.

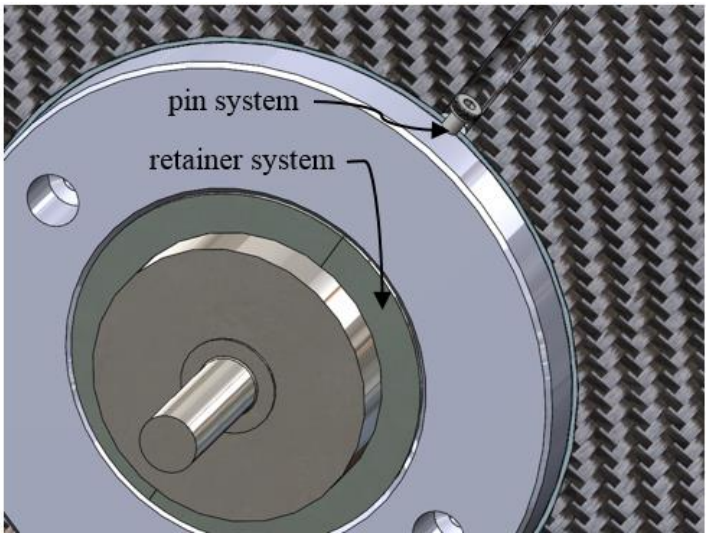

Figure 75: Illustration of the Pin System and Retainer System Used for Torque Transmission (Liner and Wrap Shown in Cutaway View)

As briefly described in Section 3.1, the pin system transmits torque between the gas side end cap and the housing. This system is made up of N_{ss} shoulder screws that, for balancing purposes, are spaced at increments of $360°/N_{ss}$. The screws must be sized such that the housing weight, torque transmission, and centrifugation do not cause them to fail. Each shoulder screw is assumed to carry an equal amount of load, and the minimum load-carrying radius, r_{ss}, is assumed to be half of the nominal thread diameter. The shear forces acting on a shoulder screw due to the housing weight and torque transmission are normal to one another, such that the resultant total shear force and maximum shear stress, respectively, are

$$F_{V,ss} = \frac{1}{N_{ss}} \sqrt{(m_h g)^2 + \left(\frac{T}{r_i}\right)^2} \tag{233}$$

$$\tau_{V,ss} = \frac{4}{3} \frac{F_{V,ss}}{\pi r_{ss}^2} \tag{234}$$

where $m_h g$ is the weight of the housing, T is the storage PM torque, and r_i is the inner radius of the housing. The leading factor in Eqn. 234 is the result of the parabolic stress distribution that arises when solid round section is loaded in shear [28]. Note that using storage PM torque is conservative, as only a portion of this torque is actually transmitted through the interface in question; the rest contributes to accelerating or decelerating components other than the housing.

The amount of normal stress in a shoulder screw due to centrifugation is a function of its own length, l_{ss}, and density, ρ_{ss}, amongst other parameters. Neglecting the fact that the head has a larger diameter than the shoulder, the maximum normal stress is [25]

$$\sigma_{N,ss} = \frac{1}{2} \rho_{ss} \omega^2 (l_{ss}^2 + 2 l_{ss} r_i) \tag{235}$$

Using the von Mises criterion and letting the pin stress reach its maximum allowable value yields

$$\left(\frac{S_{y,ss}}{SF}\right)^2 = \left[\frac{1}{2}\rho_{ss}\omega_{max}^2(l_{ss}^2 + 2l_{ss}r_i)\right]^2 + \frac{16}{3\pi^2 r_{ss}^4 N_{ss}^2}\left[(m_h g)^2 + \left(\frac{T_{max}}{r_i}\right)^2\right] \quad (236)$$

where it has been conservatively assumed that maximum angular velocity, ω_{max}, and maximum expected torque, T_{max}, may occur simultaneously.

Selecting the specific hardware can be iterative, as the dimensions of the shoulder screws influence the stresses to which they are exposed. It is, however, acceptable to make rough and conservative approximations here, as the stresses in the shoulder screws tend to be very small. For the purposes of selecting a shoulder screw with a sufficiently large minimum radius, its overall length, l_{ss}, is approximated to be 1 cm. The material is selected to be alloy steel, conservatively estimated to have a yield strength, $S_{y,ss}$, of 600 MPa and density, ρ_{ss}, of 7850 kg/m^3 [45]).

Equation 236 can be rearranged to form an expression for the minimum acceptable radius, r_{ss}, as a function of the number of shoulder screws, N_{ss}. Figure 76 shows a plot of the corresponding nominal thread diameter.

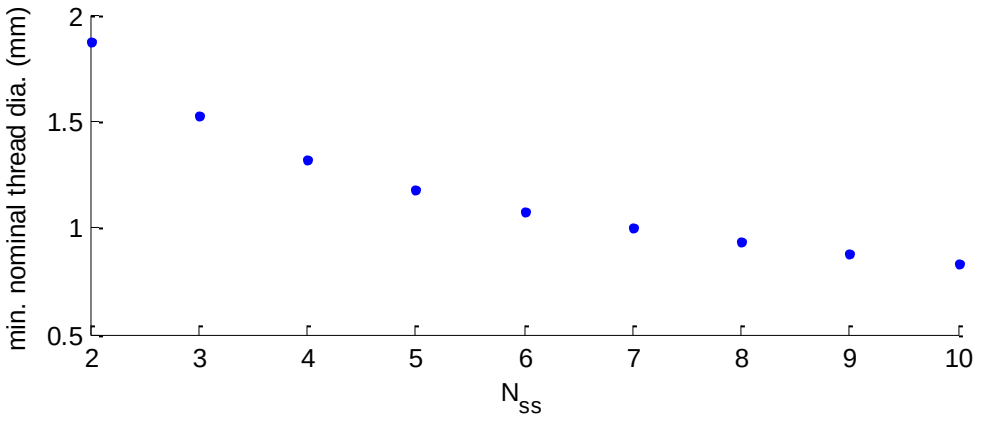

Figure 76: Minimum Allowable Nominal Screw Diameter as a Function of the Number of Shoulder Screws Used in the Pin System

Given the data in Fig. 76, it is appropriate to use two M2 x 0.4 shoulder screws. The full specifications for the shoulder screws selected for the laboratory prototype are given in Table 29.

Table 29: Selected Shoulder Screws for the Pin System

shoulder diameter	3 mm
shoulder length	4 mm
thread size	M2 x 0.4
threaded length	3.8 mm
head diameter	5 mm
number of screws	2
drive type	hex key

The radial holes cross-drilled through the wrap should provide a clearance fit for the 5 mm heads of the shoulder screws. The 4 mm long shoulder (the shortest available) is more than enough to account for the fact that the hole in the wrap cannot actually be drilled all the way down to the liner. A relatively long hex key wrench will be required to tighten the shoulder screws into the end cap.

Section 3.2 presented the methods used to select the dimensions of the retainer system such that the constituent components do not fail. Here, calculations will be shown that prove that the system has sufficient torque-carrying capacity. Each contact area of the retainer system is assumed to have a constant coefficient of friction, μ_c, and uniform contact pressure. Such an interface has a torque-carrying capacity of [28]

$$T = \frac{2}{3} F_{p,min} \mu_c \frac{r_{c,o}^3 - r_{c,i}^3}{r_{c,o}^2 - r_{c,i}^2} \tag{237}$$

where $F_{p,min}$ is the minimum expected force acting on the contact area, and $r_{c,o}$ and $r_{c,i}$ are the inner and outer radii of the contact area, respectively. The torque-carrying capacity of the retainer system is limited by the interface between the axle and retainer, where the radii and the friction coefficient are smaller than those at the end cap-retainer

interface. The normal force is a result of the pneumatic pressure, P_p, acting upon the end cap, such that the instantaneous torque-carrying capacity, T_{cap}, of the retainer system is

$$T_{cap} = \frac{2}{3} P_p \pi (r_i^2 - r_a^2) \mu_{st-st} \frac{r_a^3 - r_{r,i}^3}{r_a^2 - r_{r,i}^2} \tag{238}$$

where $\mu_{st-st} = 0.5$ is a conservative estimate for the friction coefficient at a steel-to-steel interface [46]. Equation 238 can be used after a drive cycle simulation to confirm that T_{cap} is greater than the magnitude of the storage PM torque at all times during a performance simulation.

In the unlikely event that pressure in the HFA is lost completely or that exposure to oil severely reduces the friction coefficient, the torque-carrying capacity of the retainer system may be drastically reduced. In this situation, the HFA should be considered in a state of failure, and the storage PM should apply a moderate braking torque to bring the system to rest. A key system, as shown in Fig. 91, can be implemented to transmit this braking torque from the axle to the gas side end cap. To facilitate HFA assembly, the end cap keyway is cut axially inward a distance of l_k from the outer face of the end cap. The keyway in the axle is cut inward the same distance from the inner face of the retainer groove.

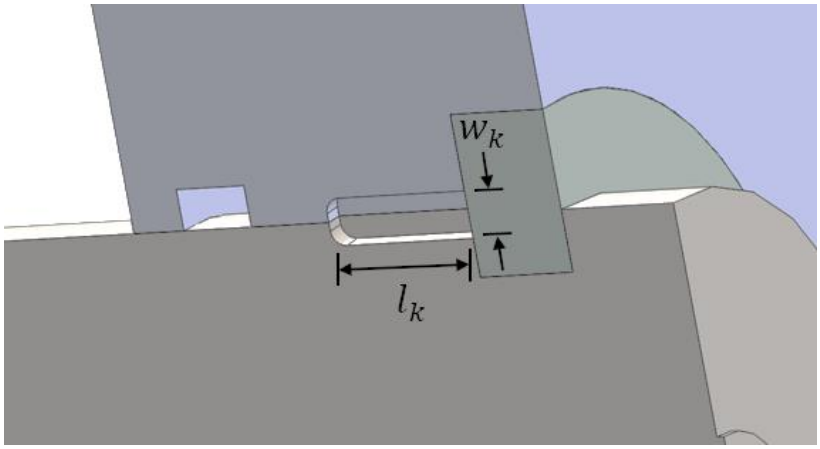

Figure 77: Illustration of the Key System (Key not Shown) that Transmits Torque in the Event of a Failure of the Retainer System

The key system must be able to carry the torque, T_{dec}, required to decelerate the rotating components from their maximum angular velocity to rest in a specified deceleration time, t_{dec}.

$$T_{dec} = \left(I_s + I_{o,max}\right)\frac{\omega_{max}}{t_{dec}} \tag{239}$$

Note the summed inertia term in Eqn. 239 is a conservative simplification; the key system only acts to decelerate the gas side end cap, the housing, and some effective fluid inertia. The shear area and key length required to prevent failure of the key are, respectively,

$$A_k = \frac{T_{dec}}{r_a}\frac{SF}{S_{s,k}} \tag{240}$$

$$l_k = \frac{A_k}{w_k} \tag{241}$$

where w_k is the width of the key. The key stock selected for the prototype is made of alloy steel and has a square cross section with 1/8" (3.2 mm) sides. The shear strength of the key is conservatively estimated to be

$$S_{s,k} = 0.58(400\ MPa) = 232\ MPa \tag{242}$$

Using a deceleration time, t_{dec}, of ten seconds, the key must be 8.6 mm long. To reduce the stress concentration, the key is terminated with a filled of radius 1 mm. The keyway length is therefore selected to be 10 mm long, and its depth should be $w_k/2$.

8.2 End Caps

Various minor design features were previously omitted from the discussion of the end caps, as these features have essentially no impact on the trajectory of a design optimization. They are important, nonetheless, to the robust operation of the HFA. In the proceeding discussion, the term "periphery" refers the cylindrical (curved) surface at

the inner or outer radius of the end cap, and the term "face" refers to the flat surface that faces inwards toward the fluid or outward toward the vacuum chamber.

To contain the pressurized fluid, each end cap must seal with the axle at its inner periphery and with the liner at its outer periphery. These seals are created using O-rings that reside in glands along the inner and outer peripheries of the end caps. In addition to O-ring glands, the gas side end cap must accommodate a keyway at its inner periphery and a hole pattern for the pin system at its outer periphery. These minor design features drive decisions for the axial location of the glands on the gas side end cap. For simplicity, the location of the O-ring glands (as well as the gland dimensions) are chosen to be the identical on both end caps, even though the oil side end cap lacks many of the minor features of the gas side end cap.

The O-ring seals must be the axially innermost features (nearest to the fluid volumes), as the pin system holes and keyway would otherwise allow for leakage on the gas side. The SAE AS5857 [76] standard is used to select the proper O-rings and gland dimensions. Because it is a more complex part, considerations related to the gas side end cap will drive these decisions. Given the radii of the two sealing interfaces (r_a and r_i) and the design pressure for the prototype, it is appropriate to use O-rings with cross-sectional diameters of 3.43 mm (AS568 numbers 210 through 247 [76]). The gland width should be 4.83 mm for all of the O-ring seals. For the interface with the axle, the inner diameter of the gland should be 53.3 mm (2.8 mm depth into the inner periphery of the end cap), and for the interface with the housing, the inner diameter of the gland should be 102.1 mm (2.5 mm depth into the outer periphery of the end cap).

To mitigate stress concentrations near the keyway on the gas side end cap, the O-ring glands should be spaced roughly between the inner face of the end cap and the terminating fillet of the keyway. Specifically, the center of each gland is selected to be located a quarter of the distance from the inner face of the end cap to the retainer. Given the proper gland width and the keyway dimensions, this leaves 5.5 mm between the gland and the keyway on the gas side end cap.

It is important to validate the simple stress models presented in Section 3.3 that were used for the design optimization. This is accomplished by FEA stress analysis, carried out using the commercial software ANSYS©. Having specified all of its dimensions, the oil side end cap is validated first. The worst case loading occurs at ω_{max} and $P_{s,max}$. The stress distributions are examined for the three axial planes shown in Fig. 78– those coincident with the inner and outer faces, as well as the plane that is coincident with the contact area between the retainer and the end cap.

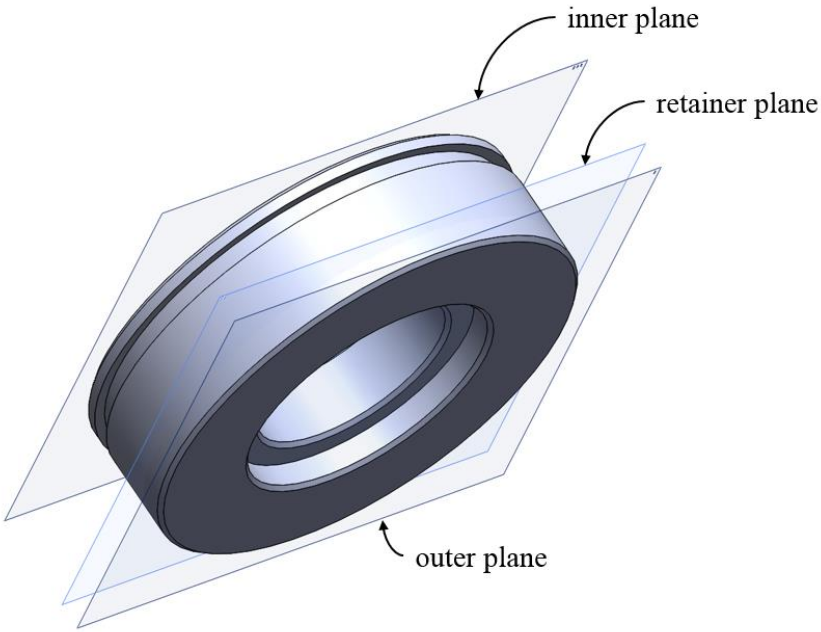

Figure 78: Illustration of the Oil Side End Cap Showing the Three Planes of Interest

Notice that, in an attempt to mitigate stress concentrations, 45° chamfers with 1 mm sides are added to several of the edges. The oil side end cap is axisymmetric, such that the radially-dependent stress distributions at each of these axial locations can be assessed at an arbitrary azimuth angle. Figures 79 through 81 compare the FEA (dotted data) and the analytical (continuous curves) results for the oil side end cap. The maximum allowable end cap stress ($S_{y,e}/SF$) is shown by the horizontal dashed line, and the vertical dotted line marks the radial location of the retainer outer radius, $r_{r,o}$. Recall that, according to the theory of plates, the bending stresses on either side of a simple and thin plate should be equal and opposite. This has been reflected in the figures below by changing the sign

of the analytical curves where appropriate (the retainer plane is nearer to and therefore should have similar qualitative distributions to the outer plane).

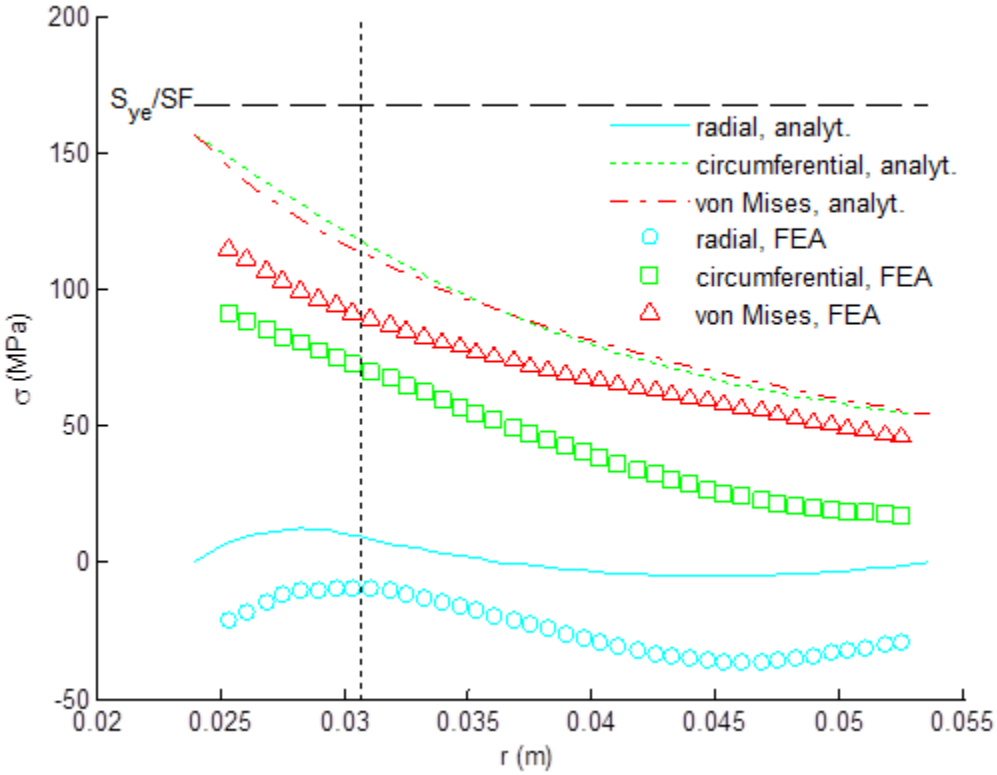

Figure 79: Oil Side End Cap Stress Distributions at the Inner Plane

In assessing the stress distributions at the inner plane shown in Fig. 79, notice that the FEA results have a negative offset. This is due to the compressive stresses that result from the oil pressure, an effect that is not taken into account in the analytical stress model. In fact, careful examination shows that the difference between the analytical and FEA results for the radial stress distribution, for example, closely resembles the parabolic oil pressure distribution, $P_o(r)$. The practical result of the compressive offset is to render the analytical model slightly conservative. In light of its use as a tool for design optimization, this is perfectly acceptable.

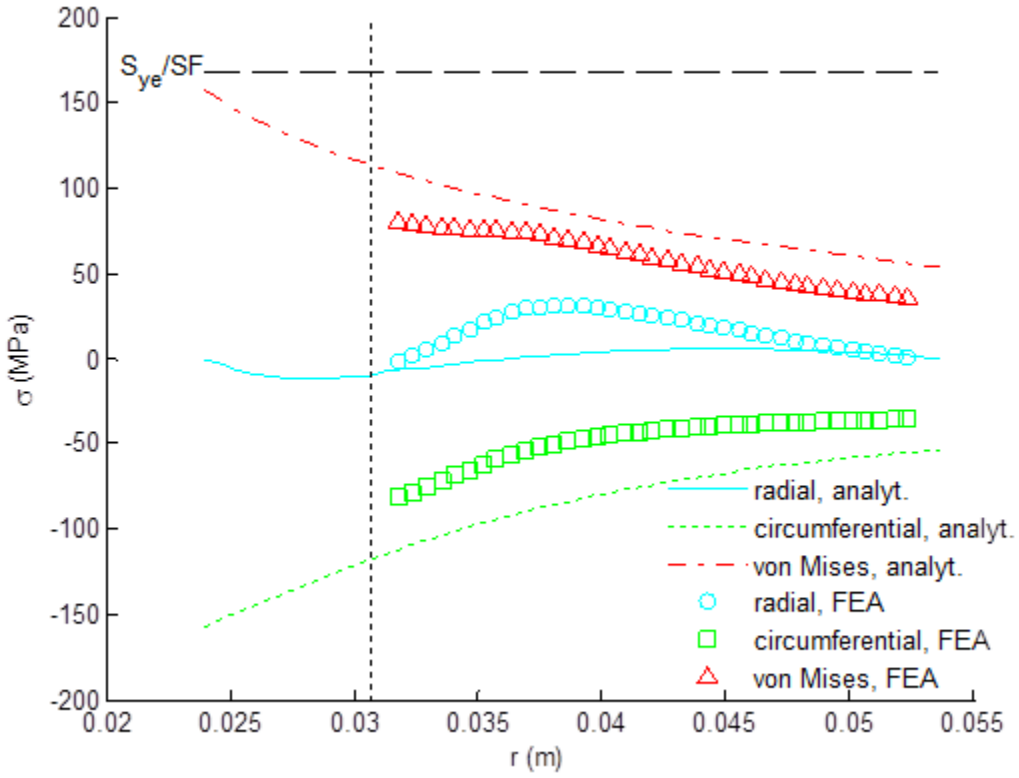

Figure 80: Oil Side End Cap Stress Distributions at the Outer Plane

The stress distributions at the outer plane (Fig. 80) do not exhibit a compressive offset, as this plane is located at the non-pressurized side of the end cap. However, as was the case for the inner plane, the analytical stress model is slightly conservative at the outer plane. Notice that the range of radial locations plotted for the FEA results is shorter, by virtue of the definition of the outer plane (see Fig. 78).

As expected, the distributions at the retainer plane shown in Fig. 81 more closely resemble those at the outer plane, with tangential stresses that are everywhere compressive. At radii greater than $r_{r,o}$, the retainer plane lies within the end cap rather than at an external face. As expected, stresses here are significantly reduced from the analytical model, which is only intended to predict stress at the inner and outer faces. This reduction is sufficient to keep stresses below the maximum allowable value, even near $r_{r,o}$, where the edge of the retainer pocket creates a stress concentration. The FEA

results confirm that the von Mises stresses should remain below $S_{y,e}/SF$ at all locations in the oil side end cap.

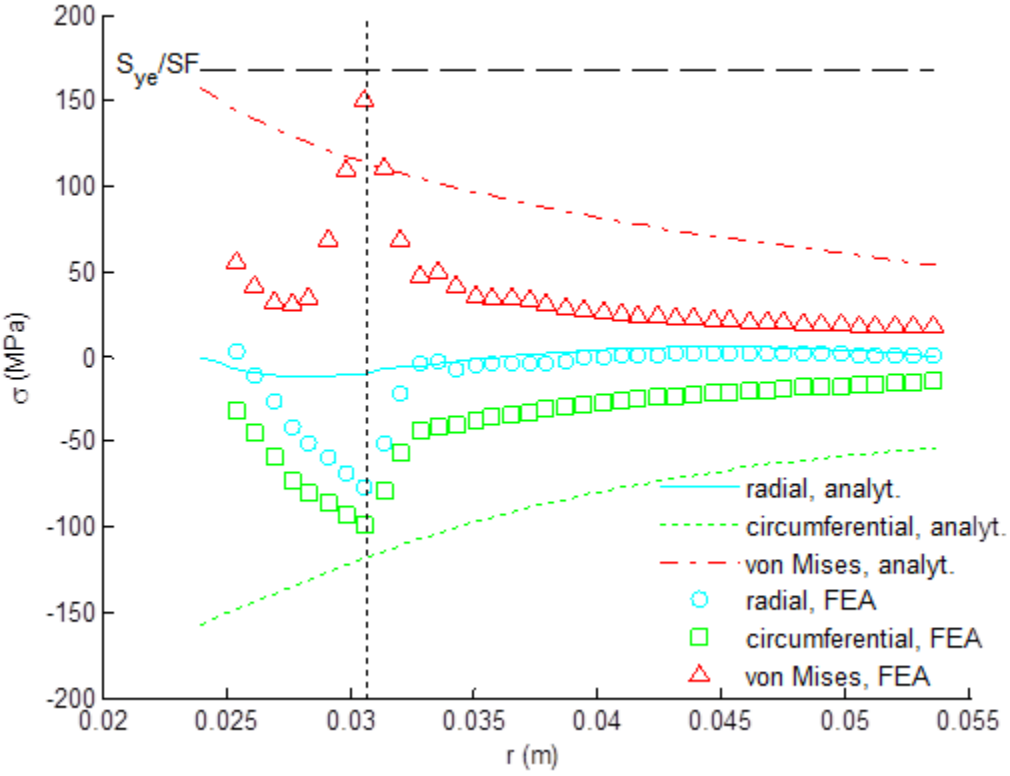

Figure 81: Oil Side End Cap Stress Distributions at the Retainer Plane

Before using FEA to validate the gas side end cap design, decisions relating to the various minor design features in the gas side end cap must be presented.

Per the pin system specifications in Table 29, the gas side end cap will have 2 radial holes spaced 180° apart with M2 x 0.4 threads. The depth of each hole is selected to be 4 mm, slightly greater than the threaded length of the shoulder screw, and a flat is machined onto the periphery of the end cap against which the axial face of the shoulder screw can be tightened. The axial location of the pin system hole pattern is 10.2 mm inward from the outer face of the gas side end cap. Because the threaded holes are so small, they should not significantly impact the stress distribution in the gas side end cap. For

simplicity, the outer O-ring gland is assigned the same axial location as the inner O-ring gland.

To facilitate charging of the HFA, the gas side end cap must have at least one axial through-hole ("charge port"). For optimal balancing, two ports are drilled 180° apart. A gas charging valve is threaded into each port from the outside of the end cap. The smallest commercially available charging valve known to the author has 1/8" NPT threads. The charge ports are threaded from the outer face a length of 1 cm, beyond which the holes reduce to 5 mm. To reduce stress concentrations, each charge port has a 2.5 mm fillet where it meets the inner face of the end cap.

As discussed in Section 3.3, the maximum bending stress in the end caps is at the inner radius, and it may therefore be advantageous to locate the charge ports at a relatively large radial position. Conversely, any imbalance introduced by slight asymmetry of the charge ports and valves is mitigated by locating them at smaller radii (this may also be advantageous from the perspective of reducing centrifugal stresses in the charging valves themselves, which will not have been designed for a rotating application). Somewhat arbitrarily, then, the radial position of the charge ports is chosen to be 11.5 mm, halfway between the retainer outer radius and the housing inner radius. The angular location is 90° offset from the holes for the pin system.

The keyway cut into the gas side end cap has identical dimensions to those discussed for the axle in Section 8.1. From the retainer plane, the keyway is cut inward 10 mm with a width and depth of 3.2 mm and 1.6 mm, respectively. A fillet with a 1 mm radius terminates the keyway. The angular location of the keyway is 45° offset from the gas charge ports (an angle halfway between the charge ports and the pin system holes).

The same three planes used in the oil side validation are also used in analyzing the FEA results for the gas side end cap. However, because the gas side end cap is non-axisymmetric, stress distributions along two different azimuth angles must be examined – one that coincides with the pin system holes and one that coincides with the gas charge ports. The gas side end cap, along with the azimuth angles and axial planes of interest, is shown in Fig. 82.

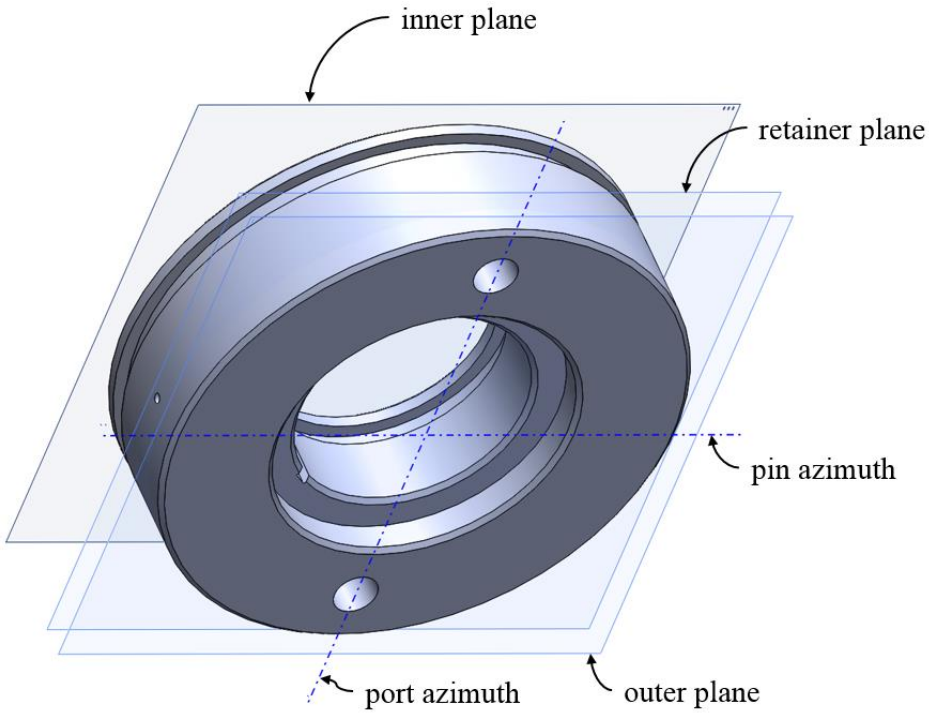

Figure 82: Illustration of the Gas Side End Cap Showing the Three Planes and Two Azimuth Angles of Interest

The stress distributions along the pin azimuth are shown in Figures 83 through 85. Again, the FEA results are shown as dots and the analytical results as continuous curves.

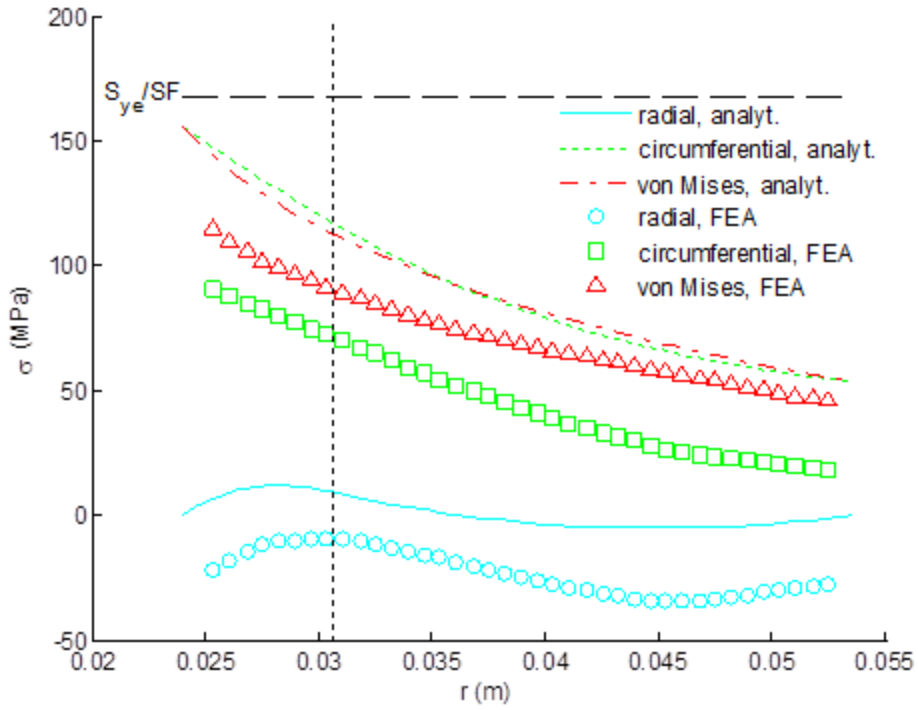

Figure 83: Gas Side End Cap Stress Distributions at the Inner Plane and Pin Azimuth

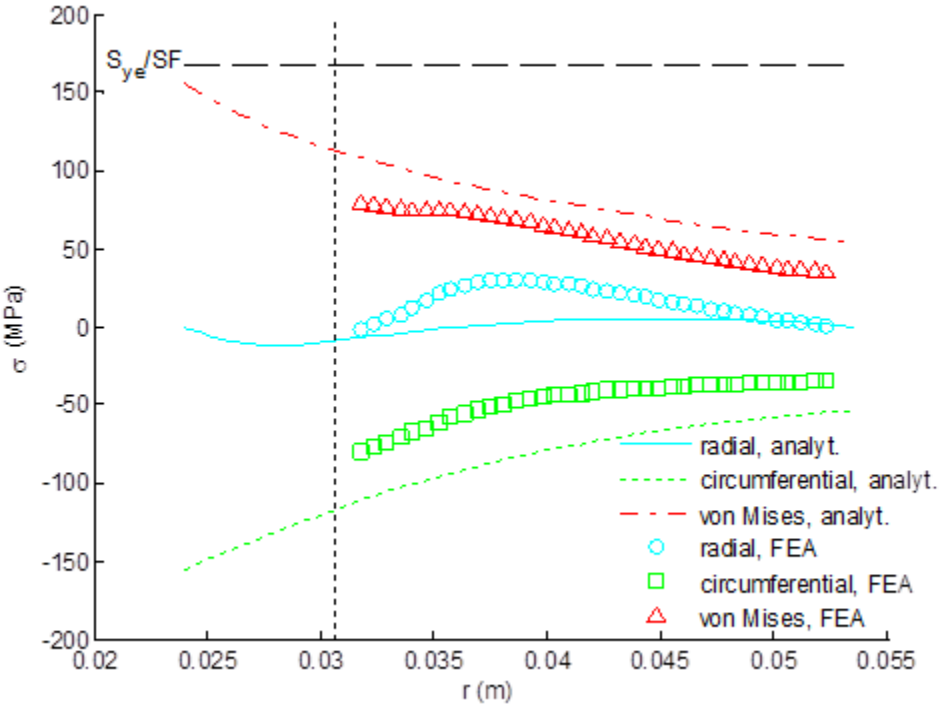

Figure 84: Gas Side End Cap Stress Distributions at the Outer Plane and Pin Azimuth

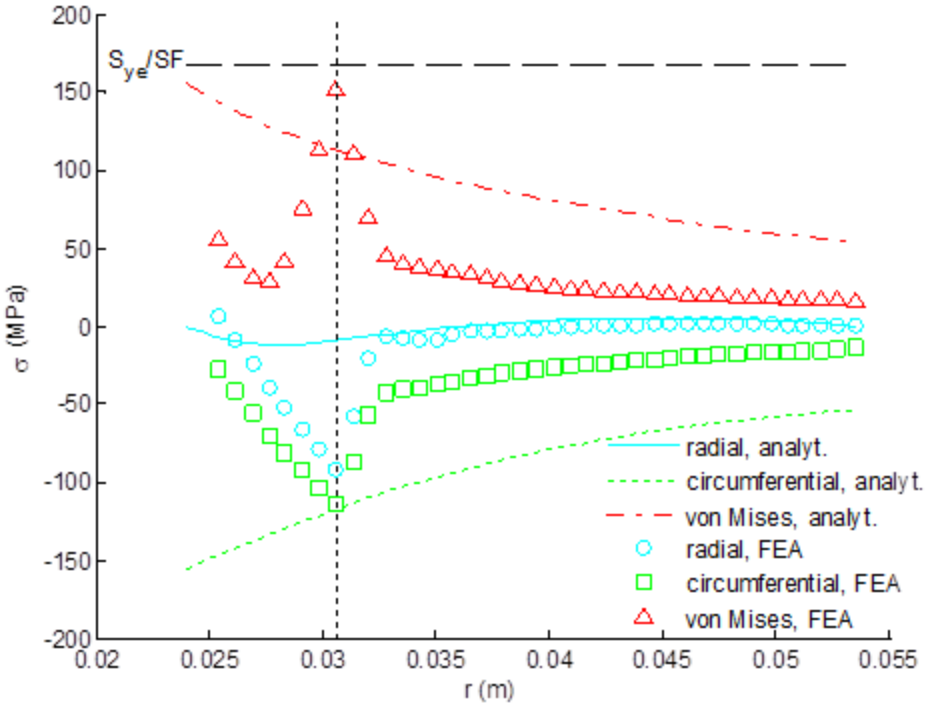

Figure 85: Gas Side End Cap Stress Distributions at the Retainer Plane and Pin Azimuth

As shown in Figures 83 through 85 the stress distributions in the gas side end cap along the pin azimuth are very similar to the results for the oil side end cap. A compressive offset is apparent at the inner plane where the gas pressure acts. Stress at the retainer plane is small enough that the stress concentration due to the retainer pocket is kept below $S_{y,e}/SF$.

Figures 86 through 88 show the stress distributions at the port azimuth. At all axial locations, the stress concentrations due to the charge ports remain below the maximum allowable stress.

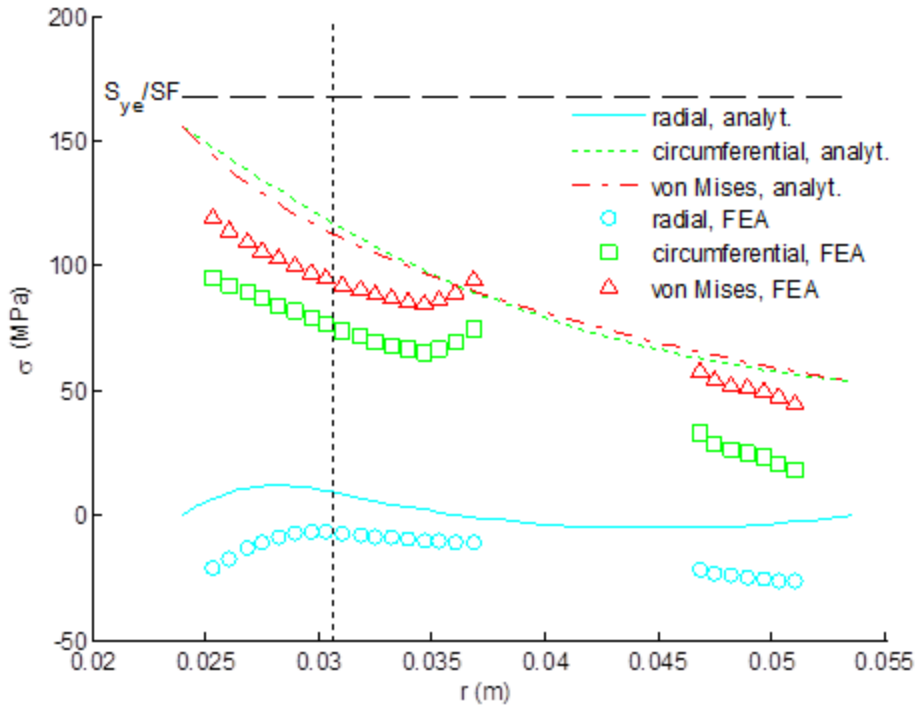

Figure 86: Gas Side End Cap Stress Distributions at the Inner Plane and Port Azimuth

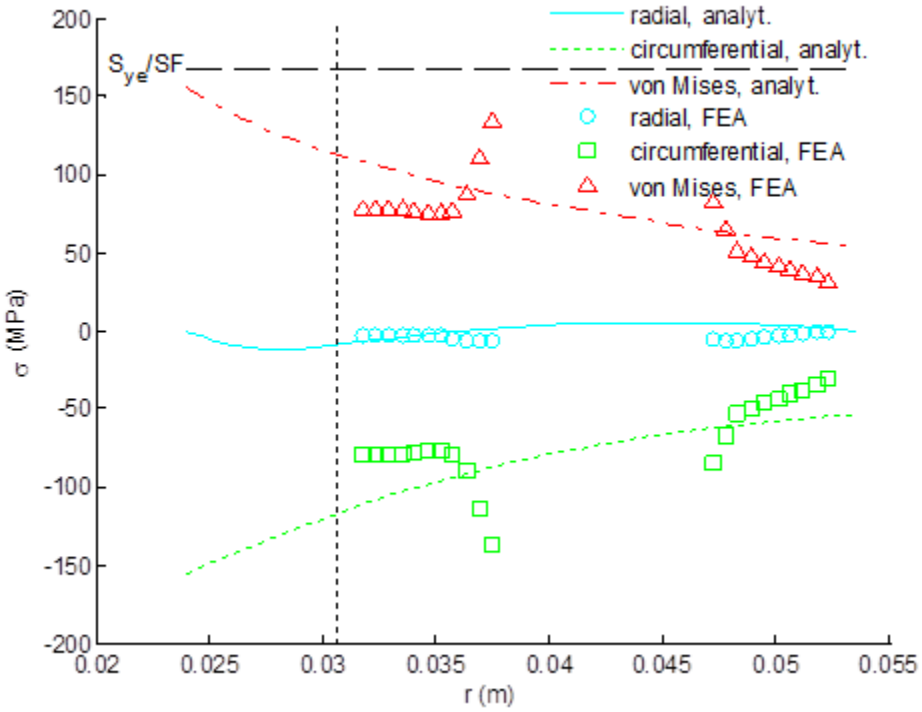

Figure 87: Gas Side End Cap Stress Distributions at the Outer Plane and Port Azimuth

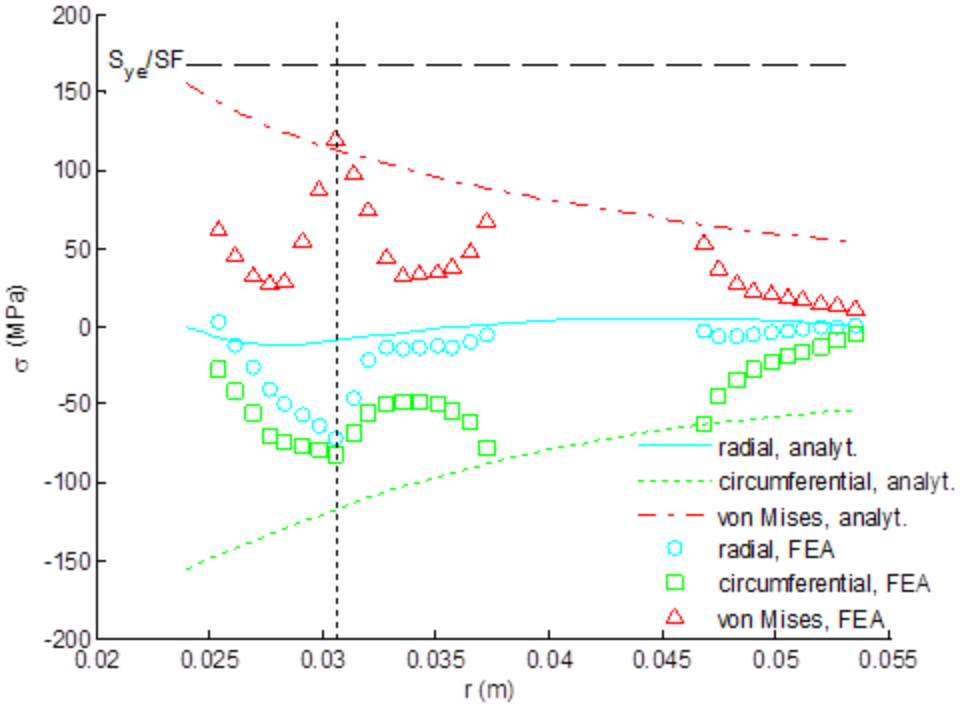

Figure 88: Gas Side End Cap Stress Distributions at the Retainer Plane and Port Azimuth

Since the spatial points plotted in Figures 86 through 88 are coplanar, they do not reflect the stress distributions along the charge port fillets. To prove that these stresses are sufficiently low, one of the charge port fillets is depicted in Fig. 89, where values of stress are given in Pa. Figure 90 shows that, along a particular azimuth, the von Mises stress actually reaches 191 MPa where the retainer contacts the end cap. While this is slightly greater than the maximum allowable stress, $S_{y,e}/SF$, of 168 MPa, the major component is compressive, and it is therefore deemed an acceptable stress concentration. The FEA results for the gas side end cap, therefore, suggest that the analytical model used for design optimization was appropriate. Additional FEA results for the end caps are provided in Appendix E.

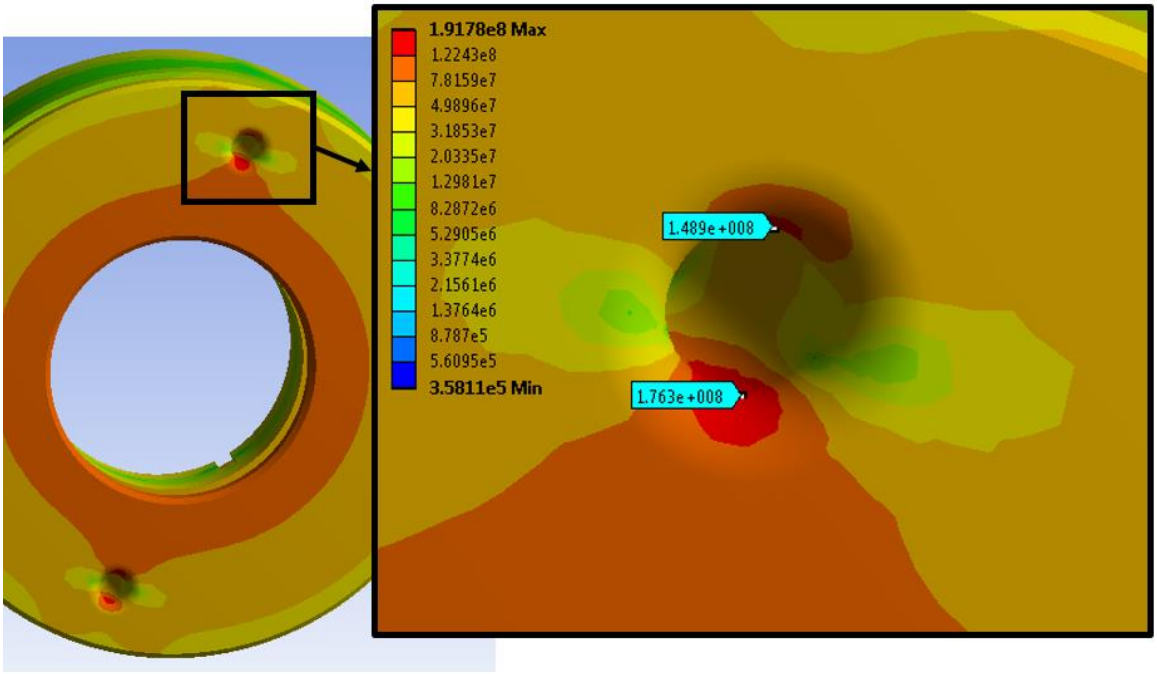

Figure 89: Stress Concentration near the Charge Port Fillet on the Inner Face of the Gas Side End Cap (Annotations in Pa)

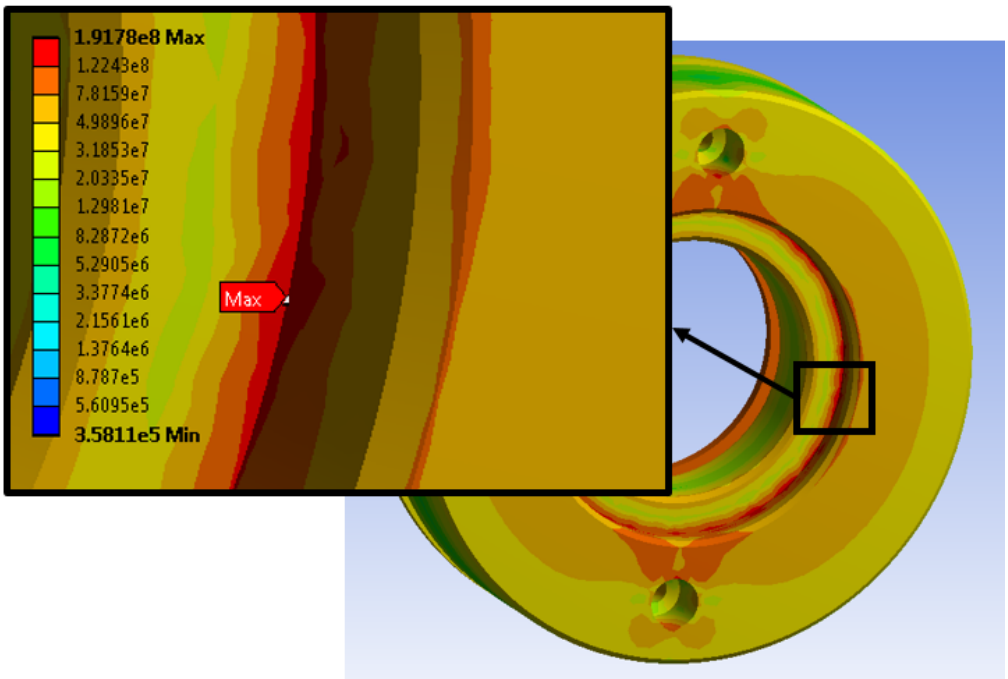

Figure 90: Stress Concentration in the Retainer Pocket on the Gas Side End Cap (Annotations in Pa)

8.3 Piston

Section 3.4 presented a basic analysis of the piston for the purposes of the design optimization. This section addresses the various minor design features of the piston that have been were previously omitted.

The operation of the HFA is relatively insensitive to the exact axial position of the inner piston seals (those which seal against the axle). In a qualitative sense, these seals should be spaced far enough apart to inhibit cocking of the piston. As in the case of the outer seals, there is no pressure gradient across the bosses which separate each seal from its adjacent pressurized fluid. To be conservative, however, these bosses are selected to be 5 mm wide, which leaves a distance of 45.7 mm between the seals.

Given that oil enters and exits the HFA via radial ports in the axle, limits must be imposed on the piston travel. If the piston were actually to abut the oil side end cap, the radial ports would be fully covered. There would be no oil pressure acting on the axial face of the piston, and the HFA would therefore be "stuck" in a pneumatically-discharged state. To prevent this from occurring, a system of small button head screws, as illustrated in Fig. 91, is employed as a mechanical stop.

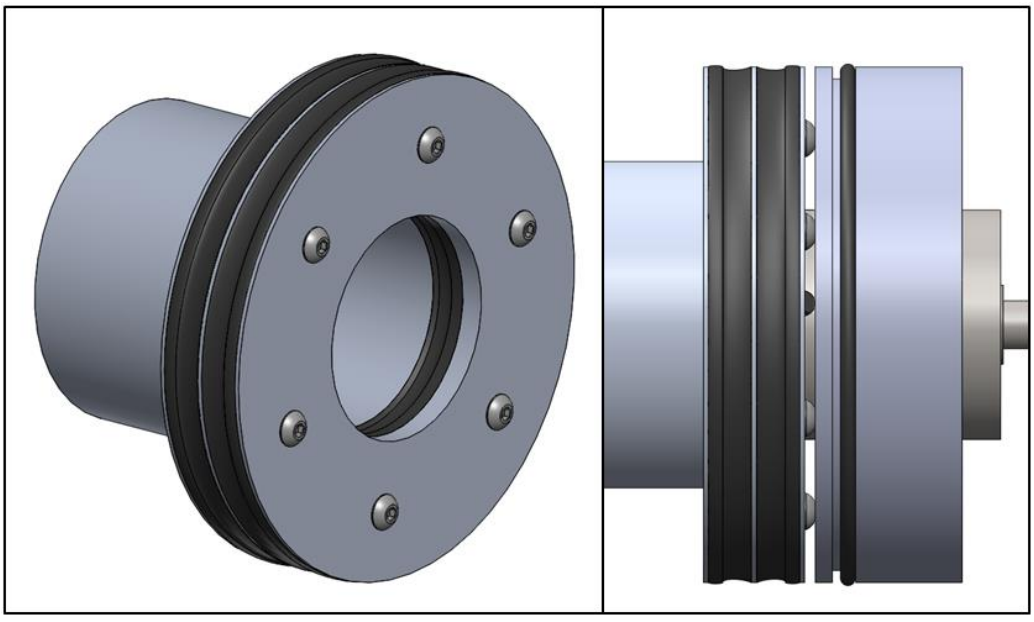

Figure 91: Illustration of the Mechanism by which Piston Travel is Limited, Isometric View (Left) and Side View (Right)

This system effectively imposes a minimum oil volume, which can be very small without impacting the functionality of the system. If the height of the screw heads is smaller than the diameter of the radial ports, d_i, the piston is allowed to partially cover the ports, exacerbating the axle port losses at low states of pneumatic charge. While this could be avoided completely by using screws with tall heads, the resultant minimum oil volume would be quite large, causing a significant decrease in the effective pneumatic energy storage capacity of the HFA. In any case, low states of pneumatic charge tend to represent a small proportion of the overall operating states of the HFA, and therefore the occasional exacerbated axle port losses are deemed acceptable.

Six equally-spaced (60° apart from one another) button head screws are used. The threaded holes in the piston are located at a radius of 38.7 mm, which splits the distance between the nominal inner and outer radii of the piston. Using a relatively large number of screws should minimize the magnitude of local stress concentrations in the piston during normal operation and the non-axisymmetric bending phenomena at the minimum oil condition.

As was discussed in Section 3.4, the fundamentally-different oil and gas pressure behaviors create complex net pressure distributions that can cause interesting bending phenomena in the disc section of the piston. For the laboratory prototype, the worst case net pressure distribution from the perspective of bending actually occurs at ω_{max} and zero system pressure. When compression is taken into account, the stresses in the piston are actually greatest at maximum pressure and maximum speed. As it turns out, however, bending and compressive stress are insignificant at all expected operating conditions for the laboratory prototype. Instead, the thickness, th_p, of the disc section of the piston is driven by seal packaging considerations.

The packaging of the outer piston seals (those which seal against the liner) was discussed in Section 3.4. When the HFA is charged, a pressure gradient of P_c exists across the boss that separates the two seals. To prevent shear failure of this feature, Eqn. 54 suggests a length of 0.84 mm for. Initial FEA analysis, however, indicates significant bending

stresses in the boss, a phenomenon not taken into account by Eqn. 54. A new boss length of 2 mm is therefore selected for the laboratory prototype. As no pressure gradient should arise across features which separate each seal from its adjacent pressurized fluid, these features can be quite narrow. A dimension of 1 mm is deemed conservative.

FEA has been carried out to confirm that the stresses in the piston remain acceptably low when the HFA is charged. A pressure of P_c is applied to the entire gas side of the piston, and no pressure acts on the oil side. The button head screws provide a compressive support at their contact areas with the piston, but the interaction at the threads is not taken into account. Because of their low stiffness, the piston seals are omitted from the FEA analysis. Figure 92 shows two images from the FEA results, which indicate that stresses remain well below $S_{y,p}/SF$ (167 MPa). The top images an isometric view of the oil side face of the piston, and the bottom is a zoomed view of the seal packaging area with deformations magnified by a factor of 200. The scale on the left is in units of Pa.

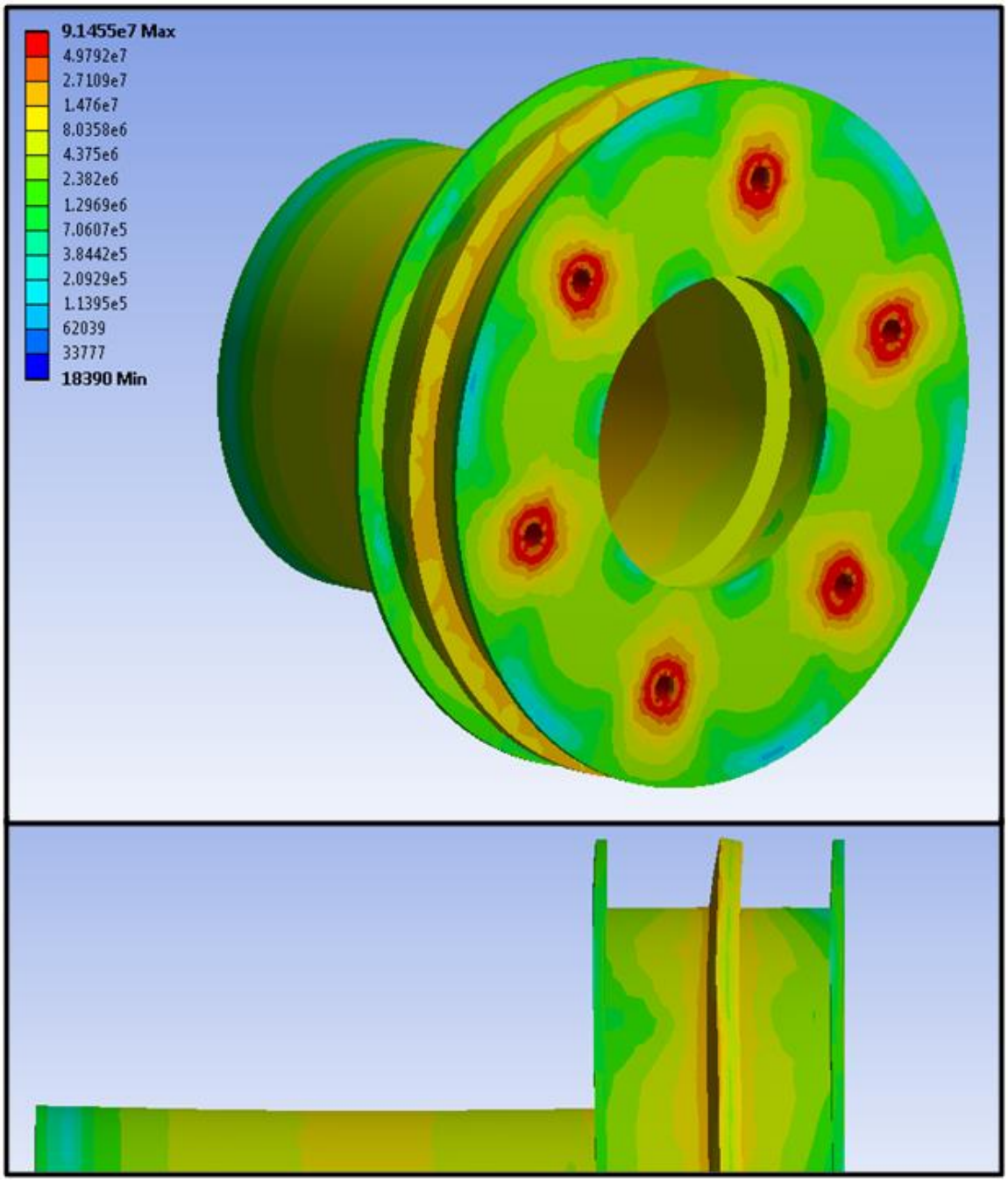

Figure 92: FEA Results for the Piston at the Charge Condition (Deformations Magnified 200x in the Bottom Image)

8.4 Housing

For the purposes of model-based design and optimization, Section 3.5 addressed the stresses in the housing that arise from pressure and centrifugation. The analytical stress model included the simplifying assumptions that the internal pressure, P_{int}, acting on the liner was axially uniform and that no axial stress is present in the housing. In reality, the differences in the gas and oil pressure distributions cause the internal pressure to be non-uniform, and the mass of the housing imposes at least some axial load.

Also excluded from the analytical housing stress model were the effects of the radial holes in the liner and wrap, which facilitate the pin system. The diameter of the two holes in the liner is equal to the shoulder diameter of the screws used for the pin system (see Table 29). To prevent chatter, these holes should be drilled for a transition fit. As all of the force from the pin system is intended to be carried by the liner, the hole in the wrap should provide a clearance fit with the head of the shoulder screw.

To prevent damage of the outer O-rings and piston seals during HFA assembly, a chamfer should be machined onto the inner edges of the liner. The proper dimensions [76] of this feature are shown in Fig. 93.

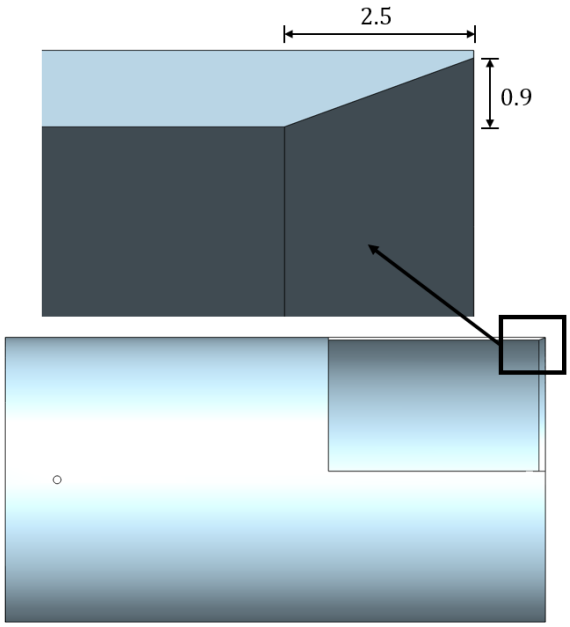

Figure 93: Diagram of Chamfer at the Inner Edge of the Liner (Dimensions in mm)

FEA has been carried out for the housing to confirm the analytical stress model used in the design optimization. The analytical and FEA results are compared for the three possible worst-case loading scenarios discussed in Section 3.5. These cases are summarized in Table 30 for the selected laboratory prototype design, with the actual observed pressures from a UDDS drive cycle simulation.

Table 30: The Three Potential Worst-case Loading Scenarios for the Housing

	Case 1	**Case 2**	**Case 3**
Description	high pressure, zero speed	loss of pressure, high speed	full SOC
$\boldsymbol{P_{int,o}}$ $[\boldsymbol{MPa}]$	26.4	0	26.4
$\boldsymbol{P_{int,g}}$ $[\boldsymbol{MPa}]$	26.4	0	26.4
$\boldsymbol{\omega}$ $[\boldsymbol{rad/s}]$	0	1154	1154
Failure Mode	radial compressive, wrap	radial tensile, wrap	tensile, liner

Note that, for load case 3, the non-uniform pressure distribution is taken into account in the FEA analysis. Given the nature of cases 1 and 2, the pressure distribution is, in fact, uniform. The weight of the housing and the presence of the radial holes for the pin system are also included in the FEA analysis. The maximum drive cycle torque, T_{max}, is extremely small compared to the fluid pressure and centrifugal loading, and therefore shear stresses due to angular acceleration have been omitted. Given the manufacturing process for the housing, the interface between the liner and wrap is presumed to behave as a bonded interaction.

Figures 94 through 96 show the radial, circumferential and von Mises stress distributions as functions of radial position in the housing for the three potential worst cases. The dotted data are the FEA results, and continuous curves are the analytical results. A dashed vertical line marks the radial position of the interface between the liner and the wrap (i.e. the position $r_i + th_l$). For the FEA results, the data have been taken at an axial position 3 cm inward from the gas side end cap. Examination of other axial positions between the O-ring seals reveals little variation in the stress distributions, which lends

credit to the uniform pressure assumption used in the analytical model. At positions outside the O-ring seals, fluid pressure does not act on the housing, and therefore the stresses tend to be far lower.

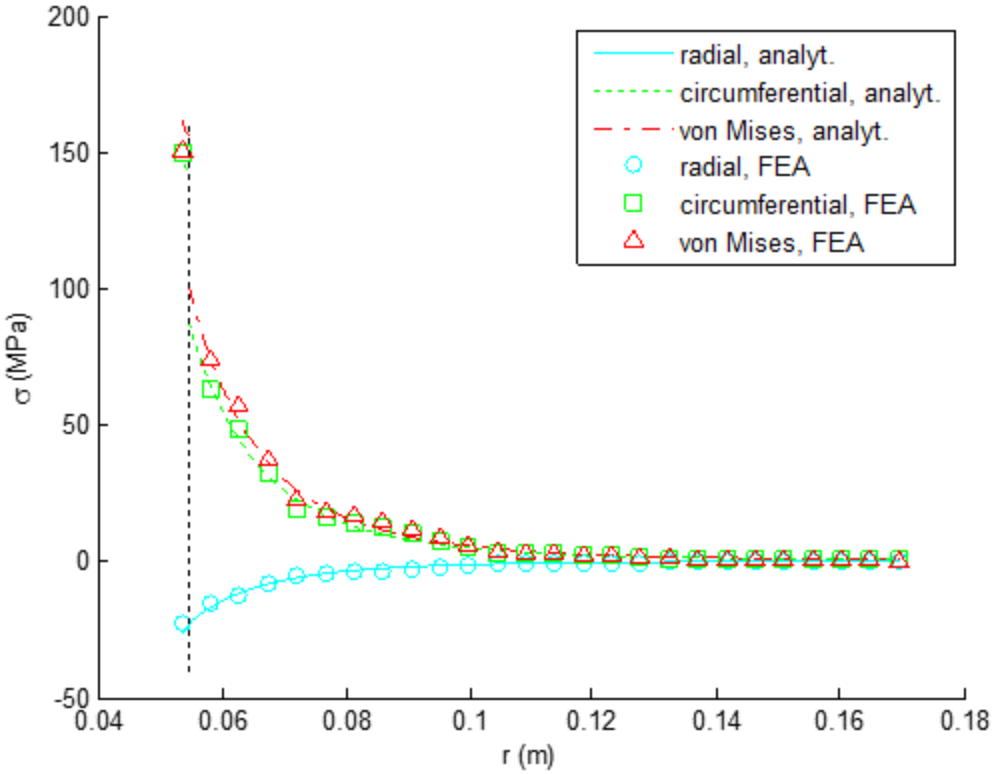

Figure 94: Housing Stress Distributions for Case 1 (Zero Speed, High Pressure)

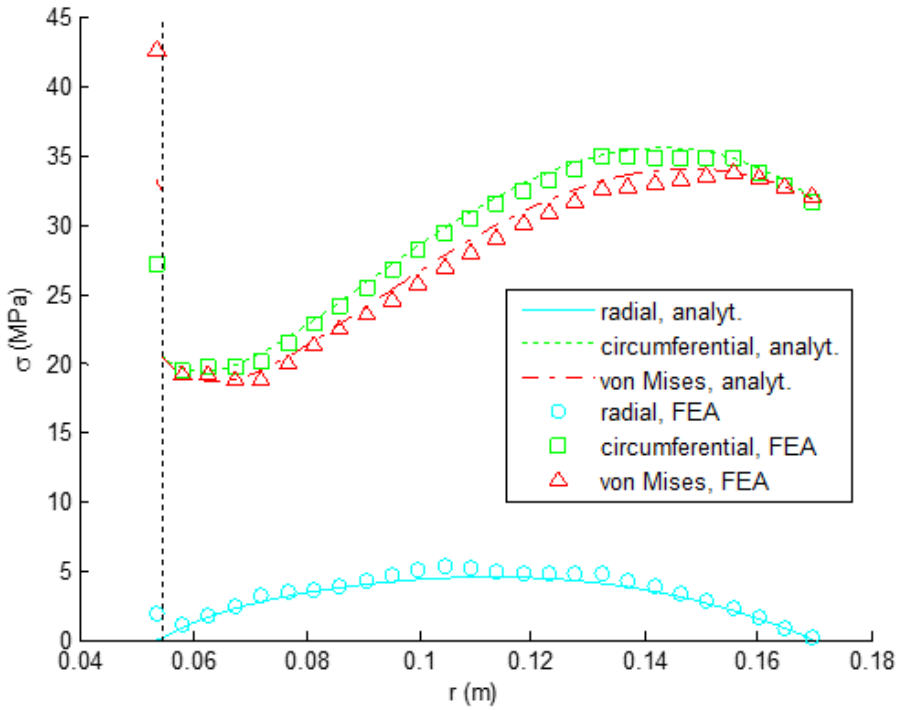

Figure 95: Housing Stress Distributions for Case 2 (Maximum Speed, Zero Pressure)

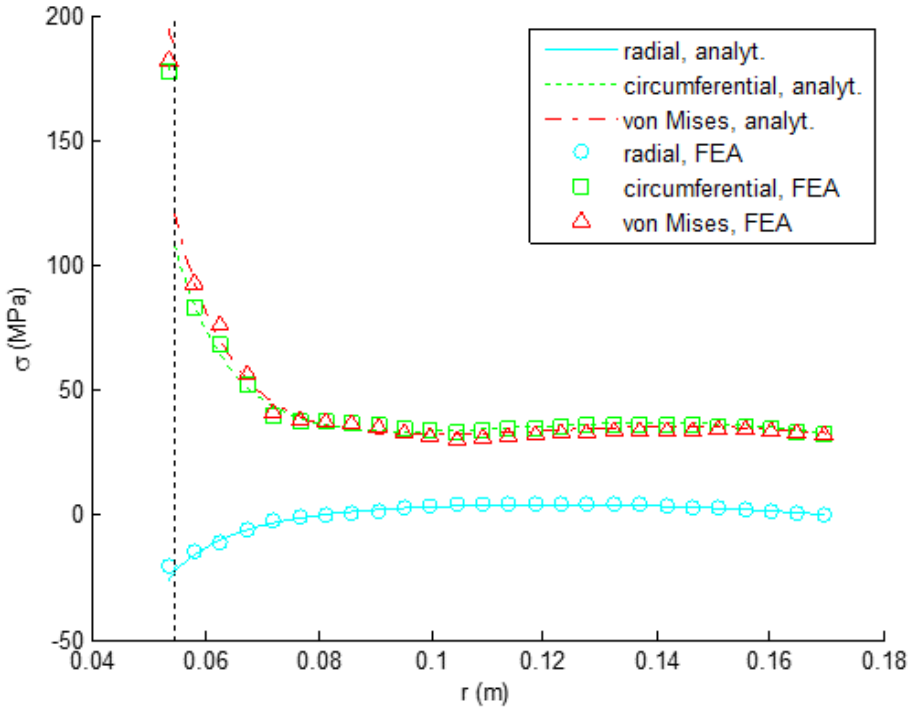

Figure 96: Housing Stress Distributions for Case 3 (Maximum Speed, High Pressure)

Figures 94 through 96 show excellent agreement between the FEA and analytical results, especially in the wrap. Recall from Section 3.5 that the Tsai-Hill criterion, rather than the von Mises criterion, is used to determine the safety factor of the wrap. Given the definition of the Tsai-Hill criterion (see Eqn. 61), the agreement between the FEA and analytical results with respect to the radial and circumferential stress distributions suggests that the Tsai-Hill criterion has been accurately evaluated during the design optimization. Additionally, note that the analytical von Mises stress distributions have been calculated two-dimensionally. The agreement between the FEA and analytical results with respect to the von Mises stress justifies the omission of axial stresses from the analytical model. Based on the FEA results, axial stresses in the wrap are generally compressive, and always $O(1\ MPa)$ or less.

At low pressure and high speed (case 2, Fig. 95), the analytical model slightly under-predicts the von Mises stresses in the liner. However, even based on the FEA results, the safety factor still remains significantly above the constraint of 3 for this case. The presence of the radial holes has a negligible impact on the stresses in the housing. More complete FEA results for the housing are provided in Appendix E.

It should be mentioned that manufacturing with composites always involves considerable uncertainties. In the case of the housing, it is very difficult to predict the nature of the residual stresses that might be induced during the curing process [38], or to project the time-dependent effects that might arise. Because the optimization presented in Section 7.4 did not drive the wrap to its largest allowable stress, the selected prototype design exhibits a safety factor of 11.5 for the wrap. It is assumed that this is sufficiently conservative to account for all of the uncertainties mentioned above. If possible, regular monitoring of the structural health of the housing should be performed.

8.5 Axle

Section 3.2 presented methods for modeling stresses in and selecting proper dimensions for the axle. Though these processes were developed for the purpose of model-based

design and optimization, they are fairly complete; the only features that have been omitted until this point are small shoulders between the main section and the shafts that prevent the stationary outer race of the bearings from contacting the rotating axle. The diameter of these shoulders, which can be seen in the figures included in this section, should be roughly equal to the outer diameter of the inner bearing race. They must be axially long enough only to accommodate the small axial displacement of the races with respect to one another. Given these considerations, the diameter and length of the bearing shoulders are 1 cm and 0.5 mm, respectively.

FEA has been carried out to confirm that the methods used in the design optimization have properly selected the various axle dimensions. Per the calculations detailed in Section 3.2, a tensile axial force of 192 kN is applied to the areas where the axle contacts the retainers. The gas and oil side shafts provide radial reactions to the eccentric force, calculated in Section 3.6 to be 4.76 kN. Figure 97 shows two images the oil side of the axle with annotations to various peak von Mises stress locations (stresses given in Pa). Note that the maximum allowable stress, $S_{y,a}/SF$, is 333 MPa.

From the top image in Fig. 97, it is clear that the seal diameter, d_s, has been properly selected, as the peak stress near the radial port is equal to $S_{y,a}/SF$. The top image of Fig. 97 also shows that the maximum stress in the oil side shaft is acceptable low (the probes are located on the side which is in tensile bending). However, as seen in the bottom image, the peak stress near the outer corner of the retainer groove exceeds the maximum allowable stress, leading to a safety factor of only about 2. Because the stress here is mostly compressive, this is deemed an acceptable stress concentration. The bottom image also shows that the axle radius, r_a, has been properly selected, such that the peak stress near the radial ports is about $S_{y,a}/SF$. This is more thoroughly proven in Fig. 98, which illustrates the von Mises stress along the radial line that coincides with the stress concentration at the radial port.

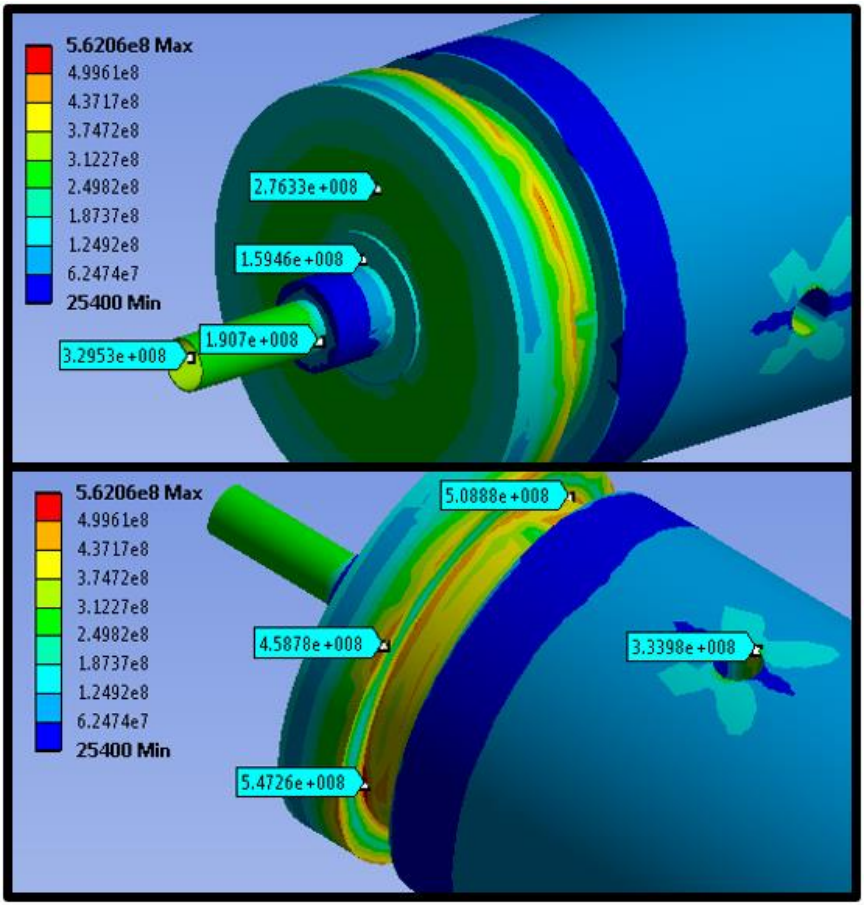

Figure 97: FEA Results Near the Oil Side of the Axle, von Mises Stress (in Pa)

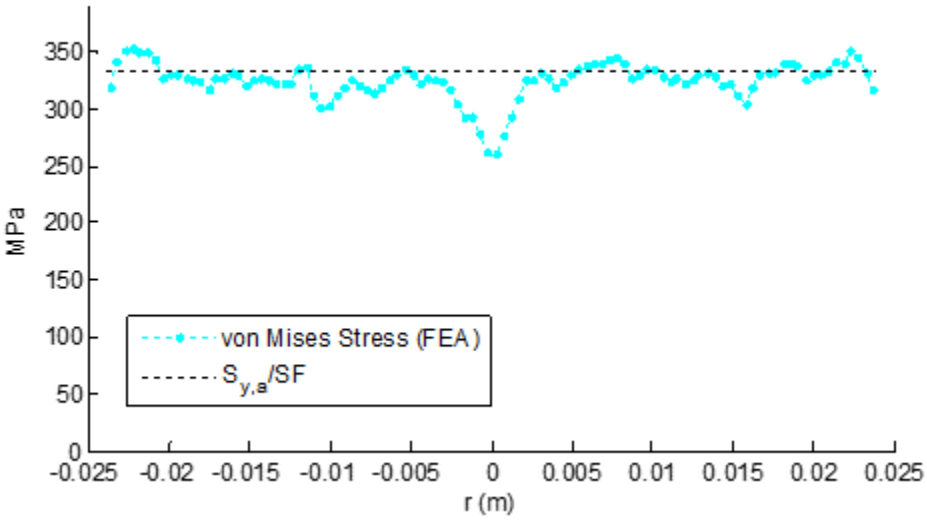

Figure 98: von Mises Stress in the Axle Along a Radial Line that Coincides with the Stress Concentration at the Radial Port

Figure 99, which depicts the FEA results or the gas side of the axle, shows that the maximum von Mises stress in the shaft is acceptably low.

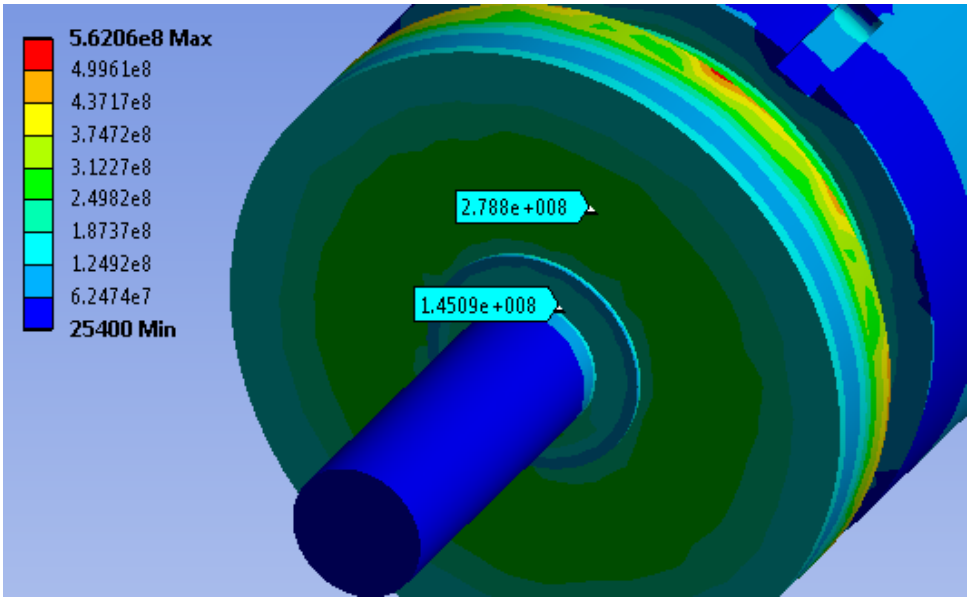

Figure 99: FEA Results Near the Gas Side of the Axle, von Mises Stress (in Pa)

8.6 High-Speed Rotary Union Case

The purpose of the HSRU case is to form the outer part of the non-contacting circumferential seal and to house the lower bearing. The design details of this component have been omitted until now, as they have little bearing on the results of a design optimization. A cross sectional view of the HSRU case, with all relevant dimensions, is shown in Fig. 100.

Some details of the HSRU case are omitted here, as they depend on choices related to the design of the containment chamber, which will be conducted by another researcher. Namely, the mechanism by which the HSRU case is secured to the containment chamber and the handling of the leakage oil must be addressed in the detailed design of the chamber.

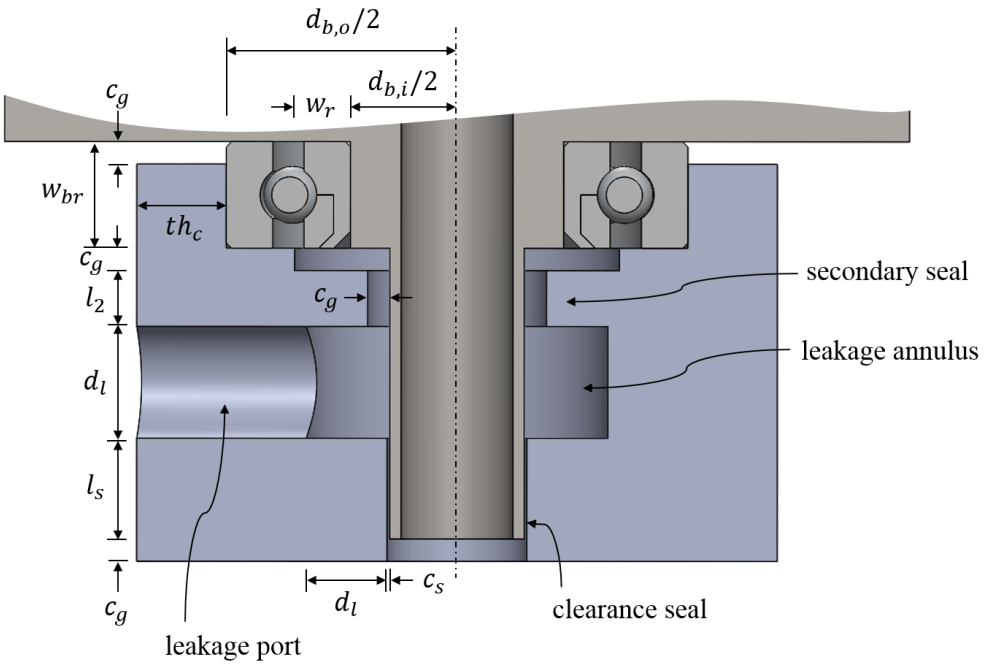

Figure 100: Cross-sectional View Illustrating the Dimensions of the High Speed Rotary Union (HSRU) Case

To form the non-contacting circumferential seal, the bottom of the case has a through-hole whose diameter is $2c_s$ larger than d_i, the diameter of the axle portion that protrudes into the case. The length of this through-hole is equal to the seal length, l_s, plus a gap, c_g, that safely allows for thermal expansion of the axle. Above the circumferential seal is an annulus of axial and radial dimensions d_l into which leakage oil enters from the circumferential seal. A radial leakage port of diameter d_l allows oil to pass from the leakage annulus to the inside of the containment chamber.

Above the leakage annulus is a secondary seal, the purpose of which is to further protect the bearings from leakage oil. The secondary seal has a length of l_2 and a clearance of c_g. At the top of the HSRU case is a groove that supports the lower bearing. The diameter of this groove should create a press fit with the bearing, and the height should allow a clearance of c_g between the HSRU case and the main section of the axle.

The case thickness, th_c, must be large enough that the maximum expected eccentric force, F_{ecc}, does not cause the material that forms the bearing pocket to shear off of the

case. It is assumed that the shear stress is distributed as if this material were a thin-walled tube, where

$$\tau_{V,c} = \frac{2F_{ecc}}{\pi d_{b,o} th_c} \tag{243}$$

As was done in sizing the bearings, the maximum eccentric force is estimated using shaft balancing standards and a safety factor of 10 (see Eqn. 65). Letting the shear stress in the case go to its maximum allowable value, the case thickness should be

$$th_c = \frac{2(SF)(m + m_o)\omega_{max}(10)6.3(10^{-3})}{\pi d_{b,o}(0.58)S_{y,c}} \tag{244}$$

To avoid compressive failure of the circumferential face of the bearing groove, the following inequality must be true

$$\frac{S_{y,c}}{SF} \geq \frac{\frac{1}{2}F_{ecc}}{\frac{1}{2}\pi d_{b,o}(w_{br} - c_g)} = \frac{(m + m_o)\omega_{max}(10)6.3(10^{-3})}{\pi d_{b,o}(w_{br} - c_g)} \tag{245}$$

Given the strength of gray iron, this inequality is easily satisfied for any reasonable set of case dimensions.

System pressure acts inside the HSRU case only between the containment chamber and the bottom of the axle. Because the non-contacting circumferential seal diameter is much smaller than the outer diameter of the bearing, it is assumed that this pressure does not create a critical stress, and therefore Eqn. 244 drives the outer diameter of the HSRU case to an appropriate value.

Because the HSRU case must interface with the containment chamber, which is outside the scope of this thesis project, actual values for th_c, c_g, and l_2 are not specified here. In general, the HSRU case can be overdesigned, as it is a relatively low-cost and low-mass component. For the laboratory prototype, the outer diameter of the HSRU case may be driven by the dimensions of gray iron roundstock that is convenient to procure.

Recall from Eqns. 114 and 116 that some amount of heat is generated in the circumferential seal formed by the HSRU case and the portion of the axle that protrudes into it. The design process described in Section 3.2 has prescribed a seal diameter, d_s, of

5.9 mm to withstand the system pressure acting inside the axle. The resultant wall thickness of the axle at the circumferential seal is only 0.25 mm thick, and therefore may be prone to significant thermal expansion. It is necessary to confirm that radial thermal expansion of the axle will not cause it to bind with the HSRU case. Since the thermal capacitance of the HSRU case should be relatively large, binding is particularly likely to happen during startup, when the small portion of the axle that protrudes into the case rapidly heats up.

A simple finite-difference computational heat transfer code has been developed to analyze the transient behavior of the circumferential seal at startup. Because this is an axisymmetric problem, the numerical scheme is spatially 2-dimensional. The computational domain includes both the fluid region and the portion of the axle that forms the circumferential seal, as depicted in Fig. 101. Arrows indicate the leakage flow of oil (that which passes through the circumferential seal).

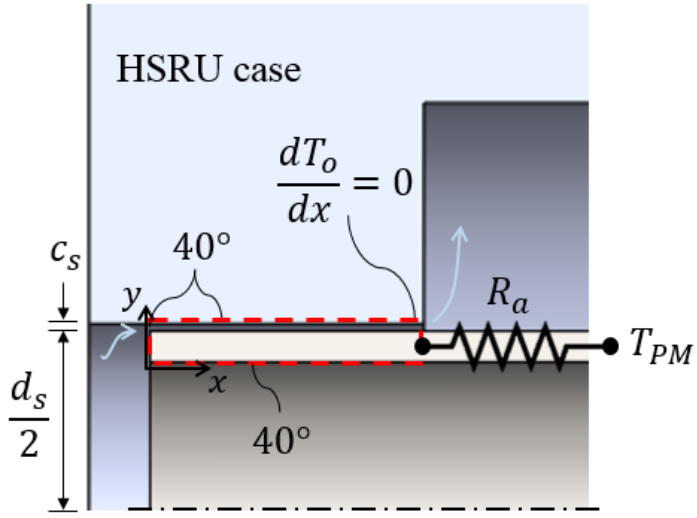

Figure 101: Computational Domain and Boundary Conditions for the Heat Transfer Analysis of the Circumferential Seal

The fluid mechanics problem for this flow case has a closed-form analytical solution that was derived in Section 4.3. The fluid velocity profiles and volumetric rate of heat generation within the seal are therefore already known (and assumed to be fully-developed at startup), and the numerical scheme need only include the energy equation.

At each time step, the temperature distribution in the oil portion of the computational domain is solved for first, and the temperature distribution along the bottom of this portion is used as the boundary condition for the axle at the seal diameter. It is assumed that the oil entering the seal (the leakage oil) and the oil inside the axle is at a constant 40° C, typical for a hydraulic system. Heat that is generated in the seal can be convected to the HSRU case or to the axle. Because the HSRU case is attached to the containment chamber, which is metal, it is modeled as an infinite heat sink at a temperature of 40° C.

Heat can be conducted axially through the axle to the storage PM, which is assumed to be a heat sink at a temperature of 50° C. The thermal resistance of the conduction path through the axle, R_a, is approximated as a series of 1-dimensional resistances, calculated by breaking the distinct portions of the axle into simple cylindrical segments. At the bottom border of the computation domain, heat can also be conducted back to the oil within the axial port, which is modeled as stagnant at a constant 40° C. A Neumann boundary condition is used on the temperature of the oil exiting the circumferential seal.

Because the HSRU case is modeled as a sink, its geometry does not change. The seal diameter changes throughout the transient simulation by the equation

$$d_s^i = d_{s,o}\left[1 + \alpha_{s,s}\left(\bar{T}_s^i - T_{s,o}\right)\right] \tag{246}$$

where $d_{s,o}$ is the initial seal diameter (assumed to be axially constant), $\alpha_{s,s}$ is the thermal diffusivity of steel, $\bar{T}_s^i$ is the temperature at the axial location i, averaged across the radial dimension of the axle, and $T_{s,o}$ is the initial temperature of the axle. The former is set to be a spatially-uniform 40° C. Changes in the seal diameter are reflected in the step sizes of the computational domain, which in turn impact the fluid velocity profiles. The complete code can be found on pg. 280 in Appendix B.

The numerical scheme described above has been implemented for the specific dimensions of the selected laboratory prototype. The initial seal clearance must be made greater than 10.2 μm (the value specified by the optimization) in order to accommodate the radial growth of d_s. By trial and error, an initial clearance of 15 μm has been selected as an appropriate value. Figure 102 shows the steady-state seal clearance as a function of axial position in the seal.

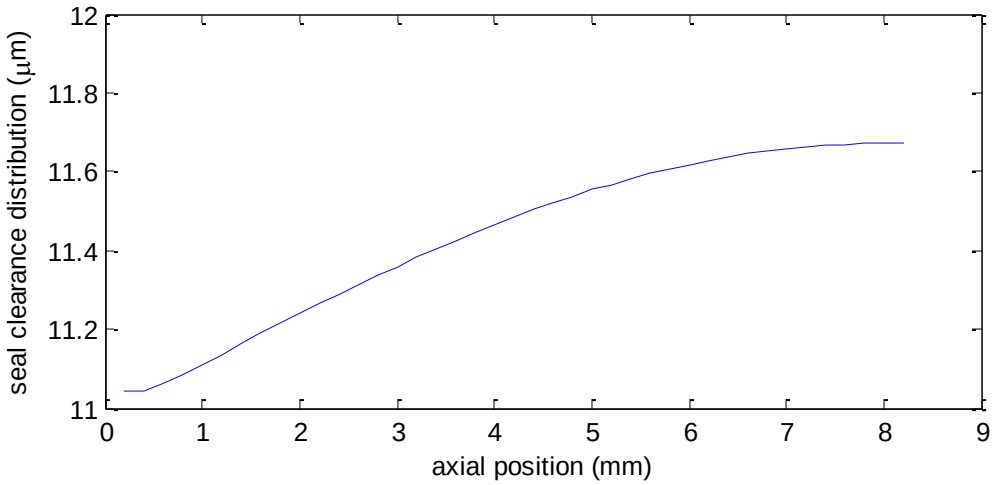

Figure 102: Steady-state Seal Clearance Distribution vs. Axial Position

Note that the initial clearance selected here has produced an average steady state clearace of 11.5 μm. This is deemed sufficiently close to the desired seal clearance of 10.2 μm. The results of this computational heat transfer study also indicate that the temperature of the leakage oil never exceeds 75° C. This ensures that the oil will not degrade.

8.7 Relative Radial Strain Analysis

The HFA components are manufactured such that, at assembly, there is some radial clearance at each interface between concentric components. Throughout various operating states, changes in pressure and/or centrifugal forces cause these radial clearances to fluctuate. The purpose of this section is to analyze the relative radial strains of the axle, end caps, housing and piston. Properly specifying the clearances between these components at assembly will ensure the integrity of the piston and O-ring seals throughout the entire range of expected operating conditions.

For the purposes of evaluating relative radial strains, the axle, end caps, housing and piston are modeled as simple cylinders, ignoring the effects of any minor design features (e.g. radial ports in the axle, radial holes in the housing, O-ring glands). Each component

is presumed to deform axisymmetrically with no end effects. Because of their low stiffness, the seals themselves (O-rings and piston seals) impose negligible radial loads. In the case of the end caps and piston, radial strain due to bending is ignored.

Radial strain is presumed to arise only due to centrifugal forces and fluid pressure acting radially on the components of interest. Equations 47 and 48 described the radially-dependent stress distributions in a homogenous, isotropic, thick-walled cylinder exposed to internal, external, and/or centrifugal loading. These equations are used for the axle, end caps and piston. Section 3.5 detailed the equivalent calculations for a hybrid cylinder with anisotropic mechanical properties, which are applied to the housing. Whether isotropic or anisotropic, the stress distributions in a cylinder can be converted to a circumferential strain distribution by

$$\epsilon_c(r) = \frac{1}{E_m}[\sigma_c(r) - \nu(\sigma_r(r) - \sigma_z)] \tag{247}$$

which, in turn, can be converted to a radial displacement distribution by

$$\delta_r(r) = r\epsilon_c(r) \tag{248}$$

In Eqn. 247, σ_c, σ_r and σ_z are the circumferential, radial and axial stresses, E_m is the elastic modulus and ν is the Poisson ratio (in the case of an anisotropic material, the longitudinal Poisson ratio, ν_L). Notice that the axial stress is presumed to be constant at all radial locations. As before, the housing is modeled as free of any axial stresses.

The remainder of this section justifies the worst-case scenarios for each sealing interface and presents the corresponding expected range of radial clearances. For a given interface, once the worst-case radial displacement distributions for each component have been calculated, the maximum expected change in the clearance is simply the difference between the outer and inner displacements, δ_r, evaluated at the radius of the interface. Note that nominal dimensions (those presented in Tables 25 and 26) are used for the present analysis, even though one of the primary purposes of this section is to specify more precise dimensions. While an iterative process could be used to address this issue, it is assumed that using nominal dimensions rather than the final selected dimensions introduces negligible error in the prediction of radial strain.

As described in Sections 3.4 and 8.3, two piston seals are used between the piston and the housing, and two rod seals are used between the piston and the axle. The clearances at these interfaces must not grow so much that the seals are prone to leakage and must not shrink so much that the components bind, preventing translation. The particular seals selected for the prototype can accommodate a 43.5 μm range of radial clearances [32].

At the interface between the axle and piston, only the bearing length of the piston is considered; effects due to the disc section of the piston are neglected. The axle is modeled as a solid infinite cylinder. Recall that the piston is made of aluminum and the axle is made of steel. Given these material selections and the fact that the axle is at a smaller radius, the piston should be more heavily affected by centrifugal forces. This interface, therefore, is most prone to leakage at ω_{max}, and the separation between the components should be exacerbated when there is a loss of pressure. Table 31 summarizes the loads and resultant radial displacements for the worst-case leakage scenario.

Table 31: Loads and Radial Displacements for the Worst-case Leakage Scenario at the Axle-Piston Interface

Loading	
Pressure outside of piston	0
Pressure acting within seal	0
Axial stress in piston	0
Axial stress in axle	0
Angular velocity	1154 rad/s
Displacements	
Axle	0.12 μm
Piston	2.2 μm
Net	**2.1 μm**

The worst case from the perspective of binding occurs when centrifugal forces are absent, the HFA is pressurized, and no pressure is acting in the seal between the piston and axle. This scenario occurs, for example, when the HFA is charged. To be conservative, the maximum observed pneumatic pressure during drive cycle simulation is used here. The loads and radial displacements for this binding scenario are summarized in Table 32.

Table 32: Loads and Radial Displacements for the Worst-case Binding Scenario at the Axle-Piston Interface

Loading	
Pressure outside of piston	26.4 MPa
Pressure acting within seal	0
Axial stress in piston	-26.4 MPa
Axial stress in axle	106.1 MPa
Angular velocity	1154 rad/s
Displacements	
Axle	-3.6 μm
Piston	-21.7 μm
Net	**-18.1 μm**

Examining the results in Tables 31 and 32, the difference between the maximum growth and maximum shrinkage of the clearance at the axle-piston interface is expected to be 20.2 μm. This is well within the acceptable range of 43.5 μm. Manufacturing the piston to have an inner radius 10 μm larger than the axle radius, r_a, should safely allow for the relative radial strain of these components.

The other location at which the piston creates a seal is at its interface with the liner of the housing. For the present analysis, the effects of the bearing section of the piston are neglected, such that it can be modeled as a simple cylinder of axial length th_p and inner and outer radii r_a and r_i, respectively. By virtue of their different material properties, the housing has a higher specific modulus than the piston. However, because its mass is concentrated at a larger radius, the housing experiences a stronger centrifugal field. It is not clear, then, which component will exhibit more radial displacement due to centrifugal effects. Therefore, two potential worst-case scenarios for leakage must be analyzed.

If centrifugation tends to create larger displacements in the piston, leakage is most likely at zero speed and maximum pressure. If, on the other hand, centrifugation causes larger displacements in the housing, leakage is most likely at maximum speed and maximum pressure. For both of these potential worst-case leakage scenarios, it is assumed that pressure acts in the seals between the piston and housing and between the piston and axle. In the zero speed case, the maximum observed value of P_p is used for both the pressure acting on the housing and the compressive axial stress in the piston. For the maximum

speed case, the maximum observed value of $P_{int,o}$ is used as the pressure on the housing, and the corresponding value of P_p is used for the axial piston stress. The two worst-case leakage scenarios, along with their resultant radial displacements, are summarized in Table 33.

Table 33: Loads and Radial Displacements for the Worst-case Leakage Scenarios at the Piston-Housing Interface

Case 1	
Loading	
Pressure acting on the housing liner	26.4 MPa
Pressure acting within piston-housing seal	26.4 MPa
Pressure acting within piston-axle seal	26.4 MPa
Axial stress in piston	-26.4 MPa
Angular velocity	0
Displacements	
Piston	-16.5 μm
Housing	40.4 μm
Net	**20.9 μm**
Case 2	
Loading	
Pressure acting on the housing liner	26.4 MPa
Pressure acting within piston-housing seal	26.4 MPa
Pressure acting within piston-axle seal	26.4 MPa
Axial stress in piston	-26.4 MPa
Angular velocity	1154 rad/s
Displacements	
Piston	-13.8 μm
Housing	49.1 μm
Net	**27.0 μm**

The piston and housing are most prone to binding when pressure acts in the seal between the axle and piston but not between the piston and housing. While this condition is unlikely, it is conservative to use it as a worst-case assumption. There are two potential worst-case scenarios from the perspective of binding. The first is when the maximum observed value of $P_o(r_a)$ acts between the axle and piston. For this case, the corresponding values of ω_s, P_p, and $P_{int,o}$ are used as the angular velocity, the axial stress in the piston, and the pressure acting on the housing. The other worst-case scenario for binding occurs when the HFA is charged, with P_c acting between the axle and piston and

imposing axial stress in the piston. Angular velocity is zero when the HFA is charged. The two potential worst-case scenarios for binding are summarized in Table 34.

Table 34: Loads and Radial Displacements for the Worst-case Binding Scenarios at the Piston-Housing Interface

Case 1	
Loading	
Pressure acting on the housing liner	26.4 MPa
Pressure acting within piston-housing seal	0
Pressure acting within piston-axle seal	26.4 MPa
Axial stress in piston	-26.4 MPa
Angular velocity	128.2 rad/s
Displacements	
Piston	42.4 μm
Housing	40.5 μm
Net	**-1.9 μm**
Case 2	
Loading	
Pressure acting on the housing liner	16.4 MPa
Pressure acting within piston-housing seal	0
Pressure acting within piston-axle seal	16.4 MPa
Axial stress in piston	-16.4 MPa
Angular velocity	0
Displacements	
Piston	26.3 μm
Housing	25.0 μm
Net	**-1.3 μm**

Given the results from Tables 66 and 34, the maximum expected range of radial clearances between the piston and housing is 28.3 μm, well within the acceptable range. To accommodate the expected relative radial strains, the piston should be manufactured such that its outer radius is 10 μm less than the inner radius of the liner, r_i. Note that the maximum expected growth of the clearance between the piston and housing increases significantly if pressure does not act between the axle and piston. To ensure this scenario does not occur, the HFA should be charged and the piston forced to translate some distance (thereby introducing pressurized fluid between the rod seals) before any angular velocity is imposed.

Like the piston, the end caps seal against the axle and the housing. Based on the SAE AS5857 O-ring standard [76], the maximum allowable clearance at these interfaces is 63.5 μm. Because the end cap seals are non-translational interfaces, however, shrinkage (even to zero) of the clearances is acceptable; it is assumed that any compressive interaction between the end caps and the axle or housing induces stresses that are insignificant compared to the other HFA loads.

With respect to the interface between the end caps and axle, the gas side end cap in particular is more prone to leakage, since the axle is solid near this interface. Because the end cap has a lower specific modulus and is exposed to a larger centrifugal field than the axle, leakage is most likely at high pressure and maximum speed. The maximum observed value of $P_o(r_a)$ acts to compress the axle, but because the O-ring seal is located near the inner face, it is assumed that no pressure acts at the inner or outer periphery of the end cap. The axial stress in the axle is calculated using Eqn. 35 at the maximum observed P_p, and the end cap is assumed to be free of any axial stress. These worst-case loads and the resultant displacements of the axle and end cap are summarized in Table 35.

Table 35: Loads and Radial Displacements for the Worst-case Leakage Scenario at the Axle-End Cap Interface

Loading	
Pressure acting on axle	26.4 MPa
Axial stress in axle	106.8 MPa
Angular velocity	1154 rad/s
Displacements	
Axle	-5.7 μm
End cap	3.1 μm
Net	**8.8 μm**

The maximum expected growth of the clearance between the end caps and housing must also be checked. Leakage here is most likely at high pressures, when the housing is highly-strained. As in the case of the piston and housing, it is unclear which component will experience greater deformation due to centrifugal effects. The worst-case scenario for leakage between the end caps and housing, then, occurs either at high speed and high

pressure or at zero speed and high pressure. Table 36 summarizes these two cases, along with the resultant displacements of the end caps and housing.

Table 36: Loads and Radial Displacements for the Worst-case Leakage Scenarios at the End Cap-Housing Interface

Case 1	
Loading	
Pressure acting on the housing liner	26.4 MPa
Angular velocity	1154 rad/s
Displacements	
End cap	2.7 μm
Housing	49.1 μm
Net	**46.4 μm**
Case 2	
Loading	
Pressure acting on the housing liner	16.4 MPa
Angular velocity	0
Displacements	
End cap	0
Housing	40.4 μm
Net	**40.4 μm**

Given the results of this study on relative radial strains, the piston, rod and O-ring seals used in the laboratory prototype should remain robust throughout the entire range of operating conditions. It should be noted that many of the cases examined were specified very conservatively by assuming, for example, that some maximum pressure can occur simultaneously with maximum HFA angular velocity. Observations from the UDDS drive cycle simulation suggest, in fact, that the maximum pressures tend to occur near low angular velocities. It is difficult to project how the piston and rod seals will behave under the influence of centrifugal forces. This issue may require special attention during the initial testing of the prototype.

9 Conclusions and Recommendations

This chapter begins by a restatement of the motivation for the work presented in this thesis. Next, a summary of the primary methods used to evaluate the HFA concept is provided, and important results are reviewed. The chapter concludes with recommendations for future research.

9.1 Summary of the Research

Hydraulic systems offer an inexpensive, power dense and robust means of power delivery and motion control. The low energy density of traditional hydraulic energy storage media, however, is an impedance to the widespread adoption of hydraulic power for mobile applications. This thesis has shown that, by combining hydro-pneumatic and rotating kinetic energy storage into one device, the hydraulic flywheel-accumulator has the potential to vastly improve the energy storage density of hydraulic systems. A simple control strategy has also been devised to illustrate the ability of the HFA to operate at near-constant system pressure. This offers the opportunity to downsize the peripheral components of the hydraulic system, reducing both cost and mass.

Model-based design is the primary means by which this thesis has assessed the potential performance capability of the HFA. Relatively simple and robust models for mechanical stress and energy exchange have been developed and integrated, forming a toolset that facilitates the performance modeling of candidate HFA designs. To minimize the computational expense of the model-based design process, special effort has been put towards developing a simple empirical model of the rotating fluid behavior. As a result, the HFA performance for a 20 minute drive cycle can be completed on the order of one second. The aforementioned toolset has been embedded into a multi-objective optimization scheme which uses a genetic algorithm to find a set of HFA designs with minimal mass and energy losses.

9.2 Conclusions

Minimizing of the HFA system mass and drive cycle losses have been identified as the two primary objectives in the design of the HFA. As discussed in Chapter 7, the multi-objectivity of the optimization problem yields a set of Pareto-optimal solutions. At one extreme end of the PO set, the solutions are small, fast-spinning and very energy dense. These flywheel-like solutions tend to have fairly small pneumatic energy capacities which, in combination with their high angular velocities, lead to relatively high drive cycle losses.

At the other extreme end of the PO set are slower-spinning and larger solutions, which more closely resemble traditional accumulators. Their lower angular velocities mitigate rotation-depenent losses, and their larger dimensions lead to higher pneumatic energy capacity, thereby decreasing dependence on the inefficient kinetic domain. The flywheel- and accumulator-like extremes of the PO front are bridged by a continuum of intermediate solutions, offering a diverse range of potential solutions for a specified HFA application.

Results from the optimizations presented in Chapter 7 indicate that, given the constraints imposed by a passenger vehicle-scale application, the HFA can achieve an energy density of more than 31 kJ/kg, operating at over 76% efficiency. Even with generous estimates of static accumulator energy density, this represents at least a six-fold improvement in the energy storage density of hydraulic systems. Setting more modest goals, the energy density can be doubled (10 kJ/kg) over traditional hydraulic storage media while operating at around 88% efficiency.

The achievable energy density at the laboratory scale is somewhat lower, owing to the inherent correlation between energy density and energy capacity for the HFA architecture. The improvement over static accumulator energy storage, however, is more pronounced. Subject to realistic packaging constraints for a small laboratory, the HFA offers at least an eleven-fold advantage in energy density over a static accumulator. The primary cause of drive cycle losses is the inefficiency of the storage PM, which contributes between 80% and 90% of losses at the vehicle scale and between 60% and

75% at the laboratory scale. This can be viewed as a promising statistic, as it indicates that none of the energy loss mechanisms that are unique (at least within the field of hydraulic energy storage) to the HFA concept are prohibitively large.

In evaluating the merits of the HFA concept, it is important to consider the benefits of the decoupling between system pressure and SOC. While it has not been included in the design optimization as an explicit objective or constraint, minimization of system pressure fluctuation indirectly serves to minimize the mass of the hydraulic system. The traction PM in a hydraulic powertrain must be sized to produce adequate flow rate to meet power demands at the minimum system pressure during a drive cycle. At both the vehicle and laboratory scales, the more accumulator-like solutions are able to limit the fluctuation of system pressure to within a 10% band about the design pressure. As a result, the traction pump-motors for these solutions need only be 4% heavier than they would be if system pressure remained perfectly constant throughout the entire drive cycle. This type of operation represents a distinct advantage over a traditional static accumulator, whose minimum SOC pressure may be as much as 63% lower than the design pressure [18], requiring significant oversizing of the traction PM.

A particular HFA design solution, whose characteristics are summarized in Tables 25 through 28, has been selected from the laboratory-scale optimization results. This solution has been subject to a detailed design process and is recommended to be built as a laboratory prototype. As a part of the detailed design process, all of the stress models used in the rapid performance assessment toolset have been validated using FEA. Various minor design features that were neglected during the design optimization have been addressed in detail, and most hardware has been specified. The laboratory prototype is projected to have an energy density of 8.8 kJ/kg and be capable of achieving a drive cycle efficiency of 87%.

9.3 Future Work

The details of numerous design features that are outside the scope of this thesis project will need to be addressed in the construction of the laboratory prototype and its test rig. After construction, for example, the laboratory prototype may require dynamic balancing. It is recommended that a professional balancing service provider perform this operation, should it be deemed necessary. The containment chamber must provide adequate protection for the experimentalists and facilitate easy service and maintenance. Additionally, a convenient process of removing leakage oil and applying vacuum to the chamber must be devised. To validate the models developed in this research and to prove the HFA concept, the prototype HFA should be interfaced with a hydraulic power system that is capable of simulating the transient tractive loads of a passenger vehicle. The details of this system, including the control scheme, are outside the scope of the presented work.

The recommended testing procedure is to drive the HFA through some power profile, measuring angular velocity, torque, piston position, pneumatic pressure, and hydraulic system pressure. The exact applied power profile should then be used as the input to the simulation toolset detailed in this thesis. The experimental and simulated results can be compared and the performance models adjusted as necessary. More accurate models will improve the robustness of future design optimization results.

In experimentally validating the HFA performance, several areas are of particular interest, as they have not been thoroughly addressed in this thesis. First, the fluid model detailed in Chapter 5 is truly applicable only to the specific geometry and working fluid with which it was developed. Second, the present model does not address the presumed exchange of kinetic energy between the oil and the solid HFA components when the pneumatic domain is charged or discharged. The HFA prototype should be used, in part, to expand upon the simple fluid model, such that it encompasses all reasonable HFA geometries and accounts for the extraction and addition of oil.

Some phenomena that are irrelevant for the recommended laboratory prototype may become important at the vehicle scale. Gyroscopic torque, for example, is a non-issue for

a stationary prototype, but in a passenger vehicle application it may affect the handling of the vehicle. The mounting orientation of the HFA has implications on which axes of the vehicle will be impacted by gyroscopic effects, and the size and rotational speed of the HFA dictate the magnitude. These should all be carefully considered when designing an HFA for a vehicle application.

The design goals for the containment chamber are also application-dependent. In the case of a laboratory prototype, the containment chamber can be heavily over-designed without significant negative impacts. For a passenger vehicle, however, the specification of the containment chamber should involve an optimization and detailed design process in itself. Namely, the chamber must not add an appreciable amount of mass to the HFA system, and its packaging volume must be non-intrusive to the passengers of the vehicle. The challenges of containment and gyroscopic effects are not unique to the present research; previous successful flywheel powertrain integrations can serve as guiding examples for HFA vehicle applications.

Finally, it should be emphasized that many of the fundamental decisions documented in this thesis have been made within the context and the constraints of academic research. It is possible that an improvement in HFA performance can be realize by altering some of these decisions. The end caps, for example have been specified as cylindrical components, simple to model and fabricate. Using hemispherical end caps would likely allow for the end cap mass to be further minimized. Similarly, given the complex nature of composite materials, the design of the housing may offer some opportunity for further optimization.

Even the architecture itself has been selected for its compatibility with model-based design; the free-floating end cap provides a simple loading case on the housing, eliminating axial stresses and facilitating a robust analytical stress model. Fundamentally-different architectures may offer advantages, albeit with the penalty of more costly and time-consuming design processes. Control strategy sophistication, too, can potentially effect a drastic improvement in the dynamic performance characteristics of the HFA.

Clearly, there is ample opportunity for further research and improvement of the HFA concept. However, the results of this early research are extremely promising. Even having made various concessions based on the present scope and constraints, it is projected that the HFA exhibits an order of magnitude higher energy density than static accumulator storage, while offering constant or near-constant pressure operation. These drastic improvements can enhance the performance of current mobile hydraulic systems and promote further adoption of hydraulics for vehicular propulsion.

Bibliography

[1] Solomon, S., Qin, D., Manning, M., Marquis, M., Averyt, K., Tignor, M., Miller, H. L. and Chen, Z., 2007, "Climate Change 2007: The Physical Science Basis," Cambridge Univeristy Press, New York, NY.

[2] McMichael, A. J., Woodruff, R. E. and Hales, S., 2006, "Climate Change and Human Health: Present and Future Risks," The Lancet, **367**, 859-869.

[3] Zhang, K., Douglas, B. C. and Leatherman, S. P., 2004, "Global Warming and Coastal Erosion," Climate Change, **64**(1), pp. 41-58.

[4] Malcom, J. R., Liu, C., Neilson, R. P., Hansen, L. and Hannah, L., 2006, "Global Warming and Extinctions of Endemic Species From Biodiversity Hotspots," Conservation Biology, **20**(2), pp. 538-548.

[5] 2014, "Inventory of U.S. Greenhouse Gas Emissions and Sinks: 1990-2012," U.S. Environmental Protection Agency, Washington, DC.

[6] Metz, B., Davidson, O., Bosch, P., Rutu, D. and Meyer, L., 2007, "Climate Change 2007: Mitigation of Climate Change," Cambridge Univeristy Press, New York, NY.

[7] Kintner-Meyer, M., Schneider, K. and Pratt, R., 2007, "Impacts Assessment of Plug-In Hybrid Electric Vehicles on Electric Utilities and Regional US Power Grids Part I: Technical Analysis," Pacific Northwest Laboratory, Richland, WA.

[8] Goering, C., Stone, M., Smith, D., Turnquist, P., 2006, *Off-Road Vehicle Engineering Principles*, American Society of Agricultural Engineers, St. Joseph, MI, Chaps. 2, 4.

[9] Parks, K., Denhold, P. and Markel, T., 2007, "Costs and Emissions Associated with Plug-In Hybrid Electric Vehicle Charging in the Xcel Energy Colorado Service Territory," NREL/TP-640-41410, National Renewable Energy Laboratory, Golden, CO.

[10] Westbrook, M. H., 2001, *The Electric Car: Development and Future of Battery, Hybrid and Fuel-Cell Cars*, The Institution of Engineering and Technology, London, UK.

[11] Lorenz, R. D. and Haines, L. P., 2000, *Understanding Modern Power Conversion*.

[12] Sclater, N., 1999, *Electronic Technology Handbook*, McGraw-Hill, New York, NY.

[13] Burke, A., 2000, "Ultracapacitors: Why, How, and Where is the Technology," J. Power Sources, **91**, pp. 37-50.

[14] Frank, A. A. and Beachley, N. H., 1979, "Evaluation of the Flywheel Drive Concept for Passenger Vehicles," No. 790049, *SAE Technical Paper*.

[15] Green Car Congress, 2014, “Ricardo TorqStor Flywheel Energy Storage Technology Recieves SAE 2014 World Congress Tech Award,” from http://www.greencarcongress.com/2014/04/20140401-torqstor.html.

[16] Filipi, Z., Louca, L., Daran, B., Lin, C.-C., Yildir, U., Wu, B., Kokkolaras, M., Assanis, D., Peng, H., Papalambros, P., Stein, J., Szkubiel, D. and Chapp, R., 2004, “Combined Optimisation of Design and Power Management of the Hydraulic Hybrid Propulsion System for the 6 x 6 Medium Truck,” Int. J. of Heavy Vehicle Systems, **11**(3/4), pp. 372-402.

[17] Flippo, W. and Rajabi, B., 2008, “Reduce Hydraulic Accumulator Cost with Back-Up Gas Bottles,” from http://www.designworldonline.com/reduce-hydraulic-accumulator-cost-with-back-up-gas-bottles.

[18] Li, P. Y., Van de Ven, J. D. and Sancken, C. S., 2007, “Open Accumulator Concept for Compact Fluid Power Energy Storage,” *Proceedings of the ASME International Mechanical Engineering Congress*, Seattle, WA, pp. 127-140.

[19] Pourmovahed, A., Baum, S. A., Fronczak, F. J., and Beachley, N. H., 1988, “Experimental Evaluation of Hydraulic Accumulator Efficiency With and Without Elastomeric Foam,” J. Propulsion, **4**(2), pp. 185-192.

[20] Sherman, M. P. and Karlekar, B. V., 1973. “Improving the Energy Storage Capacity of Hydraulic Accumulators,” *Proceeding of the AIAA 8th Intersociety Energy Conversion Engineering Conference*, pp. 202–207.

[21] Pedchenko, A. and Barth, E. J., 2009, “Design and Validation of a High Energy Density Elastic Accumulator Using Polyurethane,” *ASME Dynamic Systems and Control Conference*, Hollywood, CA, pp. 283-290.

[22] Tucker, J. M. and Barth, E. J., 2013, “Design, Fabrication, and Evaluation of a Distributed Piston Strain-Energy Accumulator,” Intl. J. Fluid Power, **14**(1), pp. 47-56.

[23] Van de Ven, J. D., 2009, “Increasing Hydraulic Energy Storage Capacity: Flywheel-Accumulator,” Intl. J. Fluid Power, **10**(3), pp. 41-50.

[24] Norton, R. L., 2008, *Design of Machinery*, McGraw-Hill, New York, NY, pp.72-73, Chap. 2.

[25] Genta, G., 1985, *Kinetic Energy Storage*, Butterworths, Cambridge, UK, pp. 55-67, Chap. 3.

[26] Pourmovahed, A., Beachley, N. H. and Fronczak, F. J., 1992, “Modeling of a Hydraulic Energy Regeneration System – Part I: Analytical Treatment,” J. Dynamic Systems, Measurement and Control, **114**, pp. 155-159.

[27] Gillespie, T. D., 1992, *Fundamentals of Vehicle Dynamics*, Society of Automotive Engineers, Inc., Warrendale, PA, pp. 111-118, Chap. 4.

[28] Juvinall, R. C., and Marshek, K. M., 2006, *Fundamentals of Machine Component Design*, Wiley, Hoboken, NJ, pp. 406-417, Chap. 10.

[29] Young, W. C., and Budynas, R. G., 2002, Roark's Formulas for Stress and Strain, McGraw-Hill, New York, NY, pp. 457-475, Chap. 11.

[30] Timoshenko, S., 1940, *Theory of Plates and Shells*, McGraw-Hill, New York, NY, pp. 55-75, Chap. 3.

[31] Heap, J. C., 1964, "Bending of Circular Plates Under a Uniform Load on a Concentric Circle," ANL-6905, Argonne National Lab, Argonne, IL.

[32] 2012, "2012 Seal Catalog," Hercules Sealing Products, Clearwater, FL.

[33] Perez-Aparicio, J. L. and Ripoll, L., 2011, "Exact, Integrated and Complete Solutions for Composite Flywheels," J. Composite Structures, **93**, pp. 1404-1415.

[34] Ha, S. K., Kim, S. J., Nasir, S. U. and Han, S. C., 2012, "Design Optimization and Fabrication of a Hybrid Composite Flywheel Rotor," J. Composite Structures, **94**, pp. 3290-3299.

[35] Ha, S. K., Kim, D. and Sung, T., 2001, "Optimum Design of a Multi-ring Composite Flywheel Rotor Using a Modified Generalized Plain Strain Assumption," Intl. J. Mechanical Sciences, **43**, pp. 993-1007.

[36] Arvin, A. C. and Bakis, C. E., 2006, "Optimal design of Press-fitted Filament Wound Composite Flywheel Rotors," J. Composite Structures, **72**, pp. 47-57.

[37] Arnold, S. M., Saleeb, A. F. and Al-Zoubi, N. R., 2002, "Deformation and Life Analysis of Composite Flywheel Disk Systems," J. Composites, **33**, pp. 433-459.

[38] Portnov, G., Uthe, A.-N., Cruz, I., Fiffe, R. P. and Arias, F., 2005, "Design of Steel-composite Multirim Cylindrical Flywheels Manufactured by Winding with High Tensioning and *In Situ* Curing. 1. Basic Relations," Mechanics of Composite Materials, **41**(2), pp. 139-152.

[39] Wild, P. M. and Vickers, G. W., 1996, "Analysis of Filament-wound Cylindrical Shells Under Combined Centrifugal, Pressure and Axial Loading," J. Composites, **28A**, pp. 47-55.

[40] Staab, G., 1999, *Laminar Composites*, Butterworth-Heinemann, Woburn, MA.

[41] International Organization for Standardization, 2003, "Mechanical Vibration –

Balance Quality Requirements for Rotors in a Constant (Rigid) State," 1940-1.

[42] Bamberger, E. N., Zaretsky, E. V. and Signer, H., 1975, "Effect of Speed and Load on Ultra-high-speed Ball Bearings," NASA TN D-7870, Lewis Research Center, Cleveland, OH.

[43] "High Precision Ball Bearings," 4000 0805, GMN Paul Muller Industrie GmbH & Co. KG, Numberg, Germnay.

[44] Smith, C., 1984, *Engineer to Win*, MBI, Osceola, WI, Chap. 3.

[45] 2014, "Online Materials Information Resource," from www.matweb.com.

[46] Bhushan, B., 2002, *Introduction to Tribology*, Wiley, Hoboken, NJ.

[47] Houpert, L., 2002, "Ball Bearing and Tapered Roller Bearing Torque: Analytical, Numerical and Experimental Results," Tribology Transactions, **45**(3), pp. 345-353.

[48] 2013, "Rolling Bearings," CAT. No. E1102m, NSK Motion and Control, Japan.

[49] 2009, "Ball and Roller Bearings," Catalog A-1000-XI, NTN, Mt. Prospect, IL.

[50] Stoneburner, M., 2005, "Hybrid Ceramic Bearings: More Mettle than Metal," *Plant Engineering*.

[51] Gorland, S. H., Kempke, E. E., Jr. and Lumannick, S., 1970, "Experimental Windage Losses for Close Clearance Rotating Cylinders in the Turbulent Flow Regime," NASA TM X-52851, Lewis Research Center, Cleveland, OH.

[52] Etemad, M. R., Pullen, K., Besant, C. B., and Baines, N., 1992, "Evaluation of Windage Losses for High-Speed Disc Machinery," *Proc. Instn. Mech. Engrs., Part A: J. Power and Energy*, Vol. 206, pp. 149-157.

[53] 2000, "A Descriptive Summary of Vickers Inline Pumps and their Applications," SE-103F, Vickers Fluid Systems, Jackson, MS.

[54] Pourmovahed, A., Beachley, N. H. and Fronczak, F. J., 1992, "Modeling of a Hydraulic Energy Regeneration System – Part II: Experimental Program," J. Dynamic Systems, Measurement and Control, **114**, pp. 160-165.

[55] Nellis, G. and Klein, S., 2009, *Heat Transfer*, Cambridge University Press, New York, NY.

[56] American National Standards Institute, 1985, "Surface Texture," B46.1-1985.

[57] White, F. M., 2008, *Fluid Mechanics*, McGraw-Hill, New York, NY, pp. 382-386, Chap. 6.

[58] Johnson, M. L., Manos, D. M. and Provost, T., 1997, "Gas Permeation and Leakage Through Reusable Seals," J. Vac. Sci. Technol. A, **15**(3), pp. 763-767.

[59] Rack, P. D., "Pumpdown and Vacuum Pumps," lecture slides.

[60] Umrath, W., 2007, "Fundamentals of Vacuum Technology," Oerlikon Leybold Vacuum, Cologne, Germany.

[61] Moran, M. J. and Shapiro, H. N., 2008, *Fundamentals of Engineering Thermodynamics*, Wiley, Hoboken, NJ, p. 308, Chap. 6.

[62] Chiggiato, P., 2006, "Outgassing," *Vacuum in Accelerators Conference*, Platja d'Aro, Spain.

[63] Perkins, W. G., 1973, "Permeation and Outgassing of Vacuum Materials," J. Vac. Sci. Technol., **10**(4), pp. 543-556.

[64] Sonderegger, K., 2006, "Vacuum Sealing Technology," *Vacuum in Accelerators Conference*, Platja d'Aro, Spain.

[65] Strohmaier, K. G. and Van de Ven, J. D., 2013, "Constrained Multi-Objective Optimization of a Hydraulic Flywheel Accumulator," *ASME/Bath Symposium on Fluid Power and Motion Control*, Sarasota, FL.

[66] Greenspan, H. P. and Howard, L. N., 1963, "On a Time-dependent Motion of a Rotating Fluid," J. Fluid Mechanics, **17**(3), pp. 385-404.

[67] Benton, E. R. and Clark Jr., A., 1974, "Spin-up," Annual Review of Fluid Mechanics, **6**(1), pp. 257-280.

[68] Wiedman, P. D., 1976, "On the Spin-up and Spin-down of a Rotating Fluid. Part 1. Extending the Wedemeyer Model," J. Fluid Mechanics, **77**(4), pp. 685-708.

[69] Duck, P. W. and Foster, M. R., 2001, "Spin-up of Homogeneous and Stratified Fluids," Annual Review of Fluid Mechanics, **33**(1), pp. 231-263.

[70] Wedemeyer, E. H., 1964, "The Unsteady Flow Within a Spinning Cylinder," J. Fluid Mechanics, **20**(3), pp. 383-399.

[71] 2013, "Dynamometer Drive Schedules," from http://www.epa.gov/nvfel/testing/dynamometer.htm.

[72] Cole, D., 1972, "Elementary Vehicle Dynamics," course notes in Mechanical Engineering, University of Michigan, Ann Arbor, MI.

[73] Deb, K., Pratap, A., Agarwal, S., and Meyarivan, T, 2002, "A Fast and Elitist

Multiobjective Genetic Algorithm: NSGA-II," *IEEE Trans. On Evolutionary Comp.*, **6**(2), pp.182-197.

[74] Michalewicz, Z., 1995, "Genetic Algorithms, Numerical Optimization, and Constraints," *Proceedings of the Sixth International Conference on Genetic Algorithms*, Morgan Kaufmann, San Mateo, CA, **195**, pp. 151-158.

[75] Cheong, K. L., Li, P. Y. and Chase, T. R., 2011, "Optimal Design of Power-Split Transmissions for Hydraulic Hybrid Passenger Vehicles," *American Control Conference*, IEEE, San Francisco, CA, pp. 3295-3300.

[76] 2007, "Parker O-ring Handbook," ORD 5700, Parker Hannifin Corporation, Cleveland, OH.

Appendix A: Nomenclature

List of Abbreviations

GHG	greenhouse gas emissions
HFA	hydraulic flywheel-accumulator
HSRU	high-speed rotary union
ICE	internal combustion engine
NVH	noise, vibration and harshness
PM	pump-motor
SOC	state-of-charge
STP	standard temperature and pressure
UDDS	Urban Dynamometer Driving Schedule
PO	Pareto-optimal

List of Variable Names from Latin Alphabet

a	inner radius, generic
a_{ch}	effective molecular diameter of gas in the containment chamber
A_f	vehicle frontal area
A_i	inner area of infinitesimal fluid volume
A_o	outer area of infinitesimal fluid volume
A_p	axial area of piston
A_q	area exposed to gas permeation
A_s	side area of infinitesimal fluid volume
$A_{x,p}$	axle cross-sectional area at the radial ports
$A_{f,scaled}$	scaled vehicle frontal area
A_k	required shear area of key
b	outer radius, generic
C_0	bearing static load rating
c_1, c_2	constants used to express P_g0
C_1, C_2	constants used to relate m and W_dc
c_{ch}	clearance between housing and containment chamber
C_D	vehicle drag coefficient
C_m	aerodynamic moment coefficient
$C_s, C_{st}, C_v, C_f, C_h$	pump-motor empirical loss coefficients
c_s	circumferential seal clearance
c_g	gap size used for various HSRU case features
d	diameter, generic
D	maximum pump-motor displacement
$d_{b,i}$	bearing inner diameter
$d_{b,o}$	bearing outer diameter
D_g	length of piston seal groove
d_i	axle inner diameter
d_{lp}	diameter of leakage port on high-speed rotary union case
d_p	port diameter
d_s	circumferential seal diameter

d_t	vehicle tire diameter
d_{unf}	unfinished distance of a drive cycle
d_l	diameter of leakage port in HSRU
e	parameter used to calculate equivalent bearing load
E	stored energy
E_a	axle modulus of elasticity
E_d	design energy capacity
E_k	stored kinetic energy
$E_{k,f}$	kinetic energy stored in the rotating fluid
$E_{k,s}$	kinetic energy stored in the container ("solid")
E_m	modulus of elasticity, generic
E_p	stored pneumatic energy
$\bar{f}$	average friction factor
F_a	axial force in axle
F_{aero}	aerodynamic drag force on vehicle
f_{af}	frontal area factor used to scale drive cycle energy and power
F_{b1}	upper bearing force
F_{b2}	lower bearing force
$F_{b,max}$	maximum axial bearing load
f_c	charge fraction
$f_{control}$	control fraction used by the control strategy
$f_{d,i}$	axle inner diameter fraction
F_{ecc}	eccentric force
f_l	liner thickness fraction
f_m	mass factor used to scale drive cycle energy and power
F_p	force acting on an end cap due to pneumatic pressure
$F_{p,max}$	maximum expected force due to pneumatic pressure
$f_{pressure}$	pressure fraction to characterize observed pressure fluctuation
f_r, f_o, f_s	vehicle rolling coefficients
F_{rl}	road load force
F_{roll}	rolling resistance force on vehicle
F_s	axial force acting on axle due to system pressure
$F_{s,max}$	maximum expected force on the axle due to system pressure
f_{switch}	maximum allowable switching frequency for kinetic domain
F_t	tractive force
f_{th}	thickness fraction for housing wall
f_{af}	frontal area factor used to scale drive cycle power and energy
f_m	mass factor used to scale drive cycle power and energy
$F_{V,ss}$	shear force acting on pin system shoulder screw
g	acceleration of gravity
H_g	height of piston seal groove
I_f	equivalent moment of inertia, fluid components
I_o	moment of inertia of oil volume
I_s	moment of inertia, solid components
k	minor loss coefficient for duct flow
K	Boltzmann constant
k_{axial}	sum of minor loss coefficients for axial port of axle
$k_{d,N}$	permeation constant for VITON® and Nitrogen

$k_{d,O}$	permeation constant for VITON® and Oxygen
$k_{entrance}$	minor loss coefficient for a duct entrance
k_{exit}	minor loss coefficient for a duct exit
k_n	stress concentration factor for normal force
$k_{n,os}$	normal stress concentration factor for axle shaft
k_o	constant offsets for the fluid model empirical correlations
k_p	permeation constant
k_{radial}	sum of minor loss coefficients for radial ports of axle
k_s	wave spring constant
k_{tee}	minor loss coefficient for a duct tee
$k_{t,gs}$	torsional stress concentration factor for axle shaft
Kn	Knudsen number
l	length, generic
l_a	length of axle port of axle
l_{as}	length of axle shoulder
l_h	housing length
l_i	housing inner length
l_o	length of oil volume
l_p	length of piston bearing section
l_b	length of boss between piston seals
L^+	dimensionless length used in duct flow calculation
l_{PM}	approximate length of storage pump-motor
l_q	gas permeation distance
l_r	retainer length
l_s	circumferential seal length
$l_{s,g}$	gas side shaft length
$l_{s,o}$	oil side shaft length
l_2	length of secondary seal in HSRU
l_k	keyway length
m	mass of primary rotating HFA components
m_a	axle mass
M_c	circular plate circumferential bending moment profile
M_{ch}	molecular mass of gas in the containment chamber
m_e	single end cap mass
m_h	housing mass
m_o	mass of oil volume
m_p	piston mass
m_{PM}	pump-motor mass, generic
$m_{PM,s}$	storage pump-motor mass
$m_{PM,t}$	traction pump-motor mass
M_r	circular plate radial bending moment profile
m_s	mass of solid components
m_{sys}	mass of HFA system, including storage and traction pump-motors
m_v	vehicle mass
$m_{v,scaled}$	scaled vehicle mass
N_{ss}	number of shoulder screws used in pin system
P	pressure, generic
P_{atm}	atmospheric pressure
ΔP_{axial}	pressure drop in axial port of axle

P_c	gas charge pressure
P_{ch}	pressure in the containment chamber
$P_{ch,d}$	desired containment chamber pressure
P_d	hydraulic system pressure, design
P_{eq}	equivalent bearing load
P_g	gas pressure distribution
P_{g0}	gas pressure at the axis of rotation
P_{int}	internal pressure acting on the liner
P_{net}	net pressure distribution across piston
P_o	oil pressure distribution
P_p	pneumatic pressure
P_r	retaining ring reaction pressure
ΔP_{radial}	pressure drop in radial ports of axle
P_s	hydraulic system pressure, actual
$P_{s,max}$	maximum expected system pressure
ΔP	pressure drop across axle due to throttling losses
$\dot{q}$	volumetric viscous dissipation rate
Q_{gas}	gas load on vacuum system
Q_{perm}	gas permeation rate
r	radial position
$R, R_s, R_f, R_{95}, R_{99}$	coefficients of determination used in assessing the fluid model
r_a	axle radius
R_c	capacity ratio
r_{ch}	approximate inner radius of containment chamber
r_{ecc}	radius of eccentricity
r_f	radius of fillet where axle shafts meet the main portion of the axle
r_i	housing inner radius
r_o	housing outer radius
$r_{r,i}$	retainer inner radius
$r_{r,o}$	retainer outer radius
R_u	control strategy usage ratio
$r_{c,i}$	inner radius of a contact area
$r_{c,o}$	outer radius of a contact area
Re	Reynolds number, generic
r_{ss}	approximate load-carrying radius of pin system should screw
S	dimensionless number used in pump-motor modeling
S_p	vacuum pumping speed
S_y	yield strength, generic
$S_{y,a}$	axle yield strength
$S_{y,e}$	end cap yield strength
$S_{y,l}$	liner yield strength
$S_{y,p}$	piston yield strength
SF	safety factor for material failure
SF_l	calculated material safety factor of liner
SF_w	calculated material safety factor for housing wrap
$S_{s,k}$	shear strength of key
$S_{y,c}$	yield strength of HSRU case
$S_{y,ss}$	yield strength of pin system shoulder screw

t	time
T	storage pump-motor torque
Δt	time step size
T_b	bearing frictional torque
T_{ch}	absolute temperature of gas in the containment chamber
t_{dec}	deceleration time
T_{dec}	deceleration torque
t_E	Ekman time constant
T_m	torque measured during fluid experiments
t_o	o-ring thickness
$t_{pumpdown}$	time required for vacuum chamber pumpdown
$t_{switch,last}$	last time that kinetic domain was toggled on or off
T_w	aerodynamic torque
th_b	thickness of piston bearing section
th_c	HSRU case thickness
th_e	end cap thickness
th_l	liner thickness
th_p	thickness of piston disc section
$\bar{u}$	mean fluid velocity
u_d	energy density
u_r	radial component of fluid velocity
u_s	axial flow velocity in circumferential seal
u_θ	azimuthal component of fluid velocity
u_z	axial component of fluid velocity
v	drive cycle velocity in m/s
$\forall$	volume, generic
$\dot{\forall}$	volume flow rate, generic
$\forall_o$	instantaneous oil volume
$\forall_c$	gas charge volume
$\forall_{ch}$	volume of gas in the containment chamber
v_{dc}	drive cycle velocity in mph
$\forall_g$	instantaneous gas volume
$\forall_l$	cumulative volume of oil leaked into containment chamber
$\dot{\forall}_l$	volumetric flow rate of high-speed rotary union leakage oil
$\forall_{l,max}$	maximum allowable cumulative oil leakage volume
$\dot{\forall}_o$	volumetric flow rate of oil in pneumatic domain
v_s	radial flow velocity in circumferential seal
w_s	tangential flow velocity in circumferential seal
$\dot{W}_k$	kinetic power
$\dot{W}_p$	pneumatic power
$\dot{W}_t$	tractive (total, road) power
$\dot{W}_a$	axle throttling power dissipation
$\dot{W}_b$	bearing power dissipation
w_{br}	bearing width
W_{dc}	drive cycle energy
$\dot{W}_f$	power to the rotating fluid volume
$\dot{W}_l$	leakage power dissipation in high-speed rotary union
$\dot{W}_{lab}$	power capacity of laboratory hydraulic power supply

W_{loss}	total cumulative energy loss
W_{loss}	total drive cycle energy losses
$\dot{W}_{PM}$	storage pump-motor power dissipation
$W_{pumpdown}$	energy required for vacuum chamber pumpdown
$\dot{W}_s$	storage PM shaft power
W_{vac}	cumulative energy consumed by vacuum system
$\dot{W}_b$	vacuum pumping power
$\dot{W}_{vh}$	viscous power dissipation in high-speed rotary union
$\dot{W}_v$	internal viscous power dissipation
$\dot{W}_w$	aerodynamic ("windage") power dissipation
w_{br}	bearing race axial width
w_k	key width
w_r	bearing race radial width
x	pump-motor fractional displacement position
X, Y, X_0, Y_0	constants used to calculate equivalent bearing loads
x_o	wave spring precompression
X_w	longitudinal tensile strength of composite material
Y_w	transverse tensile strength of composite material

List of Variable Names from Greek Alphabet

α_f	equivalent fluid angular acceleration
α_s	container ("solid") angular acceleration
β_o	oil bulk modulus
γ	ratio of specific heats for air
δ	boundary layer thickness
δ_a	axial elongation of the axle
δ_r	radial displacement
$\Delta\Omega$	step change in angular velocity for an impulsive spin-up event
$\Delta\omega$	difference between container and fluid angular velocities
ϵ_c	circumferential strain
η	drive cycle efficiency
η_m	pump-motor mechanical efficiency
η_v	pump-motor volumetric efficiency
θ	tangential position
λ	length scale that characterizes the HFA rotor
μ_{st-st}	static friction coefficient of a steel-on-steel contact area
μ_b	bearing friction coefficient
μ_c	static friction coefficient of a contact area
μ_{ch}	dynamic viscosity of gas in the containment chamber
μ_o	oil dynamic viscosity
ν	Poisson ratio
ν_L	longitudinal Poisson ratio for anisotropic material
ν_o	oil kinematic viscosity
ρ	density, generic
ρ_{atm}	gas density at atmospheric pressure
ρ_{ch}	density of gas in the containment chamber
ρ_g	gas density

ρ_o	oil density
ρ_{ss}	density of pin system shoulder screw
σ	dimensionless number used in pump-motor modeling
$\sigma_{c,bend}$	circular plate circumferential bending stress profile
$\sigma_{c,cent}$	circumferential stress due to centrifugation
$\sigma_{\mathrm{h},max}$	maximum hoop stress in the housing of a static accumulator
$\sigma_{N,ss}$	maximum normal stress in pin system shoulder screw
$\sigma_{r,bend}$	circular plate radial bending stress profile
$\sigma_{r,cent}$	radial stress due to centrifugation
$\sigma_{vm,a}$	axle maximum von Mises stress
$\sigma_{vm,e}$	end cap maximum von Mises stress
$\sigma_{vm,p}$	piston maximum von Mises stress
$\sigma_{z,s}$	maximum axial stress in oil side axle shaft
$\sigma_{z,os}$	maximum axial stress in oil side axle shaft
σ_a	axial stress in the non-ported section of the axle
σ_r	radial stress, generic
σ_z	axial stress, generic
σ_θ	circumferential stress, generic
$\tau_{T,gs}$	maximum torsional shear stress in gas side axle shaft
$\tau_{V,c}$	shear stress in HSRU case
$\tau_{V,gs}$	maximum transverse shear stress in gas side axle shaft
$\tau_{V,os}$	maximum transverse shear stress in oil side axle shaft
$\tau_{V,ss}$	maximum transverse shear stress in pin system shoulder screw
τ_d	dynamic time constant for fluid model
ω	angular velocity
Ω	angular velocity used to characterize impulsive spin-up event
ω_f	equivalent fluid angular velocity
ω_{max}	maximum angular velocity
ω_s	container (“solid”) angular velocity
ω_t	vehicle tire angular velocity

Appendix B: MATLAB© Code for the Model-based Design and Simulation Toolset

This appendix includes the MATLAB© code for the model-based design and simulation toolset that constitutes a major portion of the present research. Note that some of the features of this code allow for the analysis of alternate design choices, such as a homogenous isotropic housing, external placement of the HSRU and storage PM, or the use of a variable-displacement storage PM. It also features the ability to implement an iterative sizing algorithm for the storage PM.

main.m

This master script is a simple set of code that sets several overarching options and calls various subscripts to commence a session of model-based design and simulation. Execution of this script relies on an HFA design solution having been specified. This is done by storing a variable `spec`, a 1 by 9 array of the design variable values, in a *.mat* file called `specFile`.

```
%% Clear Data and Begin Timer
clear all;
clc;
tic;

%% Select Logistical Options
optimizing = 0; %indicator for whether code is being used for an
optimization
HUD = 0;    %toggle heads up display
makeMovie = 0;  %record a movie of the heads up display
movieFps = 1;   %set movie frames per second
maxSizeCt = 1;  %set the number of iterations to try resizing the
storage PM

%% Define Constants
defineConstants;

%% Set Up Drive Cycle
driveCycleSetup;

%% Get Design Parameters
load specFile;  %load file with HFA specs
[r_o, len_i, f_th, f_l, f_d_i, l_s, c_s, omega_d, f_charge] ...
    = loadDesignParams(spec);
clear spec; %clear array with HFA specs

%% Perform Calculations Independent of Drive Cycle Performance
preSimCalcs;

%% Perform Drive Cycle Simulation and Post-Simulation Calculations
if sum(geoInfeas)~=0 %simulation cancelled
    optimizationCalcs;
```

```
else    %simulation was run
    runSimulation;

    optimizationCalcs;

    postSimCalcs;

end

%% Display Results
displayResults;

%% Write .avi File
if makeMovie && HUD
    writerObj = VideoWriter('simMovie','Motion JPEG AVI');
    writerObj.FrameRate = movieFps;
    writerObj.Quality = 50;
    open(writerObj);
    writeVideo(writerObj,F);
    close(writerObj);
    delete(writerObj);
end
```

defineConstants.m

This script defines all of the values that are independent of the specific HFA design solution and do not change over the course of a simulation.

```
%% Load Saved Data
load('angContBearingDataFile'); %bearing database

%% Define Universal Constants
P_atm = 101.3e3;    %absolute atmospheric pressure, Pa
T_atm = 300;    %ambient temperature, K
rho_a = 1.29; %density of atmospheric air, kg/m^3
m_m = 4.782e-26;    %molecular mass of air, kg
a_m = 3.68e-10;    %effective molecular diameter, m
K_boltz = 1.38e-23;   %Boltzman constant, J/K
g = 9.81;   %acceleration of gravity, m/s2

%oil properties
rho_o = 879; %oil density, kg/m^3
nu_o = 46*(1/1000)^2; %oil kinematic viscosity, m2/s
mu_o = nu_o*rho_o;    %oil dynamic viscosity, kg/m-s
beta_o = 1.4e9;    %oil bulk modulus, Pa

%fluid model coefficients
cmat_v = [6.69 -1.77e-2 1.95e-5 -2.18e4 0 1.28e5 4.16e3];   %viscous
dissipation coefficients
cmat_t = [0 -3.76e-19 2.54 4.07 .0039]; %dynamic time constant
coefficients
n_pi_v = 3; %number of pi groups in viscous dissipation correlation
```

```
order_v = 3;    %order of polynomial fit for viscous dissipation
correlation
n_pi_t = 3; %number of pi groups in dynamic time constant correlation
order_t = 2;    %order of polynomial fit for dynamic time constant
correlation

%% Define Vehicle Specs
%vehicle external characteristics
f_af = 0.08;    %frontal area factor
f_m = 0.04; %mass factor
C_d = 0.3;    %drag coefficient
A_f = f_af*2.3;  %frontal area, m2
m_v = f_m*1800;    %mass, kg
a_1 = .009; %basic rolling coefficient
a_2 = .0035;    %speed rolling coefficient
eta_trans = 1;  %transmission efficiency
d_t = .664;   %tire diameter (P215/60R16 94V), m

%% Define Control and Drive Cycle Specs
%control strategy parameters
P_d = 3000*(101300/14.7) + P_atm;   %desired hydraulic system pressure,
Pa
t_switchMin = .5;    %minimum time between switching power methods
f_control = .06;   %control band (full range), fraction of desired
system pressure
R_control = 1.5;   %PM sizing goal for f_pressure/f_control
utilVDPM_min = 0.95;  %minimum required VDPM utilization

%select number of drive cycle "laps" and time step size
N_dc = 1;   %number of laps
dt = 0.125;    %time step size

%laboratory specifications
W_dot_lab = 3000*(101300/14.7)*5*0.000063;  %hydraulic power supply
capacity, W

%% Define Maximum Expected Loading
T_max = 200;    %guess for the maximum expected torque, N-m
G = 6.3;    %balancing grade (ISO 1943), mm/s
SF_ecc = 10; %safety factor on eccentricity, used for bearing selection

%% Define Accumulator Materials and Architecture
arch = [1 1 1];   %architecture definition array, [0=outside/1=inside;
0=VD/1=FD; 0=metal/1=composite-wrapped]
SF = 3; %safety factor for material failure

%housing
switch arch(3)
    case 0
        [rho_h, nu_h, E_h, S_y_h] = propsMetal('ti');

    case 1
        %composite
        [rho_c, E1, E2, nu12, nu21, X, Y, Yc] =
propsComposite('T300/2500');
```

```
        %liner
        [rho_l, nu_l, E_l, S_y_l] = propsMetal('4140_q_t205_1in');
end

%end caps
[rho_e, nu_e, E_e, S_y_e] = propsMetal('7075');

%axle (bolt)
[rho_b, nu_b, E_b, S_y_b] = propsMetal('4340_q800_t540_4in');

%piston
[rho_p, nu_p, E_p, S_y_p] = propsMetal('7075');
BR = 1.5; %piston-tie rod bearing ratio

%chamber
[rho_ch, nu_ch, E_ch, S_y_ch] = propsMetal('4140');

%% Define Axle and End Cap Constants
N_p = 1;    %number of radial ports
f_p_i = 1;  %port diameter fraction
k_exit = 1;    %pipe exit loss coefficient
k_entr = .4;    %pipe entrance loss coefficient
k_tee = .3;    %tee loss coefficient
epsilon = 1.6*(1e-6);    %surface roughness, smooth turned, micron
mu_st_st = .5;  %steel-on-steel friction coefficient (conservative)
mu_st_al = .61; %steel-on-aluminum friction coefficient
d_lp = .01; %leakage port diameter, m
gap = .002;  %HSRU safety gap, m

%% Define Bearing constants
C_b_m = 1.0e-3;    %bearing torque mass coefficient, Nm/kg
N_b = 2;    %number of bearings

%% Define Containment Chamber and Feedthrough Parameters
c_ch = 0.01;  %chamber-HFA clearance, m
N_ring = 2; %number of o-rings required to seal containment chamber

if arch(1) == 0
    P_ch_d = .1;   %desired chamber pressure, Pa
    Q_ft = 1e-11*(101300/1)*(1/100)^3;    %FerroTec shaft seal leakage
rate (conv. from Std ccHe/s), Pa-m3/s
    C_ft_c = 0.0148; %feedthrough drag torque constant, Nm
    C_ft_s = 9e-5;   %feedthrough drag torque slope coefficient,
Nm/rad/s
else
    P_ch_d = 14;    %desired chamber pressure (higher than P_vap for
oil), Pa
    Q_ft = 0; %no rotary shaft seal
    C_ft_c = 0; %no feedthrough
    C_ft_s = 0; %no feedthrough
end
f_band_vac = .005;   %allowable fraction above desired pressure
beta_ch = 1.4; %ratio of spec heats (air)
S_p_on = 1e-4;    %pumping speed, m3/s
```

```
%% Define HFA Pump/Motor Specs
G_PM = 1;   %pump-motor gear ratio
eta_GR = 1;    %gear reduction efficiency
a_spd = 32.04;  %a-coefficient for D-omega_max correlation
b_spd = -0.2812;    %b-coefficient for D-omega_max correlation
m_mass = 2.36e5;    %m-coefficient for D-mass correlation
b_mass = 1.123;     %b-cofficient for D-mass correlation
len_PM = .25;   %approximate length of PM (as well as shafts and HSRU
case), m

%manufacturer loss coefficients
C_s = 4.259e-9;    %laminar slip coefficient
C_st = 0;   %turbulent slip coefficient
C_v = 23523;    %viscous loss coefficient
C_f = .0537;    %frictional loss coefficient
C_h = 53.56;    %hydrodynamic loss coefficient
```

propsMetal.m

This function stores various material properties for the metals used in the HFA.

```
function [rho, nu, E, S_y] = propsMetal(matl)
%rho: material density, kg/m3
%nu: Poisson Ratio
%E: Young's Modulus, Pa
%S_y: tensile yield strength, Pa
switch matl
    % Steels
    case '4140' %AISI 4140 alloy steel (azom.com)
        rho = 7850;
        nu = .3;
        E = 200e9;
        S_y = 415e6;
    case '4340_q800_t540_4in'   %AISI 4340, oil quenched 800C, 540
temper (matweb)
        rho = 7850;
        nu = .29;
        E = 205e9;
        S_y = 1000e6;
        S_y = 1515e6;

        % Aluminums
    case '7075'   %7075-T6 aluminum (asm.matweb.com)
        rho = 2810;
        nu = .33;
        E = 72e9;
        S_y = 503e6;
    case 'gray iron'
        rho = 7150;
        nu = .29;
        E = 110e9;
        S_y = 290e6;
end
```

propsComposite.m

This function is the composite material counterpart to the function *propsMetal.m* (above). Though the material T300/#2500 was the only composite used for the present research, several others are stored in this function to facilitate material tradeoff studies.

```
function [rho, E1, E2, nu12, nu21, X, Y, Yc] = propsComposite(matl)
%rho: composite density, kg/m3
%t: ply thickness, m
%E1: fiber-direction Young's Modulus, Pa
%E2: transverse Young's Modulus, Pa
%G12: shear modulus, Pa
%nu12: 1-2 Poisson's ratio (strain in 1-direction causing strain in 2-
direction)
%nu21: 2-1 Poisson's ratio
%X: tensile strength in fiber direction, Pa
%Y: tensile strength perpendicular to fiber direction, Pa
%Yc: compressive strength perpendicular to fiber direction, Pa
switch matl
    case 'HM'    %HM Graphite/Epoxy (??)
        rho = 1.63e3;
        E1 = 230e9;
        E2 = 6.6e9;
        nu12 = .25;
        nu21 = nu12*E2/E1;
        X = 1100e6;
        Y = 21e6;
        Yc = 100e6;
    case 'T300/2500'    %T300 Carbon Fiber, 2500 Epoxy (Ha)
        rho = 1600;
        E1 = 130e9;
        E2 = 9e9;
        nu12 = .3;
        nu21 = nu12*E2/E1;
        X = 1800e6;
        Y = 80e6;
        Yc = 168e6;
    case 'T300/BSL914C'    %T300 Carbon Fiber, CSL914C Epoxy (Soden)
(V_f=0.6)
        rho = 1600;
        E1 = 138e9;
        E2 = 11e9;
        nu12 = .28;
        nu21 = nu12*E2/E1;
        X = 1500e6;
        Y = 27e6;
        Yc = 200e6;
end
```

driveCycleSetup.m

This script imports the EPA-specified UDDS from a text file in the working directory called 'uddscol.txt,' increases the drive cycle resolution, and calculates various drive cycle characteristics that are independent of the specific HFA design solution.

```
%import and duplicate drive cycle
driveCycle = importdata('uddscol.txt'); %import drive cycle
dt_unr = driveCycle(2,1) - driveCycle(1,1); %unresolved time step size,
s
v_mph = []; %build vehicle velocity array, mph
for i = 1:N_dc
    v_mph = vertcat(v_mph,driveCycle(:,2));
end
v_unr = v_mph*1609.344/3600;    %vehicle velocity, m/s

%increase drive cycle resolution
[t, v, n, dt, f_time, t_tot] = increaseDCresolution(dt_unr, v_unr, dt);

%calculate other drive cycle values
n = n-1;    %subtract last data point because of FDE for vehicle
acceleration
a = diff(v)./dt;    %vehicle acceleration, m/s2
v = v(1:n); %truncated velocity array, m/s
d = cumsum(v*dt);   %distance array, m
t = t(1:n); %truncated time array, s
```

loadDesignParams.m

This function extracts the design parameter values from the worskspace variable `specFile` and assigns them to their appropriate variables.

```
function [r_o, len_i, f_th, f_l, f_d_i, l_s, c_s, omega_d, ...
    f_charge] = loadDesignParams(array)

%housing parameters
r_o = array(1);  %housing outer radius, m
len_i = array(2);    %HFA inner length (distance between end caps), m
f_th = array(3);   %fraction of housing outer radius that is material
f_l = array(4); %fraction of wall material that is liner

%HSRU parameters
f_d_i = array(5);  %HSRU shaft inner diameter, fraction of housing
inner diameter
l_s = array(6);  %HSRU seal length, m
c_s = array(7);  %HSRU seal clearance, m

%operational parameters
omega_d = array(8);  %HFA maximum angular velocity, rad/s
f_charge = array(9);    %HFA charge pressure fraction (P_c =
f_charge*P_s)
```

```
end
```

preSimCalcs.m

This is a major script that executes all of the calculations that can or must be performed before a drive cycle simulation. This includes most of the stress-driven dimension selections covered in Chapter 3, as well as mass, inertia, energy capacity and road load calculations. The script also performs a geometric feasibility check and sizes the storage PM.

```
%% Calculate Housing Properties
th = f_th*r_o;  %total wall thickness, m
r_i = r_o - th; %housing inner radius, m

if arch(3) == 1
    th_l = f_l*(r_o - r_i);   %liner thickness, m
    th_c = th - th_l;  %composite thickness, m
    r_l = r_i + th_l;   %radius of liner-composite interface, m
end

%% Calculate Relevant Pressures
P_c = f_charge*P_d; %charge pressure, Pa
rho_g_c = rho_a*P_c/P_atm;    %gas density at charge (assume air
properties), kg/m3
P_s_min = (1 - f_control/2)*P_d;   %upper bound on control band, Pa
P_s_max = (1 + f_control/2)*P_d;   %upper bound of control band, Pa
P_int_max = P_s_max + (1/2)*rho_o*omega_d^2*r_i^2;  %wall pressure at
max pressure condition, Pa

%% Size the Axle
d_i = f_d_i*2*r_i;    %HSRU shaft inner radius, m
d_p = f_p_i*d_i;    %port diameter, m
d_s = calcSealDiameter(1.2*P_s_max,d_i,S_y_b/SF);   %clearance seal
diameter, m

[r_a, P_h_max, F_b_max, F_s_max, ~, k_s, delta_a] = sizeAxle(d_i, d_s,
...
    r_i, len_i, N_p, d_p, S_y_b/SF, E_b, rho_o, omega_d, 1.2*P_s_max,
...
    rho_l*pi*len_i*(r_l^2 - r_i^2)+rho_c*pi*len_i*(r_o^2 - r_l^2), g);
%axle outer radius, m
P_h_d = P_d + (1/4)*rho_o*omega_d^2*(r_i^2 + r_a^2);  %design pneumatic
pressure pressure, Pa
detailAxle; %perform detailed design on the axle

%% Size the End Caps
P_b_max = P_s_max + (1/2)*rho_o*omega_d^2*r_a^2;    %pressure at bolt
at max pressure condition, Pa
%calculate required end cap length, m
[len_e,P_o_worst,P_g_worst,F_b_max_check,sigma_vm_e_check] =
sizeEndCaps(r_i, r_a, r_r_o-r_a, 50, ...  %geometry
```

```
    1.2*P_s_max, omega_d, ...     %worst-case parameters
    rho_o, rho_a, P_atm, ...     %constants
    rho_e, E_e, nu_e, S_y_e/SF);   %material properties
len_h = len_i + 2*len_e;    %housing length, m
disp_b = F_b_max/E_b*(4*len_e/(pi*((2*r_a)^2 - d_i^2)) + ...
    d_p/(pi*((2*r_a)^2 - d_i^2)/4 - N_p*d_p*r_a) + ...
    4*(len_i - d_p + len_e)/(pi*(2*r_a)^2));    %maximum axial
elongation of axle, m

%% Calculate Piston Dimensions
th_p = sizePiston(r_i,r_a,0,P_o_worst-P_g_worst,omega_d,...
    rho_p,E_p,nu_p,S_y_p/SF); %piston thickness, m
H_g = .005;   %approximate groove depth for piston seals, m
D_g = .01;  %approximate groove width for piston seals, m
l_pb = H_g*(SF*P_c)/(0.58*S_y_p);   %minimum thickness of boss between
seals, m
th_p = max(th_p,l_pb+2*D_g);  %check for seal packaging
th_b = 2*H_g; %thicknes of bearing section, twice seal groove height, m
len_p = BR*2*r_a;    %piston bearing length
Vol_g_min = pi*(r_i^2-(r_a+th_b)^2)*(len_p-th_p);   %minimum gas volume
(piston dead volume), m3
Vol_o_min = 0;  %minimum oil volume -- in reality will be non-zero, m3
Vol_p = pi*(r_i^2-r_a^2)*len_p - Vol_g_min;    %piston volume, m3

%% Values Specific to Charge and Design Conditions
Vol_i = pi*len_i*(r_i^2 - r_a^2); %housing inner volume, m3
Vol_c = Vol_i - Vol_p - Vol_o_min; %gas volume at charge, m3
Vol_g_d = Vol_c*P_c/P_h_d;  %gas volume at design condition, m3
Vol_o_d = Vol_i - Vol_p - Vol_g_d;  %oil volume at design condition, m3
m_o_d = rho_o*Vol_o_d;  %design oil mass, kg
I_o_d = (1/2)*m_o_d*(r_i^2 + r_a^2);      %design oil moment of
inertia, kg-m^2

%% Size the Bearings and Shafts
%calculate primary mass contributions
switch arch(3)
    case 0
        m_h = rho_h*pi*len_h*(r_o^2 - r_i^2);   %housing mass, kg
        I_h = (1/2)*m_h*(r_o^2 + r_i^2);    %housing inertia, kg
    case 1
        m_l = rho_l*pi*len_h*(r_l^2 - r_i^2);   %liner mass, kg
        m_c = rho_c*pi*len_h*(r_o^2 - r_l^2);   %composite mass, kg
        m_h = m_l + m_c;    %housing mass, kg
        I_l = (1/2)*m_l*(r_l^2 + r_i^2);    %liner moment of inertia,
kg-m^2
        I_c = (1/2)*m_c*(r_o^2 + r_l^2);    %composite moment of
inertia, kg-m^2
        I_h = I_l + I_c;    %housing inertia, kg-m^2
end
m_e = rho_e*pi*len_e*(r_i^2 - r_a^2); %single end cap mass, kg
m_b = rho_b*pi*(len_i + 2*len_e + 2*l_sh)*r_a^2;   %approximate axle
mass, kg
m_p = rho_p*Vol_p; %piston mass, kg
m = m_h + 2*m_e + m_b + m_p;    %total HFA mass so far -- excludes oil
mass, kg
```

```
%calculate remainder of primary inertia contributions
I_e = (1/2)*m_e*(r_i^2 + r_a^2);  %single end cap moment of inertia,
kg-m^2
I_b = (1/2)*m_b*r_a^2;  %bolt moment of inertia, kg-m^2
I_p = (1/2)*m_p*(r_i^2 + r_a^2);  %piston moment of inertia, kg-m^2
I_s = I_h + 2*I_e + I_b + I_p;  %inertia of solid components, kg-m^2

%calculate radial and axial forces
r_ecc_lo = G/omega_d*10^-3; %low estimate of eccentricity (based on
balance grade), m
r_ecc_hi = r_ecc_lo*SF_ecc; %high estimate of eccentricity (based on
safety factor), m
F_r = m*omega_d^2*r_ecc_hi;  %maximum expected radial load (total), N
F_a = max(F_s_max, m*g);    %maximum expected axial load, N

%select bearings
[d_b_i, d_b_o, w_br, ~, r_f, ~, L_nah, bearingSelected] = ...
    sizeBearing(d_i, F_a, F_r, 1.2*P_s_max, f_m*T_max,...
    S_y_b/SF, omega_d, angContBearingData, eCorr);  %execute bearing
sizer function
if ~bearingSelected
    disp('WARNING: Bearings not properly sized')
end

len_pipe = len_e + l_r + l_sh + w_br + d_lp + l_s; %approximate length
of axial port, m

%% Containment Chamber
R_ch_i = r_o + c_ch;    %inner radius of containment chamber, m
Q = calcGasLoad(R_ch_i,P_atm,N_ring);   %gas load due to permeation,
Pa-m3/s
Vol_ch = pi*R_ch_i^2*(len_h + 2*c_ch + len_PM) - pi*r_o^2*len_h;
%approximate chamber air volume, m3
[mu_ch, Kn] = calcChamberGas(P_ch_d/P_atm*rho_a,T_atm,len_h); %dynamic
viscosity, kg/m-s; and Knudsen number
Vol leakage max = pi*R ch i^2*.05; %maximum allowable leakage into
containment chamber, approx, m3

%% Energy Capacities at Design Condition
e_k_d = (1/2)*(I_s + I_o_d)*omega_d^2;  %kinetic energy capacity, J
e_h_d = P_c*Vol_c*log(P_h_d/P_c); %hydraulic energy capacity, J
e_d = e_k_d + e_h_d;  %total energy capacity, J

%% Tractive Power Profile
F_aero = (1/2)*C_d*A_f*rho_a*v.^2;    %vehicle aero drag, N
F_roll = (m_v + m)*9.81*(a_1 + 3.24*a_2.*(v./44.7).^2.5); %vehicle
rolling drag, N
F_acc = (m_v + m)*a;    %force contributing to
acceleration/deceleration, N
F = F_acc + F_aero + F_roll;   %total force, N
W_dot_t = F.*v;    %tractive power, W
f_power = W_dot_lab/abs(min(W_dot_t));   %ratio of laboratory HPU power
capacity to required motoring power
W_dc_min = trapz(t,W_dot_t);    %minimum capacity to feasibly complete
drive cycle, J
```

```
%% PM Initial Sizing
omega_PM_max = G_PM*omega_d;    %maximum HFA PM angular velocity, rad/s
D_max = 2*pi*max(abs(W_dot_t))/(P_s_min*omega_PM_max);    %initial
selection of storage PM displacement, m3/rev
m_PM = m_mass*D_max + b_mass;   %HFA PM mass
omega_ax = v/(d_t/2);   %axle speed

%% Geometric Feasibility Check
geoInfeas = [Vol_c<0 ...    %negative charge volume
    Vol_g_d<Vol_g_min ...   %piston bearing length prevents achieving
design pressure
    len_i<len_p ...         %piston bearing length exceeds inner length
    (r_i-r_a)<th_b];        %piston bearing thickness is larger than
the space between the axle and liner
```

calcSealDiameter.m

This function calculates the required seal diameter, d_s, to avoid failures of the portion of the axle which forms the circumferential seal of the HSRU. This is done by initially guessing a very thin wall and incrementing by small values until the von Mises stress is acceptably low. See Section 3.2 for a detailed explanation of this logic.

```
function d_s = calcSealDiameter(P_i,d_i,sigma_vm_d)

incr = .0001;   %guessing increment, m
sigma_vm = inf(1,2);    %create variable to store von Mises stress at
inner and outer radii
diff = inf; %fractional difference between acceptable and actual stress
incrCt = 0; %iteration counter

d_s = d_i + incr;   %initial guess for outer radius, m

while diff > .01 && incrCt < 1000

    F = -P_i*pi/4*(d_s^2 - d_i^2);   %axial compressive force

    %calculate stress at inside of hollow shaft
    [sigma_vm(1), ~, ~, ~, ~] = ...
        calcShaftStress(d_i/2,F,0,0,P_i,0,0,d_i,d_s,0,0,1,1,1);

    %calculate stress at outside of hollow shaft
    [sigma_vm(2), ~, ~, ~, ~] = ...
        calcShaftStress(d_s/2,F,0,0,P_i,0,0,d_i,d_s,0,0,1,1,1);

    diff = (max(sigma_vm) - sigma_vm_d)/sigma_vm_d; %calculate fraction
difference in stress

    if diff > 0     %stress is too high
        d_s = d_s + incr;   %make diameter larger
```

```
    end

    incrCt = incrCt + 1;    %increment iteration counter
end

end
```

calcShaftStress.m

This function can be used to calculate the von Mises stress at a radial location r for a generic hollow or solid shaft. The shaft is presumed to have no end effects and can be loaded with any combination of an axial force, bending moment, shear force, internal pressure, external pressure, and torque.

```
function [sigma_vm, sigma_c, sigma_r, sigma_z, tau_rc] = ...
    calcShaftStress(r,F,M,V,P_i,P_o,T,d_i,d_o,d_p,N,k_n,k_b,k_t)
%Loads
%F -- loading (positive in tension) normal to the z-axis, N
%M -- bending moment about the r (or c, equivalently) axis, N-m
%V -- shear force
%P_i -- presure inside (if hollow), Pa
%P_o -- pressure outside, Pa
%T -- torque about the z-axis, N-m

%Dimensions
%d_i -- inner diameter, m
%d_o -- outer diameter, m
%d_p -- diameter of radial passages
%N -- number of radial passages

%Stress Concentration Factors
%k_n -- normal axial loading
%k_b -- bending axial loading
%k_t -- torsional loading

%All stresses are given in Pa.  Note that the user is responsible for
%specifying the correct stress concentration factor, and that only one
%is applied in a given calculation.  If, for example, stress is being
%calculated at a point on a shaft where radial passages coincide with a
%fillet, the user should calculate a stress concentration factor for
%normal loading as

%k_n = k_n_passage*k_n_fillet

%and pass that single value to the function as k_n.

%% Calculate Shaft Properties
d = 2*r;    %diameter of radial point of interest, m
```

```
A = pi/4*(d_o^2 - d_i^2) - N*d_p*(d_o - d_i);   %cross-sectional area
(normal to z-axis), m2
I = pi/64*(d_o^4 - d_i^4);  %area moment of inertia, m4
J = pi/32*(d_o^4 - d_i^4);  %polar area moment of inertia, m4

%% Calculate Radial Stress
%The pressure differential across the shaft wall is assumed to be the
only
%contributor to radial stress.  The mass that the shaft supports would,
in
%reality, cause some compressive radial stress, but is neglected here.
%Centrifugal effects are also neglected, as the shaft diameter is
generally
%small and the pressure differential large.
sigma_r = (d_i^2*P_i - d_o^2*P_o)/(d_o^2 - d_i^2) ...
    - (P_i - P_o)*d_i^2*d_o^2/((d_o^2 - d_i^2)*d^2);

%% Calculate Circumferential Stress
%The pressure differential across the shaft wall is assumed to be the
only
%contributor to circumferential stress.  As in the radial stress
%calculation, centrifugal effects are neglected, as the shaft diameter
is
%generally small and the pressure differential large.
sigma_c = (d_i^2*P_i - d_o^2*P_o)/(d_o^2 - d_i^2) ...
    + (P_i - P_o)*d_i^2*d_o^2/((d_o^2 - d_i^2)*d^2);

%% Calculate Axial Stress
%Both bending and normal loading are taken into account for bending
stress
%calculation.  Stress concentration factors are applied.

sigma_z_b = k_b*M*r/I;  %maximum axial stress due to bending

sigma_z_n = k_n*F/A;    %axial stress due to normal loading

sigma_z = sigma_z_b + sigma_z_n;    %total axial stress

%% Calculate Shear Stresses
tau_T = k_t*T*r/J; %torsional shear stress

if sigma_z_b == 0
    tau_V = (4/3)*V/A;  %maximum transverse shear stress
else
    tau V = 0;  %shear stress is zero at the critical point
end

tau_rc = tau_T + tau_V; %total shear stress

%% Calculate von Mises Stress
sigma_vm = sqrt(0.5*((sigma_r - sigma_c)^2 + (sigma_c - sigma_z)^2 +
...
    (sigma_z - sigma_r)^2 + 6*tau_rc^2));

end
```

sizeAxle.m

This function carries out the process by which the various axle dimensions are selected, as described in Section 3.2.

```
function [r_a, P_h, F_a, F_s, F_b, k_s, delta_a] = sizeAxle(d_i, d_s,
...
    r_i, len_i, N_p, d_p, sigma_max, E_b, rho_o, omega, P_s, m_h, g)

%coefficients for stress concentration correlation (Juvinall and
Marshek)
c_n_1 = 3.2381;
c_n_2 = -3.0857;
c_n_3 = 2.9908;

F_p = P_s*pi*d_s^2/4;   %force acting on face of axle, N

x_o = 0;    %zero preload

k_s0 = 10^7;    %initial guess for spring constant
e = inf;    %set initial error to infinity
epsilon = 1e-6; %convergence criterion
iterCt = 0; %iteration counter

while e >= epsilon && iterCt < 10^3;

    %solve for axle radius, m
    r_a = fzero(@(r_a) ((P_s +
(1/4)*rho_o*omega^2*(r_i^2+r_a^2))*pi*(r_i^2-r_a^2) ...
        - k_s0*x_o - m_h*g)/(1 + k_s0*len_i/(pi*r_a^2*E_b)) - ...
        ...
        sigma_max*(pi*(r_a^2 - d_i^2/4)-N_p*d_p*(2*r_a-d_i))...

/(c_n_1*min(d_p/(2*r_a),3.5)^2+c_n_2*min(d_p/(2*r_a),3.5)+c_n_3)...
        ...
        ,.05);

    %calculate new spring constant
    F_h = (P_s + (1/4)*rho_o*omega^2*(r_i^2+r_a^2))*pi*(r_i^2-r_a^2);
%hydraulic force, N
    F_a = (F_h - k_s0*x_o - m_h*g)/(1 + k_s0*len_i/(pi*r_a^2*E_b));
%axle force, N
    k_s = pi*r_a^2*E_b/(len_i*F_a)*(P_s*pi*d_s^2/4 - m_h*g);    %spring
constant, N/m

    %iteration operations
    e = abs(k_s-k_s0)/k_s;  %error
    k_s0 = k_s; %set new guess for spring constant
    iterCt = iterCt + 1;    %increment iteration counter
end

%calculate other relevant values
sigma_a = F_a/(pi*r_a^2);   %average axial stress in axle, Pa
delta_a = len_i*sigma_a/E_b;    %axial elongation of axle, m
```

```
F_s = k_s0*(x_o + delta_a); %spring force, N
F_b = F_s + m_h*g - F_p;    %reaction force at bottom bearing (should
be zero), N
P_h = P_s + (1/4)*rho_o*omega^2*(r_i^2+r_a^2);    %hydraulic pressure,
Pa

end
```

sizeEndCaps.m

This function calculates the required end cap thickness based on the centrifugal and pressure loading on the end caps. The gas and oil side end caps are evaluated separately, using their respective pressure distributions. The end cap that experiences more bending dictates the required end cap length, per the discussion in Section 3.3.

```
function [len_e, P_o, P_g, F_g_max, sigma_vm_max] = ...
    sizeEndCaps(r_i, r_a, dp, nr, ...
    P_s, omega, rho_o, rho_atm, P_atm, rho_e, E_e, nu_e, sigma_max)

r = linspace(r_a,r_i,nr);   %radial position vector, m

%% Calculate Centrifugal Stresses
[~, sigma_r_cent, sigma_c_cent, ~] = calcStressIso(r_a, r_i, nr, ...
    omega, 0, 0, 0, rho_e, E_e, nu_e);

%% Calculate Bending Moments
free = 1;   %free support at inner edge

%calculate oil-side loading
P_o = P_s + (1/2)*rho_o*omega^2*r.^2; %oil-side pressure distn, Pa

%calculate gas-side loading
P_avg = P_s + (1/4)*rho_o*omega^2*(r_i^2 + r_a^2);    %average
pressure, Pa
A_p = pi*(r_i^2-r_a^2); %area of piston face, m2
Cg0 = rho_atm/P_atm;    %constant 0, used for gas pressure profile
Cg1 = Cg0*omega^2/2;    %constant 1, used for gas pressure profile
Cg2 = P_avg*A_p/(2*pi); %constant 2, used for gas pressure profile
P_g0 = 2*Cg1*Cg2/(exp(Cg1*r_i^2) - exp(Cg1*r_a^2)); %gas pressure at
radial center
P_g = exp(Cg0*omega^2*r.^2/2 + log(P_g0));  %gas pressure distribution,
Pa

%calculate oil side end cap bending moments
[M_t_o, M_r_o, F_g_max, ~] = bendingHeap(r_i, r_a, dp, free, ...
    P_o, nu_e);

%calculate gas side end cap bending moments
[M_t_g, M_r_g, ~, ~] = bendingHeap(r_i, r_a, dp, free, ...
    P_g, nu_e);    %end cap length required on gas side, m
```

```
%% Find Required Thickness
incr = 0.0001;   %sizing increment, m
maxLen = .2;    %maximum reasonable end cap length, m
sized = 0;  %default to not yet properly sized
len_e = 0;  %initial guess for end cap length, m

%cycle through end cap sizes
while ~sized && (len_e < maxLen)

    len_e = len_e + incr;   %incrememnt end cap length

    %check oil side
    sigma_r = sigma_r_cent + 6*M_t_o/len_e^2; %total radial stress
distn, Pa
    sigma_c = sigma_c_cent + 6*M_r_o/len_e^2; %total circumferential
stress distn, Pa
    sigma_vm = sqrt(sigma_r.^2 - sigma_r.*sigma_c + sigma_c.^2);
%von Mises stress distn, Pa

    if max(sigma_vm) <= sigma_max %if oil side passes, check gas side

        sigma_r = sigma_r_cent + 6*M_t_g/len_e^2; %total radial stress
distn, Pa
        sigma_c = sigma_c_cent + 6*M_r_g/len_e^2; %total
circumferential stress distn, Pa
        sigma_vm = sqrt(sigma_r.^2 - sigma_r.*sigma_c + sigma_c.^2);
%von Mises stress distn, Pa

        if max(sigma_vm) <= sigma_max   %check to see if stress is
acceptably low
            sized = 1;
        end

    end

end

sigma_vm_max = max(sigma_vm);   %get maximum von Mises stress value

end
```

calcStressIso.m

This function calculates the stresses and radial strain due to internal pressure, external pressure and centrifugal forces in an isotropic solid or hollow cylinder. Methods used are presented by Genta [25].

```
function [r, sigma_r, sigma_c, u_r] = calcStressIso(r_i, r_o, nr,
omega, ...
```

```
    P_int, P_ext, sigma_z, rho, E, nu)

beta = r_i/r_o; %calculate radius ratio
X = linspace(beta,1,nr);    %create dimensionless radial position
vector

if beta==0   %solid

    %radial stress, Pa
    sigma_r_cent = rho*omega^2*r_o^2*(3+nu)/8*(1 - X.^2);  %centrifugal
component
    sigma_r_ext = -P_ext;   %external pressure component
    sigma_r = sigma_r_cent + sigma_r_ext;   %total

    %circumferential stress, Pa
    sigma_c_cent = rho*omega^2*r_o^2*(3+nu)/8*(1 -
(1+3*nu)/(3+nu)*X.^2);   %centrifugal component
    sigma_c_ext = -P_ext;   %external pressure component
    sigma_c = sigma_c_cent + sigma_c_ext;   %total

else    %central hole

    %radial stress, Pa
    sigma_r_cent = rho*omega^2*r_o^2*(3+nu)/8*(1 + beta^2 - ...
        beta^2./X.^2 - X.^2);   %centrifugal component
    sigma_r_int = -P_int*beta^2/(1 - beta^2)*(1/beta^2 - 1);
%internal pressure component
    sigma_r_ext = -P_ext/(1 - beta^2)*(1 - beta^2./X.^2);   %external
pressure component
    sigma_r = sigma_r_cent + sigma_r_int + sigma_r_ext; %total

    %circumferential stress, Pa
    sigma_c_cent = rho*omega^2*r_o^2*(3+nu)/8*(1 + beta^2 + ...
        beta^2./X.^2 - (1+3*nu)/(3+nu)*X.^2);   %centrifugal component
    sigma_c_int = P_int*beta^2/(1 - beta^2)*(1/beta^2 + 1); %internal
pressure component
    sigma_c_ext = -P_ext/(1 - beta^2)*(1 + beta^2./X.^2);   %external
pressure component
    sigma_c = sigma_c_cent + sigma_c_int + sigma_c_ext; %total

end

%calculate displacement
r = r_o*X;  %radial position vector, m
epsilon_c = 1/E*(sigma_c - nu*(sigma_r + sigma_z)); %circumferential
strain, m/m
u_r = r.*epsilon_c; %radial displacement, m

end
```

bendingHeap.m

This function uses methods presented by Heap [31], as described in Section 3.3, to calculate the radial distribution of bending moments in component that can be approximated as a circular plate.

```
function [M_t, M_r, F_b, r] = bendingHeap(a, b, dp, bFree, P_net, nu)

dp = min(dp,a-b);   %limit retainer contact area
nr = length(P_net); %radial spatial resolution
r = linspace(b,a,nr);   %radial position vector
dr = r(2)-r(1); %radial step size, m
rsq = r.^2; %vectorized square of radial position vector
A = 2*pi*r*dr;  %area of each numerical discretization, m2
np = round(dp/dr);  %number of discrete steps across which the reaction
force spans

%calculate net pressure and force distn
F_net = P_net.*A;   %net force distn
F_b = sum(F_net);   %axle reaction force
F_net(1:np) = F_net(1:np) - F_b/np; %net line load distribution, N

%create moment arrays
M_r = zeros(1,nr);  %radial moment distribution, Nm/m
M_t = zeros(1,nr);  %tangential moment distribution, Nm/m


if bFree    %inner edge free (Heap load case VIII)

    %calculate constants for efficiency
    %interior moments
    C0_i = (1/2)*(1-nu)/(1+nu);
    Cr_i = 1/(4*pi)*(1+nu)*(1-b^2./rsq)*(a^2/(a^2-b^2));
    Ct_i = 1/(4*pi)*(1+nu)*(1+b^2./rsq)*(a^2/(a^2-b^2));
    %exterior moments
    C0_o = 1/(4*pi)*(1+nu)*(a^2/(a^2-b^2));
    Cr_o1 = (1/2)*(1-nu)/(1+nu)*(1 - rsq/a^2);
    Cr_o2 = log(a./r);
    Ct_o1 = (1/2)*(1-nu)/(1+nu)*(1+a^2./rsq);
    Ct_o2 = (1/2)*(1-nu)/(1+nu)*(1-rsq/a^2)*(a^2-b^2)./rsq;
    Ct_o3 = log(a./r);

    for j=1:nr  %cycle through line loads
        d = r(j);    %get postiion of line load

        %calculate bending moments interior to line load
        M_r(1:j) = M_r(1:j) + F_net(j)*Cr_i(1:j)*(C0_i*(1-d^2/a^2) +
log(a/d));
        M_t(1:j) = M_t(1:j) + F_net(j)*Ct_i(1:j)*(C0_i*(1-d^2/a^2) +
log(a/d));

        %calculate bending moments exterior to line load
        M_r(j+1:nr) = M_r(j+1:nr) + F_net(j)*C0_o*(Cr_o1(j+1:nr)*(d^2-
b^2)./rsq(j+1:nr) ...
```

```
            + Cr_o2(j+1:nr) + b^2/a^2*log(r(j+1:nr)/d) -
b^2./rsq(j+1:nr)*log(a/d));
        M_t(j+1:nr) = M_t(j+1:nr) + F_net(j)*C0_o*(Ct_o1(j+1:nr)*(1 -
d^2/a^2) ...
            - Ct_o2(j+1:nr) + Ct_o3(j+1:nr) + b^2/a^2*log(r(j+1:nr)/d)
+ b^2./rsq(j+1:nr)*log(a/d));

    end

else    %moment reaction at inner edge (Heap load case IX)

    %calculate constants for efficiency
    C0 = (1+nu)/(1-nu);
    %interior moments
    Cr_i = 1/(4*pi)*(1-nu)*(C0 + b^2./rsq)/(C0 + b^2/a^2);
    Ct_i = 1/(4*pi)*(1-nu)*(C0 - b^2./rsq)/(C0 + b^2/a^2);
    %exterior moments
    C_o = 1/(4*pi)*((1+nu)/(C0 + b^2/a^2));
    Cr_o1 = (1/2)*(1-rsq/a^2)./rsq;
    Cr_o2 = Cr_o1*b^2/C0 + C0*log(a./r);
    Cr_o3 = b^2./rsq;
    Cr_o4 = b^2/a^2;
    Ct_o2 = Cr_o3;
    Ct_o3 = Cr_o4;
    Ct_o1 = (1/2)*(Ct_o3 - Ct_o2)/C0;
    for j=1:nr  %cycle through line loads
        d = r(j);    %get postiion of line load

        %calculate bending moments interior to line load
        M_r(1:j) = M_r(1:j) + F_net(j)*Cr_i(1:j)*((1-d^2/a^2)/2 +
C0*log(a/d));
        M_t(1:j) = M_t(1:j) + F_net(j)*Ct_i(1:j)*((1-d^2/a^2)/2 +
C0*log(a/d));

        %calculate bending moments exterior to line load
        M_r(j+1:nr) = M_r(j+1:nr) + F_net(j)*C_o*(Cr_o1(j+1:nr)*d^2 +
...
            Cr_o2(j+1:nr) + Cr_o3(j+1:nr)*log(a/d) -
Cr_o4.*log(r(j+1:nr)./d));
        M_t(j+1:nr) = M_t(j+1:nr) + F_net(j)*C_o*(1 ...
            - (d^2/a^2 + d^2./rsq(j+1:nr))/2 + Ct_o1(j+1:nr) ...
            - Ct_o2(j+1:nr)*log(a/d) - Ct_o3*log(r(j+1:nr)/d));

    end

end

end
```

sizePiston.m

This function uses the methods described in Section 3.4 to properly select the piston thickness.

```
function th_p =
sizePiston(r_i,r_a,dp,P_net,omega,rho_p,E_p,nu_p,sigma_max)

%% Calculate Centrifugal Stresses
[~, sigma_r_cent, sigma_c_cent, ~] = calcStressIso(r_a, r_i,
length(P_net), ...
    omega, 0, 0, 0, rho_p, E_p, nu_p);

%% Calculate Bending Moments
free = 0;   %moment reaction at inner edge

%calculate oil side end cap bending moments
[M_t, M_r, ~, ~] = bendingHeap(r_i, r_a, dp, free, ...
    P_net, nu_p);

%% Find Required Thickness
incr = 0.0001;   %sizing increment, m
maxTh = .2;    %maximum reasonable end cap length, m
sized = 0;  %default to not yet properly sized
th_p = 0;  %initial guess for end cap length, m

while ~sized && (th_p < maxTh)

    th_p = th_p + incr;   %incrememnt end cap length

    %calculate stresses
    sigma_r = sigma_r_cent + 6*M_t/th_p^2; %total radial stress distn,
Pa
    sigma_c = sigma_c_cent + 6*M_r/th_p^2; %total circumferential
stress distn, Pa
    sigma_vm = sqrt(sigma_r.^2 - sigma_r.*sigma_c + sigma_c.^2);
%von Mises stress distn, Pa

    sized = max(sigma_vm) <= sigma_max; %check for proper sizing

end

end
```

sizeBearing.m

This function uses the logic present in Section 3.6 to properly select the bearings.

```
function [d, D, B, P, r_f, omega_max, L_nah, selected] = ...
    sizeBearing(d_i, F_a, F_r, P_i, T,...
```

```
    sigma_max, omega_min, angContBearingData, eCorr)

%% Find Minimum Bearing Inner Diameter to Prevent Failure at Axle
Shoulders
br = 0; %start at beginning of bearing data
sigma_vm = inf(1,3);    %initialize von Mises stress array for axle
shoulders
while (max(sigma_vm) >= sigma_max) && (br < size(angContBearingData,1))
    br = br + 1;
    d = angContBearingData(br,1)/1000;   %bearing inner diameter, m
    r_f = angContBearingData(br,6)/1000;    %bearing fillet radius, m
    roverd = min(0.3,max(0.025,r_f/d)); %ratio of fillet radius to
bearing inner diameter
    k_n = 21.143*roverd^2 - 11.55*roverd + 3.072;   %normal stress
conc. factor
    k_t = 0.8235*roverd^(-0.264);   %torsion stress conc. factor

    %oil side
    [sigma_vm(1), ~, ~, ~, ~] = ...
        calcShaftStress(d_i/2,-F_a,0,F_r,P_i,0,0,d_i,d,0,0,k_n,1,k_t);
%inside

    [sigma_vm(2), ~, ~, ~, ~] = ...
        calcShaftStress(d/2,-F_a,0,F_r,P_i,0,0,d_i,d,0,0,k_n,1,k_t);
%outside

    %gas side
    [sigma_vm(3), ~, ~, ~, ~] = ...
        calcShaftStress(d/2,0,0,F_r,0,0,T,0,d,0,0,k_n,1,k_t);

end

%% Select Smallest Allowable Bearing that Can Withstand Axial and
Radial Loads
selected = 0;   %default to not yet properly selected
while ~selected && (br <= size(angContBearingData,1))    %cycle through
bearings

    %get specs of current bearing
    d = angContBearingData(br,1)/1000;   %bearing inner diameter, m
    D = angContBearingData(br,2)/1000;   %bearing outer diameter, m
    B = angContBearingData(br,3)/1000;   %bearing width, m
    alpha_0 = angContBearingData(br,16);  %contact angle, deg
    C = angContBearingData(br,17);    %dynamic load rating, N
    C_0 = angContBearingData(br,18);  %static load rating, N
    omega_max = angContBearingData(br,19)*pi/30;  %speed value, rad/s

    %get X and Y factors
    X_0 = 0.5;
    if alpha_0 == 25    %25 degree contact angle
        Y_0 = 0.38;
        e = 0.68;
        if F_a/F_r <= e
            X = 1;
            Y = 0;
```

```
        else
            X = 0.41;
            Y = 0.87;
        end
    else    %15 degree contact angle
        Y_0 = 0.46;
        e = interp1(eCorr(:,1),eCorr(:,2),F_a/C_0,'pchip');
        if F_a/F_r <= e
            X = 1;
            Y = 0;
        else
            X = 0.44;
            Y = interp1(eCorr(:,1),eCorr(:,3),F_a/C_0,'pchip');
        end
    end

    P = X*F_r + Y*F_a;  %equivalent dynamic load, N
    P 0 = max(F r,X 0*F r + Y 0*F a);    %equivalent static load, N

    if (P < C) && (omega_min < omega_max) %&& (P_0 < C_0)
        selected = 1;
    else
        br = br + 1;
    end

    a1 = .62;   %95% relability factor
    ft = 1; %150 max temp
    n = 30*omega_min/pi/2;    %avg operating speed, 1/min
    L_nah = a1*ft*10^6/(60*n)*(C/P)^3;  %corrected operating life, h

end

end
```

calcChamberGas.m

This function uses the methods presented in Section 4.4 to calculate the viscosity of the low-pressure gas in the containment chamber.

```
function [mu, Kn] = calcChamberGas(rho,T,len_h)

%constants
m = 4.782e-26;    %molecular mass of air, kg
K = 1.38e-23;   %Boltzman constant, J/K
a_inf = 2.96e-10;   %effective molecular diameter at infinite temp, m
T_c = 113; %Sutherland constant, K

%calculate Knudsen number and viscosity
a = a_inf*sqrt(1 + T_c/T);  %effective molecular diameter, m
lambda = m/(sqrt(2)*a^2*rho*pi);    %mean free path, m (4.8)
Kn = lambda/len_h;  %Knudsen number
```

```
mu = sqrt(K*m*T)/(a^2*pi^(3/2));    %dynamic viscosity, kg/m-s (4.11)

end
```

runSimulation.m

This script executes the drive cycle simulation, the details of which were given in Section 6.4. The script also includes code which facilitates an iterative pump-sizing algorithm.

```
%% Make Initial Calculations
%calculations for effiency
C_1 = 1/(pi*(r_i^2 - r_a^2));
C_2 = (1/2)*rho_o*(r_i^2 + r_a^2);
C_3 = (1/4)*rho_o*(r_i^2 + r_a^2);
C_4 = rho_a/P_atm;
C_5 = 1/G_PM;
C_6 = pi*d_s*c_s^3/(12*mu_o*l_s);
C_7 = beta_ch/(beta_ch-1);
C_8 = (beta_ch-1)/beta_ch;
C_9 = P_c*Vol_c;

sized = 0;  %default to incorrectly sized PM
sizeCt = 0; %counter for PM sizing iterations

%% Iterate to Find Correct PM Size
while ~sized %loop while PM is not properly sized

    D_max = min(max(D_max,0.01e-6),200e-6);  %enforce reasonable bounds
on PM size
    fprintf([num2str(sizeCt+1),'. Attempting pump size
',num2str(D_max*1e6),' cc/rev\n']);

    %% Initialize Arrays for Data Storage
    %HFA state
    omega_s = zeros(n,1);
    omega_f = zeros(n,1);
    P_s = zeros(n,1);
    P_0 = zeros(n,1);
    P_h = zeros(n,1);
    Vol_o = zeros(n,1);
    Vol_g = zeros(n,1);
    L = zeros(n,1);
    I_o = zeros(n,1);
    e_k = zeros(n,1);
    e_h = zeros(n,1);
    e_k_check = zeros(n,1);
    e_h_check = zeros(n,1);
    e_check = zeros(n,1);
    e_dot_k = zeros(n,1);
    e_dot_h = zeros(n,1);
    e = zeros(n,1);
    SOC = zeros(n,1);
```

```
SOC_k = zeros(n,1);
SOC_h = zeros(n,1);
W_dot_loss = zeros(n,1);
eta_inst = zeros(n,1);
P_int_o = zeros(n,1);

%control and results
W_dot = zeros(n,1);
D = zeros(n,1);
omega_PM = zeros(n,1);
x = zeros(n,1);
W_dot_s = zeros(n,1);
eta_m = zeros(n,1);
eta_v = zeros(n,1);
W_dot_k = zeros(n,1);
W_dot_h = zeros(n,1);
pwrMode = zeros(n,1);
T = zeros(n,1);

%fluid model
tau_dyn = zeros(n,1);
W_dot_vi = zeros(n,1);
deltaO = zeros(n,1);
pi1_v = zeros(n,1);
pi1_t = zeros(n,1);
p_v_t = zeros(n,n_pi_v-1);
p_t_t = zeros(n,n_pi_t-1);

%kinetic parameters
alpha_s = zeros(n,1);
alpha_f = zeros(n,1);
W_dot_PM = zeros(n,1);
W_dot_vh = zeros(n,1);
W_dot_w = zeros(n,1);
W_dot_b = zeros(n,1);
W_dot_ft = zeros(n,1);
Sigma_kl = zeros(n,1);

%pneumatic parameters
Vol_dot_o = zeros(n,1);
Vol_dot_l = zeros(n,1);
dP_p = zeros(n,1);
dP_c = zeros(n,1);
I_dot_o = zeros(n,1);
dP_main = zeros(n,1);
dP_port = zeros(n,1);
f_bar_main = zeros(n,1);
f_bar_port = zeros(n,1);
W_dot_l = zeros(n,1);
W_dot_p = zeros(n,1);

%containment chamber vacuum system
P_ch = zeros(n,1);
P_dot_ch = zeros(n,1);
rho_ch_a = zeros(n,1);
vacOn = zeros(n,1);
```

```
    W_dot_vac = zeros(n,1);

    %% Initialize Values for Drive Cycle
    t_switchLast = -inf;    %set last switch beginning
    Vol_leakage = 0;    %total amount of oil leaked into chamber, m3

    if optimizing
        setICs;
    else
        %         simulationICs;
        setICs;
    end

    %% Initialize Movie Parameters
    if HUD

        maxSizeCt = 1;
        F = struct('cdata',[],'colormap',[]);
        frameInitialization
        frameUpdate
        F(1) = getframe(allFigs);
        frameNumber = 2;

    end

    %% Run Drive Cycle
    for i=2:n

        %% New HFA State
        omega_s(i) = omega_s(i-1) + alpha_s(i-1)*dt;    %container
angular velocity, rad/s
        omega_f(i) = omega_f(i-1) + alpha_f(i-1)*dt;    %oil angular
velocity, rad/s
        deltaO(i) = omega_s(i) - omega_f(i);    %angular velocity
difference, rad/s
        Vol_o(i) = Vol_o(i-1) + Vol_dot_o(i-1)*dt;   %oil volume, m^3
        L(i) = C_1*(Vol_o(i) - Vol_o_min);    %oil length, m
        I_o(i) = C_2*Vol_o(i);   %oil moment of inertia, kg-m^2
        Vol_g(i) = Vol_g(i-1) - Vol_dot_o(i-1)*dt;    %gas volume, m^3
        P_h(i) = C_9/Vol_g(i);    %gas pressure, Pa
        P_0(i) = P_h(i) - C_3*omega_f(i)*omega_f(i); %pressure at
center of oil volume, Pa
        P_int_o(i) = P_0(i) + (1/2)*rho_o*omega_f(i)^2*r_i^2;
        omega_PM(i) = C_5*omega_s(i);   %PM speed after gear reduction,
rad/s

        %% New HFA Energy
        e_k(i) = (1/2)*I_s*omega_s(i)^2 + (1/2)*I_o(i)*omega_f(i)^2;
%kinetic energy stored, J
        e_h(i) = C_9*log(P_h(i)/P_c); %hydraulic energy stored, J
        e(i) = e_k(i) + e_h(i); %total energy stored, J
        SOC(i) = e(i)/e_d;    %SOC
        SOC_k(i) = e_k(i)/e_k_d;    %kinetic SOC
        SOC_h(i) = e_h(i)/e_h_d;    %hydraulic SOC
```

```
        %% Vacuum Equations and Control
        P_ch(i) = P_ch(i-1) + P_dot_ch(i-1)*dt;    %chamber pressure,
Pa
        rho_ch_a(i) = C_4*P_ch(i);    %chamber air density, kg/m3
        vacOn(i) = vacuumToggle(P_ch(i),P_ch_d,vacOn(i-1),f_band_vac);
%vacuum pump deadband control
        S_p = vacOn(i)*S_p_on;  %vacuum pumping speed (on or off),
m^3/s
        if arch(1) == 1
            Vol_ch = Vol_ch - Vol_dot_l(i-1)*dt;   %account for oil
leakage
        end
        P_dot_ch(i) = (Q - P_ch(i)*S_p + P_ch(i)*Vol_dot_l(i-
1))/Vol_ch;   %rate of change of chamber pressure, Pa/s
        W_dot_vac(i) = P_ch(i)*S_p*C_7*((P_atm/P_ch(i))^C_8 - 1);
%vacuum pumping power consumption, W

        %% Control Strategy and Power Calculations
        W_dot(i) = pwrMgmt(W_dot_t(i), SOC(i), 1);   %power into (+) or
out of (-) HFA, W

        %disregard switching frequency limit if PM must switch
direction anyway
        if W_dot(i)*W_dot(i-1) <= 0
            t_switchLast = 0;
        end

        %call control strategy
        [pwrMode(i), depleted, t_switchLast] =
cfun_simpleBand(W_dot(i), ...
            Vol_o(i), Vol_o_min, Vol_g(i), Vol_g_min, pwrMode(i-1),
i*dt, ...
            t_switchLast, t_switchMin, P_s(i-1), P_s_min, P_s_max, dt);

        %% Pump/motor Equations
        %calculate efficiencies, displacement position, shaft, and
fluid
        %power
        switch arch(2)
            case 0  %VDPM
                [eta_m(i),eta_v(i),x(i),W_dot_k(i),W_dot_s(i)] = ...
                    calcPwrVDPM(W_dot(i),pwrMode(i),P_s(i-
1),omega_PM(i),...

D_max,C_v,C_f,C_h,C_s,C_st,rho_o,mu_o,beta_o,eta_GR);
            case 1  %FDPM
                [eta_m(i),eta_v(i),x(i),W_dot_k(i),W_dot_s(i)] = ...
                    calcPwrFDPM(W_dot(i),pwrMode(i),P_s(i-
1),omega_PM(i),...

D_max,C_v,C_f,C_h,C_s,C_st,rho_o,mu_o,beta_o,eta_GR);
        end
        W_dot_PM(i) = W_dot_k(i) - W_dot_s(i); %PM loss, W
        D(i) = x(i)*D_max;  %instantaneous displacement, m3/rev

        %% Pneumatic Equations
```

```
        W_dot_h(i) = W_dot(i) - W_dot_k(i); %pneumatic power, W

        %assign minor loss coefficients for flow through axle ports
        if W_dot_h(i) >=0   %pneumatic charging
            k_pipe = k_entr + k_tee;
            k_port = 2*k_exit;
        else    %pneumatic discharging
            k_pipe = k_tee + k_exit;
            k_port = 2*k_entr;
        end

        %calculate pressure drop due to flow through axle ports
        [dP_main(i), f_bar_main(i)] = calcDeltaP(Vol_dot_o(i-
1),d_i/2,len_pipe,epsilon,...
            k_pipe,rho_o,mu_o); %pressure drop thru axial section, Pa
        [dP_port(i), f_bar_port(i)] = calcDeltaP(Vol_dot_o(i-
1)/(2*N_p),d_p/2,r_a,...
            epsilon,k_port,rho_o,mu_o); %pressure drop thru radial
ports, Pa
        dP_p(i) = dP_main(i) + dP_port(i);  %pressure drop through
ports, Pa

        %perform remainder of pneumatic calculations
        P_s(i) = P_0(i) + sign(W_dot_h(i))*dP_p(i);

        Vol_dot_l(i) = C_6*P_s(i);    %leakage from HSRU, based on
internal pressure, m3/s
        Vol_leakage = Vol_leakage + Vol_dot_l(i)*dt;    %increment
leaked oil volume, m3

        Vol_dot_o(i) = W_dot_h(i)/P_s(i) - Vol_dot_l(i);  %oil flow
rate into (+) accumulator, m3/s
        I_dot_o(i) = C_2*Vol_dot_o(i);  %rate of change of moment of
inertia, kg-m2/s

        W_dot_l(i) = Vol_dot_l(i)*P_s(i); %power loss due to leakage, W
        W_dot_p(i) = abs(Vol_dot_o(i)*dP_p(i));   %port loss, W

        %% Dynamic Time Constant Calculation
        p_t_t(i,1) = L(i)^4*alpha_s(i-1)/nu_o^2;    %first tau Pi group
        p_t_t(i,2) = alpha_s(i-1)/omega_s(i)^2;     %second tau Pi
group
        pi1_t(i) = cmat_t(length(cmat_t));    %apply offset
        for j=1:n_pi_t-1    %cycle thru Pi groups
            for k=1:order_t     %cycle thru polynomial terms
                pi1_t(i) = pi1_t(i) + cmat_t((j-
1)*order_t+k)*p_t_t(i,j)^k;
            end
        end
        tau_dyn(i) = max(0,1/(pi1_t(i)*omega_s(i)));    %dynamic time
constant, s

        %% Viscous Dissipation Calculation
        p_v_t(i,1) = sqrt(max(0,rho_o*omega_s(i)*L(i)^2/mu_o));
        p_v_t(i,2) = deltaO(i)/omega_s(i);
```

```
        pi1_v(i) = cmat_v(length(cmat_v));    %apply offset
        for j=1:n_pi_v-1    %cycle thru pi groups
            for k=1:order_v     %cycle thru polynomial terms
                pi1_v(i) = pi1_v(i) + cmat_v((j-
1)*order_v+k)*p_v_t(i,j)^k;
            end
        end
        W_dot_vi(i) = max(0,mu_o*r_i^3*deltaO(i)^2*pi1_v(i));
%internal viscous loss, W

        %% Rotational Losses
        W_dot_vh(i) = mu_o*pi*omega_s(i)^2*d_s^3*l_s/(4*c_s);    %HSRU
viscous loss, W
        [W_dot_w(i), ~, ~] = calcAeroDrag(omega_s(i),r_o,...
            len_h,c_ch,rho_ch_a(i),mu_ch,Kn);  %windage loss, W
        W_dot_b(i) = C_b_m*(m +
rho_o*Vol_o(i))*omega_s(i)^3*r_ecc_lo*d_b_i/2; %bearing loss (assumes
10% of max eccentricity), W
        W_dot_ft(i) = omega_s(i)*(C_ft_c + C_ft_s*omega_s(i));
%feedthrough loss, W
        Sigma_kl(i) = W_dot_vi(i) + W_dot_vh(i) + W_dot_w(i) + ...
            W_dot_b(i) + W_dot_ft(i) + W_dot_PM(i);  %sum of kinetic
losses

        %% Kinetic Equations
        alpha_f(i) = deltaO(i)*(1 - exp(-dt/tau_dyn(i)))/dt;    %fluid
acceleration, rad/s^2
        alpha_s(i) = 1/(I_s*omega_s(i))*(W_dot_k(i) ...
            - Sigma_kl(i) -  W_dot_vac(i) ...
            - I_o(i)*omega_f(i)*alpha_f(i) -
(1/2)*I_dot_o(i)*omega_f(i)^2);    %solid acceleration, rad/s^2

        %% Calculations Not Required for Optimization
        if ~optimizing     %non-essential transient properties
            %energy conservation checks
            e_h_check(i) = e_h(i-1) + (W_dot_h(i-1) - W_dot_p(i-1) -
W_dot_l(i-1))*dt;
            e_k_check(i) = e_k(i-1) + (W_dot_k(i-1) - Sigma_kl(i-1) -
W_dot_vac(i-1))*dt;
            e_check(i) = e(i-1) + Vol_dot_o(i-1)*P_s(i-1)*dt + ...
                (W_dot_k(i) -
(1/4)*rho_o*Vol_dot_o(i)*omega_f(i)^2*(r_a^2 + 3*r_i^2) ...
                - Sigma_kl(i) - W_dot_vac(i))*dt;

            T(i) = W_dot_s(i)/omega_PM(i);  %PM torque
            W_dot_loss(i) = Sigma_kl(i) + W_dot_vac(i) + W_dot_p(i) +
...
                W_dot_l(i); %total rate of energy loss, W
            eta_inst(i) = 1 - W_dot_loss(i)/(abs(W_dot(i)) +
W_dot_loss(i));    %instantaneous HFA efficiency

            e_dot_k(i-1) = (e_k(i) - e_k(i-1))/dt;  %rate of change of
stored kinetic energy, W
            e_dot_h(i) = Vol_dot_o(i)*P_h(i);   %rate of change of
stored pneumatic energy, W
```

```
        end

        %% Check for Physical or Numerical Faults
        if i<n
            if e(i) < W_dot(i+1)*dt     %energy depletion fault
                disp(['ABORTED -- SOC dropped to ', ...
                    num2str(round(100*100*SOC(i))/100), '% at mile
',...
                    num2str(d(i)/1609.34)]);
                break;
            end
            if Vol_o(i) <= 0    %oil depletion fault
                disp(['ABORTED -- Oil depleted at mile ',...
                    num2str(d(i)/1609.34)]);
                break;
            end
            if P_s(i) <= 0  %excessive pressure drop fault
                disp(['ABORTED -- Pressure fault at mile ',...
                    num2str(d(i)/1609.34)]);
                break;
            end
            if Vol_leakage > Vol_leakage_max    %excessive oil leakage
fault
                disp(['ABORTED -- Chamber flooded at mile ', ...
                    num2str(d(i)/1609.34)]);
                break;
            end
            if ~isreal(alpha_f(i))  %numerical fault -- complex number
                disp(['ABORTED -- Complex number encountered at time
step ',...
                    num2str(i)])
                break;
            end
        end

        %% Save Frame if Making Movie
        if HUD && (rem(t(i),1/movieFps) == 0)
            frameUpdate
            F(frameNumber) = getframe(allFigs);
            frameNumber = frameNumber + 1;
        end

    end     %end simulation

    %% Run Pump Re-sizing algorithm
    if ~optimizing %check for proper pump/motor sizing
        utilVDPM = max(abs(D))/D_max; %PM utilization
        f_pressure = range(P_s(1:i))/P_d;   %actual pressure
fluctuation band
        nMaxPwr = find(abs(W_dot)==max(abs(W_dot)));    %index of time
of maximum power
        switch arch(2)
            case 0  %VDPM
                if (max(abs(D)) < D_max) && (utilVDPM >= utilVDPM_min)
...
                        && ~depleted %VDPM is properly sized
```

```
                    sized = 1;
                else    %VDPM is improperly sized
                    fprintf(['PM Utilization:
',num2str(100*utilVDPM),'\n']);
                    D_max = 1.05*max(abs(D)); %resize PM -- oversize by
5 percent to speed process
                end
            case 1  %FDPM
                if f_pressure < R_control*f_control %FDPM is properly
sized
                    sized = 1;
                else    %FDPM is improperly sized
                    fprintf(['Pressure Band:
',num2str(100*f_pressure),' %%\n']);
                    D_max =
1.0*2*pi*max(abs(W_dot))/(P_s(nMaxPwr)*omega_PM(nMaxPwr));    %resize
PM
                end
        end
        sizeCt = sizeCt + 1;    %increment sizing iteration counter
        if sizeCt == maxSizeCt     %give up on sizing PM
            fprintf('FAILED TO PROPERLY SIZE PUMP-MOTOR\n\n')
            sized = 1;
        end
    else    %force PM to be sized correctly if running an optimization
        sized = 1;
    end

end
```

vacuumToggle.m

This function implements deadband control to toggle the vacuum pump on and off, as is required to keep the containment chamber pressure within its acceptable band.

```
function vacOn = vacuumToggle(P,P_set,vacOn,f_band)

    P_max = P_set*(1 + f_band); %max pressure, Pa

    if P >= P_max   %pressure is too high
        vacOn = 1;
    elseif P < P_set    %pressure is lower than setpoint
        vacOn = 0;
    else    %pressure is within deadband
        vacOn = vacOn;
    end

end
```

cfun_simpleBand.m

This function implements the simple band control strategy introduced in Section 6.2.

```
function [pwrMode, depleted, t_switchLast] = cfun_simpleBand(W_dot, ...
    Vol_o, Vol_o_min, Vol_g, Vol_g_min, lastPwrMode, t_now, ...
    t_switchLast, t_switchMin, P_s_o, P_min, P_max, dt)

depleted = 0;   %depletion indicator defaults to not depleted

if W_dot == 0   %no flow rate demanded
    pwrMode = 0;

    %% Special Cases
elseif (W_dot <=0) && (Vol_o - Vol_o_min < -W_dot/P_s_o*dt)    %power
out of HFA and little oil left
    pwrMode = 1;

elseif (W_dot >=0) && (Vol_g - Vol_g_min < W_dot/P_s_o*dt)    %power
into HFA and full of oil
    pwrMode = 1;

elseif t_now - t_switchLast < t_switchMin     %switching time threshold
not met
    pwrMode = lastPwrMode;

    %% Standard Logic
elseif W_dot < 0    %power out of HFA
    if P_s_o <= P_min     %system pressure too low
        pwrMode = 1;  %use some kinetic flow
    else    %system pressure is too high or in acceptable band
        pwrMode = 0;  %use all pneumatic flow
    end

elseif W_dot > 0    %power into HFA
    if P_s_o >= P_max   %system pressure too high
        pwrMode = 1;  %use some kinetic flow
    else    %system pressure is too low or in acceptable band
        pwrMode = 0;  %use all pneumatic flow
    end
else
    pwrMode = 0;
end

%record current time if mode was switched
if pwrMode ~= lastPwrMode
    t_switchLast = t_now;
end

end
```

calcPwrFDPM.m

This function implements the PM model presented in Section 4.2 to calculate the storage PM shaft power as a function of the demanded or supplied power in the kinetic domain and the instantaneous PM efficiency.

```
function [eta_m, eta_v, x, W_dot_f, W_dot_s] = calcPwrFDPM(W_dot, ...
    pwrMode, P, omega, D_max, C_v, C_f, C_h, C_s, C_st, rho, mu, beta,
...
    eta_GR)

if pwrMode == 0     %kinetic domain is inactive

    %set PM parameters to zero
    eta_m = 0;
    eta_v = 0;
    x = 0;
    W_dot_f = 0;
    W_dot_s = 0;

else    %kinetic domain is active

    D = D_max/(2*pi);   %convert to m3/radian
    x = 1; %set displacement to 1 for efficiency calculations

    %calculate dimensionless numbers
    S = mu*omega/P;
    sigma = omega*D^(1/3)/sqrt(2*P/rho);

    %calculate real displacement position and efficiencies
    if W_dot < 0    %pumping

        %calculate mechanical and volumetric efficiencies
        eta_m = 1/(1 + C_v*S/x + C_f/x + C_h*x^2*sigma^2);
        eta_v = 1 - C_s/(x*S) - P/beta - C_st/(x*sigma);

        %protect against non-physical model error
        eta_m = max(.01,min(1,eta_m));
        eta_v = max(.01,min(1,eta_v));

        %calculate fluid and shaft power
        x = -1; %reset displacement to satisfy sign convention for
pumping
        W_dot_f = P*x*D*omega*eta_v;  %real fluid power produced, W
        W_dot_s = W_dot_f/(eta_v*eta_m*eta_GR); %required shaft power,
W

    else%if W dot >= 0   %motoring

        %calculate mechanical and volumetric efficiencies
        eta_m = 1 - C_v*S/x - C_f/x - C_h*x^2*sigma^2;  %mechanical
efficiency
        eta_v = 1/(1 + C_s/(x*S) + P/beta + C_st/(x*sigma));
%volumetric efficiency
```

```
        %protect against non-physical model error
        eta_m = max(.01,min(1,eta_m));
        eta_v = max(.01,min(1,eta_v));

        %calculate fluid and shaft power
        W_dot_f = P*x*D*omega;  %real fluid power available, W
        W_dot_s = W_dot_f*eta_v*eta_m*eta_GR;   %available shaft power,
W
    end

end

end
```

calcDeltaP.m

This function uses classical duct flow theory to calculate the pressure drop in a round pipe.

```
function [dP, f_bar] = calcDeltaP(Vol_dot,D,L,e,k_loss,rho,mu)

    r = D/2;    %radius, m
    v = abs(Vol_dot/(pi*r^2));  %mean velocity, m/s
    Re = rho*v*D/mu;    %Reynold's number
    f_bar = min(10,fBar(Re,L,D,e));   %avg friction factor
    dP = (1/2)*rho*v^2*(f_bar*L/D + k_loss);    %pressure drop, Pa

end
```

fBar.m

This function calculates the average friction factor for a duct flow, as described in Section 4.3.

```
function f_bar = fBar(Re, L, D, e)

    Re_crit = 2800; %critical Reynolds number

    if(Re <= Re_crit)   %laminar flow

        L_plus = L/(D*Re);  %dimensionless length

        f_bar = (4/Re)*(3.44/sqrt(L_plus) + (1.25/(4*L_plus) + ...
            64/4 - 3.44/sqrt(L_plus))/(1 + .00021/L_plus^2));
%average friction factor

    else    %turbulent flow
```

```
        f_turb = (-2*log10(2*e/(7.54*D) - ...
            (5.02/Re)*log10(2*e/(7.54*D) + 13/Re)))^(-2);   %turbulent
friction factor

        f_bar = f_turb*(1 + (D/L)^(.7));    %average friction factor
    end

end
```

calcAeroDrag.m

This function calculates the rate of energy dissipation due to aerodynamic drag on a rotating cylinder. These methods were detailed in Section 4.1.

```
function [W_dot_w, Re_D, C_m] = calcAeroDrag(omega,r_o,L,d,rho,mu,Kn)

%define constants
K = 1.38e-23;   %Boltzman constant, J/K
m = 4.782e-26;    %molecular mass of air, kg
Kn_lo = .1; %high threshold for low Knudsen number regime
Kn_hi = 10; %low threshhold for high Knudsen number regime
T = 300;    %approximate gas temperature, K

%calculate Reynolds number and BL thickness
Re_D = rho*omega*r_o^2/mu;  %Re based on diameter
if Re_D <= 3e5
    delta = sqrt(mu/(rho*omega));   %boundary layer thickness, m
else
    delta = r_o^(3/5)*(mu/(rho*omega))^(1/5);   %boundary layer
thickness, m
end

%select appropriate correlation and calculate moment coefficient
if delta >= d  %small gap

    if Re_D <= 3e5  %laminar BL
        C_m = 2.67/sqrt(Re_D); %Genta, Eqn. 4.23
    else    %turbulent BL
        C m = 0.0622*Re D^(-1/5);    %Genta, Eqn. 4.24
    end

elseif Kn < Kn_lo   %large gap, continous medium

    if Re_D <= 5e4  %laminar BL
        C_m = 3.87/sqrt(Re_D); %Genta, Eqn. 4.14
    else    %turbulent BL
        C_m = 0.146*Re_D^(-1/5);    %Genta, Eqn. 4.15
    end

elseif Kn < Kn_hi  %large gap, transitional medium (.1 < Kn < 10)
```

```
    %low Kn regime
    if Re_D <= 5e4  %laminar BL
        C_lo = 3.87/sqrt(Re_D); %Genta, Eqn. 4.14
    else    %turbulent BL
        C_lo = 0.146*Re_D^(-1/5);    %Genta, Eqn. 4.15
    end

    %hi Kn regime
    C_hi = sqrt(m/(2*K*T))*1/(omega*r_o);  %Genta, Eqn. 4.17

    %linear interpolation
    C_m = C_lo + (C_hi - C_lo)*(Kn - Kn_lo)/(Kn_hi - Kn_lo);

else    %large gap, free molecular flow

    C_m = sqrt(m/(2*K*T))*1/(omega*r_o);  %Genta, Eqn. 4.17

end

%calculate aerodynamic power dissipation
C_m = C_m*(r_o + (5/2)*L)/r_o;    %correct for disk thickness
M_a = rho*omega^2*r_o^5*C_m;    %torque on flywheel, N-m
W_dot_w = M_a*omega;    %power dissipation due to aero drag, W

end
```

optimizationCalcs.m

This script is run after the drive cycle simulation has been completed. It calculates the various metrics that are required in the optimization algorithm. Note that the variable `i` is the final time step reached in the simulation.

```
%% Simulation Was Run
if sum(geoInfeas)==0 && isreal(SOC(i)) && SOC(i) < 2

    %% Objective 1: System Mass
    D_max_t = 2*pi*max(abs(W_dot_t(1:i)./omega_ax(1:i)./P_s(1:i)));
%actual required traction PM size, m3/rev
    if isinf(D_max_t) || D_max_t < 0      %numerical error occured due
to pressure or speed going to zero
        D_max_t = 2*pi*max(abs(W_dot_t(1:i)./omega_ax(1:i)))/P_s_min;
%conservative estimate for traction PM size, m3/rev
    end
    m_PM_t = m_mass*D_max_t + b_mass;   %actual PM mass, kg
    f_mass = (m + m_PM + m_PM_t)/(m_v + m + m_PM + m_PM_t); %mass of
HFA as a proportion of total vehicle mass

    %% Objective 2: HFA Energy Conversion Efficiency
    W_vi = sum(W_dot_vi(1:i))*dt;   %internal viscous loss, J
    W_l = sum(W_dot_l(1:i))*dt; %HSRU leakage loss, J
```

```
    W_vh = sum(W_dot_vh(1:i))*dt;   %HSRU viscous loss, J
    W_p = sum(W_dot_p(1:i))*dt; %HSRU pipe loss, J
    W_w = sum(W_dot_w(1:i))*dt; %windage loss, J
    W_b = sum(W_dot_b(1:i))*dt; %bearing loss, J
    W_ft = sum(W_dot_ft(1:i))*dt;   %feedthrough loss, J
    W_PM = sum(W_dot_PM(1:i))*dt;   %PM losses, J
    W_vac = sum(W_dot_vac(1:i))*dt +
calcPumpdown(P_ch_d,P_ch(i),P_atm,...
        beta_ch,Q,Vol_ch,S_p_on);    %vacuum pumping loss, J
    W_conv = sum(abs(W_dot(1:i)))*dt;   %energy converted (+/-) at HFA,
J
    W_loss = W_l + W_p + W_vi + W_vh + W_w + W_b + W_ft + W_PM + W_vac;
%total losses, J
    eta = 1 - W_loss/(W_conv + W_loss);  %efficiency: losses as a
proportion of total work conversion

    %% Constraint 1: Unifinished Distance
    dist_unf = d(n) - d(i); %unfinished distance, m
    SOC_f = SOC(i); %final SOC

    %% Constraint 2: Housing Safety Factor
    %each row of "loadCases" represents an extreme operating condition.
    %1) max pressure at zero speed case
    %2) min pressure and max speed
    %3) max pressure at max speed
    %using P_c as a minimum pressure is conservative, as the wall
pressure is actually higher due to rotational speed omega_d
    loadCases = [max(P_h) 0; 0 omega_d; max(P_int_o) omega_d];  %three
worst cases for housing
    switch arch(3)
        case 0 %all-metal housing
            SF_h = housingSFmetal(r_i, r_o, omega_d, rho_h, nu_h,
P_int_max, ...
                S_y_h);

        case 1 %filament-wound with metal liner
            [SF_l, SF_c, TH, ur_h, ~, ~, ~, ~, ~, ~, ~, ~] = ...
                housingSFcomposite(r_i, r_o, r_l, rho_l, ...
                E_l, nu_l, rho_c, nu12, E1, E2, loadCases, S_y_l, X, Y,
Yc);
            SF_h = min(SF_l, SF_c);
    end

    %% Simulation Was Not Run
else
    dist_unf = d(n);    %drive cycle is completely unfinished
    eta = 0;    %zero efficiency
    W_loss = inf;   %set losses to infinity
    SOC_f = NaN;    %final SOC is meaningless
    D_max_t = 2*pi*max(abs(W_dot_t./omega_ax))/P_s_min;  %conservative
estimate for traction PM size, m3/rev
    m_PM_t = m_mass*D_max_t + b_mass;   %actual PM mass, kg
    f_mass = (m + m_PM + m_PM_t)/(m_v + m + m_PM + m_PM_t); %mass
fraction
    loadCases = [P_h_max 0; 0 omega_d; P_int_max omega_d];  %three
worst cases for housing
```

```
    switch arch(3)
        case 0 %all-metal housing
            SF_h = housingSFmetal(r_i, r_o, omega_d, rho_h, nu_h,
P_int_max, ...
                S_y_h);

        case 1 %filament-wound with metal liner
            [SF_l, SF_c, TH, ur_h, ~, ~, ~, ~, ~, ~, ~, ~] = ...
                housingSFcomposite(r_i, r_o, r_l, rho_l, ...
                E_l, nu_l, rho_c, nu12, E1, E2, loadCases, S_y_l, X, Y,
Yc);
            SF_h = min(SF_l, SF_c);
    end

end
```

calcPumpdown.m

This function calculates the time and energy required to return the containment chamber pressure to its desired value after the simulation is complete.

```
function [W_pumpdown, t_pumpdown] =
calcPumpdown(P_d,P_i,P_amb,beta,Q,Vol_ch,S_p)

dt = .1;    %time-step size, s

%specify initial conditions
P_ch = P_i;   %chamber pressure, Pa
W_pumpdown = 0; %work done in pumping down, J
t_pumpdown = 0;  %time, s

%run simulation
while P_ch > P_d

    P_dot = (Q - P_ch*S_p)/Vol_ch;   %rate of change of chamber
pressure, Pa/s

    P_ch = P_ch + P_dot*dt;    %new chamber pressure, Pa

    W_pumpdown = W_pumpdown + ...
        dt*(P_ch*S_p*beta/(beta-1)*((P_amb/P_ch)^((beta-1)/beta)-1));
%increment pumpdown work, J

    t_pumpdown = t_pumpdown + dt;   %increment pumpdown time, s

end

end
```

housingSFcomposite.m

This function calculates the safety factor of both housing components, the liner and the wrap, based on the methods described in Section 3.5. It also returns the entire radially-dependent stress and strain distributions in these components.

```
function [SF_l, SF_w, TH, ur_i, rl, rw, sigma_rl, sigma_cl, sigma_rw,
sigma_cw, ur_l, ur_w] = ...
    housingSFcomposite(r_i, r_o, r_m, rho_l, E_l, nu_l, rho_w, nu12,
E1, ...
    E2, cases, S_y_l, X, Y, Yc)
%AUTHOR: Kyle Strohmaier, University of Minnesota-Twin Cities
%DATE: 4/15/14

%% Initial Definitions and Calculations
n_cases = size(cases,1);    %number of cases to test

%liner -- isotropic
E_Tl = E_l; %liner elastic modulus
beta_l = E_Tl/E_l;  %ratio of elastic moduli (unity for the liner)
%model-specific pre-calculations
Sigma_l = sqrt(1/beta_l);
m1l = -1 + Sigma_l;
m2l = -1 - Sigma_l;

%wrap -- transversly isotropic composite
beta_w = E2/E1; %ratio of elastic moduli
%model-specific pre-calculations
Sigma_w = sqrt(1/beta_w);
m1w = -1 + Sigma_w;
m2w = -1 - Sigma_w;

%geometric and assembly
delta = 0;  %initial interference fit between liner and wrap, m

%results arrays
VM = zeros(n_cases,1);  %maximum von Mises stress in liner
TH = zeros(n_cases,1);  %maximum Tsai-Hill value in wrap
ur_i = zeros(n_cases,1);    %displacement at inner radius

%% Cycle Through the Two Cases
for k=1:n_cases

    P_int = -cases(k,1);    %get internal pressure, Pa
    omega = cases(k,2); %get angular velocity, rad/s

    %Q-functions
    Q1l_ri = calcQ1(r_i,rho_l,omega,nu_l,beta_l);
    Q2l_ri = calcQ2(r_i,rho_l,omega,nu_l,beta_l);
    Q1w_ro = calcQ1(r_o,rho_w,omega,nu12,beta_w);
    Q2w_ro = calcQ2(r_o,rho_w,omega,nu12,beta_w);
    Q1l_rm = calcQ1(r_m,rho_l,omega,nu_l,beta_l);
    Q2l_rm = calcQ2(r_m,rho_l,omega,nu_l,beta_l);
    Q1w_rm = calcQ1(r_m,rho_w,omega,nu12,beta_w);
```

```
    Q2w_rm = calcQ2(r_m,rho_w,omega,nu12,beta_w);

    %% Construct Matrices
    %coefficient matrix
    %[C1l C2l C1c C2c sigma_int sigma_clm sigma_ccm]
    C = zeros(7,7);
    C(1,:) = [r_i^m1l r_i^m2l 0 0 0 0 0];
    C(2,:) = [0 0 r_o^m1w r_o^m2w 0 0 0];
    C(3,:) = [r_m^m1l r_m^m2l 0 0 -1 0 0];
    C(4,:) = [0 0 r_m^m1w r_m^m2w -1 0 0];
    C(5,:) = [(m1l+1)*r_m^m1l (m2l+1)*r_m^m2l 0 0 0 -1 0];
    C(6,:) = [0 0 (m1w+1)*r_m^m1w (m2w+1)*r_m^m2w 0 0 -1];
    C(7,:) = [0 0 0 0 (nu_l/E_l - nu12/E1) -1/E_l 1/E1];

    %B matrix
    B = zeros(7,1);
    B(1) = P_int - (Q1l_ri - Q2l_ri);
    B(2) = -(Q1w_ro - Q2w_ro);
    B(3) = -(Q1l_rm - Q2l_rm);
    B(4) = -(Q1w_rm - Q2w_rm);
    B(5) = -((m1l+1)*Q1l_rm - (m2l+1)*Q2l_rm + rho_l*omega^2*r_m^2);
    B(6) = -((m1w+1)*Q1w_rm - (m2w+1)*Q2w_rm + rho_w*omega^2*r_m^2);
    B(7) = delta;

    %% Solve System
    %fix scaling to improve condition of coefficient matrix
    C(7,:) = C(7,:)*10^13;
    B(7) = B(7)*10^13;
    C(2,:) = C(2,:)*10^2;
    B(2) = B(2)*10^2;

    %solve system and retrieve important parameters
    x = C\B;
    C1l = x(1);
    C2l = x(2);
    C1c = x(3);
    C2c = x(4);

    %% Calculate Stress Distributions
    %make radius vector and calculate important indicies
    dr = .0001; %radial spatial step size, m
    r = r_i:dr:r_o; %radial position vector
    ni = 1; %index of inner radius
    no = length(r); %index of outer radius
    [~, nm] = min(abs(r-r_m));  %index of radius of liner-wrap
interface
    rl = r(ni:nm);  %radial position vector for liner
    rw = r(nm+1:no);    %radial position vector for wrap

    %calculate Q-curves
    Q1l = rl.^2*rho_l*omega^2*(3+nu_l)/(2*sqrt(1/beta_l)*(-3 +
sqrt(1/beta_l)));
    Q2l = rl.^2*rho_l*omega^2*(3+nu_l)/(2*sqrt(1/beta_l)*(-3 -
sqrt(1/beta_l)));
    Q1w = rw.^2*rho_w*omega^2*(3+nu12)/(2*sqrt(1/beta_w)*(-3 +
sqrt(1/beta_w)));
```

```
    Q2w = rw.^2*rho_w*omega^2*(3+nu12)/(2*sqrt(1/beta_w)*(-3 -
sqrt(1/beta_w)));

    %calculate stresses
    sigma_rl = C1l*rl.^m1l + C2l*rl.^m2l + Q1l - Q2l;   %radial stress
in the liner, Pa
    sigma_cl = C1l*(m1l+1)*rl.^m1l + C2l*(m2l+1)*rl.^m2l + (m1l+1)*Q1l
...
        - (m2l+1)*Q2l + rho_l*omega^2*rl.^2;    %circumferential stress
in the liner, Pa
    sigma_rw = C1c*rw.^m1w + C2c*rw.^m2w + Q1w - Q2w;   %radial stress
in the wrap, Pa
    sigma_cw = C1c*(m1w+1)*rw.^m1w + C2c*(m2w+1)*rw.^m2w + (m1w+1)*Q1w
...
        - (m2w+1)*Q2w + rho_w*omega^2*rw.^2;    %circumferential stress
in the wrap, Pa

    %calculate radial displacements
    ur_l = rl./E_l.*(sigma_cl - nu_l*sigma_rl);  %radial displacement
distribution in liner, m
    ur_w = rw./E1.*(sigma_cw - nu12*sigma_rw);   %radial displacement
distribution in wrap, m
    ur_i(k) = r_i/E_l*(sigma_cl(ni) - nu_l*sigma_rl(ni));   %radial
displacement at inner radius, m

    %calculate maximum von Mises stress in liner
    VM(k,:) = max(sqrt(sigma_cl.^2 - sigma_cl.*sigma_rl +
sigma_rl.^2));

    %calculate maximum Tsai-Hill value for wrap
    TH(k) = max((sigma_cw/X).^2 + (sigma_rw/Y).^2 -
sigma_cw.*sigma_rw/X^2);


end

%% Determine Safety Factors
SF_l = min(S_y_l./VM);  %liner safety factor
SF_w = min(1./TH);  %wrap safety factor

end
```

postSimCalcs.m

This script executes the calculations of various performance metrics that are not required for the optimization algorithm, but that are informative nonetheless.

```
%results of drive cycle
SOC_f = SOC(i);   %final SOC
P_s_avg = mean(P_s(1:i)); %average system pressure, Pa
```

```
W_HFA = e(1) - e(i);    %energy extracted from HFA over drive cycle, J
W_noncons = sum(v(1:i).*(F_aero(1:i) + F_roll(1:i)))*dt;   %sum of non-
conservative work, J
W_regen = sum(abs(W_dot_h(W_dot_h.*W_dot_k<0)))*dt;    %energy
regenerated between kinetic to pneumatic, J
f_regen = W_regen/(W_conv + W_loss);
W_k = sum(abs(W_dot_k(1:i)))*dt;    %total energy converted through
kinetic domain, J
W_h = sum(abs(W_dot_h(1:i)))*dt;    %total energy converted through
pneumatic domain, J
W_pure = sum(abs(W_dot(W_dot_k==0)))*dt;
f_kinetic = W_k/W_conv;    %kinetic fraction
f_pneumatic = W_h/W_conv;   %pneumatic fraction
R_usage = W_k/W_pure; %domain usage ratio
R_cap = e_k_d/e_h_d;    %domain capacity ratio
Vol_l = sum(Vol_dot_l(1:i))*dt; %total leakage from HSRU, m3

%PM results
Pwr_max = max(abs(W_dot_s))/1000; %maximum PM power, kW
eta_PM_avg = mean(eta_v(eta_v~=0).*eta_m(eta_v~=0));  %average PM
efficiency (for non-zero power)

%traction PM results
D_max_t_ideal = 2*pi*max(abs(W_dot_t./omega_ax))/P_d;   %ideal (zero
pressure fluctuation) traction PM size, m3/rev
m_PM_t_ideal = m_mass*D_max_t_ideal + b_mass;   %ideal traciton PM
mass, kg
per_mass = (m_PM_t-m_PM_t_ideal)/m_PM_t_ideal;  %required fractional
increase in PM size due to pressure fluctuation
```

therm.m

This script executes the computational heat transfer scheme detailed in Section 8.6.

```
%% Define Physical Properties
%oil properties
rho_o = 879; %oil density, kg/m^3
nu_o_init = 46*(1/1000)^2; %oil kinematic viscosity, m2/s
mu_o_init = nu_o_init*rho_o;    %oil dynamic viscosity, kg/m-s
c_o = 1670; %heat capacity of oil, J/kg-K
k_o = 0.1;  %thermal conductivity of oil, W/m-K

%system properties
P_s = 2.0673e+07;   %system pressure, Pa
omega = 1154;   %angular velocity, rad/s
T_in = 40;  %temperature of oil entering seal, C

%shaft/HSRU properties
d_i = .0054;    %axle inner diameter, m
l_s = .0082; %seal length
d_s_init = .059;    %
c_init = 15e-6; %initial clearance
```

```
d_c = d_s_init + 2*c_init;  %case inner diameter, m
T_PM = 50;  %pump-motor temperature, C
Ts_init = 30;   %initial axle temperature, C
T_c = 40;   %HSRU case temperature, C
rho_s = 7800;   %density of axle, kg/m3
c_s = 490; %heat capacity of axle, J/kg-K
k_s = 35;    %thermal conductivity of axle, W/m-K
alpha_s = k_s/(rho_s*c_s);  %thermal diffusivity of axle, m2/s
alpha_s_thermal = 13e-6;    %thermal expansion coefficient of axle,
m/m-K

%shaft axial thermal resistance
w_br = .008;    %bearing width, m
d_b_i = .009;   %bearing inner diameter, m
len_e = .0305;  %end cap length, m
d_o = .0478;    %outer radius of major axle section (d_o=2*r_a)
len_i = .1467;  %inner length of HFA, m

%1-D axle thermal resistances
R_tot = 4*w_br/(k_s*pi*(d_b_i^2-d_i^2));    %oil side axle shaft
R_tot = R_tot + 4*len_e/(k_s*pi*(d_o^2-d_i^2)); %axially-ported section
R_tot = R_tot + 4*(len_i+len_e)/(k_s*pi*d_o^2); %non-ported section
R_tot = R_tot + 4*w_br/(k_s*pi*d_b_i^2);  %gas side axle shaft

%define BC assumptions
shaftIns = 0;   %front end and bottom (inside) of shaft are insulated
caseIns = 0;    %HSRU case is insulated from fluid in seal

%% Set Up Numerical Problem
%mesh properties in the oil
dx = .0002; %x step size, m
nx = l_s/dx + 1;    %number of x points
x = 0:dx:l_s;   %x array

ny = 20;    %number of y points
dy = c_init/(ny-1); %y step size
y = 0:dy:c_init;    %y array

%mesh properties in the axle
nxs = nx;
dxs = dx;
xs = x;
nys = 16;
dys = (d_s_init-d_i)/(nys-1);
ys = 0:dys:(d_s_init-d_i);

%time step properties
t_tot = .15;    %total time to simulate
dt = 2e-6;  %time step size, s
nt = round(t_tot/dt) + 1;   %number of time steps

%% Initialize Arrays and Matricies
%x-dependent arrays
c = zeros(1,nx);
d_s = zeros(1,nx);
```

```
ux_mean = zeros(1,nx);
ux_max = zeros(1,nx);

%x- and y-dependent matricies
To = zeros(nx,ny);
ToLast = zeros(nx,ny);
Ts = zeros(nxs,nys);
TsLast = zeros(nxs,nys);
q_dot_gen_z = zeros(nx,ny);
q_dot_gen_x = zeros(nx,ny);
q_dot_gen = zeros(nx,ny);
mu_o = zeros(nx,ny);
ux = zeros(nx,ny);

%saved data
To_data = zeros(nx,ny,1);
Ts_data = zeros(nxs,nys,1);
q_dot_gen_z_data = zeros(nx,ny,1);
q_dot_gen_x_data = zeros(nx,ny,1);
ux_data = zeros(nx,ny,1);
d_s_data = zeros(nx,1);
c_data = zeros(nx,1);
t = zeros(1,1);

%% Set ICs and BCs
ToLast(:,:) = T_in;
TsLast(:,:) = Ts_init;
c(:) = c_init;
d_s(:) = d_s_init;
q_dot_gen_z(:,:) = 0;
q_dot_gen_x(:,:) = 0;
mu_o(:,:) = linFit(40,100,46,7.8,T_in)*(1/1000)^2*rho_o;

%% Run Simulation
%prepare progress reporting
per prog = 0:.1:100;
k = 1;
abort = 0;

for n=2:nt

    %% Fluid
    %new flow characteristics
    Vol_dot_l =
P_s*pi*mean(d_s(:))*mean(c(:))^3/(12*mean(mu_o(:))*l_s);

    for i=2:nx-1    %cycle through x-dimension

        %new dy and y-dimension array
        dy = c(i)/(ny-1);
        y = 0:dy:c(i);

        %new x-velocity
        ux_mean(:) = 4*Vol_dot_l./(pi*(d_c^2 - d_s(:).^2));
        ux_max(:) = (3/2)*ux_mean(:);
```

```
        for j=1:ny

            yi = (j-1)*dy;

            %new x-velocity distribution
            ux(i,j) = ux_max(i)*(1 - (2*yi/c(i) - 1)^2);

            %new heat generation
            q_dot_gen_z(i,j) = mu_o(i,j)*(omega*d_s(i)/(2*c(i)))^2;
            q_dot_gen_x(i,j) = mu_o(i,j)*(4*ux_max(i)/c(i) -
8*ux_max(i)*yi/c(i)^2)^2;

            if j==1     %bottom BC -- mate with shaft
                To(i,j) = ToLast(i,j) + ...
                    dt*(1/(rho_o*c_o)*(k_o*((ToLast(i-1,j) -
2*ToLast(i,j) + ToLast(i+1,j))/dx^2 ...
                    + (TsLast(i,nys-1) - 2*ToLast(i,j) +
ToLast(i,j+1))/dy^2) ...
                    + q_dot_gen_z(i,j) + q_dot_gen_x(i,j)) ...
                    - ux(i,j)*(ToLast(i+1,j) - ToLast(i-1,j))/(2*dx));
            elseif j==ny    %top BC
                if caseIns
                    To(:,ny) = To(:,ny-1);
                else
                    To(:,ny) = T_c;
                end
            else
                To(i,j) = ToLast(i,j) + ...
                    dt*(1/(rho_o*c_o)*(k_o*((ToLast(i-1,j) -
2*ToLast(i,j) + ToLast(i+1,j))/dx^2 ...
                    + (ToLast(i,j-1) - 2*ToLast(i,j) +
ToLast(i,j+1))/dy^2) ...
                    + q_dot_gen_z(i,j) + q_dot_gen_x(i,j)) ...
                    - ux(i,j)*(ToLast(i+1,j) - ToLast(i-1,j))/(2*dx));
            end

            %new oil properties
            mu_o(i,j) = linFit(40,100,46,7.8,To(i,j))*(1/1000)^2*rho_o;


            if c(i) <= 0
                fprintf(['ABORTED -- Seal interference at t = ',...
                    num2str(n*dt),' and l = ',num2str(i*dx)])
                abort = 1;
            end
            if To(i,j) >= 100
                fprintf(['ABORTED -- Oil temp 100 C at t = ',...
                    num2str(n*dt),' and l = ',num2str(i*dx)])
                abort = 1;
            end
        end
```

```
    end

    %entrance and exit BCs
    To(1,:) = T_in;  %BC: entry temp at every y-position is T_in
    To(nx,:) = To(nx-1,:);    %BC: set exit temperatures to dT/dx = 0

    ToLast = To;


    %% Shaft

    for i=2:nxs

        for j=2:nys-1

            yi = (j-1)*dys;

            if i==nxs   %interface between computational domain and the
1-D axle resistance
               Ts(i,j) = 1/(1 + dx/(k_s*R_tot*pi/4*(d_s(i)^2 -
d_i^2)))*(Ts(i-1,j) + dx/(k_s*R_tot*pi/4*(d_s(i)^2 - d_i^2))*T_PM);
            else    %regular axle domain
            Ts(i,j) = TsLast(i,j) + ...
                dt*alpha_s/yi*((TsLast(i-1,j) - 2*TsLast(i,j) +
TsLast(i+1,j))/dxs^2 ...
                + yi*(TsLast(i,j-1) - 2*TsLast(i,j) +
TsLast(i,j+1))/dys^2 ...
                + (TsLast(i,j+1) - TsLast(i,j-1))/(2*dys));
            end

        end
        Ts(:,nys) = To(:,1);    %top of axle portion is equal to bottom
of oil portion
        if shaftIns
            Ts(:,1) = Ts(:,2);  %BC: insulated shaft inner radius
        else
            Ts(:,1) = T_in; %BC: stagnant oil as a sink
        end

        %new shaft dimensions
        d_s(i) = d_s_init*(1 + alpha_s_thermal*(mean(Ts(i,:)) -
Ts_init));  %calculate new seal diameter, m
        c(i) = (d_c - d_s(i))/2;    %calculate new seal clearance, m
    end
    if shaftIns
        Ts(1,:) = Ts(2,:);  %BC: insulated shaft front end
    else
        Ts(1,:) = T_in;   %BC: stagnant oil as a sink
    end
%     Ts(nx,:) = T_PM;

    TsLast = Ts;
```

```
    %dimensions at the far-right of the axle portion
    d_s(nx) = d_s_init*(1 + alpha_s_thermal*(mean(Ts(nx,:)) -
Ts_init));    %calculate new seal diameter, m
    c(nx) = (d_c - d_s(nx))/2;  %calculate new seal clearance, m

    %% Update and Save
    per_comp = 100*n/nt;    %percent complete
    if per_comp>=per_prog(1)
        %SAVING
        t(k) = dt*n;
        To_data(:,:,k) = To(:,:);
        Ts_data(:,:,k) = Ts(:,:);
        q_dot_gen_z_data(:,:,k) = q_dot_gen_z(:,:);
        q_dot_gen_x_data(:,:,k) = q_dot_gen_x(:,:);
        ux_data(:,:,k) = ux(:,:);
        d_s_data(:,k) = d_s(:);
        c_data(:,k) = c(:);
        k = k+1;

        clc
        fprintf([num2str(round(per_comp)),' %% complete\n']);
        per_prog(1)=[];


    end
    if abort
        break;
    end

end
```

Appendix C: Complete Experimental Results from the Fluid Behavior Model Development

Eleven experimental datasets were used to generate and evaluate the correlatations for the fluid behavior model developed in Chapter 5. This appendix provides the complete results for these datasets, in order of the correlation numbers used in Tables 13 and 14. For each dataset, the following three figures are provided, with all parameters plotted against time for the highly transient region:

- Torque, measured and net (corrected for friction and windage); net power and the components of power applied to the solid and fluid components
- Solid and fluid angular velocities, measured and model-predicted
- Dynamic time constant and viscous dissipation rate, measured and model-predicted

In the plots that show model-predicted values, two sets of correlations are used. The dots correspond to predictions based on the final selected correlations for the fluid model (see Eqns. 156 and 157). The crosses correspond to predictions based on the correlations generated from the specific dataset being plotted. Unsurprisingly, then, the crosses generally show very good agreement with the measured data. The dots show that the final selected correlation performs fairly well for the entire range of datasets.

The overall R^2 values for the dataset-specific correlations are also listed here. The calculation of these values was detailed in Section 5.5. Due to the production of complex numbers, predictions based on the the dataset-specific correlations are omitted for datasets 2 through 4.

Dataset 1	
$R^2_{overall}$, viscous dissipation rate	0.99795
$R^2_{overall}$, dynamic time constant	0.99151

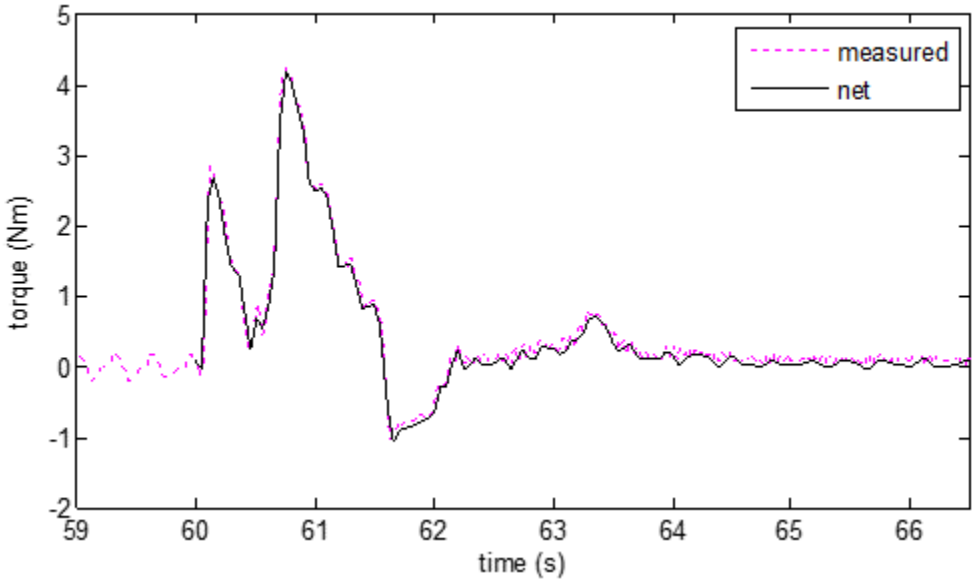

Figure 103: Measured and Net Torque vs. Time, Dataset 1

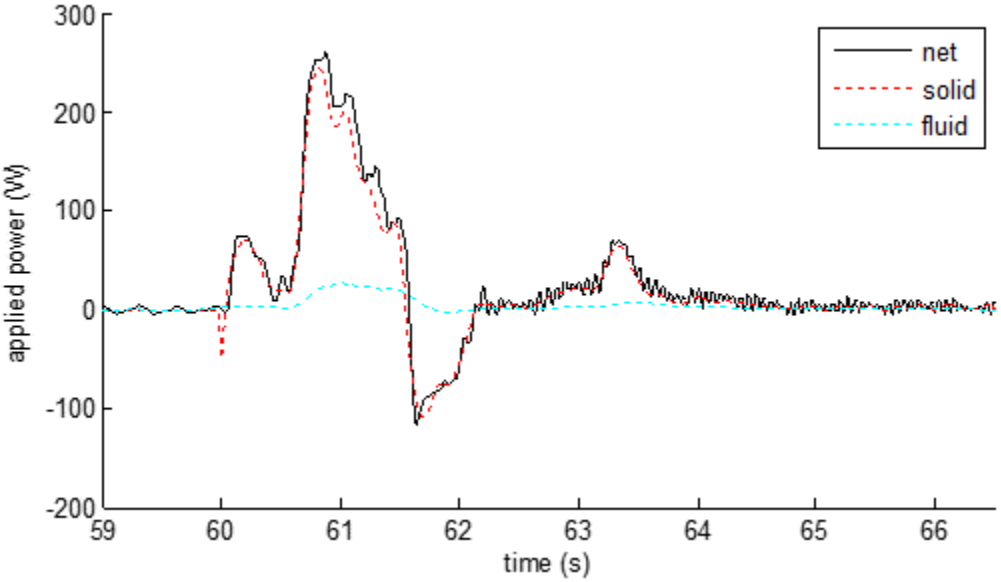

Figure 104: Power vs. Time, Dataset 1

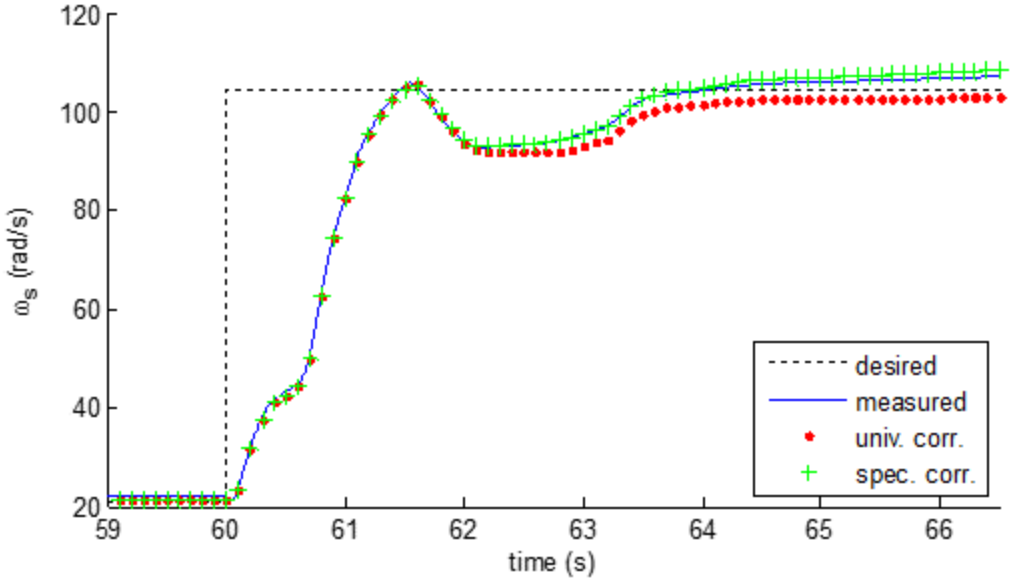

Figure 105: Solid Angular Velocity vs. Time, Dataset 1

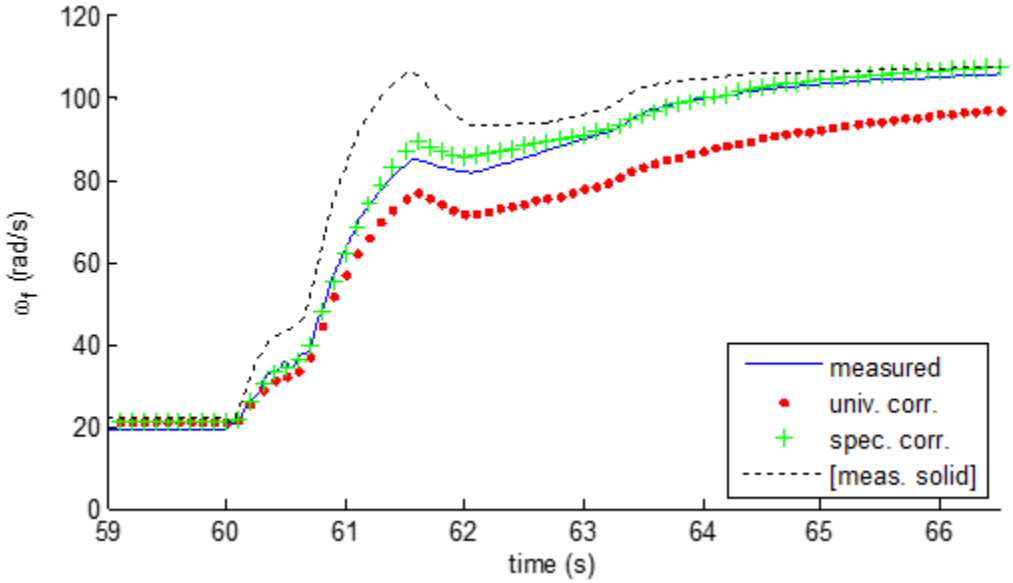

Figure 106: Fluid Angular Velocity vs. Time, Dataset 1

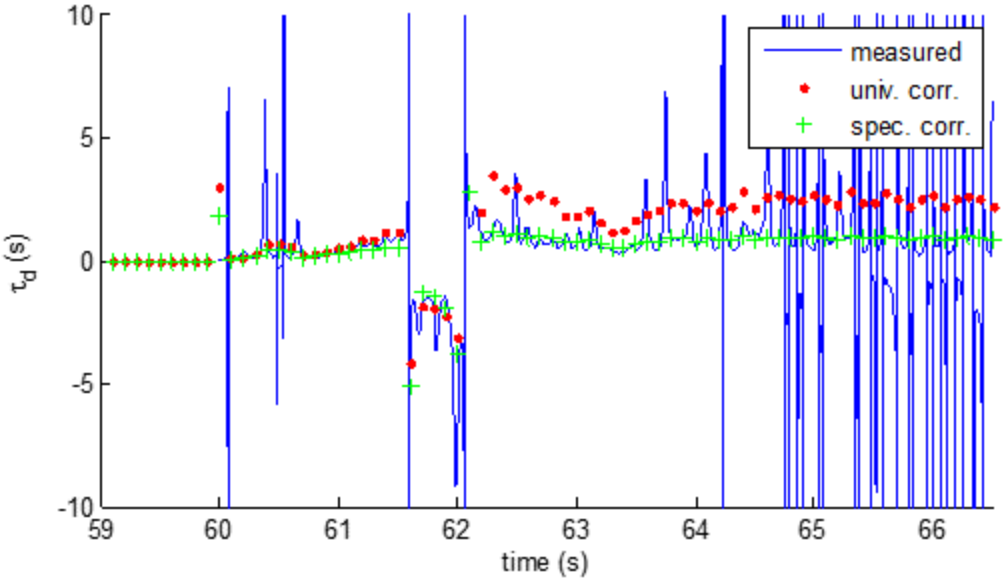

Figure 107: Dynamic Time Constant vs. Time, Dataset 1

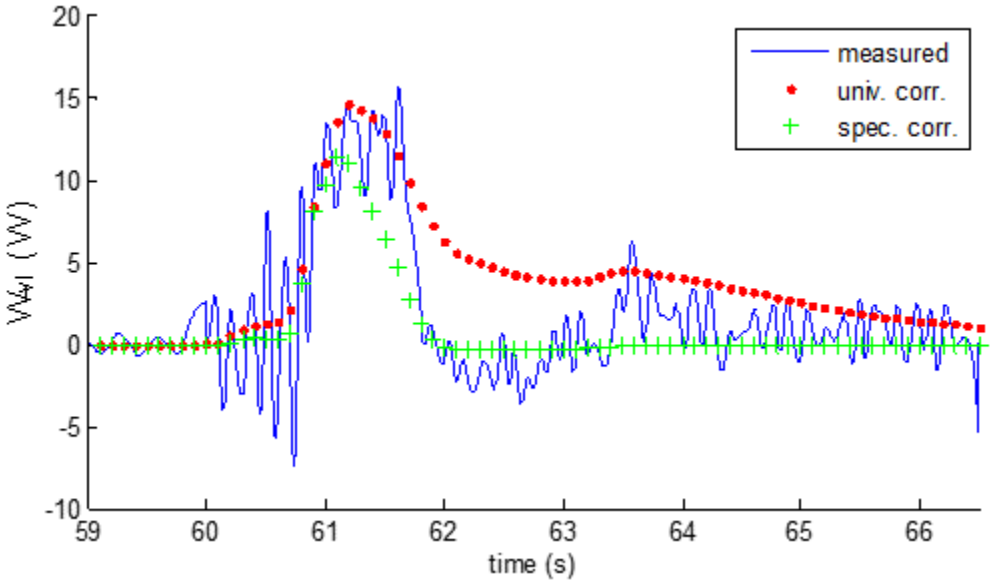

Figure 108: Viscous Dissipation Rate vs. Time, Dataset 1

Dataset 2	
$R^2_{overall}$, viscous dissipation rate	0.99685
$R^2_{overall}$, dynamic time constant	-

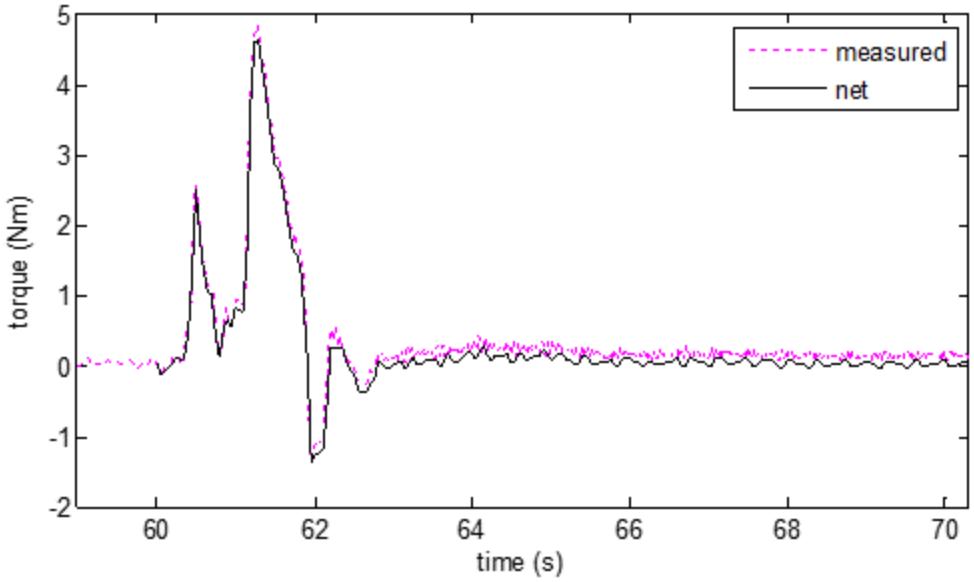

Figure 109: Measured and Net Torque vs. Time, Dataset 2

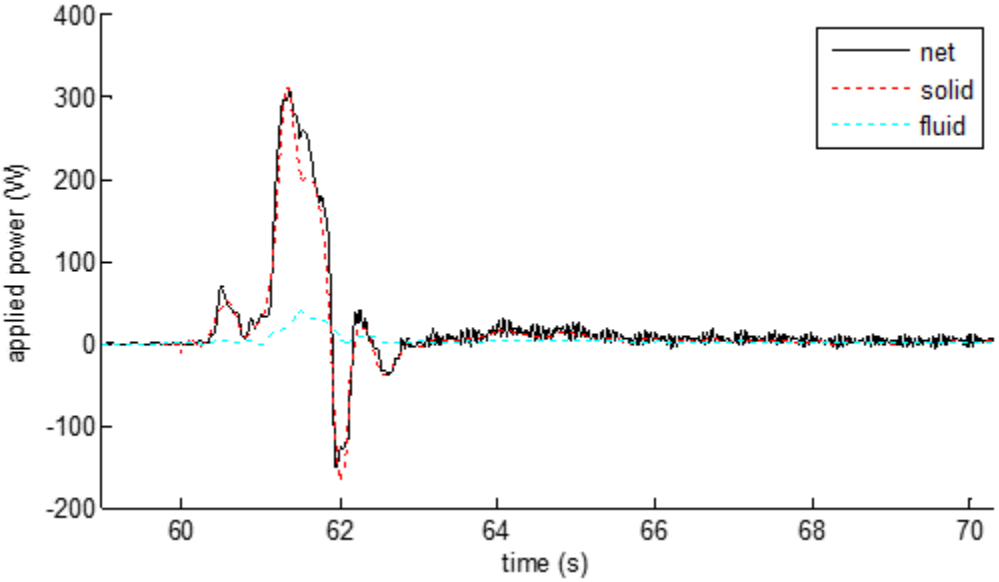

Figure 110: Power vs. Time, Dataset 2

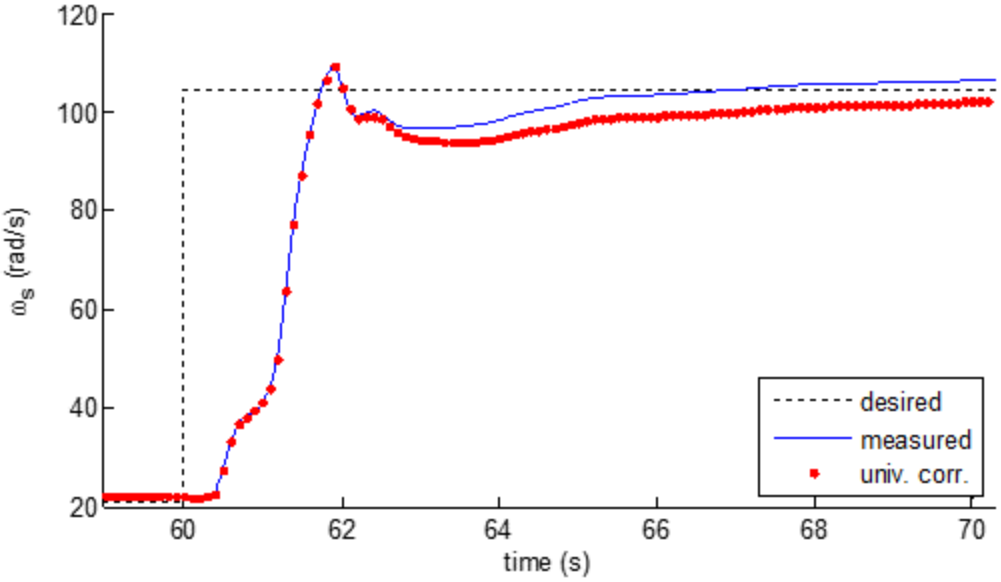

Figure 111: Solid Angular Velocity vs. Time, Dataset 2

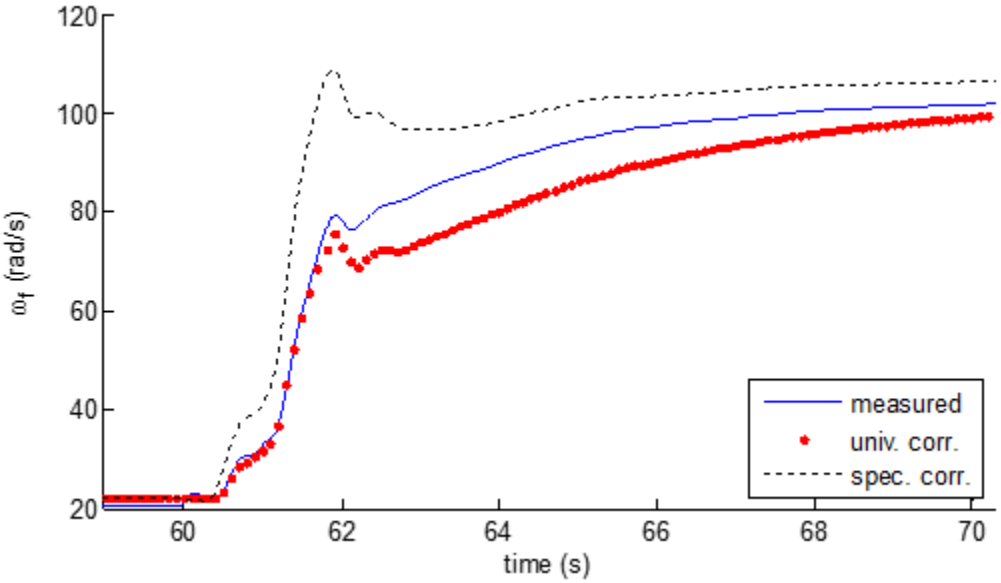

Figure 112: Fluid Angular Velocity vs. Time, Dataset 2

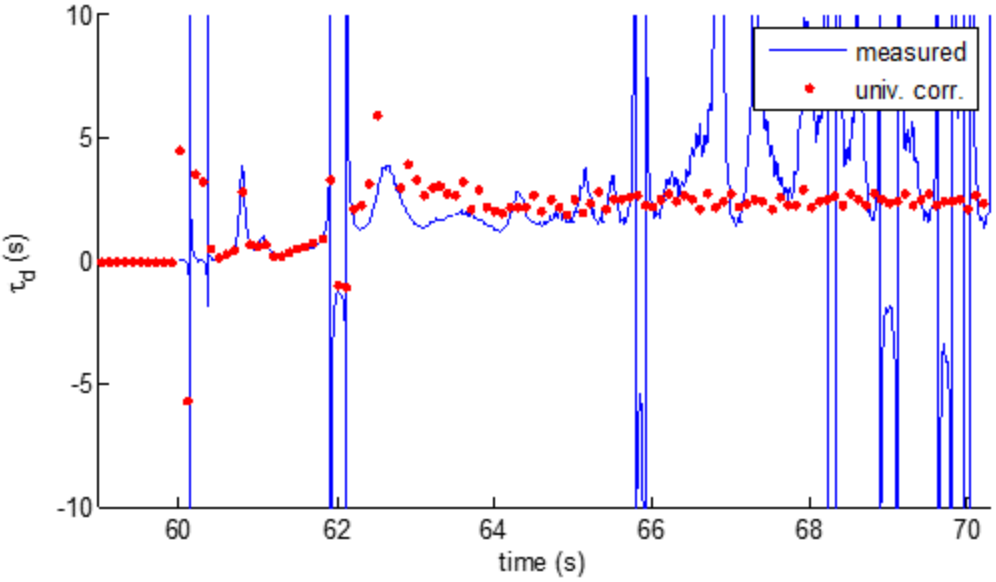

Figure 113: Dynamic Time Constant vs. Time, Dataset 2

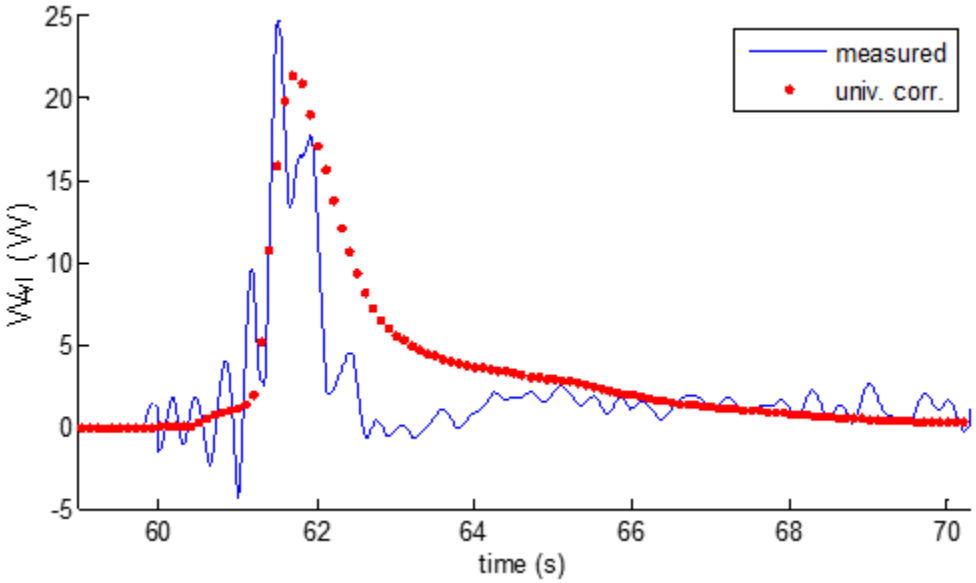

Figure 114: Viscous Dissipation Rate vs. Time, Dataset 2

Dataset 3	
$R^2_{overall}$, viscous dissipation rate	0.99816
$R^2_{overall}$, dynamic time constant	-

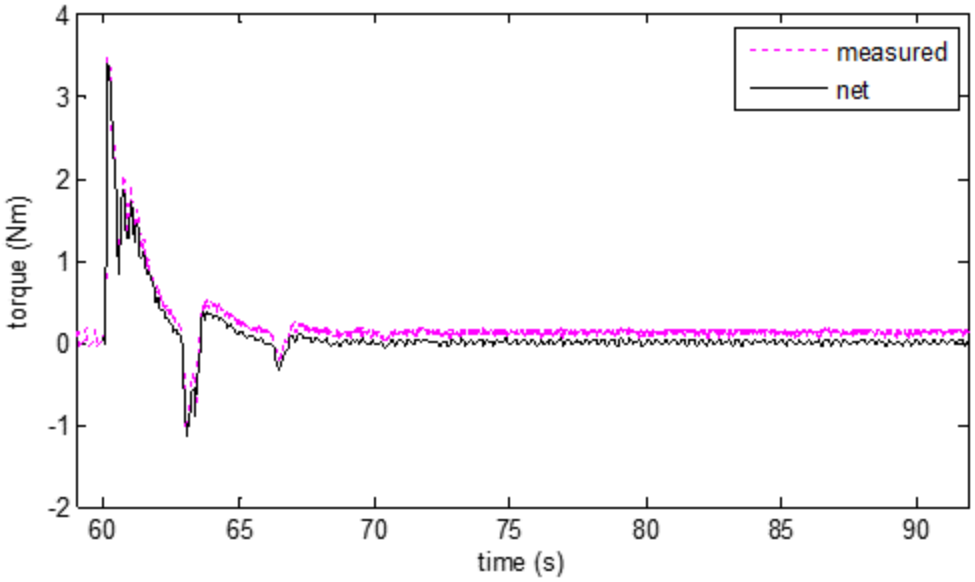

Figure 115: Measured and Net Torque vs. Time, Dataset 3

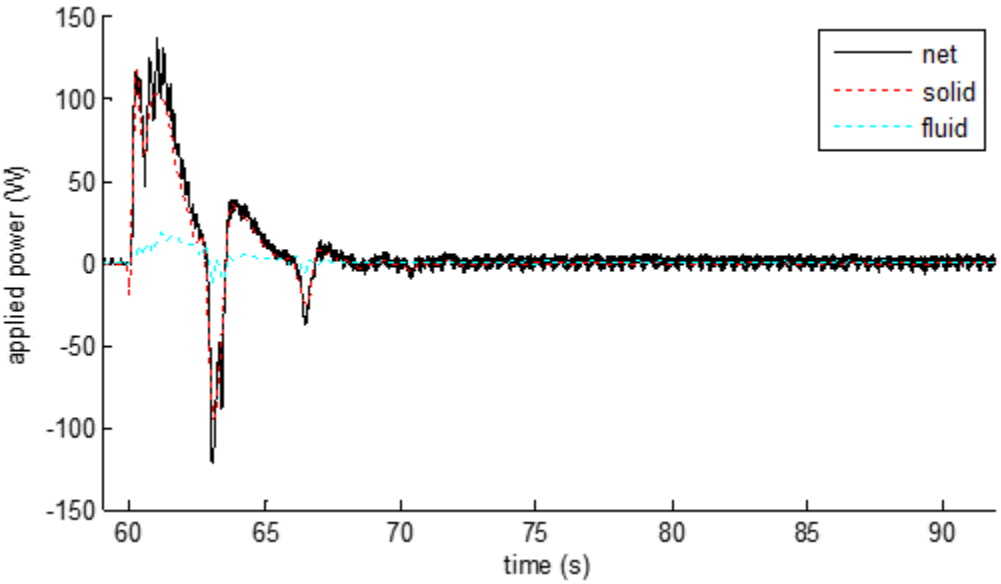

Figure 116: Power vs. Time, Dataset 3

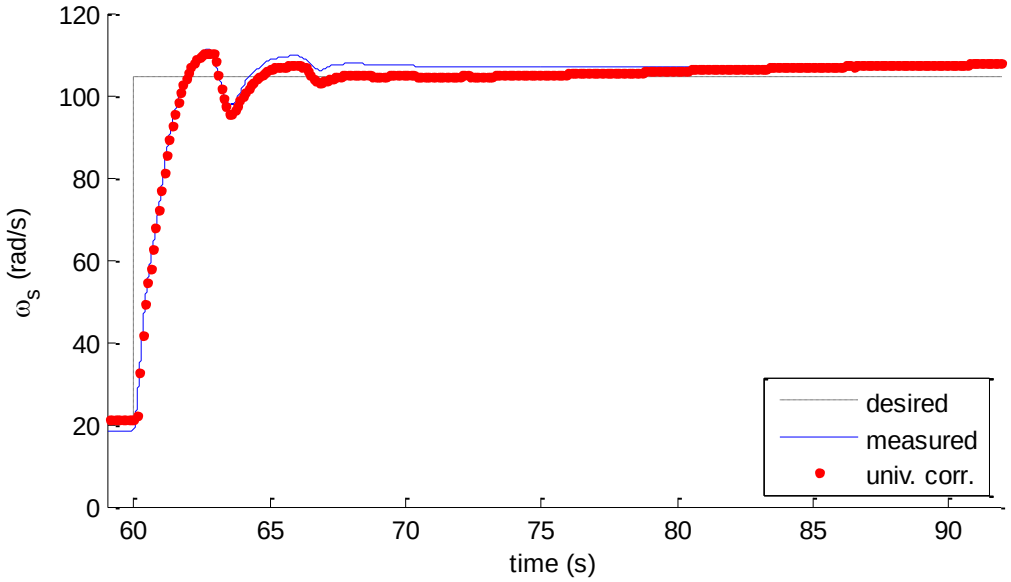

Figure 117: Solid Angular Velocity vs. Time, Dataset 3

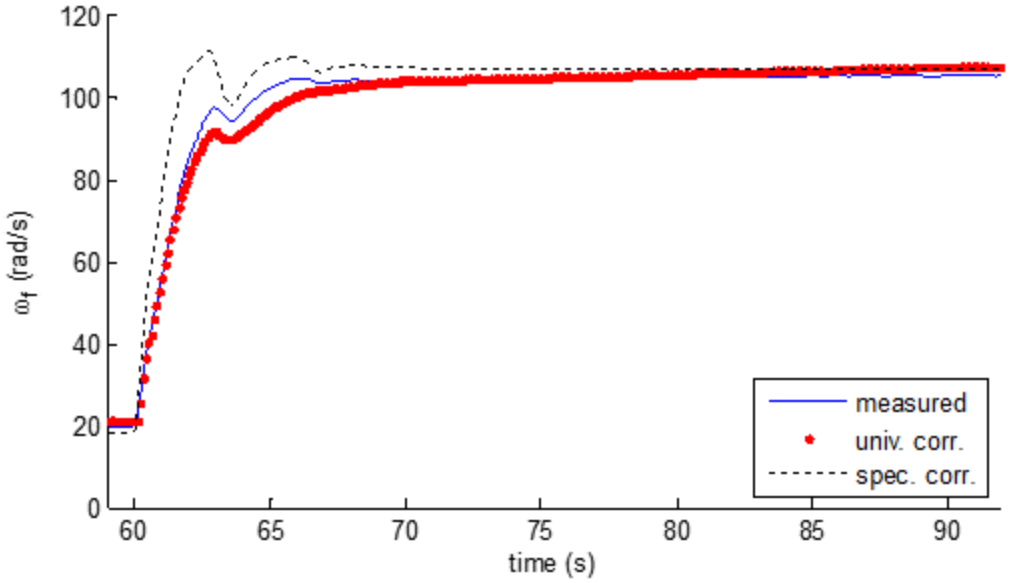

Figure 118: Fluid Angular Velocity vs. Time, Dataset 3

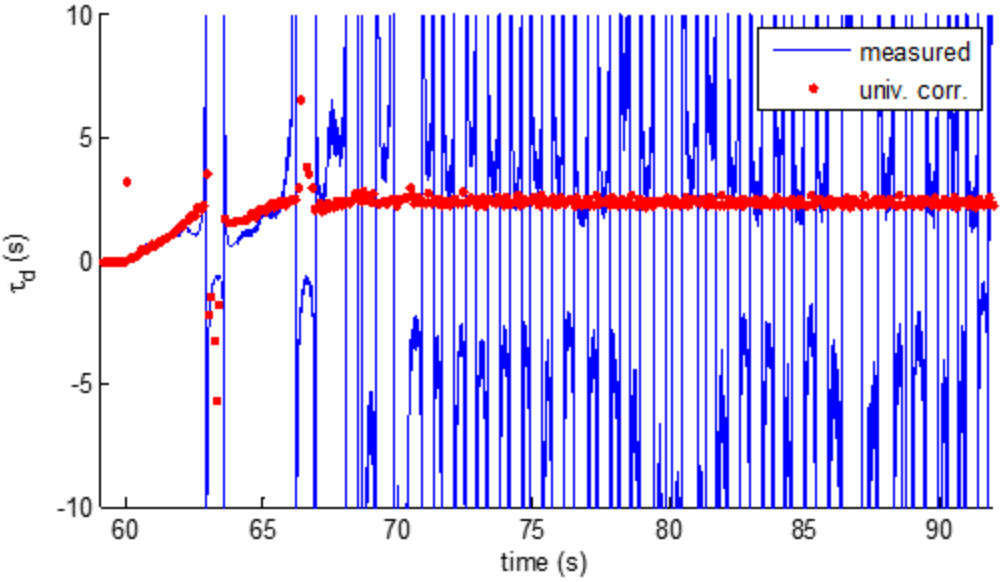

Figure 119: Dynamic Time Constant vs. Time, Dataset 3

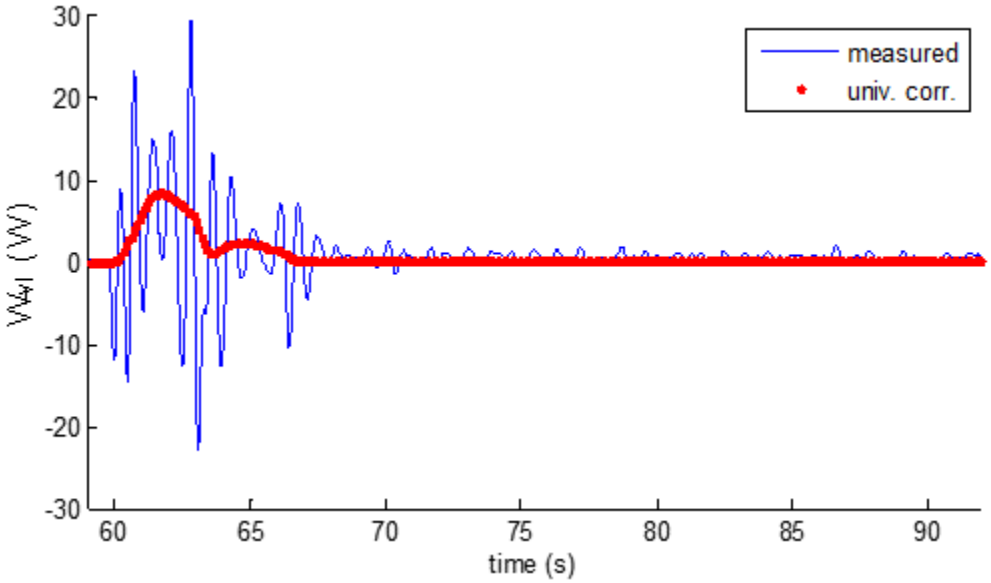

Figure 120: Viscous Dissipation Rate vs. Time, Dataset 3

Dataset 4	
$R^2_{overall}$, viscous dissipation rate	0.99805
$R^2_{overall}$, dynamic time constant	-

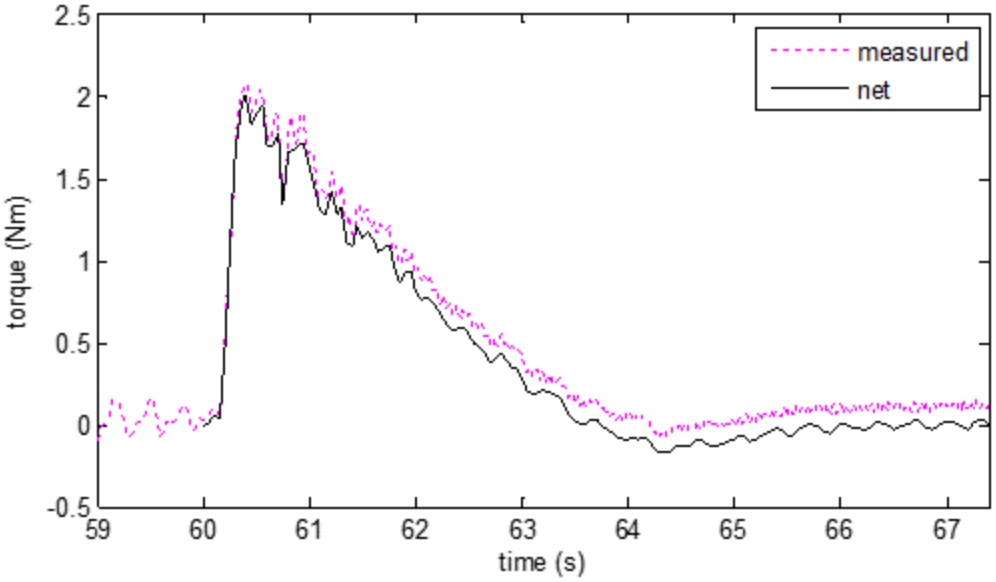

Figure 121: Measured and Net Torque vs. Time, Dataset 4

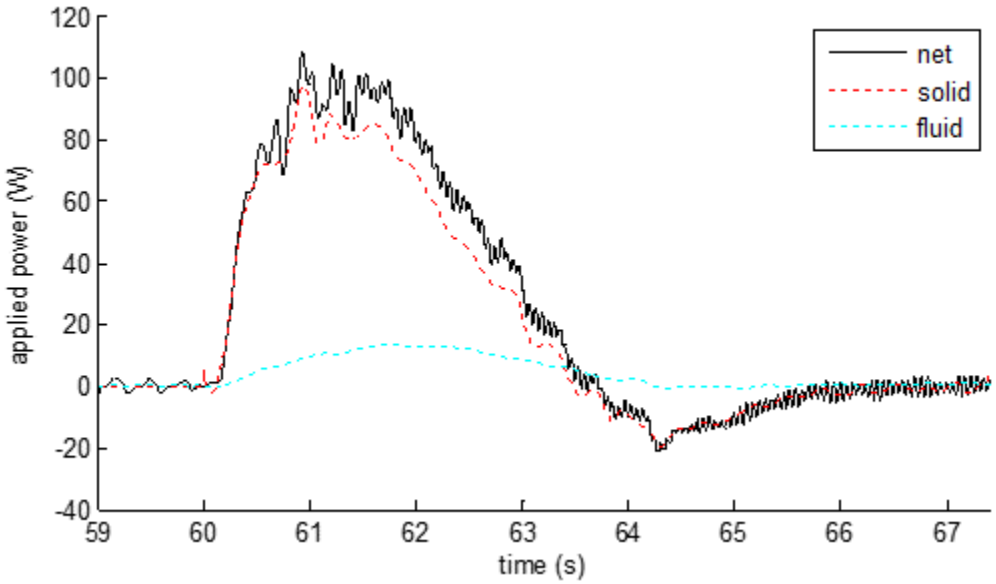

Figure 122: Power vs. Time, Dataset 4

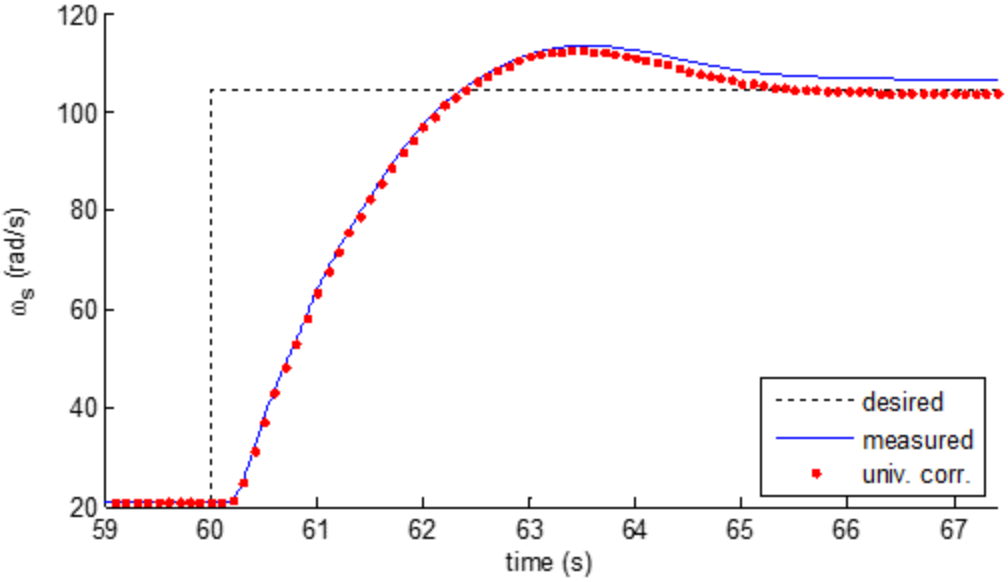

Figure 123: Solid Angular Velocity vs. Time, Dataset 4

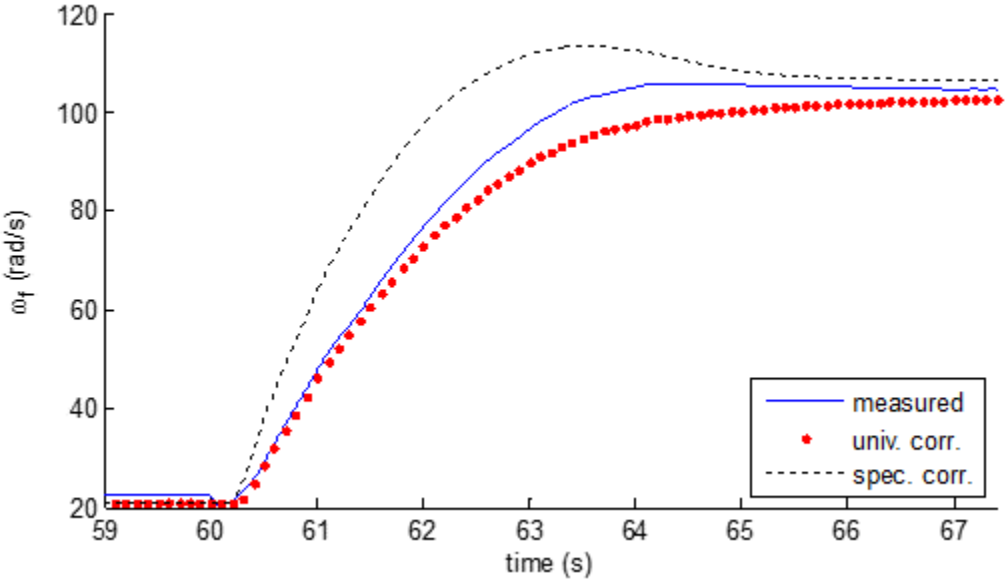

Figure 124: Fluid Angular Velocity vs. Time, Dataset 4

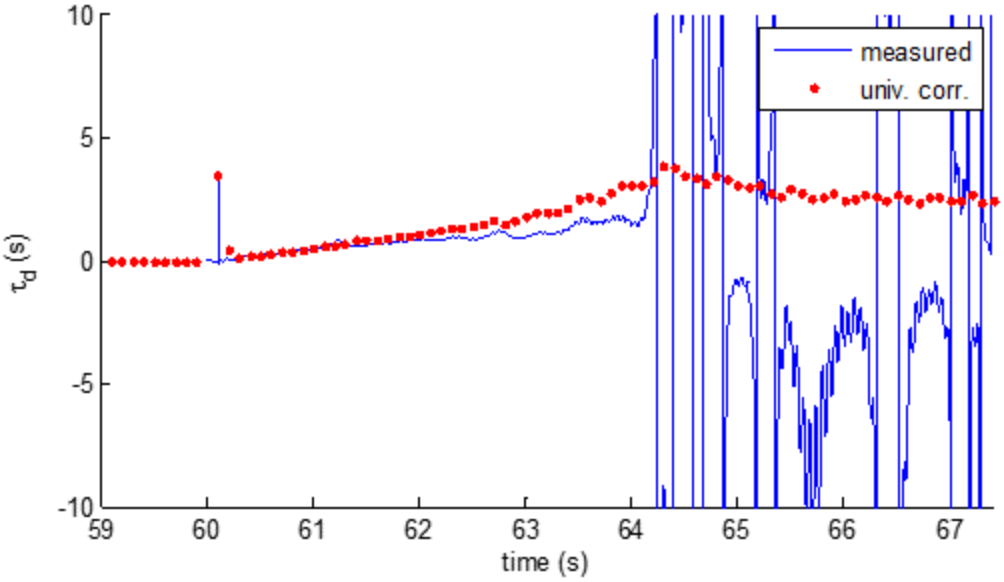

Figure 125: Dynamic Time Constant vs. Time, Dataset 4

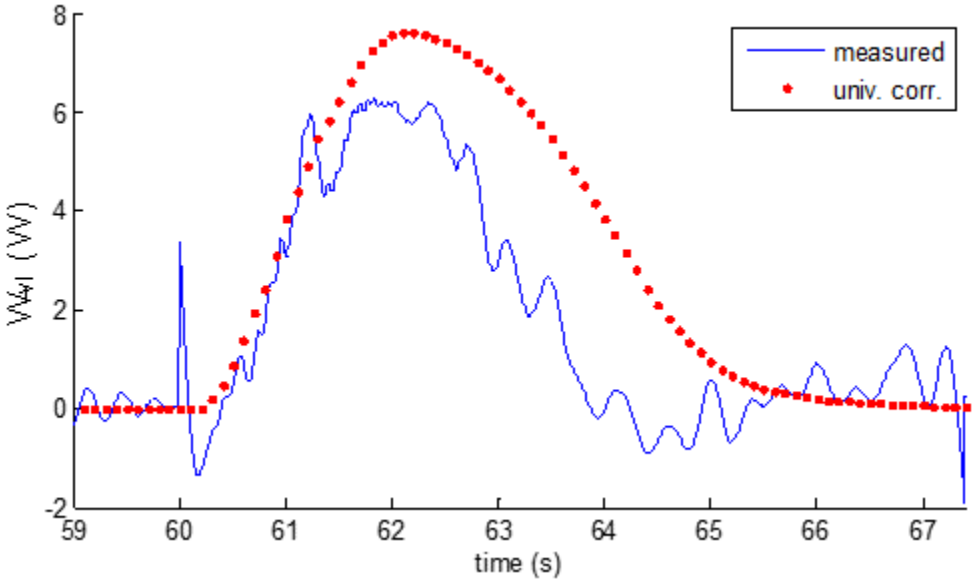

Figure 126: Viscous Dissipation Rate vs. Time, Dataset 4

Dataset 5	
$R^2_{overall}$, viscous dissipation rate	0.99646
$R^2_{overall}$, dynamic time constant	0.99286

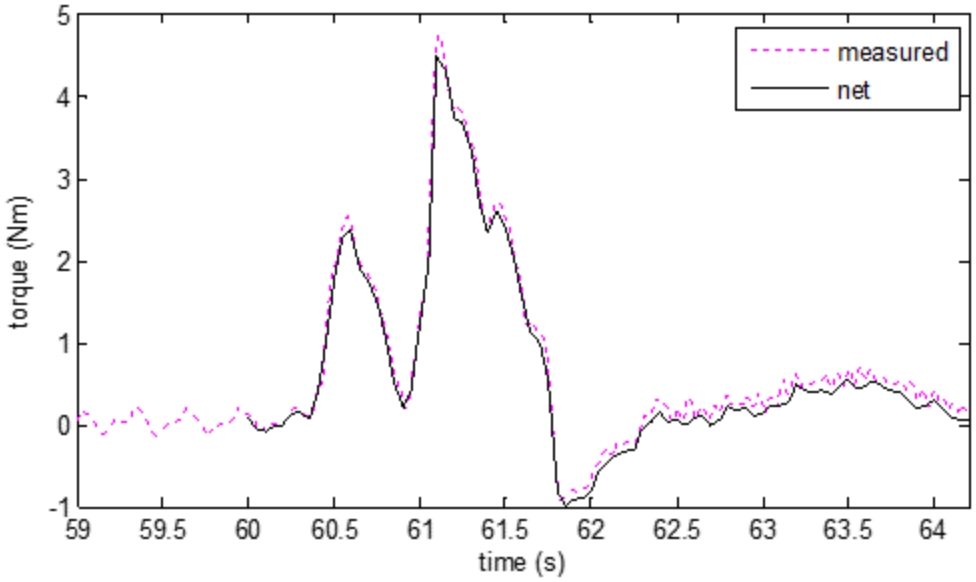

Figure 127: Measured and Net Torque vs. Time, Dataset 5

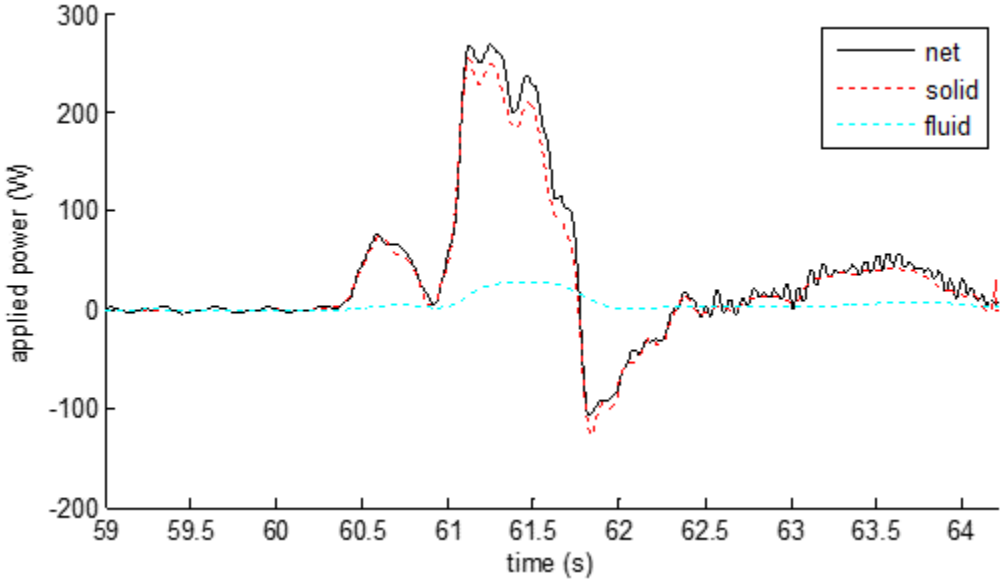

Figure 128: Power vs. Time, Dataset 5

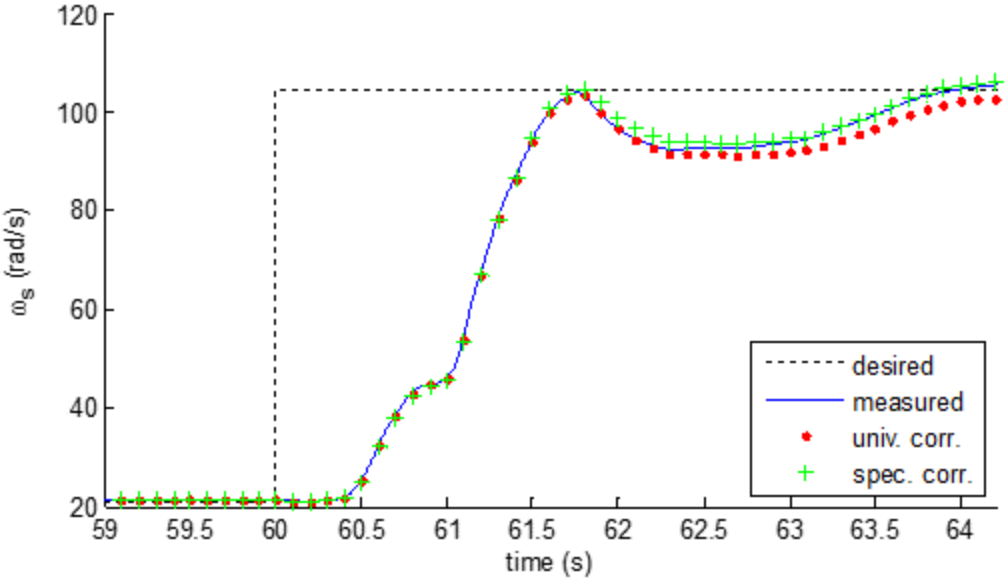

Figure 129: Solid Angular Velocity vs. Time, Dataset 5

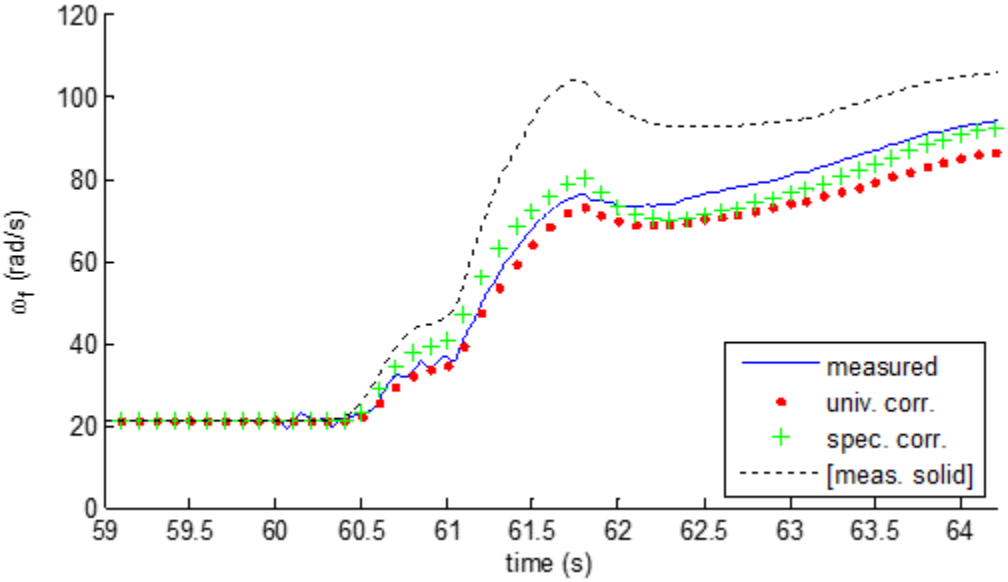

Figure 130: Fluid Angular Velocity vs. Time, Dataset 5

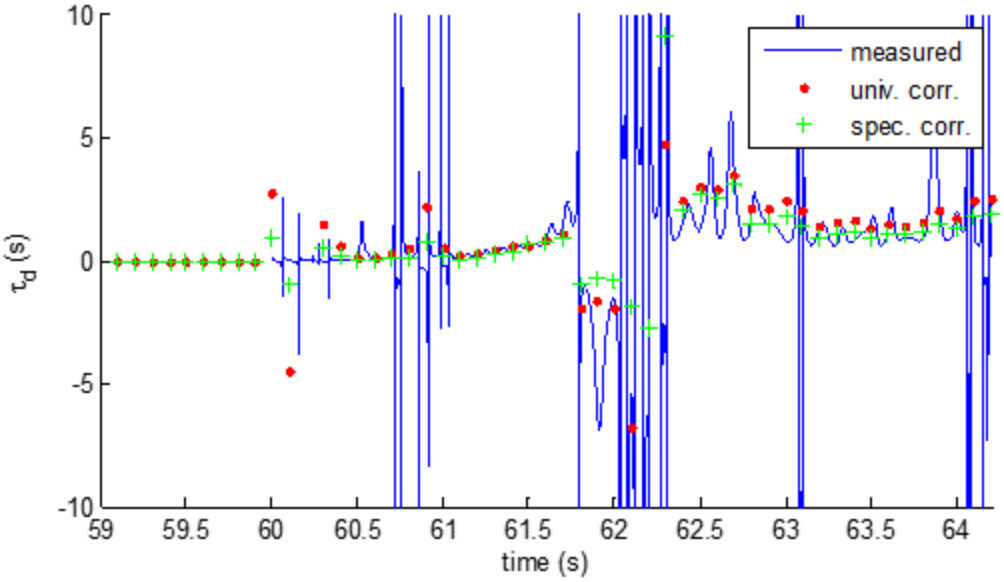

Figure 131: Dynamic Time Constant vs. Time, Dataset 5

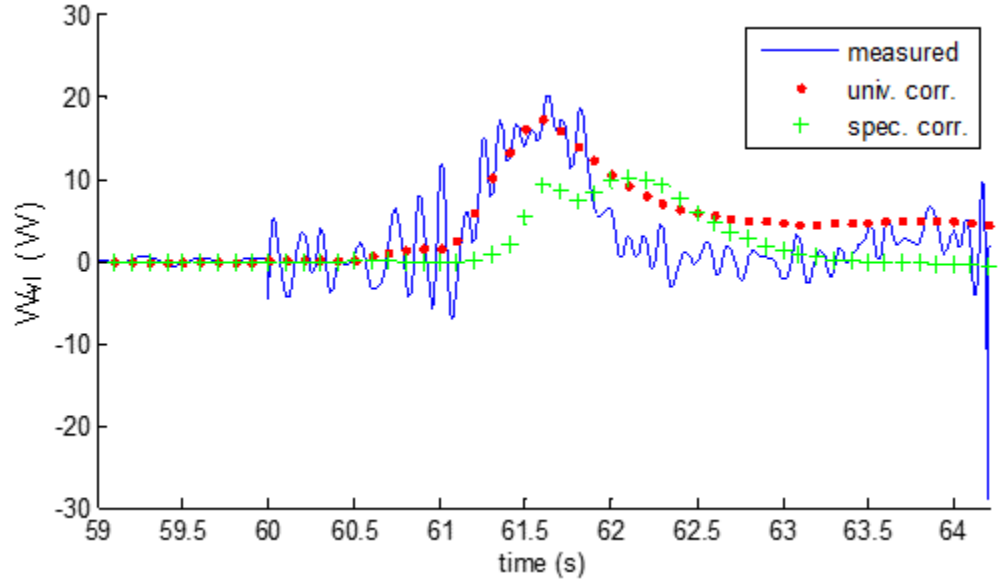

Figure 132: Viscous Dissipation Rate vs. Time, Dataset 5

Dataset 6	
$R^2_{overall}$, viscous dissipation rate	0.99794
$R^2_{overall}$, dynamic time constant	0.99513

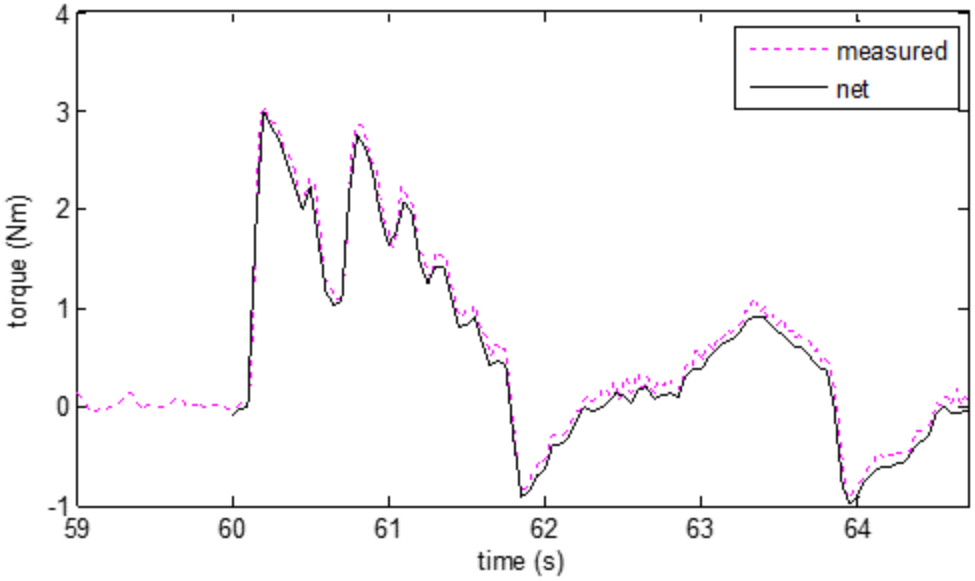

Figure 133: Measured and Net Torque vs. Time, Dataset 6

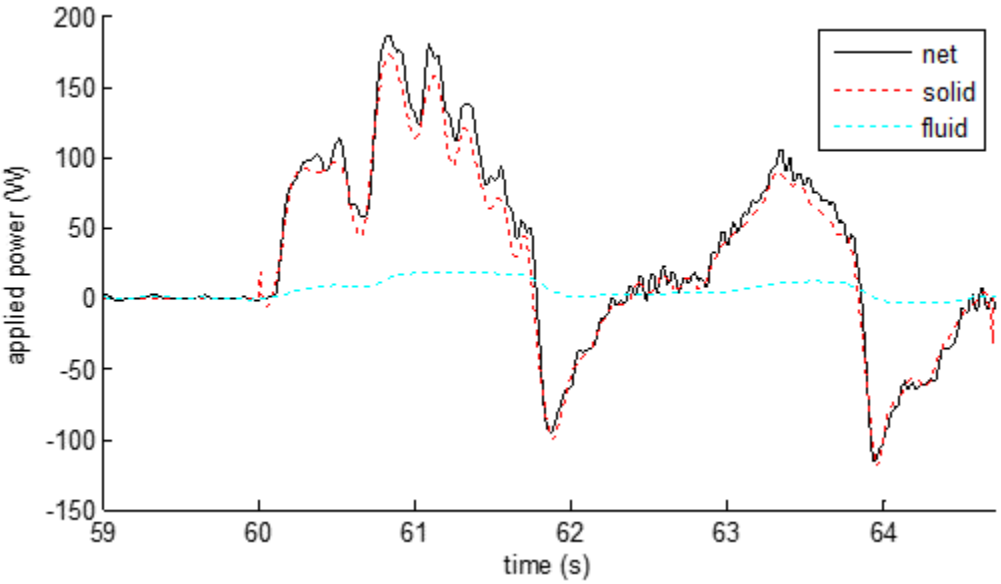

Figure 134: Power vs. Time, Dataset 6

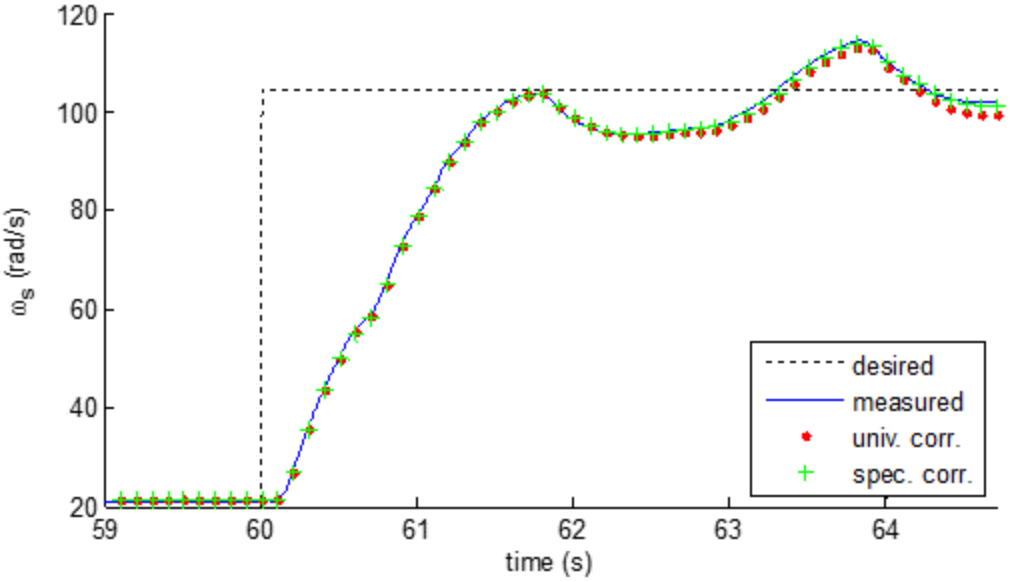

Figure 135: Solid Angular Velocity vs. Time, Dataset 6

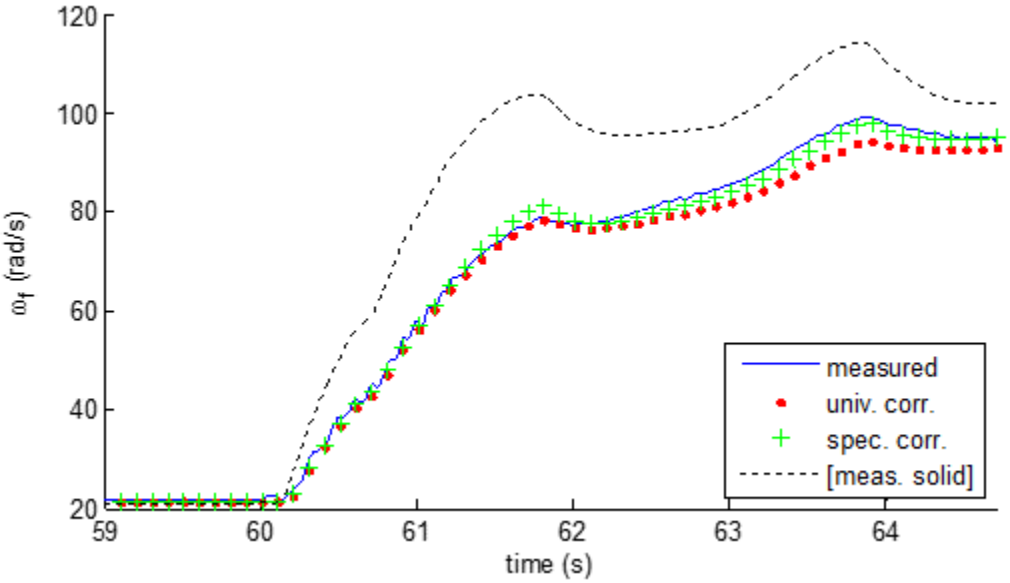

Figure 136: Fluid Angular Velocity vs. Time, Dataset 6

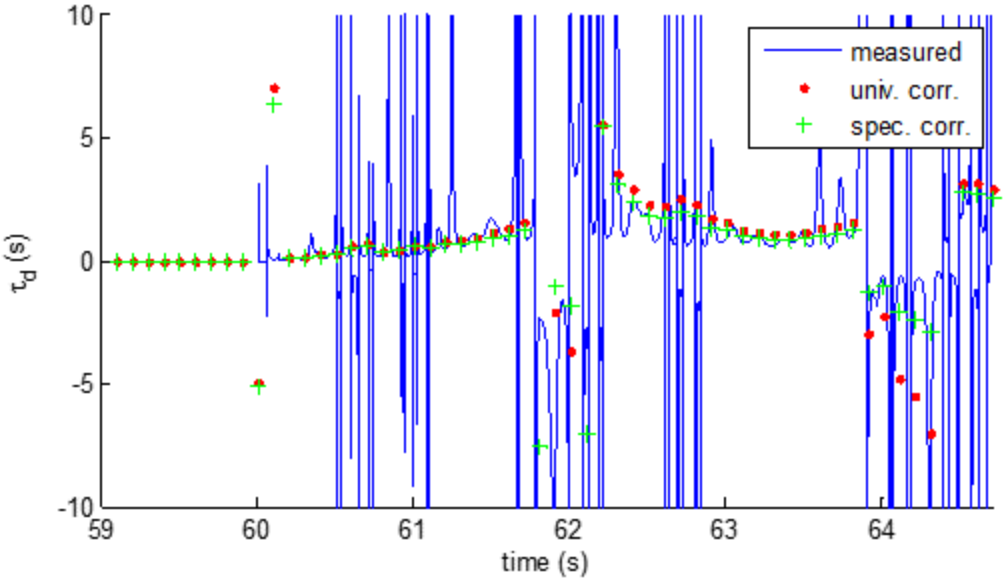

Figure 137: Dynamic Time Constant vs. Time, Dataset 6

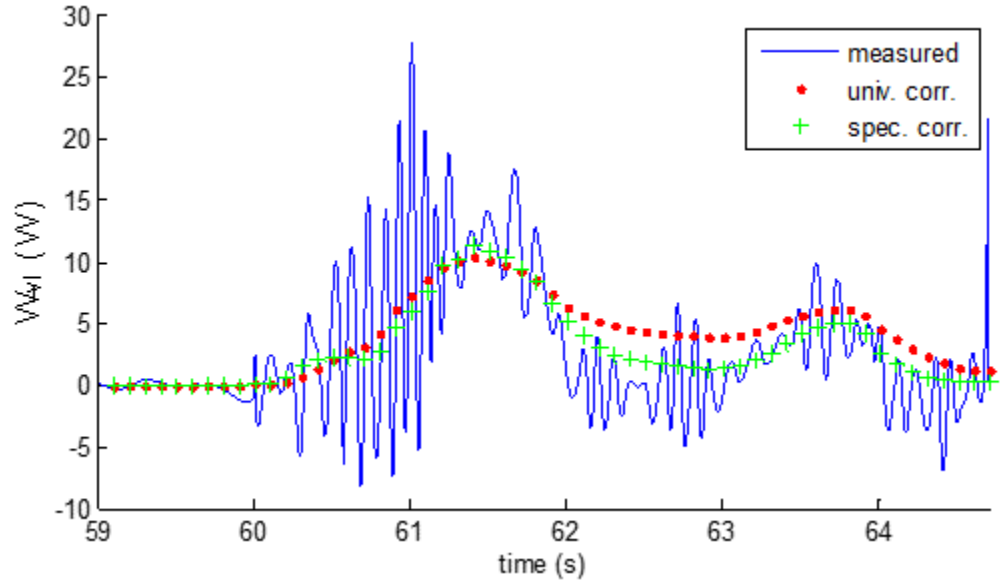

Figure 138: Viscous Dissipation Rate vs. Time, Dataset 6

Dataset 7	
$R^2_{overall}$, viscous dissipation rate	0.99845
$R^2_{overall}$, dynamic time constant	0.99444

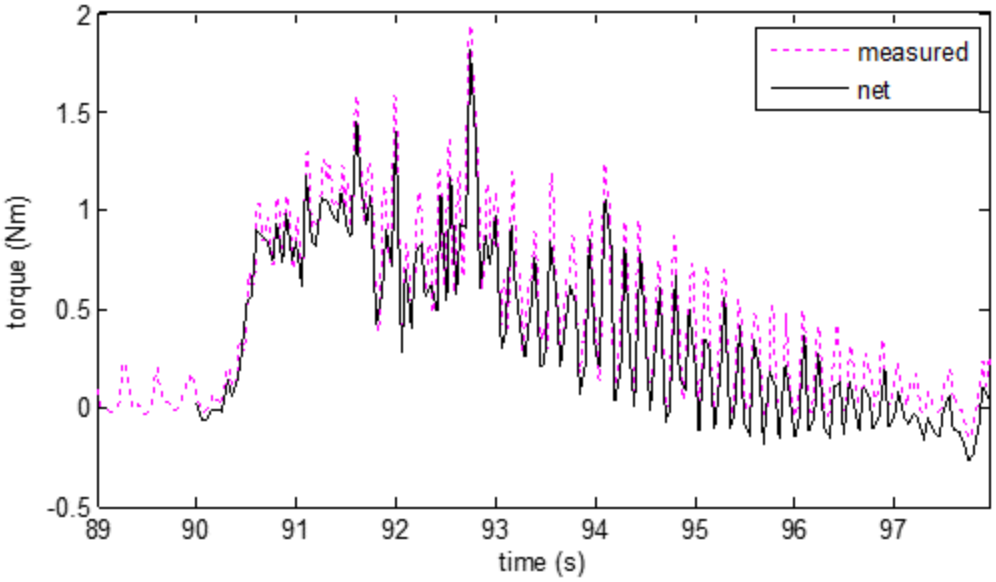

Figure 139: Measured and Net Torque vs. Time, Dataset 7

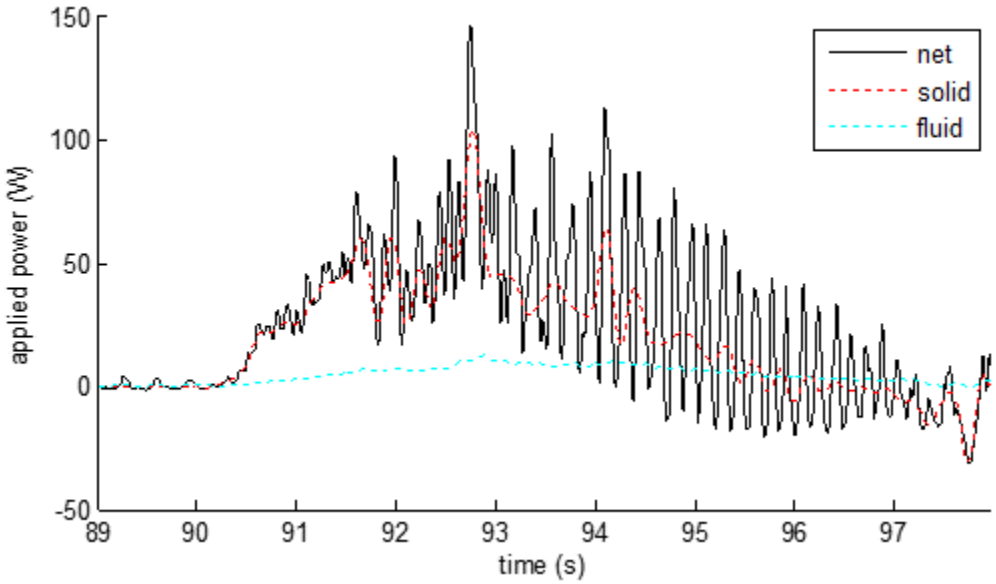

Figure 140: Power vs. Time, Dataset 7

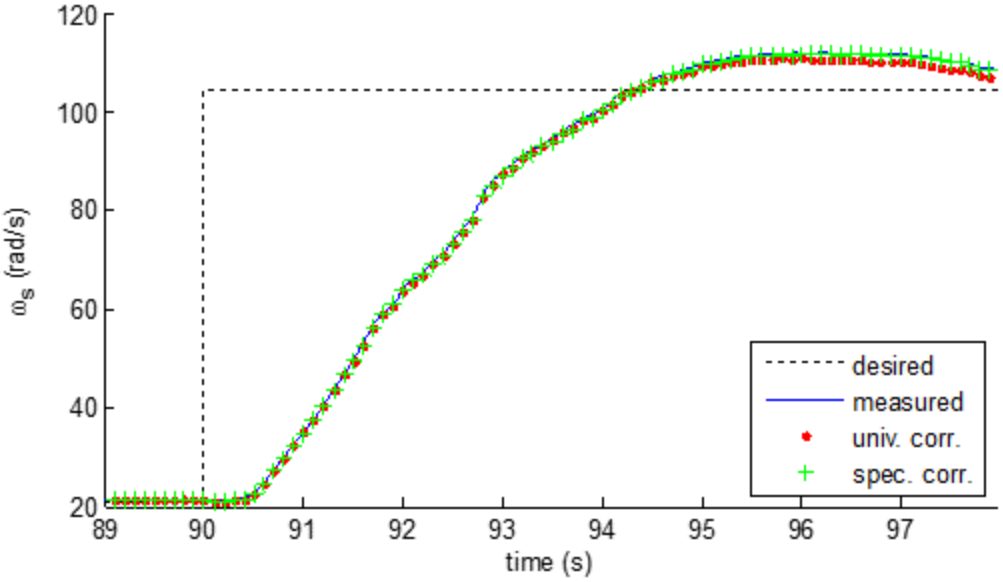

Figure 141: Solid Angular Velocity vs. Time, Dataset 7

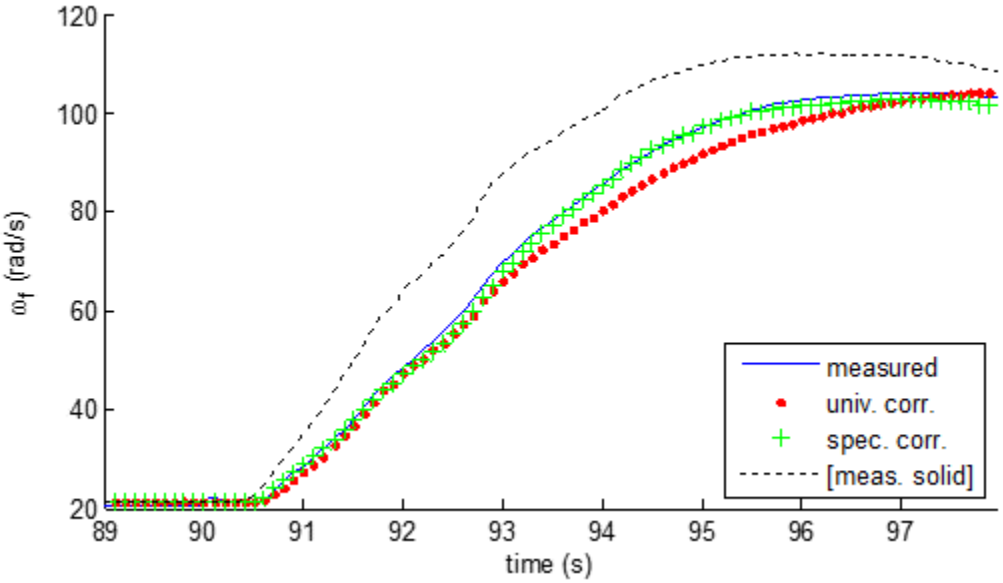

Figure 142: Fluid Angular Velocity vs. Time, Dataset 7

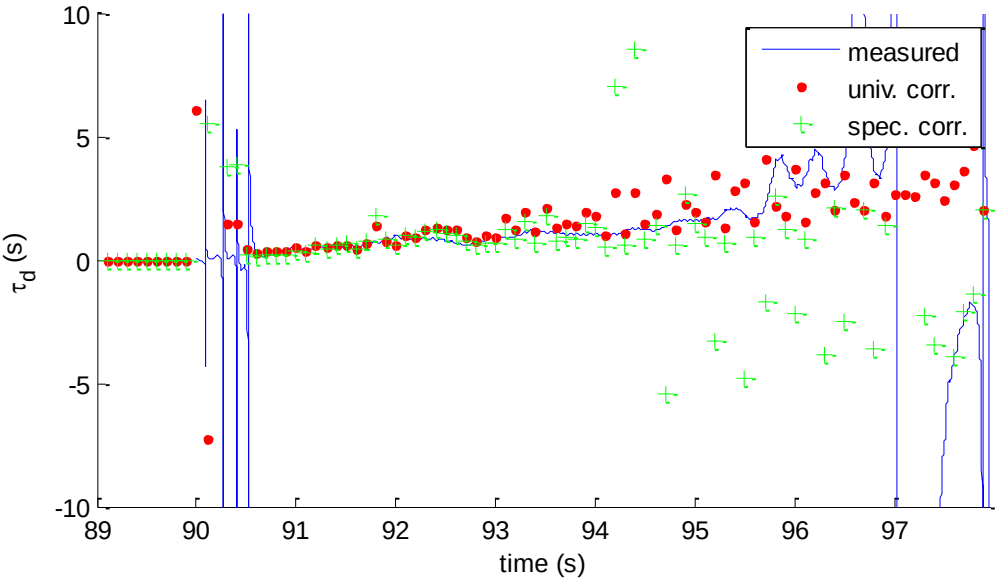

Figure 143: Dynamic Time Constant vs. Time, Dataset 7

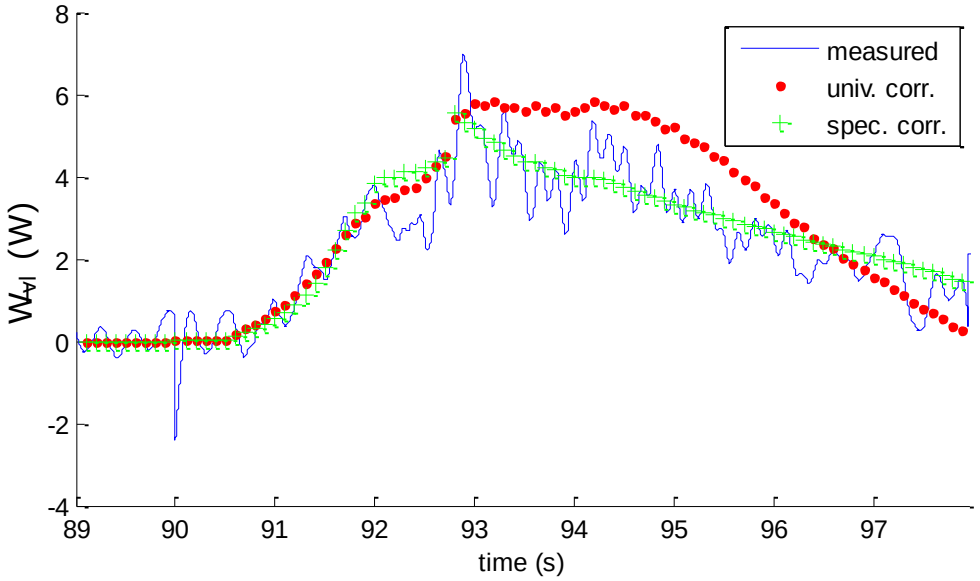

Figure 144: Viscous Dissipation Rate vs. Time, Dataset 7

Dataset 8	
$R^2_{overall}$, viscous dissipation rate	0.99781
$R^2_{overall}$, dynamic time constant	0.99549

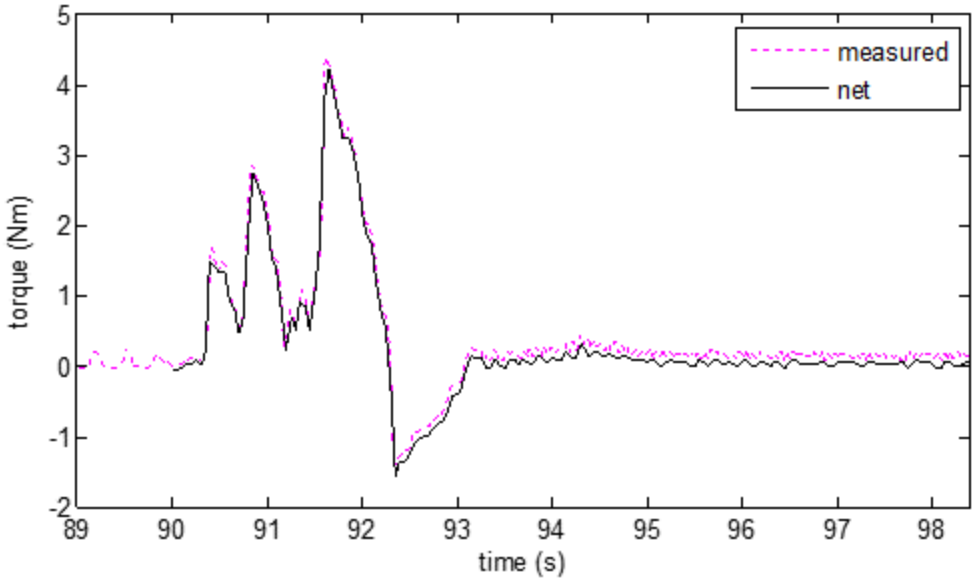

Figure 145: Measured and Net Torque vs. Time, Dataset 8

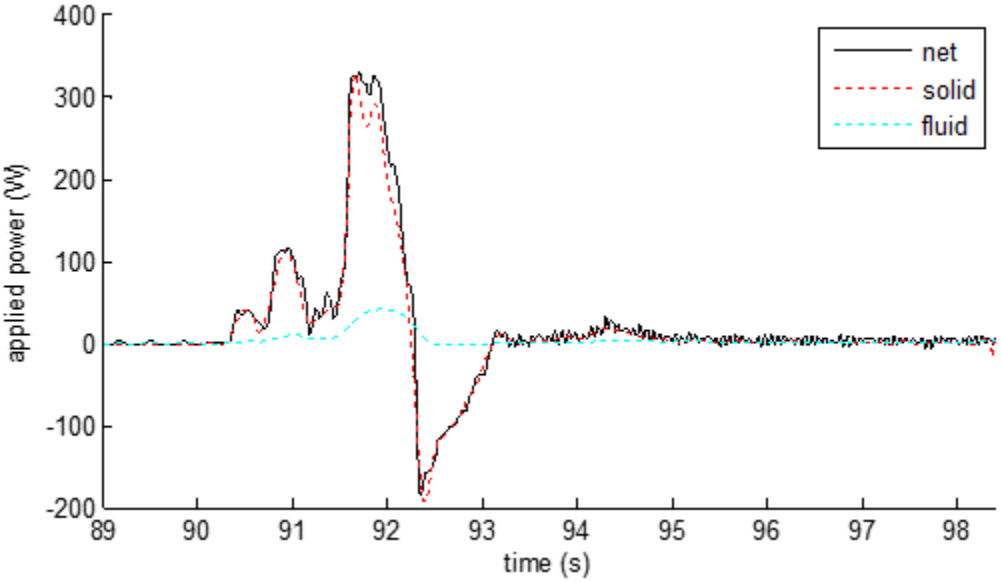

Figure 146: Power vs. Time, Dataset 8

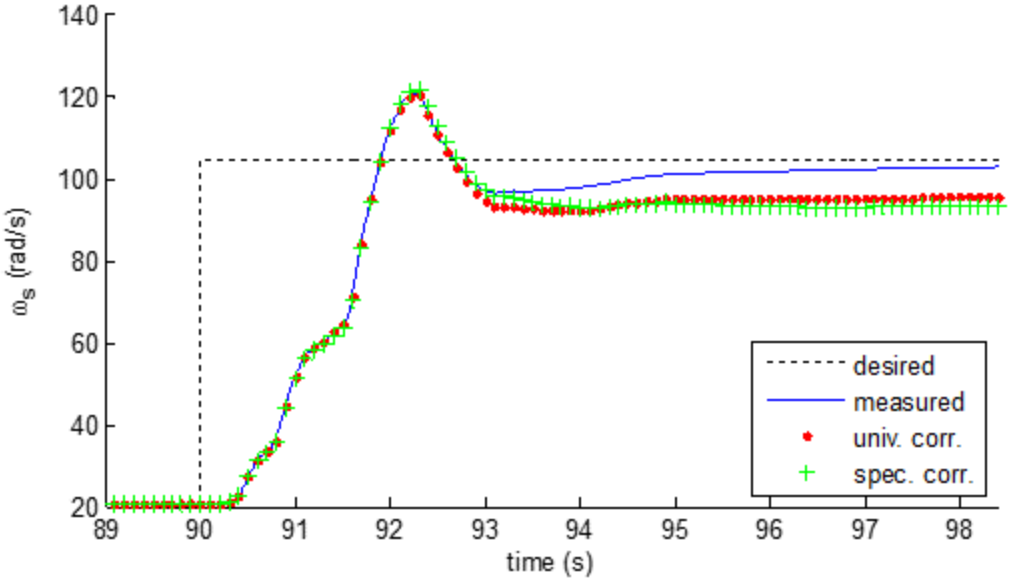

Figure 147: Solid Angular Velocity vs. Time, Dataset 8

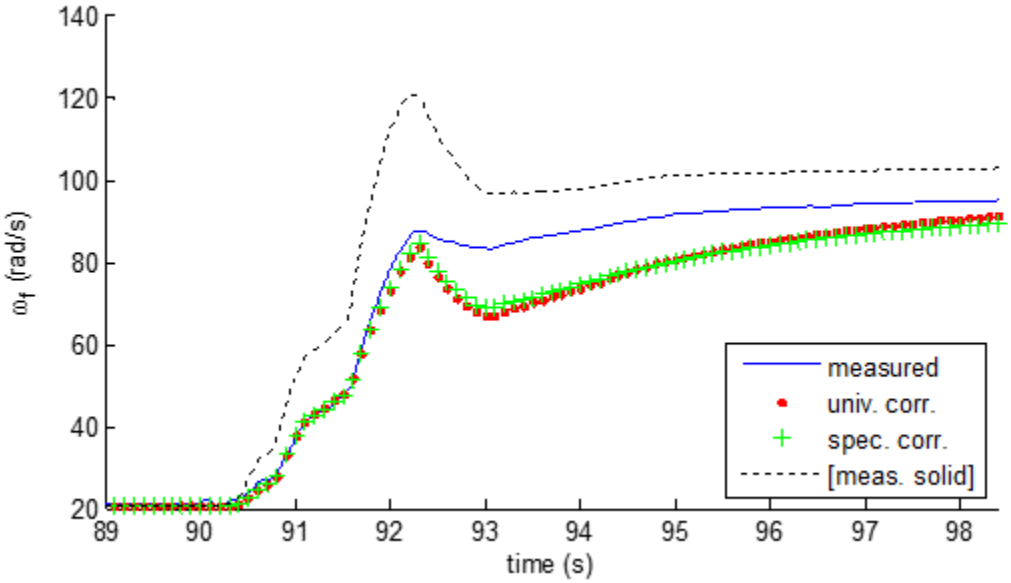

Figure 148: Fluid Angular Velocity vs. Time, Dataset 8

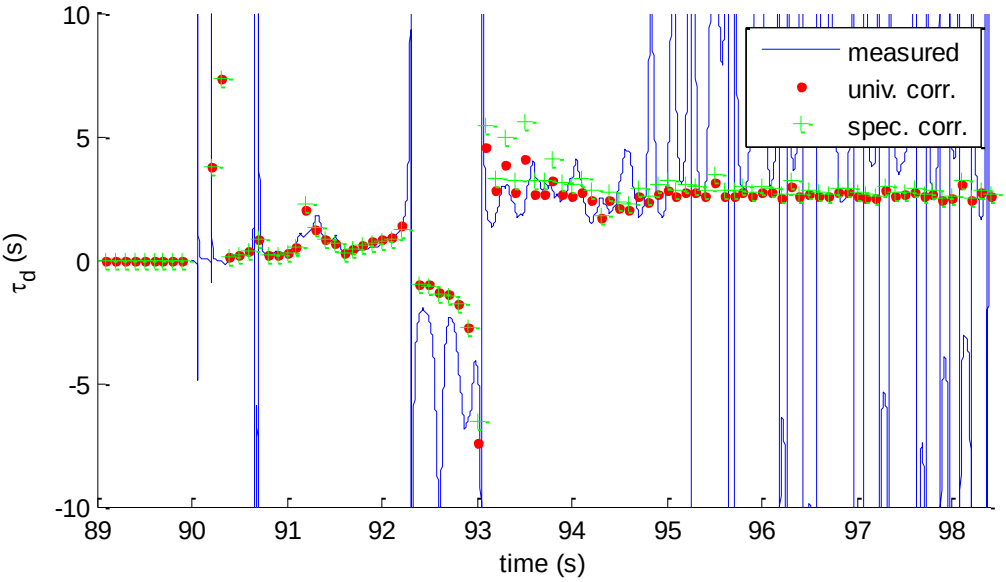

Figure 149: Dynamic Time Constant vs. Time, Dataset 8

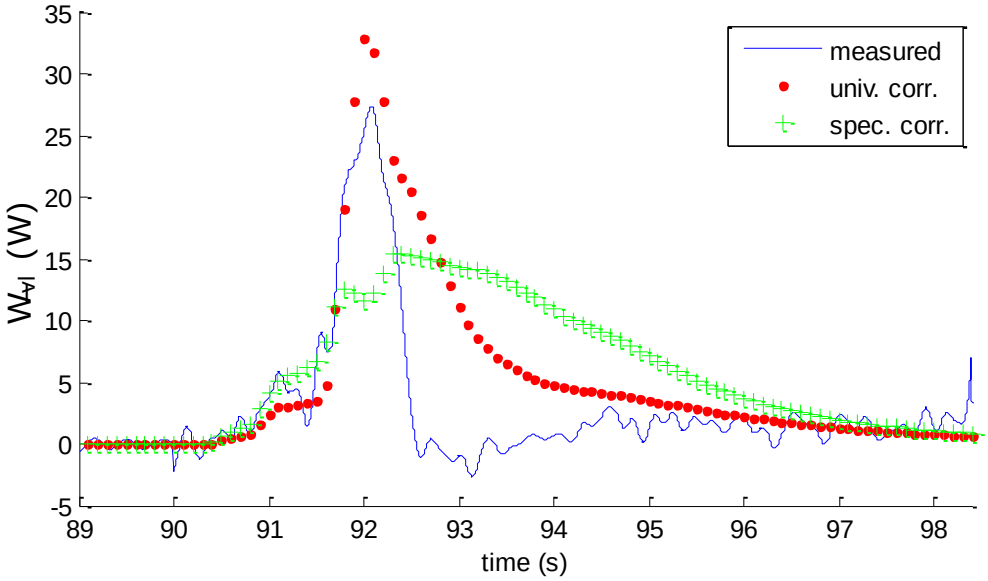

Figure 150: Viscous Dissipation Rate vs. Time, Dataset 8

Dataset 9	
$R^2_{overall}$, viscous dissipation rate	0.99843
$R^2_{overall}$, dynamic time constant	0.99247

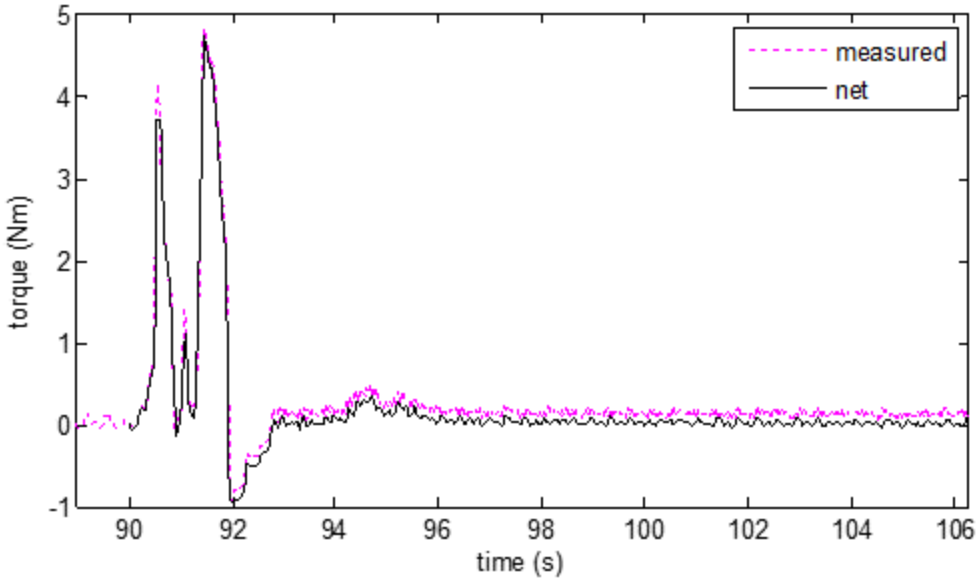

Figure 151: Measured and Net Torque vs. Time, Dataset 9

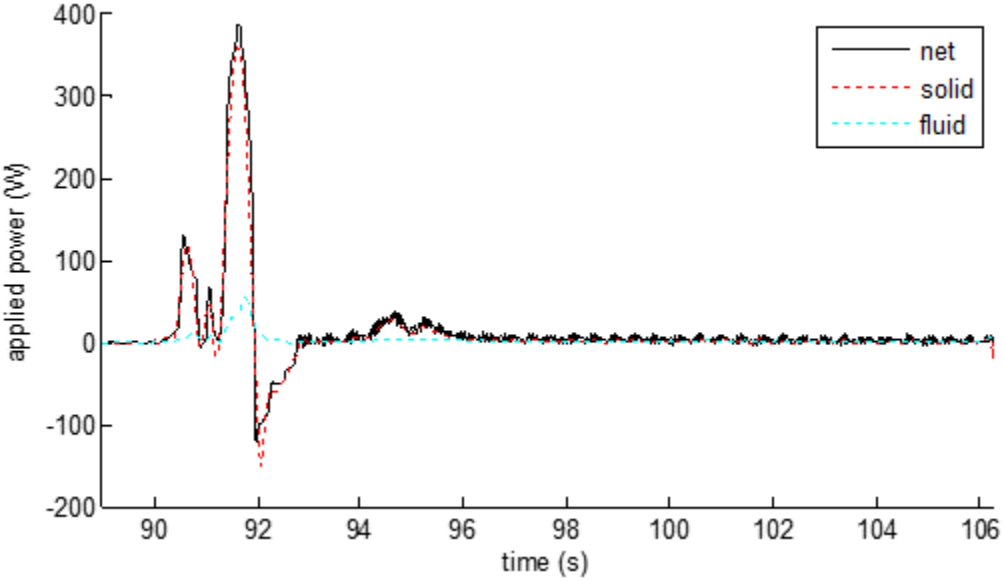

Figure 152: Power vs. Time, Dataset 9

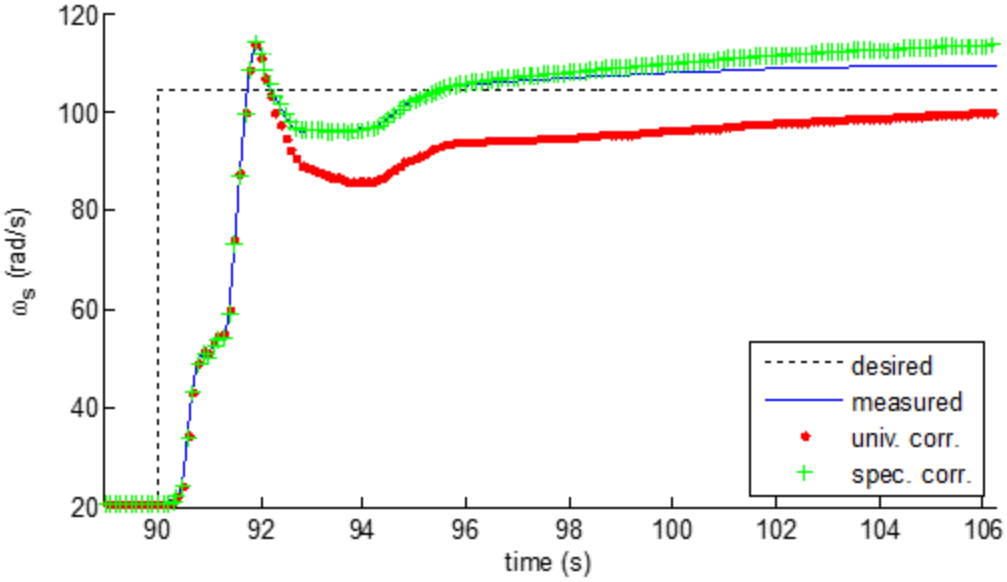

Figure 153: Solid Angular Velocity vs. Time, Dataset 9

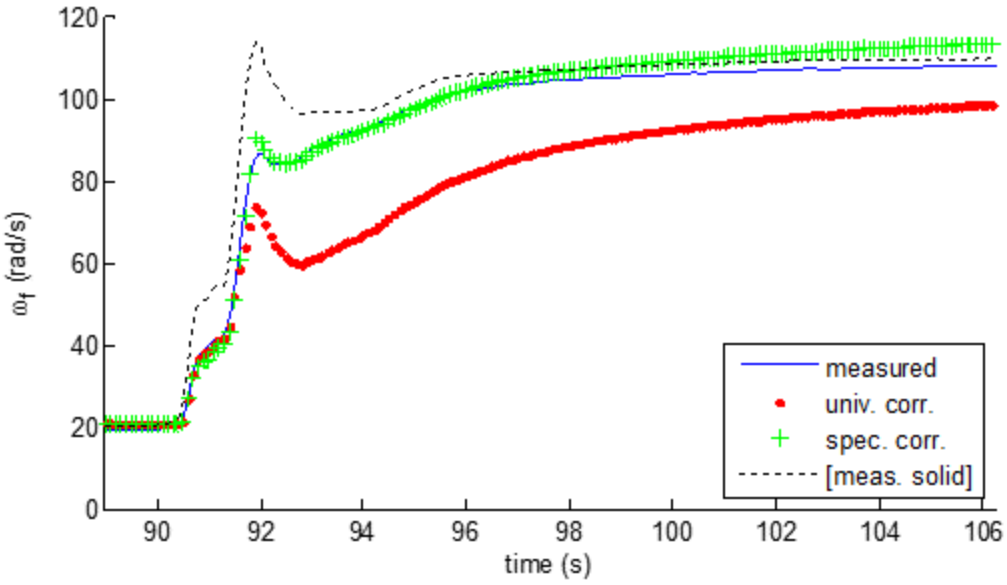

Figure 154: Fluid Angular Velocity vs. Time, Dataset 9

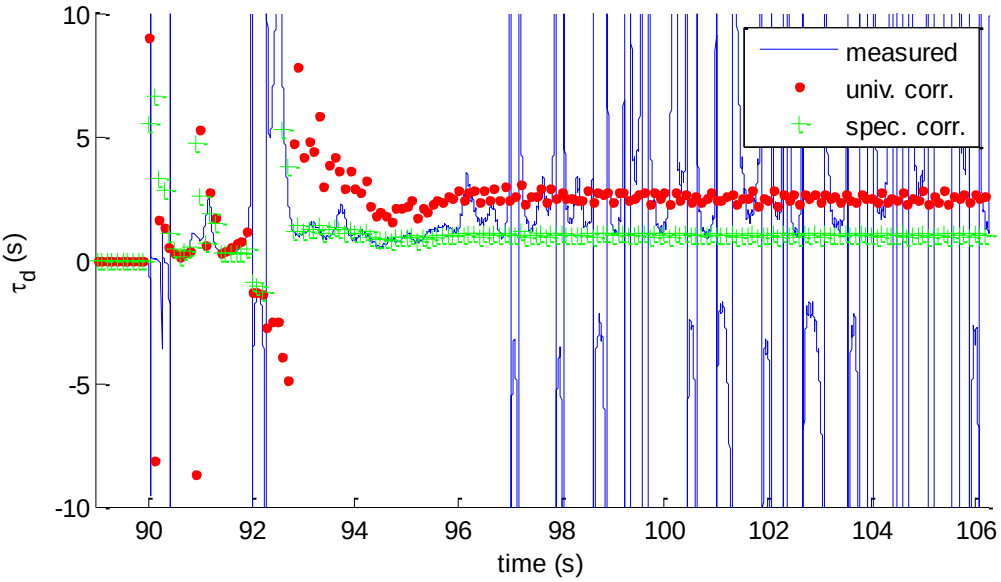

Figure 155: Dynamic Time Constant vs. Time, Dataset 9

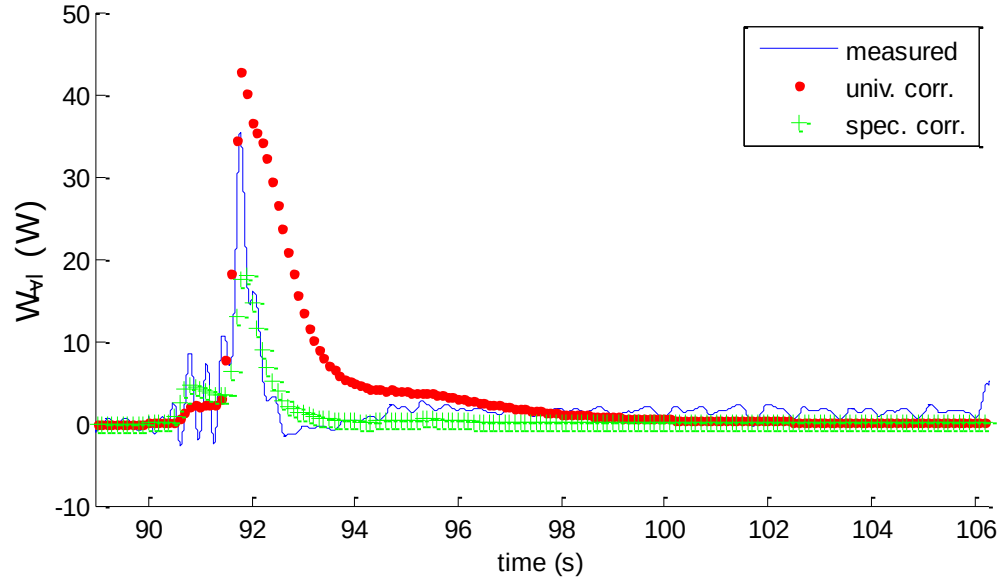

Figure 156: Viscous Dissipation Rate vs. Time, Dataset 9

Dataset 10	
$R^2_{overall}$, viscous dissipation rate	0.99624
$R^2_{overall}$, dynamic time constant	0.64704

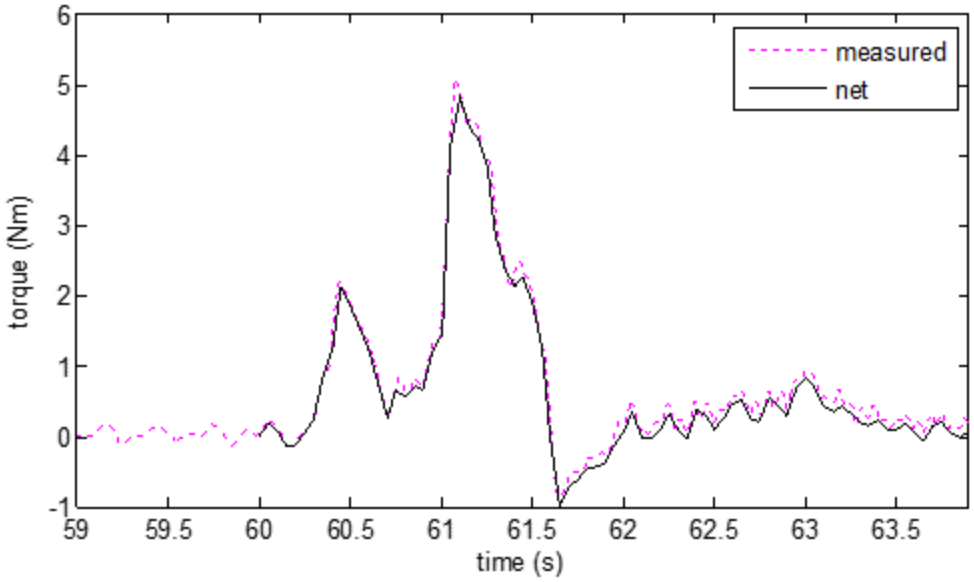

Figure 157: Measured and Net Torque vs. Time, Dataset 10

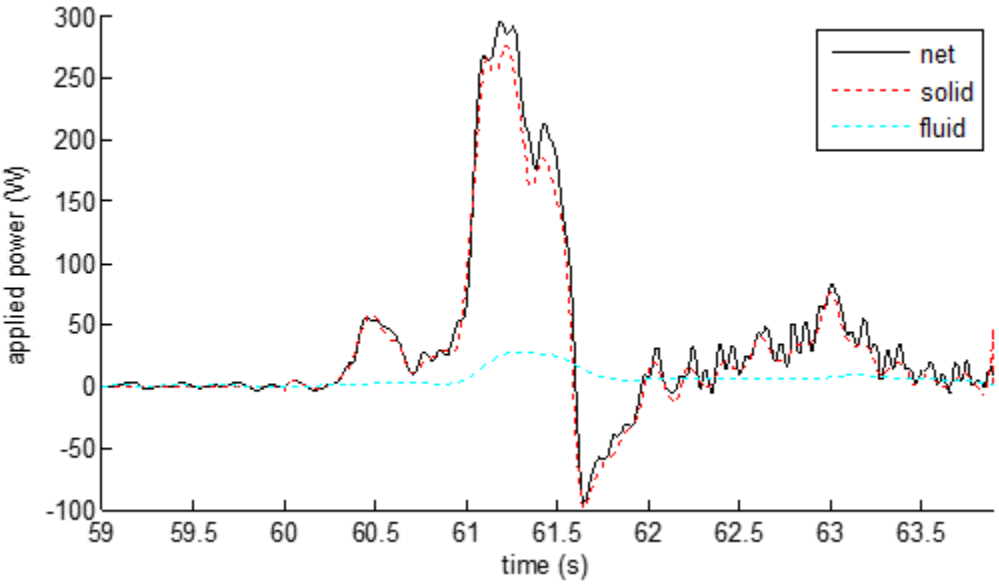

Figure 158: Power vs. Time, Dataset 10

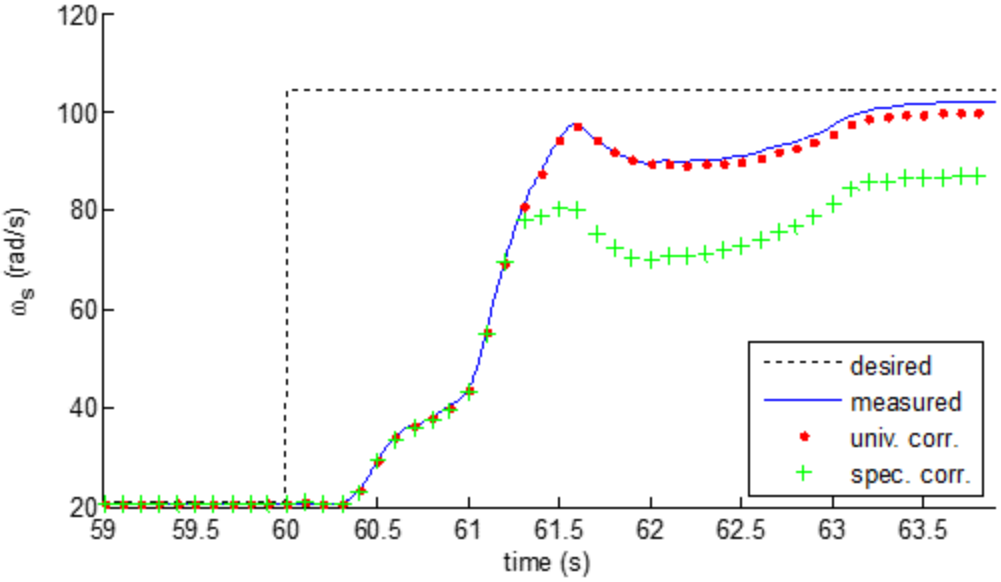

Figure 159: Solid Angular Velocity vs. Time, Dataset 10

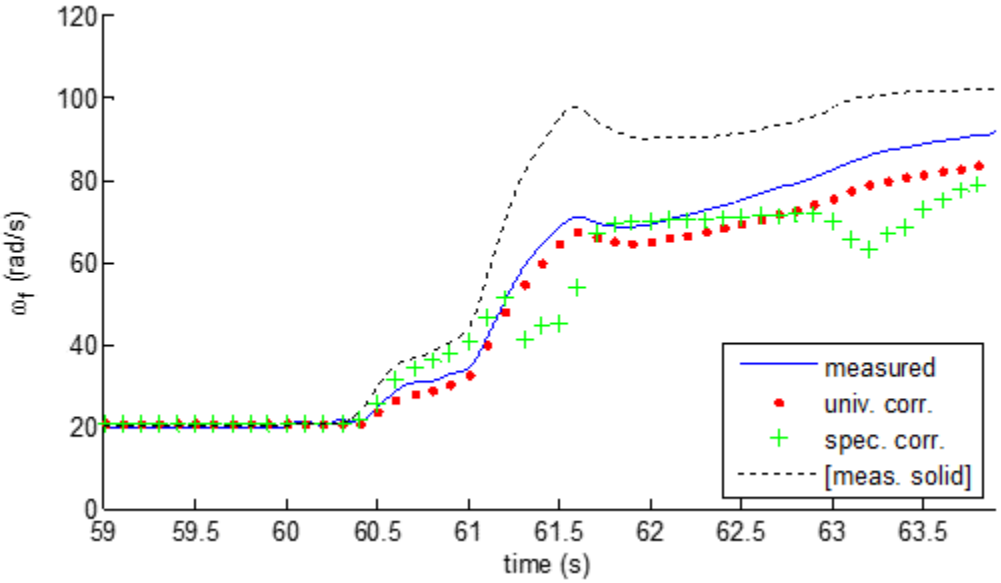

Figure 160: Fluid Angular Velocity vs. Time, Dataset 10

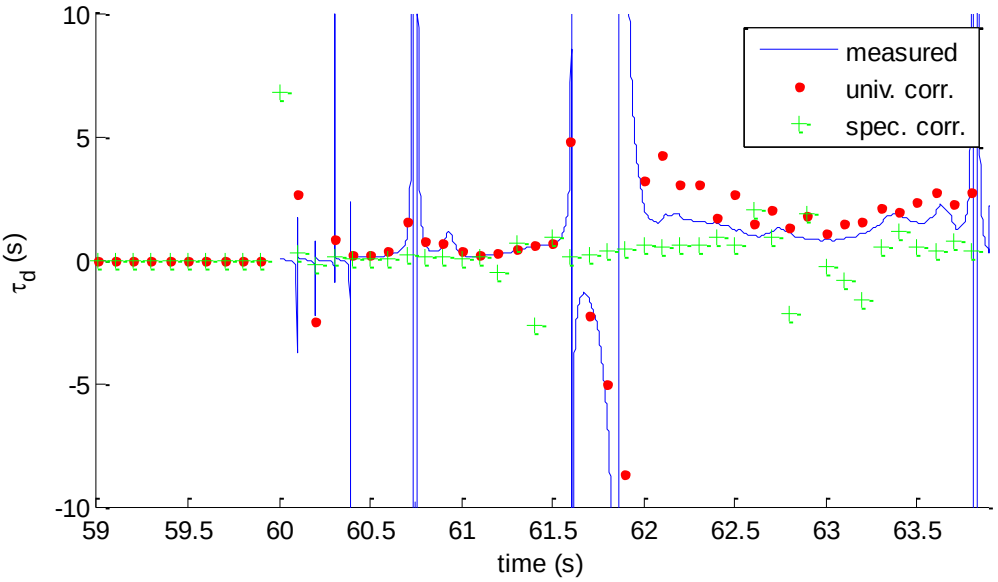

Figure 161: Dynamic Time Constant vs. Time, Dataset 10

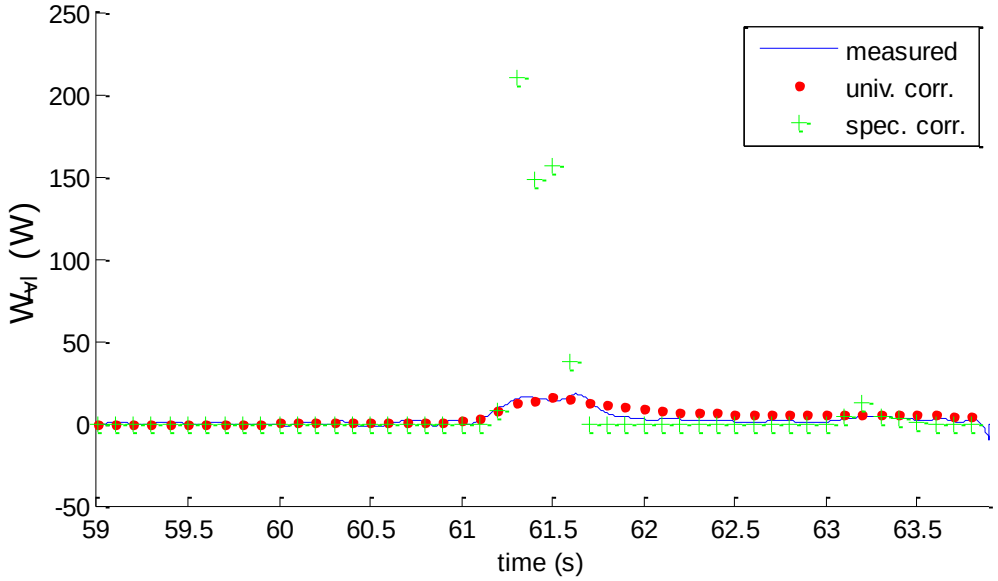

Figure 162: Viscous Dissipation Rate vs. Time, Dataset 10

Dataset 11	
$R^2_{overall}$, viscous dissipation rate	0.99675
$R^2_{overall}$, dynamic time constant	0.99371

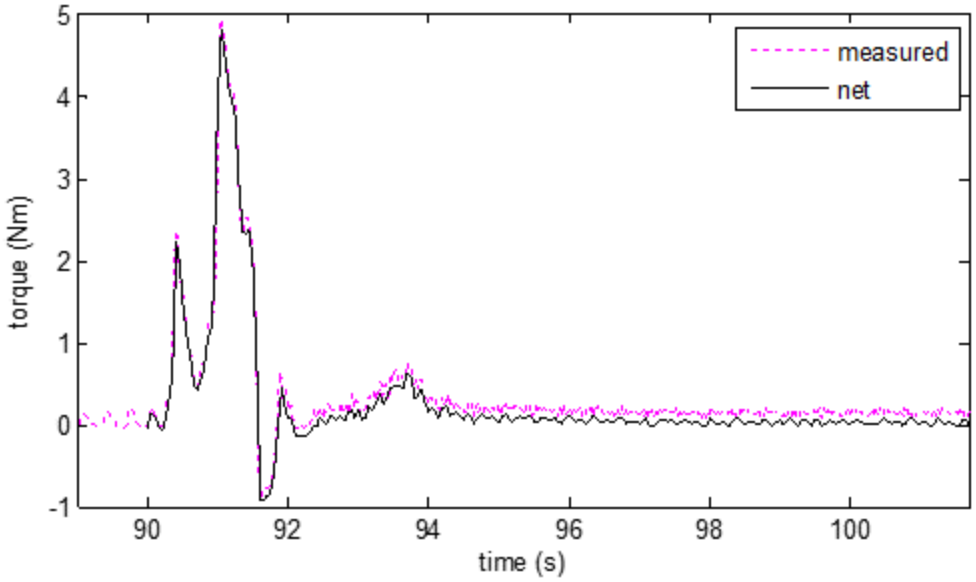

Figure 163: Measured and Net Torque vs. Time, Dataset 11

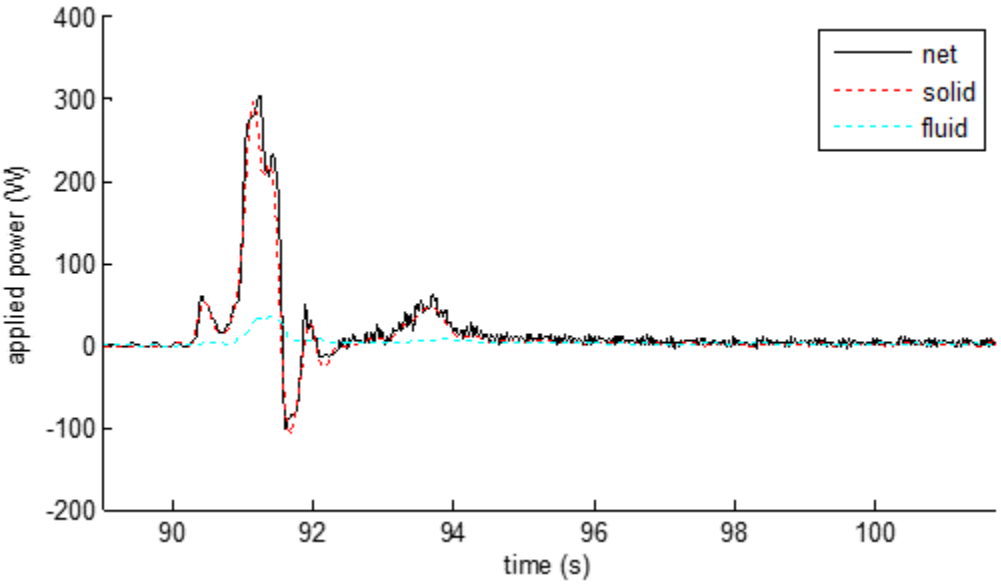

Figure 164: Power vs. Time, Dataset 11

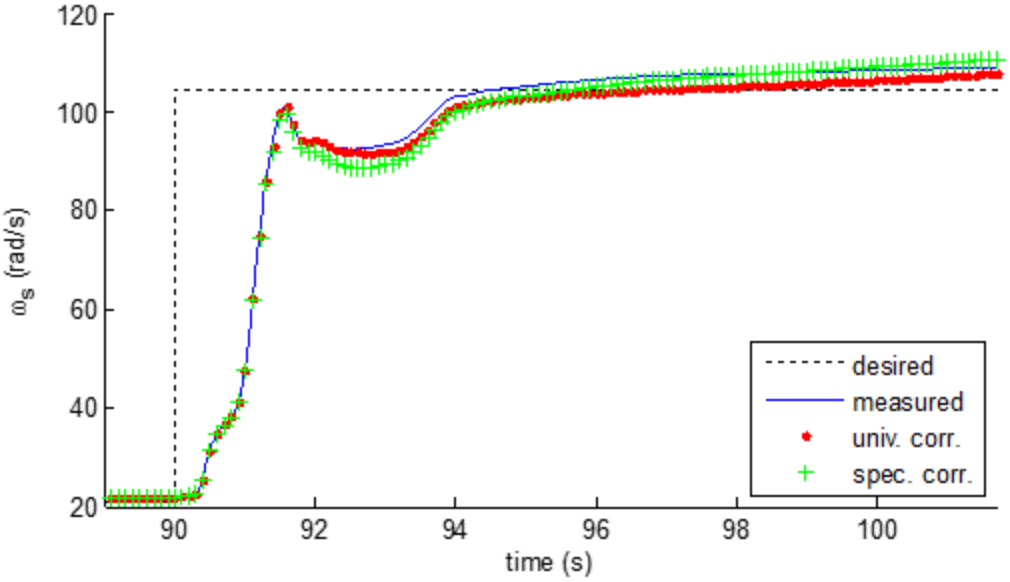

Figure 165: Solid Angular Velocity vs. Time, Dataset 11

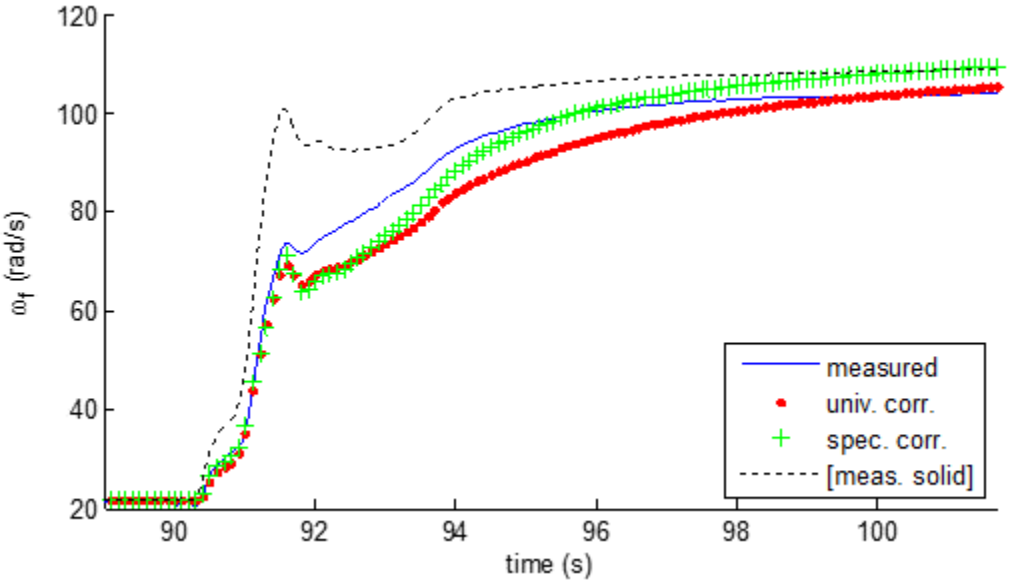

Figure 166: Fluid Angular Velocity vs. Time, Dataset 11

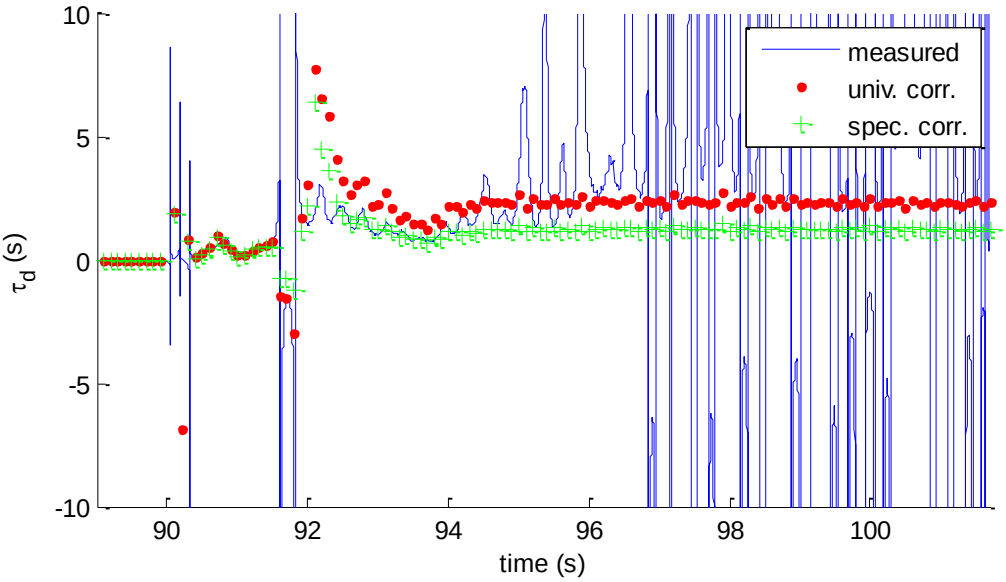

Figure 167: Dynamic Time Constant vs. Time, Dataset 11

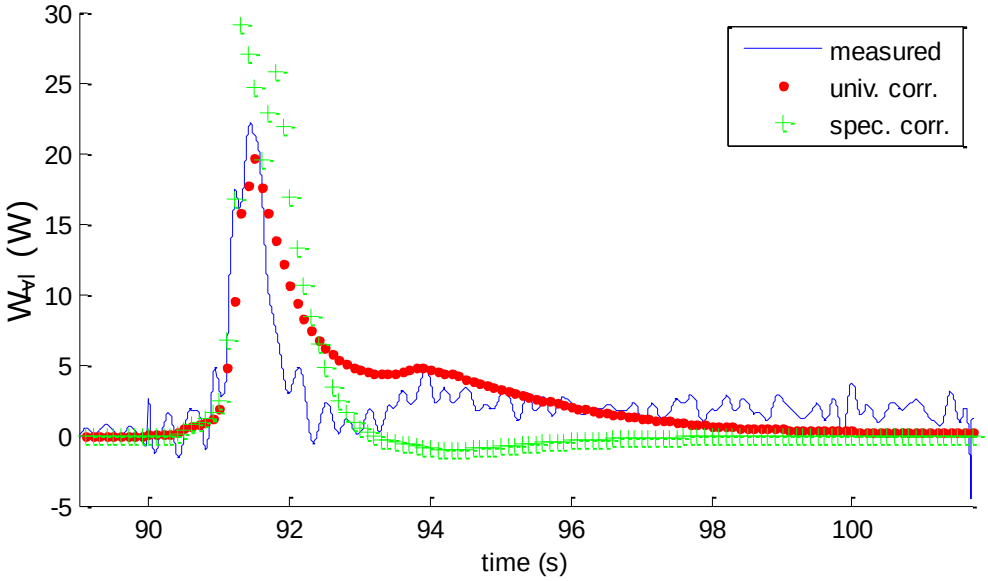

Figure 168: Viscous Dissipation Rate vs. Time, Dataset 11

Appendix D: Simulated Prototype Performance

This appendix illustrates the projected performance of the seleted laboratory prototype. The drive cycle simulation is carried out exactly as detailed in Chapter 6.

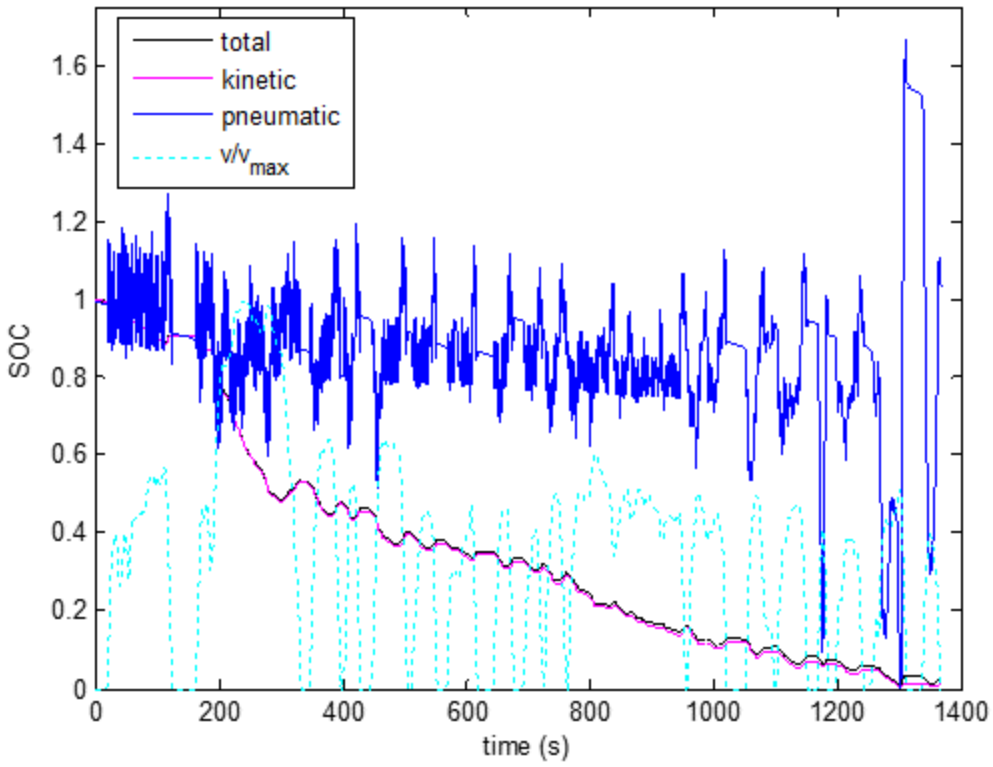

Figure 169: Total and Domain-Specific States-of-Charge vs. Time, Projected Laboratory Prototype Performance

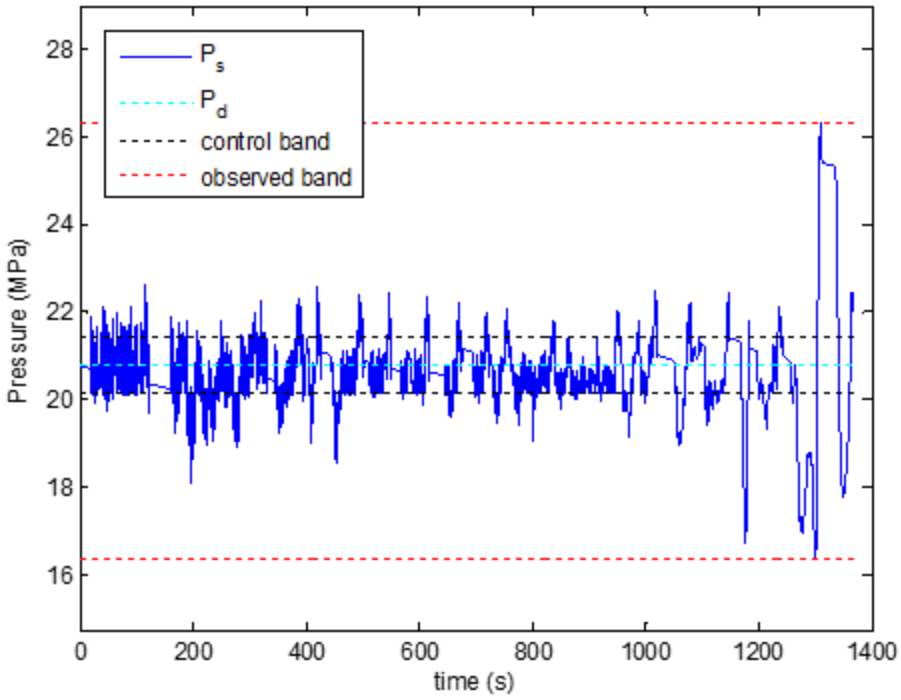

Figure 170: System Pressure vs. Time, Projected Laboratory Prototype Performance

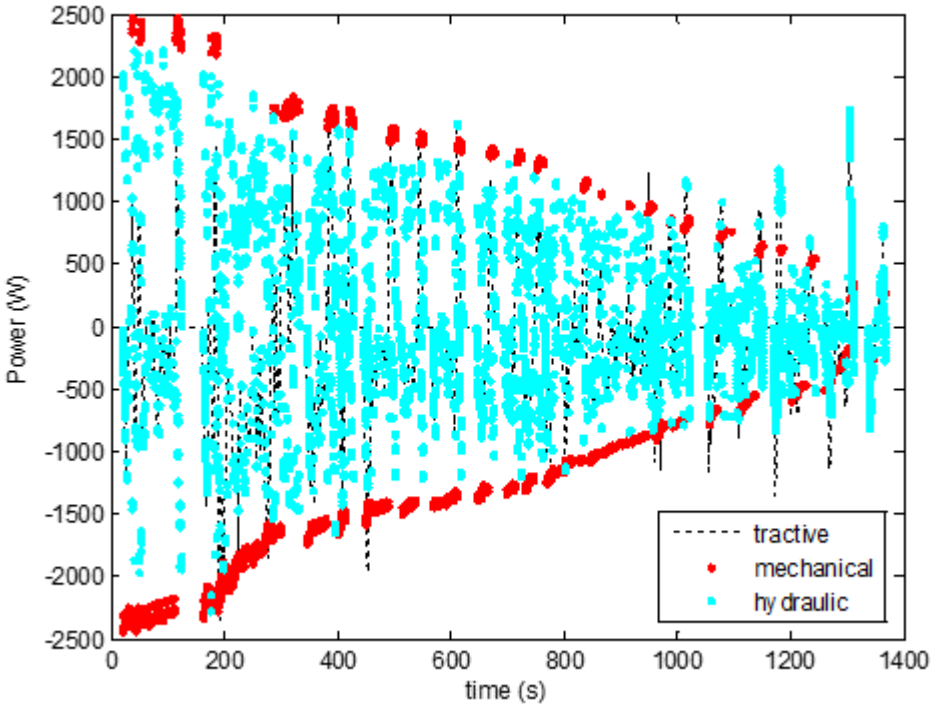

Figure 171: Tractive and Domain-Specific Power vs. Time, Projected Laboratory Prototype Performance

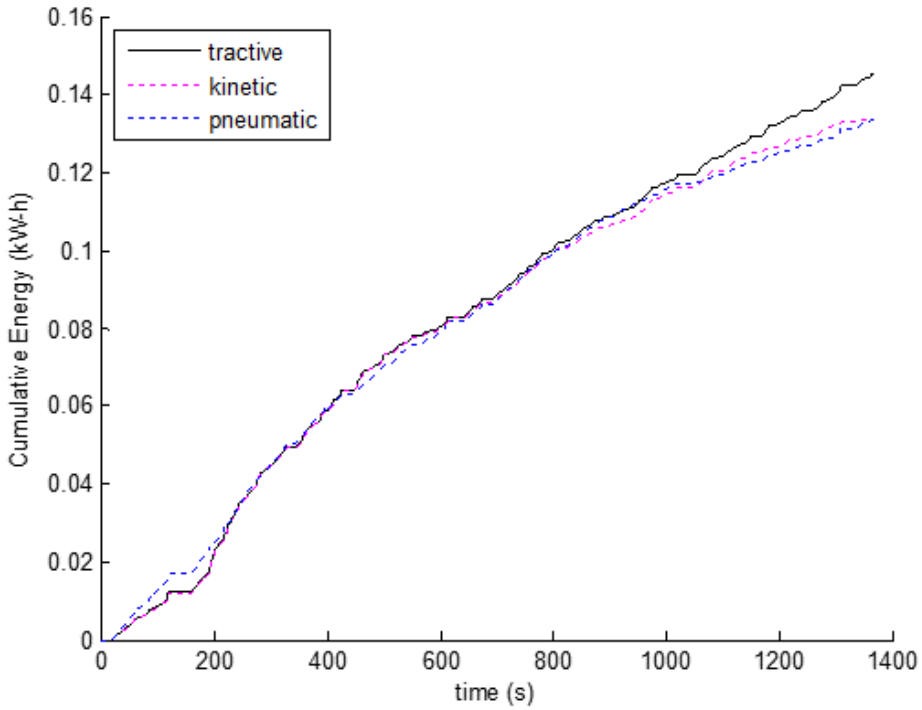

Figure 172: Cumulative Tractive and Domain-Specific Energy Usage vs. Time, Projected Laboratory Prototype Performance

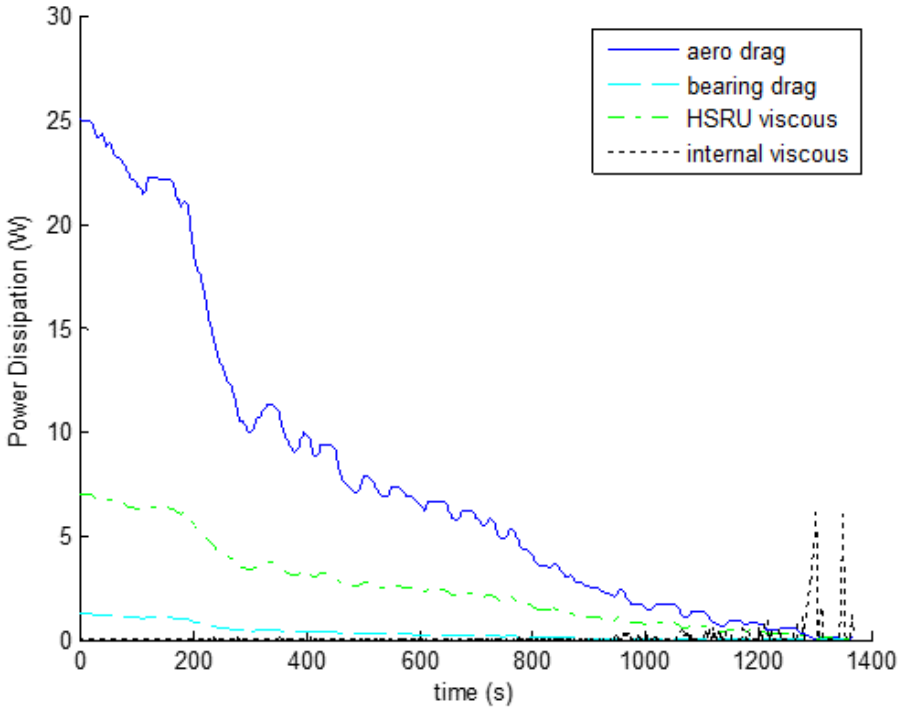

Figure 173: Mechanical Power Dissipation Mechanisms vs. Time, Projected Laboratory Prototype Performance

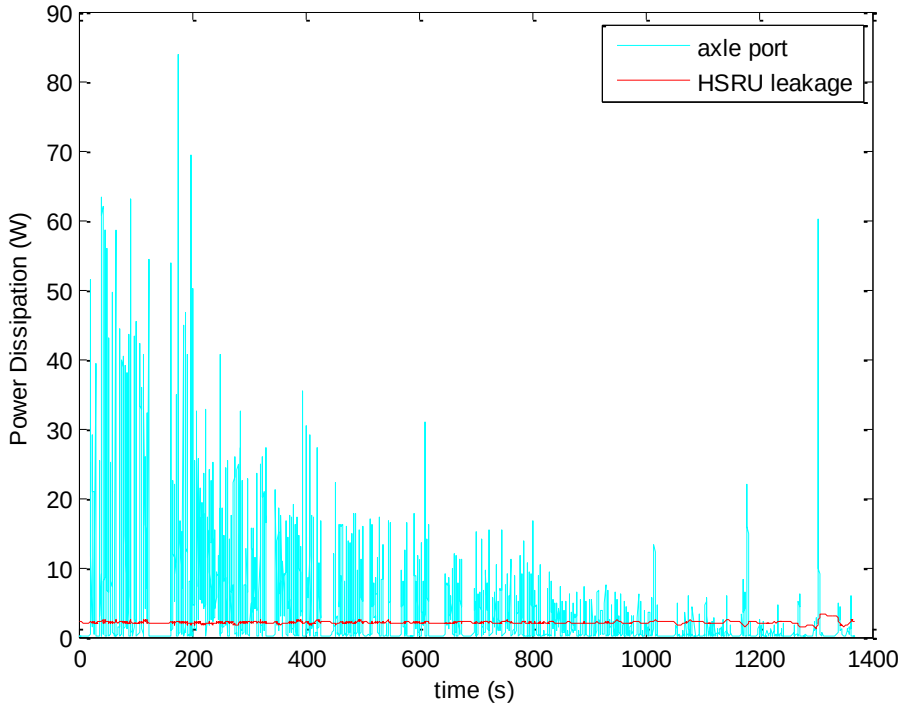

Figure 174: Hydraulic Power Dissipation Mechanisms vs. Time, Projected Laboratory Prototype Performance

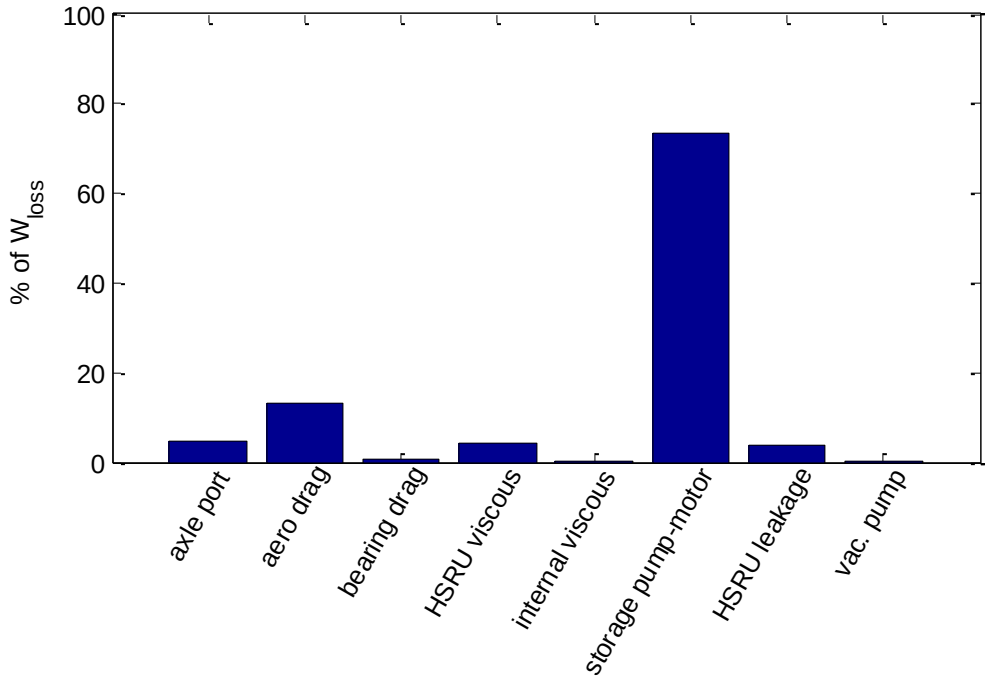

Figure 175: Relative Contributions of the Energy Loss Mechanisms vs. Time, Projected Laboratory Prototype Performance

Appendix E: Additional FEA Results

The mesh and von Mises stress distrubtions for the gas side end cap are shown in Figures 176 and 177, respectively. Figure 178 shows the stress distribution in the vicinity of the keyway. Annotations are given in units of Pa. The yield strength of 7075-T6 Aluminum divided by a safety factor of 3 is 168 MPa.

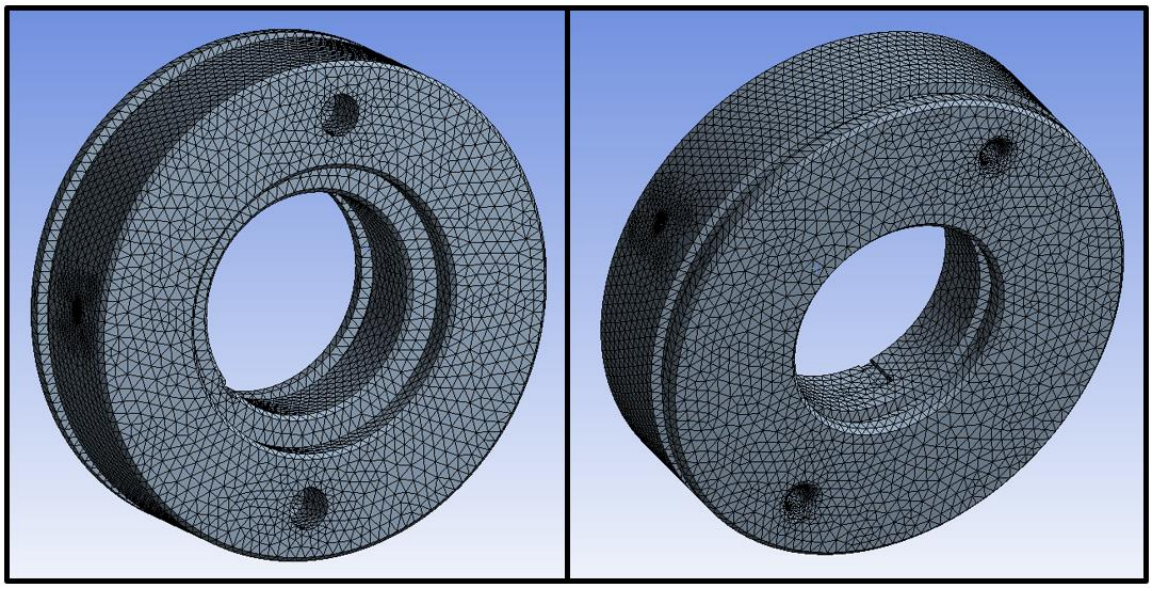

Figure 176: Mesh Used for the FEA Analysis of the Gas Side End Cap, Outer Face (Left) and Inner Face (Right)

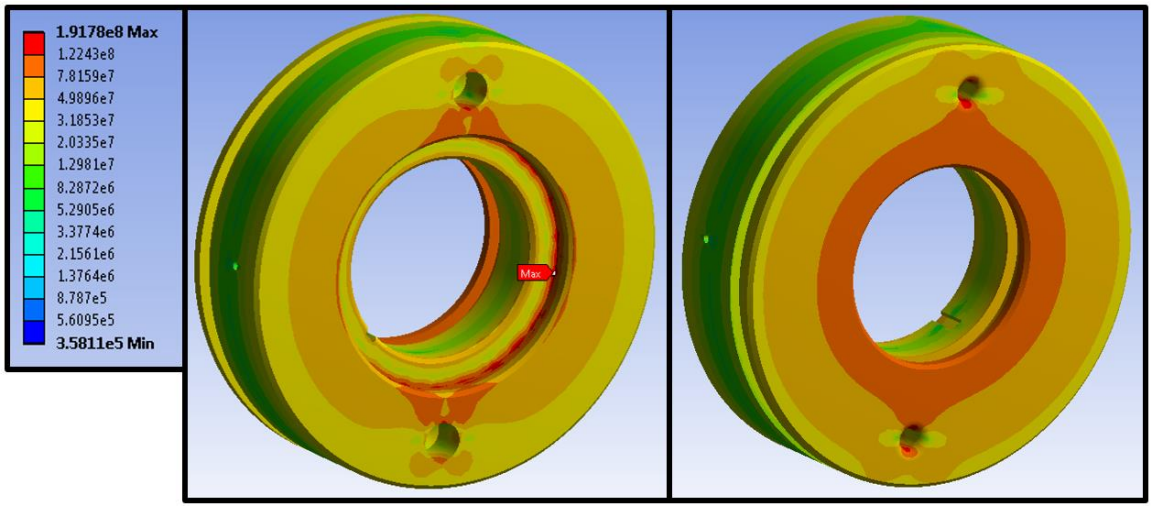

Figure 177: FEA Results, von Mises Stress Distribution in the Gas Side End Cap, Outer Face (Left) and Inner Face (Right) (Annotations in Pa)

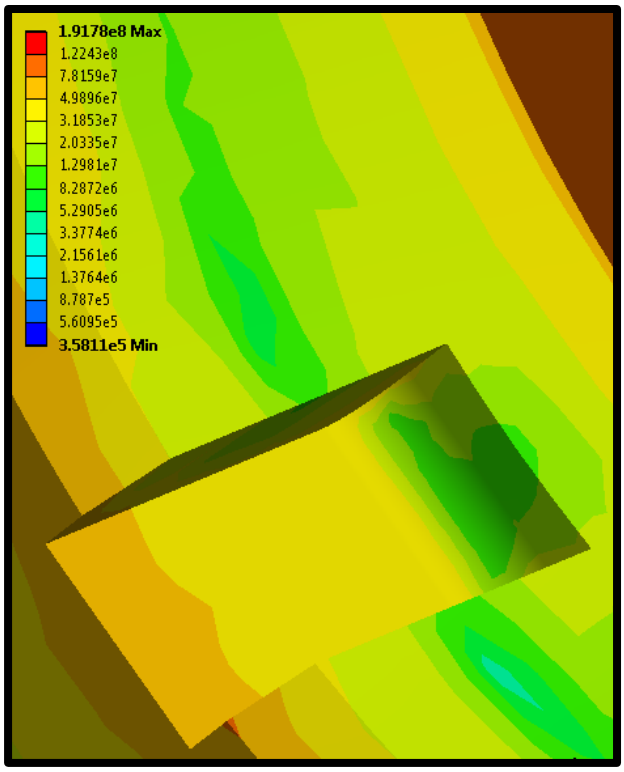

Figure 178: FEA Results, von Mises Stress Distribution Near the Keyway in the Gas Side End Cap (Annotations in Pa)

The mesh used in the FEA analysis of the housing in shown in Fig. 179. Figures 180 and 181, respectively, show the stress concentration in the liner near the pin system hole and the axial stress distribution in the wrap. Annotations are given in Pa. For reference, the acceptable stress in the liner is 505 MPa and the transverse tensile yield strength of the carbon fiber composite is 80 MPa.

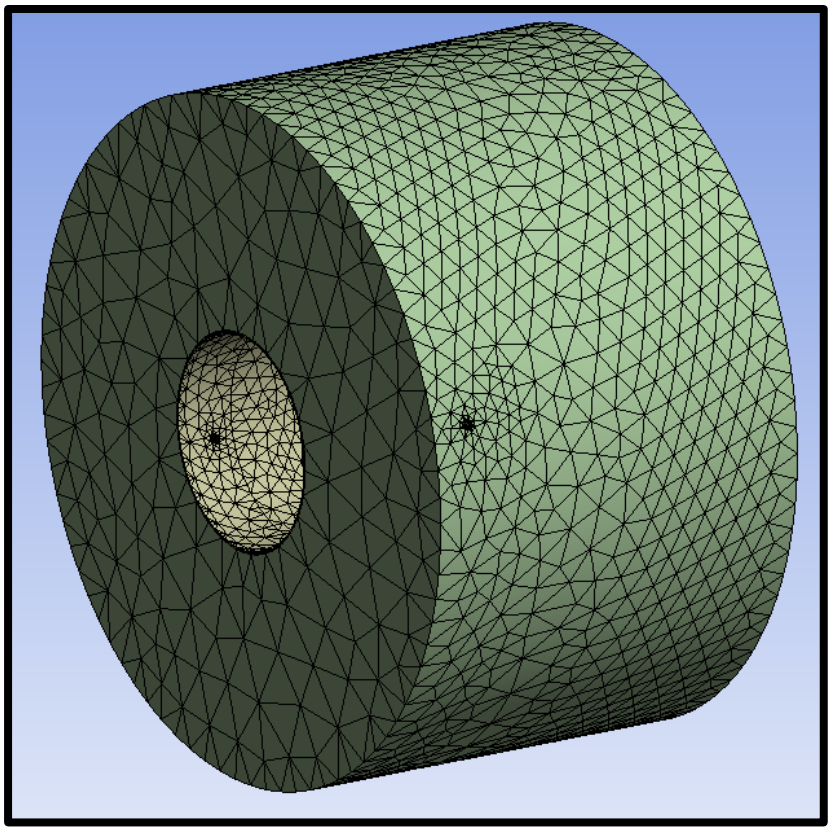

Figure 179: Mesh Used for the FEA Analysis of the Housing

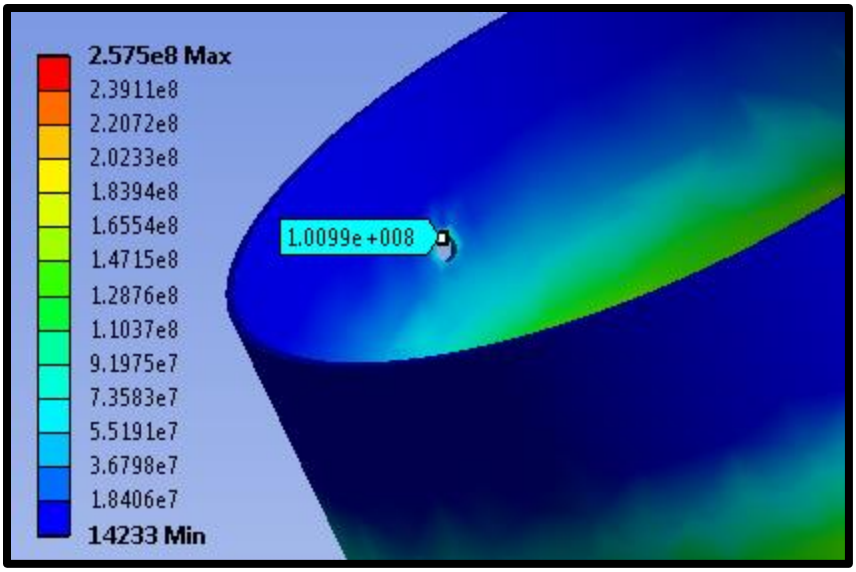

Figure 180: Stress Concentration in the Liner Near the Pin System Holes (Annotations in Pa)

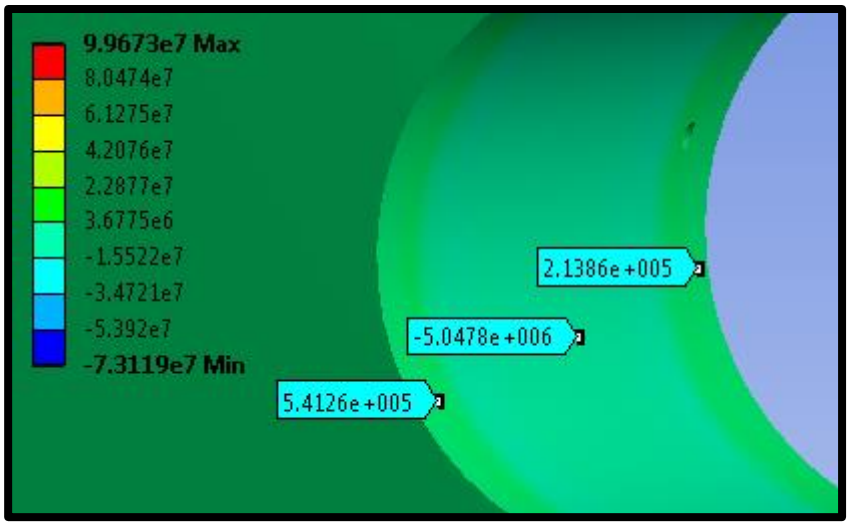

Figure 181: Axial Stress in the Wrap (Annotations in Pa)

Figures 182 and 183, respectively, show the mesh used for the FEA analysis of the axle and the von Mises stress distribution. In the former figure, deformation is magnified by a factor of 200, and annotations are given in Pa.

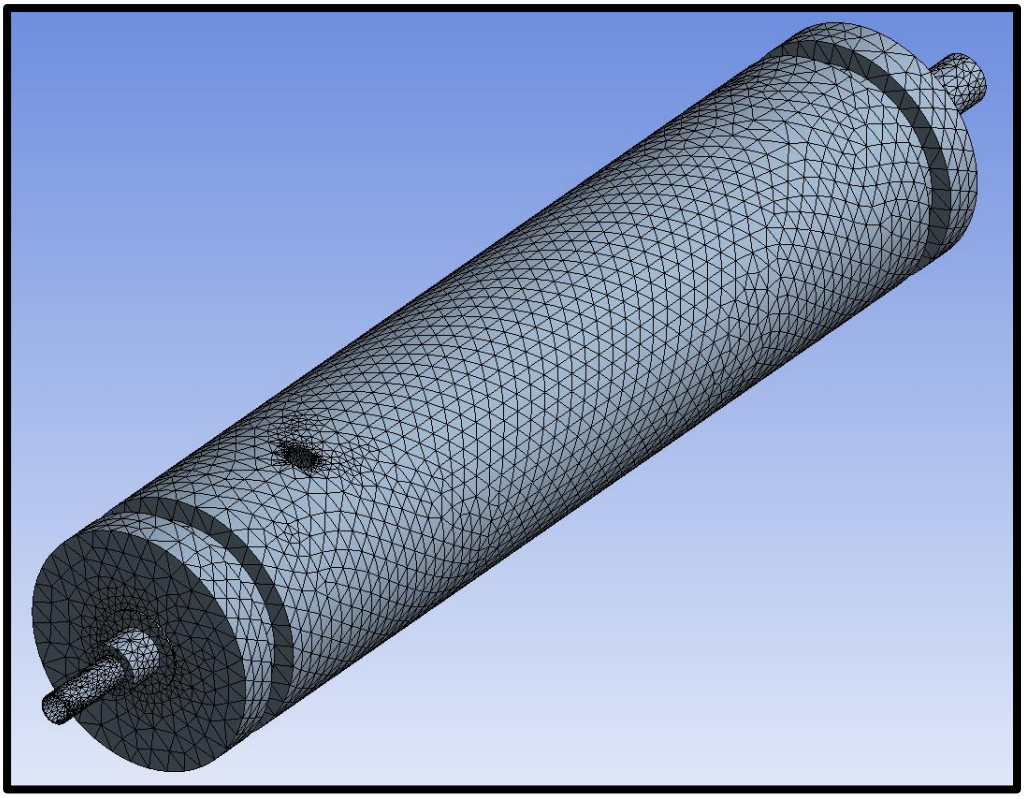

Figure 182: Mesh Used for the FEA Analysis of the Axle

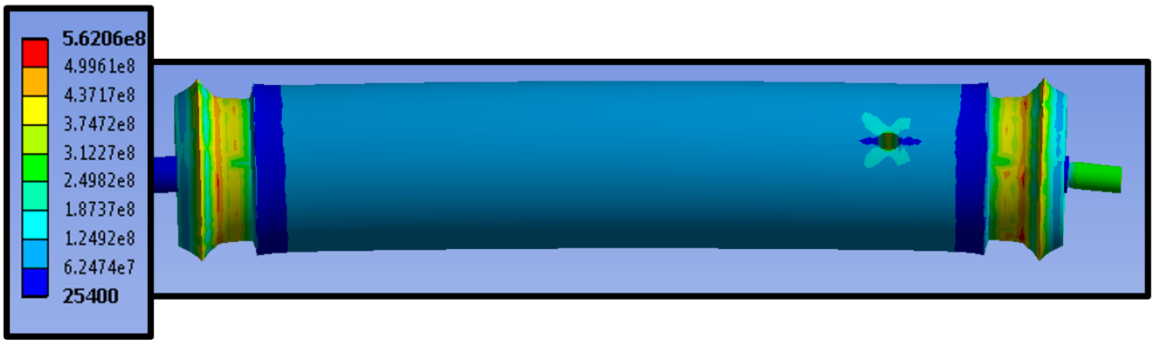

Figure 183: FEA Results, von Mises Stress Distribution in the Axle, Deformations Magnified 200x (Annotations in Pa)